Stefan Grebien

Position-related Parameter Estimation in Dense Multipath Environments

DOCTORAL THESIS

to achieve the university degree of

Doktor der technischen Wissenschaften

submitted to

Graz University of Technology

Supervisor

Assoc.Prof. Dipl.-Ing. Dr. Klaus Witrisal

Signal processing and speech communication laboratory

Graz, September 2020

d = 30.6 m

d = 61.2 m

ii

Abstract

In clear line-of-sight conditions, positioning systems using radio signal measurements are capable to deliver high accuracy. These conditions prevail outdoors, if the distances of the radio nodes to objects are large. However, in urban areas and especially indoors, the line-of-sight signal is interfered by diffuse reflections, the so-called dense multipath component. This dense multipath component biases the estimation of position-related parameters, e.g., the delay or the angle-of-arrival, if not treated appropriately. This thesis tackles the problem of estimating position-related parameters in dense multipath environments.

The first research contribution examines the achievable performance of position-related parameter estimators in dense multipath environments. To this end, the Cramér Rao lower bound is derived and analyzed for the delay and angle estimation problems with multiple-input multiple-output measurements. This theoretical investigation provides insights into the influence of system parameters, like the bandwidth or the number of antennas, on the estimation accuracy.

The second research contribution analyzes the concurrent estimation of the parameters of the dense multipath component and the position-related information contained in the line-of-sight component. To this end, deterministic maximum likelihood estimators are derived for ranging and direct positioning. Utilizing single-snapshot measurements and multiple antennas in a radio frequency identification backscatter setting, it is shown how the robustness and accuracy is increased if the dense multipath component is considered.

Finally, the third research contribution investigates the joint estimation and detection of specular multipath components within the dense multipath component. By increasing the bandwidth or the number of antennas, multipath components stemming from specular reflections can potentially be resolved. It is well known that these specular multipath components contain position-related information and positioning becomes possible even in obstructed line-of-sight conditions. However, the number of specular multipath components is unknown and has to be estimated jointly with their parameters. A detection threshold is derived and verified within a sparse Bayesian learning algorithm to reliably detect the number of resolvable specular multipath components while limiting the probability of estimating artifacts.

d = 30.3 m

d = 60.6 m

iv

Kurzfassung

Positionierungssysteme, die auf Funksignalmessungen basieren, können bei klarer Sichtverbindung eine hohe Genauigkeit liefern. Diese Bedingungen herrschen im Außenbereich vor, wenn die Abstände der Funkknoten zu Objekten groß genug sind. In städtischen Gebieten und insbesondere in Innenräumen wird die direkte Sichtverbindung jedoch durch diffuse Reflexionen, die sogenannte diffuse Mehrwegekomponente, gestört. Diese diffuse Mehrwegekomponente verschlechtert die Schätzung positionsbezogener Signalparameter, z.B. Laufzeit oder Ankunftswinkel, wenn sie nicht angemessen behandelt wird. Diese Dissertation befasst sich mit dem Problem der Schätzung positionsbezogener Signalparameter in diffusen Mehrwegeumgebungen.

Der erste Forschungsbeitrag untersucht die theoretisch erreichbare Genauigkeit positionsbezogener Parameterschätzer in diffusen Mehrwegeumgebungen. Zu diesem Zweck wird die Cramér Rao Schranke hergeleitet und die Laufzeit- und Winkelschätzung bei Messungen mit Mehrantennensystemen an Sender und Empfänger analysiert. Diese theoretische Untersuchung liefert Einblicke in den Einfluss von Systemparametern wie Bandbreite oder Anzahl der Antennen auf die Schätzgenauigkeit.

Der zweite Forschungsbeitrag analysiert die gemeinsame Schätzung der Parameter der diffusen Mehrwegekomponente und der informationstragenden Line-of-Sight Komponente. Zu diesem Zweck werden deterministische Maximum-Likelihood-Schätzer für die Laufzeitschätzung und für eine direkte Positionierung abgeleitet. Anhand von Einzelmessungen mit einem breitbandigen Mehrantennen-Lesegerät in einer RFID-Anwendung wird gezeigt, wie die Robustheit und Genauigkeit erhöht werden, wenn die diffuse Mehrwegekomponente berücksichtigt wird.

Der dritte Forschungsbeitrag untersucht die gemeinsame Schätzung und Detektion von Mehrwegekomponenten, welche als Spiegelreflexionen modelliert werden können. Durch Erhöhen der Bandbreite oder der Anzahl der Antennen können mehrere solche Spiegelreflexionen in den Messdaten aufgelöst werden. Es ist bekannt, dass diese Spiegelreflexionen positionsbezogene Informationen enthalten und die Positionierung daher auch unter eingeschränkter Sichtverbindung möglich machen. Die Anzahl der Spiegelreflexionen ist jedoch unbekannt und muss gemeinsam mit ihren Parametern geschätzt werden. Eine Detektionsschwelle innerhalb eines Bayes'schen Lernalgorithmus wird hergeleitet und verifiziert, um die Anzahl der auflösbaren Spiegelreflexionen zuverlässig zu erfassen und gleichzeitig die Wahrscheinlichkeit der Schätzung von Artefakten zu begrenzen.

d = 30.0 m

vi

d = 60.0 m

Acknowledgements

First and foremost, I want to express my sincere gratitude to Klaus for being my PhD advisor. You gave me the freedom to pursue the research avenues that I found interesting but at the same time you helped me get back on track when I got stuck in a dead end. Your ability to focus on the main aspects of a topic helped me a lot in organizing my ideas. Thanks.

I would also like to say thank you to Bernard H. Fleury for giving me the opportunity to work with you over the last three years, helping me deepen my understanding of array signal processing, and for agreeing to examine this work. I want to thank Holger Arthaber for helping me grasp basic aspects of micro-electronics and for agreeing to examine this work.

Next, I would like to say thank you to Erik and Josef. Our countless discussions about "Gott und die Welt" have been joyful, insightful and inspiring. Without you, this work would not have been finished. A huge thanks to the entire SPSC. It has been a pleasure working with all of you over the last years. Thanks to you, the lab has become more than a workplace to me.

Finally, a big thanks to Romy for always staying by my side, listening to my self doubts and for getting my mind away from work.

d = 29.7 m

viii

Contents

Acronyms

ADPS angular delay power spectum.

AEB angulation error bound.

AoA angle of arrival.

AoD angle of departure.

AWGN additive white Gaussian noise.

CDMA code division multiple access.

CRLB Cramér Rao lower bound.

DMC dense multipath component.

DML deterministic maximum likelihood.

DoA direction of arrival.

DOAPS direction of arrival power spectrum.

DoD direction of departure.

DODPS direction of departure power spectrum.

DPS delay power spectrum.

EFI equivalent Fisher information.

EFIM equivalent Fisher information matrix.

FIM Fisher information matrix.

KLD Kullback-Leibler divergence.

LOS line-of-sight.

LSE line-spectral estimation.

MF matched filter.

MIMO multiple-input multiple-output.

ML maximum likelihood.

MPC multipath component.

pdf probability distribution function.

PEB position error bound.

REB ranging error bound.

RFID radio frequency identification.

RVM relevance-vector machine.

RX receiver.

SBL sparse Bayesian learning.

SDR specular to dense ratio.

SIMO single-input multiple-output.

SINR signal to interference plus noise ratio.

SISO single-input single-output.

SMC specular multipath component.

SML stochastic maximum likelihood.

SNR signal to noise ratio.

TX transmitter.

UHF ultra-high frequency.

ULA uniform linear array.

UWB ultra-wideband.

AFFIDAVIT

I declare that I have authored this thesis independently, that I have
not used other than the declared sources/resources, and that I have
explicitly indicated all material which has been quoted either literally
or by content from the sources used. The text document uploaded
to TUGRAZonline is identical to the present doctoral thesis.

Date, Signature

d = 28.8 m

d = 57.6 m

Part I

Introduction to Researched Topics

d = 28.5 m

d = 57.0 m

Chapter 1

Introduction

Radio positioning, the determination of the position of people or objects using radio measurements, has become ubiquitous in our everyday life. In rural areas outdoors, global navigation satellite systems deliver accuracies down to the centimeter level [39]. In urban areas and especially indoors, the situation is more challenging as the satellite signals are attenuated by buildings and are affected by multipath propagation. Thus, local positioning systems are needed to provide reliable and accurate positioning indoors [110]. Some of these local positioning systems may be already in place, like WLAN or cellular [24], and its signals are used in an opportunistic fashion, or dedicated systems are deployed, like Bluetooth low energy or ultra-wideband (UWB) based systems [24, 25] [N15].

To achieve radio positioning, a two-way process is often utilized: first position-related parameters are extracted from received signals which are in turn used to determine the position, using dedicated positioning algorithms [39, 110]. The received signal can be modeled by the convolution of the measurement aperture and the propagation channel. While the propagation channel outdoors is often dominated by a strong line-of-sight (LOS) component, indoors the propagation channel is characterized by severe multipath propagation. This multipath propagation can be modeled by two components, the specular multipath components (SMCs) and the dense multipath component (DMC) [3, 61, 67, 71, 86]. SMCs can be seen as the part of the radio channel which is resolvable with the applied aperture in the spatial and temporal domain. The DMC is then everything which cannot be explained by SMCs and is often described by a stochastic model. Physical phenomena that can be used to explain the DMC include scattering at objects, diffraction around corners, but also reflections at small objects, like the roughness of surfaces [26, 48, 71]. Regarding positioning, the SMCs are described by position-related parameters, e.g., the delay or the angle-of-arrival. However, the SMCs are superimposed by the DMC, often acting as hindrance in the estimation procedure of the parameters of the SMCs [50, 56, 71, 73, 80].

Recent trends in hardware and software components enable not only large transmission bandwidth but also allow the usage of multi-antenna configurations at the transmitter (TX) and receiver (RX). These multiple-input multiple-output (MIMO) systems do not only provide means to estimate the direction of departure (DoD) and/or direction of arrival (DoA) of the SMCs, but also enables the estimation of the parameters of the stochastic DMC process from a single measured snapshot. Without multiple measurements per snapshot, the

estimation of the parameters of the DMC has to be aided by multiple consecutive measurements and a suitable tracking algorithm [73].

This thesis tackles the estimation of position-related parameters using radio signals. Its particular interest is set on the concurrent estimation of the parameters of the DMC and the SMC using MIMO systems.

1.1 Research Hypothesis

In this thesis, three research questions are formulated. The first topic targets fundamental limits on the estimation of position-related parameters and analyzes the influence of system parameters. The second topic treats the maximum likelihood (ML) estimation of position-related parameters and uses a passive RFID application to show the validity of the approach to measured data. Finally, the third topic treats the detection of SMCs showing how to reliably detect SMCs without being prone to estimation artifacts due to additive white Gaussian noise (AWGN) and the DMC. These three questions can be combined into the overall hypothesis of the thesis:

It is hypothesized that the use of multiple-input, multiple-output techniques can enable accurate and robust position-related parameter estimation in dense multipath environments.

1.1.1 Fundamental limits for position-related parameter estimation in dense multipath environments

It is well known that the SMCs contain position-related information [35,78,107]. Using a suitable channel and signal model combined with a geometric representation of the environment it is shown in [35,48,50,56] how this information relates to the achievable positioning accuracy. However, the DMC process conceals the influence of system parameters like bandwidth or the number of antenna elements and only a numeric evaluation is possible. Thus, the first research question tackled by this thesis is:

Research question 1

How accurate can position-related parameters be estimated in dense multipath environments and how do system parameters influence these estimation problems?

1.1.2 Estimation in dense multipath environments

Theory shows that the estimation performance is severely degraded if the DMC process is not included in the estimation procedure [50, 71] [N3]. This effect becomes especially relevant for non-UWB systems, as fewer multipath components (MPCs) are resolvable by the measurement aperture and the interference of the DMC process increases. To be able to estimate the parameters of the DMC process from single snapshot measurements, multi-antenna configurations are essential. These MIMO data provides multiple measurements needed for the estimation of the parameters of the DMC process and additionally enables the exploitation of angle-information. Thus, the second research question is:

4

1.2. CONTRIBUTIONS AND OUTLINE

Research question 2

Is it possible to increase the robustness and accuracy of the estimation of position-related parameters by concurrently estimating the parameters of the DMC process using MIMO systems?

1.1.3 Towards joint estimation and detection of specular multipath components

By increasing the number of antennas and increasing the signal bandwidth toward UWB systems, the number of resolvable MPCs increases. Classic algorithms [15, 30, 49, 69, 72, 75, 90] assume a certain (large) number of SMCs and estimate their parameters accordingly. Certainly, many of the estimated SMCs in such a way can be attributed to physically existing propagation paths. However, many of the estimated SMCs do not have a physical counterpart and should be regarded as estimation artifacts. These artifacts do not only clutter subsequent applications like positioning or channel modeling, but also influence the estimation of the actual components. Even if the algorithms are supported by an additional model-order estimation on the basis of information theoretic criteria, a positive model bias is often encountered [53]. Hence, the performance and reliability of positioning systems or the development of channel models building upon these estimated parameters are degraded by the artifacts. Thus, the third research question is given:

Research question 3

Is it possible to reliably infer the number of SMCs and their parameters in dense multipath environments?

1.2 Contributions and outline

This thesis consists of two parts. The introduction to the investigated topics is covered in Part I, and representative publications are attached in Part II. The first part starts by introducing the radio channel and signal models in Chapter 2. The next three chapters are tied to the three research questions. Finally, Chapter 6 answers the research questions and the hypothesis.

Own publications included in this thesis are referenced by [T#] and not included publications are marked by [N#]. Note that my early publications are published with my birth name *Hinteregger*.

List of included contributions

[T1] S. Hinteregger, E. Leitinger, P. Meissner, J. Kulmer, and K. Witrisal, "Bandwidth dependence of the ranging error variance in dense multipath," in *2016 24th European Signal Processing Conf. (EUSIPCO)*, Aug. 2016, pp. 733–737.

[T2] S. Hinteregger, E. Leitinger, P. Meissner, and K. Witrisal, "MIMO gain and bandwidth scaling for RFID positioning in dense multipath channels," in *2016 IEEE Int. Conf. RFID*, May 2016, pp. 1–6.

[T3] S. Grebien, J. Kulmer, F. Galler, M. Goller, E. Leitinger, H. Arthaber, and K. Witrisal, "Range estimation and performance limits for UHF-RFID backscatter channels," *IEEE Journal of Radio Frequency Identification*, vol. 1, no. 1, pp. 39–50, March 2017.

[T4] S. Grebien, F. Galler, D. Neunteufel, U. Mühlmann, S. J. Maier, H. Arthaber, and K. Witrisal, "Experimental evaluation of a UHF-MIMO RFID system for positioning in multipath channels," in *2019 IEEE International Conference on RFID Technology and Applications (RFID-TA)*, Sep. 2019, pp. 95–100.

[T5] S. Grebien, E. Leitinger, K. Witrisal, and B. H. Fleury, "Super-resolution channel estimation including the dense multipath component — A sparse variational Bayesian approach," in preperation for submission to IEEE Trans. Sig. Proc.

[T1] analyses the achievable ranging performance over a wide range of bandwidths and different channel parameters. It analyses measured data and shows that the ranging error bound (REB), i.e., the Cramér Rao lower bound (CRLB) for the ranging problem, is (approximately) achievable at intermediate and high bandwidth, using a genie aided ML estimator. Furthermore, an approximation for the performance bound is derived, related to the accuracy of the matched filter (MF) estimator.

[T2] employs the REB to a wideband passive RFID setup and highlights differences for fully correlated and uncorrelated individual channels. By adding diversity, i.e., exploiting multi-antenna configurations, the gain in ranging performance is examined and the achievable positioning accuracy is quantified for monostatic and bistatic setups.

[T3] develops an algorithm capable of estimating the parameters of the LOS component for an RFID system, exploiting MIMO data, in a dense multipath environment. It analyzes measured data from two scenarios, a laboratory and an industrial hall, applies the estimator over a wide range of bandwidths and compares its performance with the theoretical limits.

[T4] designs a direct positioning algorithm capable of exploiting information included in the DMC process for positioning. The algorithm coherently processes measurements from closely-spaced antennas, thus, it inherently adds angle information to the position solution. A dual-frequency passive RFID system is analyzed and a position error below $15\,\mathrm{cm}$ is achieved for $80\,\%$ of the measured data using a bandwidth of $25\,\mathrm{MHz}$.

[T5] develops a Type-II ML estimator with a hierarchical Gaussian prior for a single-input multiple-output (SIMO) system. It derives an adapted threshold to reliably detect SMCs and limits the number of estimation artifacts by deriving the excursion probability of a non-stationary χ^2 random field. The algorithm is tested with synthetic data and compared to a Type-I deterministic maximum likelihood (DML) estimator. Finally, the estimated parameters of the SMCs are compared to a room-geometry-related prediction which highlights the performance of the algorithm using measured data.

CHAPTER 1. INTRODUCTION

List of not included contributions

[N1] S. Hinteregger, J. Kulmer, M. Goller, F. Galler, H. Arthaber, and K. Witrisal, "UHF-RFID backscatter channel analysis for accurate wideband ranging," in *2017 IEEE Int. Conf. RFID*, May 2017, pp. 117–123.

[N2] J. Kulmer, S. Grebien, M. Rath, and K. Witrisal, "On the unimportance of phase-coherent measurements for beampattern-assisted positioning," in *2018 IEEE Wireless Communications and Networking Conference (WCNC)*, April 2018, pp. 1–6.

[N3] K. Witrisal, E. Leitinger, S. Hinteregger, and P. Meissner, "Bandwidth scaling and diversity gain for ranging and positioning in dense multipath channels," *IEEE Wireless Commun. Lett.*, vol. 5, no. 4, pp. 396–399, Aug. 2016.

[N4] T. Wilding, S. Grebien, U. Mühlmann, and K. Witrisal, "Accuracy bounds for array-based positioning in dense multipath channels," *Sensors*, vol. 18, no. 12, 2018.

[N5] T. Wilding, S. Grebien, E. Leitinger, U. Mühlmann, and K. Witrisal, "Single-anchor, multipath-assisted indoor positioning with aliased antenna arrays," in *Proc. Asilomar-18*, Pacifc Grove, CA, USA, Oct. 2018, pp. 525–531.

[N6] T. Wilding, S. Grebien, U. Mühlmann, and K. Witrisal, "AoA and ToA accuracy in dense multipath channels," in *2018 IEEE ICL-GNSS*, June 2018.

[N7] E. Leitinger, S. Grebien, B. H. Fleury, and K. Witrisal, "Detection and estimation of a spectral line in MIMO systems," submitted to Asilomar 2020.

[N8] E. Leitinger, S. Grebien, X. Li, F. Tufvesson, and K. Witrisal, "On the use of MPC amplitude information in radio signal based SLAM," in *Proc. IEEE SSP-18*, Freiburg, Germany, June 2018, pp. 633–637.

[N9] E. Leitinger, S. Grebien, and K. Witrisal, "Multipath-based SLAM exploiting AoA and amplitude information," in *Proc. IEEE ICC-19*, 5 2019.

[N10] F. Galler, S. Hinteregger, T. Faseth, N. Leder, K. Witrisal, G. Magerl, and H. Arthaber, "Performance evaluation and verification of Spread-Spectrum based UHF RFID ranging," in *2017 IEEE Int. Conf. RFID*, May 2017, pp. 124–129.

[N11] F. Galler, S. Grebien, T. Faseth, K. Witrisal, G. Magerl, and H. Arthaber, "Extension of an SDR UHF RFID testbed for MIMO and monostatic time of flight based ranging," *IEEE Journal of Radio Frequency Identification*, vol. 1, no. 1, pp. 32–38, March 2017.

[N12] J. Kulmer, S. Grebien, E. Leitinger, and K. Witrisal, "Delay estimation in presence of dense multipath," *IEEE Wireless Commun. Lett.*, vol. 8, no. 5, pp. 1481–1484, Oct 2019.

[N13] D. Neunteufel, S. Grebien, S. Hechenberger, K. Witrisal, and H. Arthaber, "Coherent chirp generation by narrowband transceiver chips for ToF indoor localization," in *2020 IEEE Global Communications Conference: Wireless Communications (Globecom2020 WC)*, Taipei, Taiwan, Dec. 2020, submitted.

[N14] J. Kulmer, E. Leitinger, S. Grebien, and K. Witrisal, "Anchorless cooperative tracking using multipath channel information," *IEEE Trans. Wireless Commun.*, vol. PP, no. 99, pp. 1–1, 2018.

[N15] J. Kulmer, S. Hinteregger, B. Großwindhager, M. Rath, M. S. Bakr, E. Leitinger, and K. Witrisal, "Using DecaWave UWB transceivers for high-accuracy multipath-assisted indoor positioning," in *2017 IEEE International Conference on Communications Workshops (ICC Workshops)*, May 2017, pp. 1239–1245.

[N16] J. Kulmer, E. Leitinger, P. Meissner, S. Hinteregger, and K. Witrisal, "Cooperative localization and tracking using multipath channel information," in *Localization and GNSS (ICL-GNSS), 2016 Int. Conf.*, Jun. 2016.

[N17] F. Geigl, C. Moik, S. Hinteregger, and M. Goller, "Using machine learning and RFID localization for advanced logistic applications," in *2017 IEEE Int. Conf. RFID*, May 2017, pp. 73–74.

[N18] A. N. Hong, M. Rath, E. Leitinger, S. Hinteregger, K. N. Van, and K. Witrisal, "Channel capacity analysis of indoor environments for location-aware communications," in *2016 IEEE Global Commun. Conf.: Second IEEE Int. Workshop on Localization and Tracking: Indoors, Outdoors, and Emerging Networks (GC16 Workshops LION)*, Washington, USA, Dec 2016, pp. 1–6.

[N19] A. N. Hong, M. Rath, J. Kulmer, S. Grebien, K. N. Van, and K. Witrisal, "Gaussian process modeling of UWB multipath components," in *2018 IEEE Seventh International Conference on Communications and Electronics (ICCE)*, July 2018, pp. 291–296.

[N20] K. Witrisal, S. Hinteregger, J. Kulmer, E. Leitinger, and P. Meissner, "High-accuracy positioning for indoor applications: RFID, UWB, 5G, and beyond," in *2016 IEEE Int. Conf. RFID*, May 2016, pp. 1–7.

[N21] B. Großwindhager, M. Rath, J. Kulmer, S. Hinteregger, M. Bakr, C. A. Boano, K. Witrisal, and K. Römer, "UWB-based single-anchor low-cost indoor localization system," in *Proceedings of the 15th ACM Conference on Embedded Network Sensor Systems*, ser. SenSys '17. New York, NY, USA: ACM, 2017, pp. 34:1–34:2.

Chapter 2

Channel and signal model

This thesis treats the estimation of the position or of position-related quantities using radio channel measurements. Position-related quantities can, e.g., be the distance, the angle of departure (AoD) or the angle of arrival (AoA) between a TX and an RX, or combinations of these parameters. This thesis tries to highlight the influence of the so-called dense multipath component (DMC) on the estimation and detection performance. In most contributions to this thesis, this DMC is seen as a channel-inherent interference to the estimation of position-related quantities, from so-called specular multipath components (SMCs). However, it is also possible that parameters describing the DMC include position-related information [48] [N3] [T4].

In the individual contributions to this thesis, different channel and signal models are employed, depending on the setup and the available infrastructure. For example, in three contributions [T2–T4], a passive RFID setup is utilized. Thus, in this chapter we will first introduce the basic wireless channel model in Section 2.1. Next, the received signal is described in Section 2.2 which is, based on a MIMO setup, sampled in the delay and spatial domains to arrive at a discrete signal model in Section 2.3. Section 2.5 introduces the basis to derive many closed-form solutions in this thesis, the so-called single-SMC in DMC channel model. Finally, in Section 2.6 the RFID-MIMO system model is derived.

2.1   Channel model

The propagation channel in-between a TX antenna and an RX antenna models the interactions of an electromagnetic wave with its surrounding environment. In literature different levels of abstraction are used to model its behavior. While ray-tracing tries to solve (or approximate) the Maxwell equations using an accurate geometric model including boundary conditions, in communication applications the propagation channel is often described by few parameters, e.g., the path-loss and the root-mean-square delay spread. The choice for a certain level of abstraction is highly dependent on the application and on system parameters like bandwidth and the number of employed antennas.

To be able to cope with the different system configurations treated in this thesis, a deterministic-stochastic channel model is utilized [3, 56, 61, 68, 73]. The

9

deterministic part models propagation effects related directly to the geometry of the scenario and thus carries position-related information. This part is described by so-called specular multipath components (SMC) and is described in more detail in Section 2.1.1. The stochastic part models propagation effects that cannot be attributed directly to the geometry of the scenario. However, position-related information can still be hidden in the parameters describing the underlying statistical model. This part is composed of a multitude of low-amplitude MPCs, called a dense multipath component (DMC) and is described in more detail in Section 2.1.2.

We consider a scenario with a TX and an RX distributed and operating in a multipath environment. Such a multipath environment is characterized by reflections at objects, so called multipath components (MPCs). The direction-delay spread function between a TX and an RX for a plane wave model in the far-field[1] can be defined as [26, 50, 60, 71]

$$
\begin{aligned}
h(\tau, \boldsymbol{\Omega}_{\mathrm{TX}}, \boldsymbol{\Omega}_{\mathrm{RX}}; \boldsymbol{p}_{\mathrm{TX}}, \boldsymbol{p}_{\mathrm{RX}}) =& h_{\mathrm{SMC}}(\tau, \boldsymbol{\Omega}_{\mathrm{TX}}, \boldsymbol{\Omega}_{\mathrm{RX}}; \boldsymbol{p}_{\mathrm{TX}}, \boldsymbol{p}_{\mathrm{RX}}) \\
&+ h_{\mathrm{DMC}}(\tau, \boldsymbol{\Omega}_{\mathrm{TX}}, \boldsymbol{\Omega}_{\mathrm{RX}}; \boldsymbol{p}_{\mathrm{TX}}, \boldsymbol{p}_{\mathrm{RX}}).
\end{aligned}
\tag{2.1}
$$

Eq. (2.1) is a function of the delay τ, the unit-length DoD at the TX $\boldsymbol{\Omega}_{\mathrm{TX}} = [\cos(\varphi_{\mathrm{D}}), \sin(\varphi_{\mathrm{D}})]^{\mathrm{T}}$ with φ_{D} as the AoD, and the unit-length DoA at the RX $\boldsymbol{\Omega}_{\mathrm{RX}} = [\cos(\varphi_{\mathrm{A}}), \sin(\varphi_{\mathrm{A}})]^{\mathrm{T}}$ with φ_{A} as the AoA.[2] Furthermore, the direction-delay spread function is parametrized by the positions of the TX $\boldsymbol{p}_{\mathrm{TX}}$ and the RX $\boldsymbol{p}_{\mathrm{RX}}$, highlighting the influence of these. The right hand side of (2.1) is split into the sum of two terms, the SMCs and the DMC.

In Fig. 2.1 the floorplan of a room where measurements have been performed is depicted. It includes the TX (■) at position $\boldsymbol{p}_{\mathrm{TX}}$ and the RX (●) at $\boldsymbol{p}_{\mathrm{RX}}$. The DMC (〰) and some SMCs are illustrated, including the LOS component (——) and three first-order reflections (——,——,——).

You certainly noticed the small pictures in the corners of this thesis. We performed many measurements that we often highlight in our presentations by short videos. I did not want to sacrifice these illustrative videos, therefore I decided to use a flipbook. The little pictures in the corners of this thesis are always all measurements of the setup depicted in Fig. 2.1 for different bandwidths. The grey square in Fig. 2.1 is made up of 4686 individual points () where measurements have been performed, using an automated measurement system.[3] Further details about the measurements and the setup can be found in [T1]. The distance, given below the pictures, is the distance the transmitted pulse has traveled. Throughout the thesis I will use the different flipbooks to highlight certain aspects. And now it is time for some action. Have fun looking at the 'videos'.

---

[1]In our context, the plane wave far-field model means that the distance between the TX/RX to the reflecting objects is large enough. Otherwise, a spherical wave model has to be employed.

[2]The contributions to this thesis are restricted to horizontal-only propagation. However, the extensions to 3-dimensions are straightforward.

[3]In fact, there are 4 of these grey squares and 8 TX positions, hence 149952 measurements have been performed in this room alone.

10
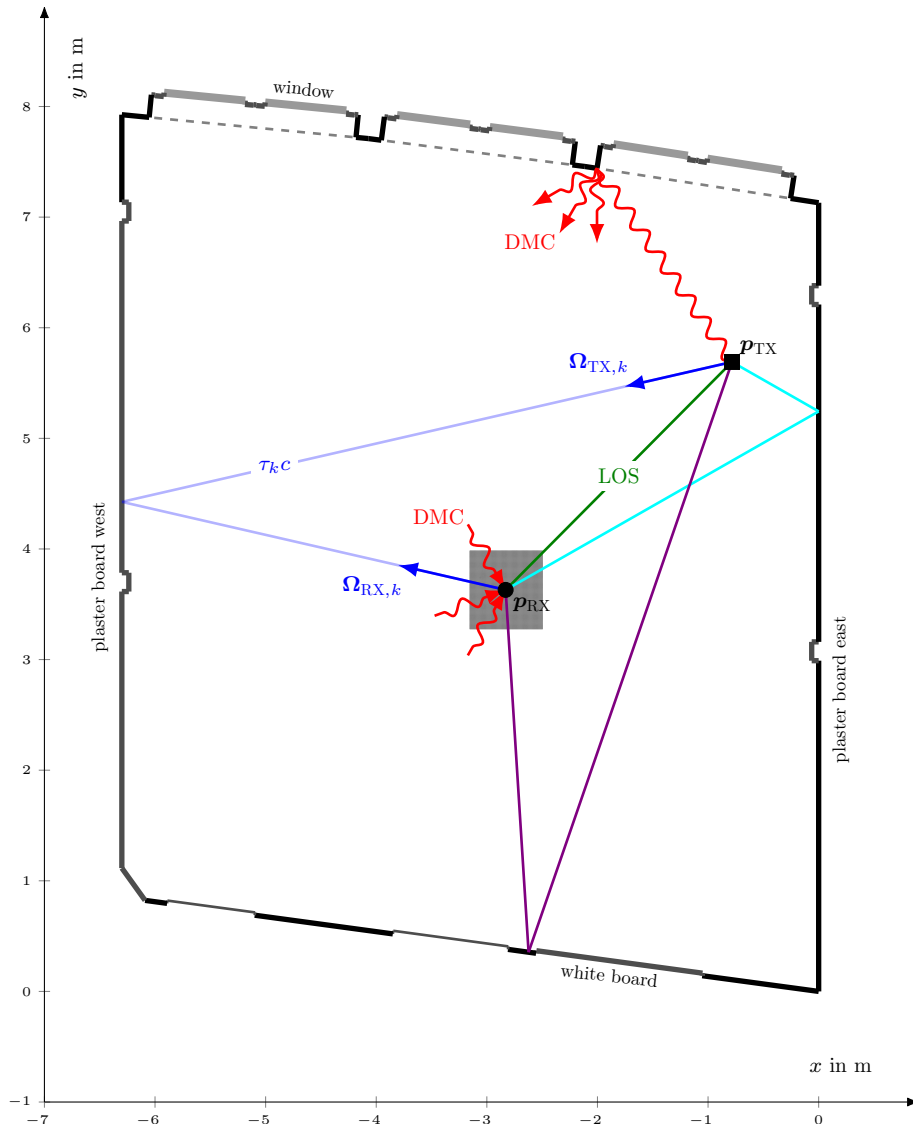
Figure 2.1: Floorplan of the room where measurements have been performed, including the TX (■) at position $\boldsymbol{p}_{\mathrm{TX}}$ and the RX (●) at position $\boldsymbol{p}_{\mathrm{RX}}$. Some exemplary SMCs are shown, including the LOS component (——) and three SMCs based on first-order reflections (——,——,——). For the kth SMC the direction of departure, the direction of arrival and the delay are highlighted. The generation of the DMC (〜〜) is illustrated by scattering at an edge. Furthermore, the positions () where measurements have been performed are illustrated, forming a rectangular grid with a spacing of $2\,\mathrm{cm}$ in x and y. These are the positions used throughout this thesis in the flipbook.

2.1.1   Specular Multipath Components

The first part in (2.1) describes specular wave components. Each of these SMCs may be described by a single plane wave [26, 28]

$$h_{\mathrm{SMC},k}(\tau, \boldsymbol{\Omega}_{\mathrm{TX}}, \boldsymbol{\Omega}_{\mathrm{RX}}; \boldsymbol{p}_{\mathrm{TX}}, \boldsymbol{p}_{\mathrm{RX}}) \tag{2.2}$$
$$= \bar{\alpha}_k \delta(\tau - \tau_k) \delta(\boldsymbol{\Omega}_{\mathrm{TX}} - \boldsymbol{\Omega}_{\mathrm{TX},k}) \delta(\boldsymbol{\Omega}_{\mathrm{RX}} - \boldsymbol{\Omega}_{\mathrm{RX},k}).$$

11

The kth SMC is described by its complex amplitude $\bar{\alpha}_k$, its delay $\tau_k = \frac{d_k}{c}$, with d_k as the propagation distance, its unit-length DoD $\mathbf{\Omega}_{\mathrm{TX},k} = [\cos(\varphi_{\mathrm{D},k}), \sin(\varphi_{\mathrm{D},k})]^{\mathrm{T}}$, and its unit-length DoA $\mathbf{\Omega}_{\mathrm{RX},k} = [\cos(\varphi_{\mathrm{A},k}), \sin(\varphi_{\mathrm{A},k})]^{\mathrm{T}}$. In Fig. 2.1 these parameters are illustrated for the SMC stemming from the reflection at plaster board west (——). It is important to note, that all four parameters describing an SMC, $\bar{\alpha}_k$, and the dispersion parameters τ_k, $\mathbf{\Omega}_{\mathrm{TX},k}$, and $\mathbf{\Omega}_{\mathrm{RX},k}$, are functions of the positions of the TX $\boldsymbol{p}_{\mathrm{TX}}$ and the RX $\boldsymbol{p}_{\mathrm{RX}}$. For easier readability, we show this dependency only on the left hand side of (2.2). Furthermore, we included the complex beampattern[4] of the antenna in the complex amplitude $\bar{\alpha}_k$. Note that we will use the terms *delay* and *propagation distance* interchangeably throughout this thesis.

Examples of SMCs are the LOS (—— in Fig. 2.1), the direct path between a TX and an RX antenna, and reflections at flat surfaces (e.g., ——,——, —— in Fig. 2.1). In Fig. 2.1 only first-order reflections are depcited. However, of course also higher-order reflections are possible. By the superposition principle, these K plane waves can be combined to form the specular part of (2.1)

$$h_{\mathrm{SMC}}(\tau, \mathbf{\Omega}_{\mathrm{TX}}, \mathbf{\Omega}_{\mathrm{RX}}; \boldsymbol{p}_{\mathrm{TX}}, \boldsymbol{p}_{\mathrm{RX}}) = \sum_{k=1}^{K} h_{\mathrm{SMC},k}(\tau, \mathbf{\Omega}_{\mathrm{TX}}, \mathbf{\Omega}_{\mathrm{RX}}; \boldsymbol{p}_{\mathrm{TX}}, \boldsymbol{p}_{\mathrm{RX}}) \quad (2.3)$$

$$= \sum_{k=1}^{K} \bar{\alpha}_k \delta(\tau - \tau_k) \delta(\mathbf{\Omega}_{\mathrm{TX}} - \mathbf{\Omega}_{\mathrm{TX},k}) \delta(\mathbf{\Omega}_{\mathrm{RX}} - \mathbf{\Omega}_{\mathrm{RX},k}).$$

Flipbook: Let's have a look at some SMCs that can be attributed to certain reflections in the room depicted in Fig. 2.1. Look at the flipbook in the top right and bottom right corner, utilizing a bandwidth of 4 GHz and 2 GHz, respectively, centered at a frequency of 7 GHz. At a distance of about 2.8 m, the LOS arrives at the center of the measurement table.[5] The SMC at 4.1 m stems from the reflection at plaster board east. The next identifiable SMC travels over the table from 5.7 m to 6.5 m and corresponds to the reflection from the window.[6] The next SMC is only visible in approximately half the table, arrives at 8.8 m and stems form the white board. By looking at the floor plan in Fig. 2.1, a reflection stemming from the southern wall around the white board would be expected to arrive slightly after the white board reflection. However, as the white board is made from metal, while the wall is plaster board, the reflection is probably already dampened too much to be visible. The reflection arriving at 9.4 m is a second-order reflection, which is first reflected at plaster board east and then at the white board.

2.1.2 Dense Multipath Component

Empirical observations [3, 48, 61, 68] show that a description with solely SMCs does not suffice to accurately model the radio channel. This phenomenon can be explained with a multitude of non-specular waves which arrive at the RX antenna [26]. These non-specular waves stem from all propagation effects that

---

[4]We usually assume non-dispersive antennas. Dispersive antennas could be included by introducing additional components or by changing the aperture function given in (2.10).

[5]The following distances will all be given with respect to the center of the measurement table.

[6]The windows in the room where the measurements have been performed are metal coated.

do not result in SMCs, e.g., scattering at objects, diffraction around corners, but also reflections at small objects, including the roughness of surfaces [48]. Based on the resolution of the used measurement equipment, all MPCs not modeled as SMCs are lumped together in a single term, called *dense* multipath component (DMC) $h_{\mathrm{DMC}}(\tau, \boldsymbol{\Omega}_{\mathrm{TX}}, \boldsymbol{\Omega}_{\mathrm{RX}}; \boldsymbol{p}_{\mathrm{TX}}, \boldsymbol{p}_{\mathrm{RX}})$. This DMC is modeled as a complex circular Gaussian random process, i.e., [26, 41, 48, 59, 71],

$$\mathbb{E}\big[h_{\mathrm{DMC}}(\tau, \boldsymbol{\Omega}_{\mathrm{TX}}, \boldsymbol{\Omega}_{\mathrm{RX}}; \boldsymbol{p}_{\mathrm{TX}}, \boldsymbol{p}_{\mathrm{RX}})\big] = 0, \tag{2.4}$$

$$\mathbb{E}\big[h_{\mathrm{DMC}}(\tau, \boldsymbol{\Omega}_{\mathrm{TX}}, \boldsymbol{\Omega}_{\mathrm{RX}}; \boldsymbol{p}_{\mathrm{TX}}, \boldsymbol{p}_{\mathrm{RX}})h_{\mathrm{DMC}}^{*}(\tau', \boldsymbol{\Omega}_{\mathrm{TX}}', \boldsymbol{\Omega}_{\mathrm{RX}}'; \boldsymbol{p}_{\mathrm{TX}}, \boldsymbol{p}_{\mathrm{RX}})\big] \tag{2.5}$$
$$= S_{\mathrm{DMC}}(\tau, \boldsymbol{\Omega}_{\mathrm{TX}}, \boldsymbol{\Omega}_{\mathrm{RX}}; \boldsymbol{p}_{\mathrm{TX}}, \boldsymbol{p}_{\mathrm{RX}})\delta(\tau - \tau')\delta(\boldsymbol{\Omega}_{\mathrm{TX}} - \boldsymbol{\Omega}_{\mathrm{TX}}')\delta(\boldsymbol{\Omega}_{\mathrm{RX}} - \boldsymbol{\Omega}_{\mathrm{RX}}').$$

The random process describing the DMC is zero-mean (2.4), uncorrelated in the delay, the direction of departure and the direction of arrival (2.5), and is thus described solely by its variance $\mathbb{E}[|h_{\mathrm{DMC}}(\tau, \boldsymbol{\Omega}_{\mathrm{TX}}, \boldsymbol{\Omega}_{\mathrm{RX}}; \boldsymbol{p}_{\mathrm{TX}}, \boldsymbol{p}_{\mathrm{RX}})|^{2}]$. The angular delay power spectrum (ADPS) $S_{\mathrm{DMC}}(\tau, \boldsymbol{\Omega}_{\mathrm{TX}}, \boldsymbol{\Omega}_{\mathrm{RX}}; \boldsymbol{p}_{\mathrm{TX}}, \boldsymbol{p}_{\mathrm{RX}})$ is often denoted as power profile in literature [61].

Flipbook: Next, we will make use of the flipbooks in the top left and bottom left corners, using a bandwidth of 1000 MHz and 500 MHz, respectively. Of course, these flipbooks run from the back to the front. The colorbar is in such a way that white color is 30 dB below the maximum value. By looking at the first few pictures (before the LOS arrives), we see that the noise floor corresponds to pretty white pixels. By playing the flipbooks, the LOS and some additional SMCs can be identified. However, after the first few meters, there seems to be an increased noise floor which diminishes towards larger distances. This is what we call DMC. After about 35 m the pictures again are rather white, meaning that the DMC process has been attenuated to values below the AWGN noise floor.

2.2 Multiple input, multiple output signal model

We place the origin of a coordinate system at the position of the RX $\boldsymbol{p}_{\mathrm{RX}}$. The position of a receiving antenna in close vicinity of $\boldsymbol{p}_{\mathrm{RX}}$ is then solely determined by $\Delta\boldsymbol{p}_{\mathrm{RX}}$. For the transmitting antenna we define its position as $\Delta\boldsymbol{p}_{\mathrm{TX}}$ with respect to a coordinate system placed at $\boldsymbol{p}_{\mathrm{TX}}$. The received signal in complex baseband is given as[7]

$$r(t, \Delta\boldsymbol{p}_{\mathrm{TX}}, \Delta\boldsymbol{p}_{\mathrm{RX}}) = \int_{\mathbb{S}_{1}}\int_{\mathbb{S}_{1}}\int a(t, \tau, \boldsymbol{\Omega}_{\mathrm{TX}}, \boldsymbol{\Omega}_{\mathrm{RX}}, \Delta\boldsymbol{p}_{\mathrm{TX}}\Delta\boldsymbol{p}_{\mathrm{RX}}) \tag{2.6}$$
$$\times h(\tau, \boldsymbol{\Omega}_{\mathrm{TX}}, \boldsymbol{\Omega}_{\mathrm{RX}})d\tau ds_{1}(\boldsymbol{\Omega}_{\mathrm{TX}})ds_{1}(\boldsymbol{\Omega}_{\mathrm{RX}}) + w(t)$$

where $w(t)$ is circular symmetric complex AWGN with double-sided power spectral density of $N_{0}/2$. For the integration over the 1-sphere $\mathbb{S}_{1}$ we need the differential angle $ds_{1}(\boldsymbol{\Omega}_{\mathrm{TX}}) = d\varphi_{\mathrm{D}}$ and $ds_{1}(\boldsymbol{\Omega}_{\mathrm{RX}}) = d\varphi_{\mathrm{A}}$ [44].[8] To reduce notational complexity we dropped the parametrization by the positions of the TX and RX. In (2.6) the aperture function $a(t, \tau, \boldsymbol{\Omega}_{\mathrm{TX}}, \boldsymbol{\Omega}_{\mathrm{RX}}, \Delta\boldsymbol{p}_{\mathrm{TX}}, \Delta\boldsymbol{p}_{\mathrm{RX}})$ is introduced.

---

[7]When not specified, the integration domain of the integrals is the entire range of the integration variable(s).

[8]In 3-dimensions the integration is over the 2-sphere and the differential solid angle $s_{2}(\Omega)$ is needed [44].

Wideband aperture function   Classical wideband multipath models [26, 28, 65, 71] make use of the assumption that the envelope of the observed signals are indistinguishable in a local area, around each, the TX and the RX.[9] This assumption leads to the wideband aperture function

$$a_{\mathrm{wb}}(t, \tau, \boldsymbol{\Omega}_{\mathrm{TX}}, \boldsymbol{\Omega}_{\mathrm{RX}}, \Delta\boldsymbol{p}_{\mathrm{TX}}, \Delta\boldsymbol{p}_{\mathrm{RX}}) = \mathrm{e}^{-j2\pi f_{\mathrm{c}}(\tau - \boldsymbol{\Omega}_{\mathrm{TX}}^{\mathrm{T}}\Delta\boldsymbol{p}_{\mathrm{TX}}/c - \boldsymbol{\Omega}_{\mathrm{RX}}^{\mathrm{T}}\Delta\boldsymbol{p}_{\mathrm{RX}}/c)} \\ \times s_{\mathrm{TX}}(t - \tau), \tag{2.7}$$

with f_{c} as carrier frequency and $s_{\mathrm{TX}}(t)$ as the transmitted pulse shape[10]. For the RX the above assumption is justified if [29]

$$\max_{l,l'} \frac{B}{c}\|\Delta\boldsymbol{p}_{\mathrm{RX}}^{(l)} - \Delta\boldsymbol{p}_{\mathrm{RX}}^{(l')}\| \ll 1, \tag{2.8}$$

with c as the speed-of-light and B as the signal bandwidth. A different approach is used in [26], where the frequency-space cross product term $\frac{2\pi f}{c}\boldsymbol{\Omega}_{\mathrm{RX}}^{\mathrm{T}}\Delta\boldsymbol{p}_{\mathrm{RX}}$ is used to define a local area[11]. The frequency-space cross product is limited to be below $\frac{\pi}{2}$. Then, by assuming that the maximum difference between two observed frequencies is B and the maximum space displacement is the local area L_{A}, a condition on the size of the local area is found as

$$L_{\mathrm{A}} < \frac{c}{4B}. \tag{2.9}$$

It is important to note that the local area is independent of the carrier frequency f_c. However, for array processing the carrier wavelength is paramount in defining the size of the array. For an ultrawideband signal with a bandwidth of 1 GHz, the local area has to be below 7.5 cm. If this signal is centered at a carrier frequncy of 6 GHz, a 4-element uniform linear array (ULA) with an antenna-spacing of $\lambda/2$ already violates the local area assumption.

Ultra-wideband aperture function   To overcome this problem, we employ the ultra-wideband aperture function

$$a_{\mathrm{uwb}}(t, \tau, \boldsymbol{\Omega}_{\mathrm{TX}}, \boldsymbol{\Omega}_{\mathrm{RX}}, \Delta\boldsymbol{p}_{\mathrm{TX}}, \Delta\boldsymbol{p}_{\mathrm{RX}}) = \mathrm{e}^{-j2\pi f_{\mathrm{c}}(\tau - \boldsymbol{\Omega}_{\mathrm{TX}}^{\mathrm{T}}\Delta\boldsymbol{p}_{\mathrm{TX}}/c - \boldsymbol{\Omega}_{\mathrm{RX}}^{\mathrm{T}}\Delta\boldsymbol{p}_{\mathrm{RX}}/c)} \\ \times s_{\mathrm{TX}}(t - (\tau - \boldsymbol{\Omega}_{\mathrm{TX}}^{\mathrm{T}}\Delta\boldsymbol{p}_{\mathrm{TX}}/c - \boldsymbol{\Omega}_{\mathrm{RX}}^{\mathrm{T}}\Delta\boldsymbol{p}_{\mathrm{RX}}/c)). \tag{2.10}$$

Compared to (2.7), the envelope of the received signal is shifted additionally by the relative delays due to the DoD and DoA. In the following, we will usually employ the ultra-wideband aperture function, if not otherwise stated. Hence, $a(t, \tau, \boldsymbol{\Omega}_{\mathrm{TX}}, \boldsymbol{\Omega}_{\mathrm{RX}}, \Delta\boldsymbol{p}_{\mathrm{TX}}, \Delta\boldsymbol{p}_{\mathrm{RX}}) \equiv a_{\mathrm{uwb}}(t, \tau, \boldsymbol{\Omega}_{\mathrm{TX}}, \boldsymbol{\Omega}_{\mathrm{RX}}, \Delta\boldsymbol{p}_{\mathrm{TX}}, \Delta\boldsymbol{p}_{\mathrm{RX}})$.

---

[9]This assumption is often called *narrowband* assumption. Here, we did not want to use this term, as the relative delay to the center of gravity of the array is still included in the received signal. A *full* narrowband assumption, would neglect this delay as well and all waves would impinge simultaneously, only distinguishable by their phases.

[10]In this description of the signal and channel model the influence of the antenna is included in the spread function (2.1). However, one could easily change the aperture function to include the influence of an antenna.

[11]Here, only the local area for the RX is analyzed. For the TX similar considerations can be derived.

Spatio-temporal signals and the Fourier transform   By inspecting the integrals with respect to $\boldsymbol{\Omega}_{\mathrm{TX}}$ and $\boldsymbol{\Omega}_{\mathrm{RX}}$ in (2.6) with the wideband aperture function given in (2.7), it is easy to interpret these as Fourier transforms from the directions to the positions. However, using the ultra-wideband aperture function given in (2.10) this Fourier pair is not possible. In fact, the often used Fourier pair 'direction-position' is only viable for the classical wideband signal model. For an ultra-wideband model, the Fourier pair is the spatial frequency $\boldsymbol{u}$ and the position $\boldsymbol{p}$. One can also look at it in the following way: The Fourier pair is always the spatial frequency $\boldsymbol{u}$ and the position $\boldsymbol{p}$. For the wideband model, the possible values for the wideband spatial frequency $\boldsymbol{u}_{\mathrm{wb}}$ are located on a sphere with length $(\frac{1}{\lambda_{\mathrm{c}}})$ with λ_{c} as carrier wavelength. This means that the three-dimensional variable $\boldsymbol{u}_{\mathrm{wb}}$ can actually be described by two-dimensions only (neglecting the length), making it possible to describe it by the direction $\boldsymbol{\Omega}$. For the ultra-wideband model this is not possible, meaning that a scaling-only relation between the direction $\boldsymbol{\Omega}$ and the spatial frequency $\boldsymbol{u}$ does not hold, but its length has to be taken into account. In fact, its length is depending on the frequency f which can easily be seen by taking the Fourier transform of the received signal of a single SMC

$$R_{\mathrm{SMC},k}(f, \boldsymbol{u}_{\mathrm{TX}}, \boldsymbol{u}_{\mathrm{RX}}) = \bar{\alpha}_k S(f) \mathrm{e}^{-j2\pi(f+f_\mathrm{c})\tau_k}$$
$$\delta\Big(\boldsymbol{u}_{\mathrm{TX}} - \frac{f+f_\mathrm{c}}{c}\boldsymbol{\Omega}_{\mathrm{TX},k}\Big)\delta\Big(\boldsymbol{u}_{\mathrm{RX}} - \frac{f+f_\mathrm{c}}{c}\boldsymbol{\Omega}_{\mathrm{RX},k}\Big).$$

2.3   Sampled Signal Model

The received signal in (2.6) is sampled in the temporal and spatial domains. In the temporal domain, the sampling frequency is given as $f_\mathrm{s} = \frac{1}{T_\mathrm{s}}$ and the number of samples N leads to the total observation time $T = N T_\mathrm{s}$. In the spatial domain, the signal is sampled with the TX (⦂) and RX (⦂) arrays consisting of I and L antennas, respectively. In Fig. 2.2 an example for the arrays is depicted, including the two local coordinate systems.[12]

The sampled received signal for antenna pair (i, l) is given as

$$\boldsymbol{r}^{(i,l)} = \boldsymbol{r}_{\mathrm{SMC}}^{(i,l)} + \boldsymbol{r}_{\mathrm{DMC}}^{(i,l)} + \boldsymbol{w}^{(i,l)}, \qquad (2.11)$$

where

$$\boldsymbol{r}^{(i,l)} = [r(0, \Delta\boldsymbol{p}_{\mathrm{TX}}^{(i)}, \Delta\boldsymbol{p}_{\mathrm{RX}}^{(l)}), r(T_\mathrm{s}, \Delta\boldsymbol{p}_{\mathrm{TX}}^{(i)}, \Delta\boldsymbol{p}_{\mathrm{RX}}^{(l)}), \ldots,$$
$$r((N-1)T_\mathrm{s}, \Delta\boldsymbol{p}_{\mathrm{TX}}^{(i)}, \Delta\boldsymbol{p}_{\mathrm{RX}}^{(l)})]^{\mathrm{T}},$$

and $\boldsymbol{r}_{\mathrm{SMC}}^{(i,l)}$, $\boldsymbol{r}_{\mathrm{DMC}}^{(i,l)}$, and $\boldsymbol{w}^{(i,l)}$ are sampled versions of the SMC, the DMC, and the AWGN, respectively. The individual entries for the SMC are given as

$$\boldsymbol{r}_{\mathrm{SMC}}^{(i,l)} = \sum_{k=1}^{K} \alpha_k \boldsymbol{s}^{(i,l)}(\boldsymbol{\theta}_k)$$
$$= \boldsymbol{S}^{(i,l)}(\boldsymbol{\Theta})\boldsymbol{\alpha}, \qquad (2.12)$$

---

[12]Note that if the frame of reference for an array is rotated with respect to the global frame of reference (x, y), the according direction has to be corrected for the rotation. Without knowning this rotation, the orientation of the RX and TX cannot be inferred directly form the directions, but additional information is necessary [48, 76] [N9].
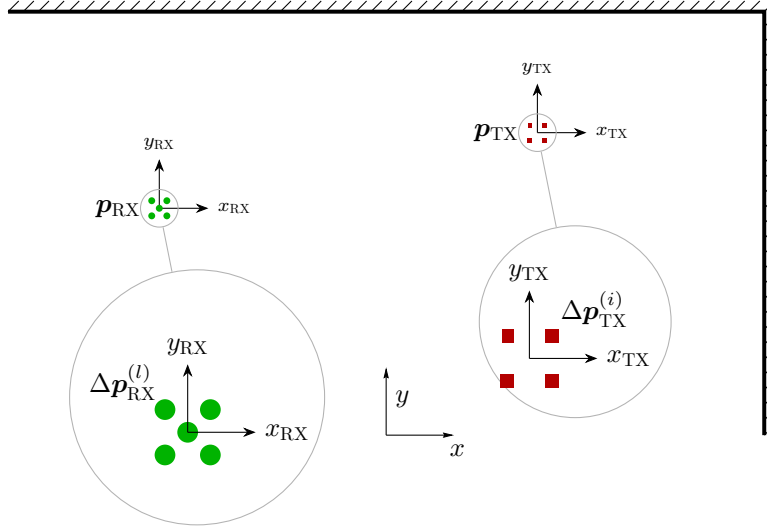
Figure 2.2: Layout of the array geometries of the TX (⠒⠒) and the RX (⠶)
with the center of gravities at $\boldsymbol{p}_{\mathrm{TX}}$ and $\boldsymbol{p}_{\mathrm{RX}}$, respectively, in the coordinate
system (x, y), defining the global frame of reference. Each array is described by
a local frame of reference and an according coordinate system. The individual
antenna element positions are denoted by $\Delta\boldsymbol{p}_{\mathrm{TX}}^{(i)}, i \in \{1, \ldots, I\}$ for the TX, and
by $\Delta\boldsymbol{p}_{\mathrm{RX}}^{(l)}, l \in \{1, \ldots, L\}$ for the TX.

where we introduced the dispersion parameter vector $\boldsymbol{\theta}_k = [\tau_k, \varphi_{\mathrm{D},k}, \varphi_{\mathrm{A},k}]^{\mathrm{T}}$, and
the vector $\boldsymbol{\Theta} = [\boldsymbol{\theta}_1^{\mathrm{T}}, \ldots, \boldsymbol{\theta}_K^{\mathrm{T}}]^{\mathrm{T}}$. The distance-dependent phase term is incorpo-
rated into the complex amplitude[13] , i.e., $\alpha_k = \bar{\alpha}_k e^{-j2\pi f_{\mathrm{c}}\tau_k}$ and the vector of
complex amplitudes $\boldsymbol{\alpha} = [\alpha_1, \ldots, \alpha_K]^{\mathrm{T}}$ are defined. Furthermore, we define the
matrix $\boldsymbol{S}^{(i,l)}(\boldsymbol{\Theta}) = [\boldsymbol{s}^{(i,l)}(\boldsymbol{\theta}_1), \ldots, \boldsymbol{s}^{(i,l)}(\boldsymbol{\theta}_K)]$ and the sampled received pulse

$$
\begin{aligned}
\boldsymbol{s}^{(i,l)}(\boldsymbol{\theta}) &\equiv \boldsymbol{s}^{(i,l)}(\tau, \boldsymbol{\Omega}_{\mathrm{TX}}, \boldsymbol{\Omega}_{\mathrm{RX}}) \\
&= \boldsymbol{s}_{\mathrm{TX}}(\tau - \boldsymbol{\Omega}_{\mathrm{TX}}^{\mathrm{T}} \Delta\boldsymbol{p}_{\mathrm{TX}}^{(i)}/c - \boldsymbol{\Omega}_{\mathrm{RX}}^{\mathrm{T}} \Delta\boldsymbol{p}_{\mathrm{RX}}^{(l)}/c) \\
&\qquad \mathrm{e}^{j2\pi f_{\mathrm{c}}/c(\boldsymbol{\Omega}_{\mathrm{TX}} \Delta\boldsymbol{p}_{\mathrm{TX}}^{(i)} + \boldsymbol{\Omega}_{\mathrm{RX}} \Delta\boldsymbol{p}_{\mathrm{RX}}^{(l)})},
\end{aligned}
\tag{2.13}
$$

where

$$
\boldsymbol{s}_{\mathrm{TX}}(\tau) = [s_{\mathrm{TX}}(0 - \tau), s_{\mathrm{TX}}(T_{\mathrm{s}} - \tau), \ldots, s_{\mathrm{TX}}((N-1)T_{\mathrm{s}} - \tau)]^{\mathrm{T}}.
$$

The overall sampled received signal is then given as

$$
\boldsymbol{r} = \boldsymbol{r}_{\mathrm{SMC}} + \boldsymbol{r}_{\mathrm{DMC}} + \boldsymbol{w},
\tag{2.14}
$$

---

[13]As long as an unknown phase term in included in the amplitude, it is not possible to
utilize the distance dependent phase term for ranging.

16

2.3. SAMPLED SIGNAL MODEL

where

$$\boldsymbol{r} = [\boldsymbol{r}^{(1,1)\,\mathrm{T}}, \boldsymbol{r}^{(1,2)\,\mathrm{T}}, \ldots, \boldsymbol{r}^{(1,L)\,\mathrm{T}}, \ldots, \boldsymbol{r}^{(i,l)\,\mathrm{T}}, \ldots, \boldsymbol{r}^{(I,L)\,\mathrm{T}}]^{\mathrm{T}},$$

$$\boldsymbol{r}_{\mathrm{SMC}} = [\boldsymbol{r}_{\mathrm{SMC}}^{(1,1)\,\mathrm{T}}, \boldsymbol{r}_{\mathrm{SMC}}^{(1,2)\,\mathrm{T}}, \ldots, \boldsymbol{r}_{\mathrm{SMC}}^{(1,L)\,\mathrm{T}}, \ldots, \boldsymbol{r}_{\mathrm{SMC}}^{(i,l)\,\mathrm{T}}, \ldots, \boldsymbol{r}_{\mathrm{SMC}}^{(I,L)\,\mathrm{T}}]^{\mathrm{T}},$$

$$\boldsymbol{r}_{\mathrm{DMC}} = [\boldsymbol{r}_{\mathrm{DMC}}^{(1,1)\,\mathrm{T}}, \boldsymbol{r}_{\mathrm{DMC}}^{(1,2)\,\mathrm{T}}, \ldots, \boldsymbol{r}_{\mathrm{DMC}}^{(1,L)\,\mathrm{T}}, \ldots, \boldsymbol{r}_{\mathrm{DMC}}^{(i,l)\,\mathrm{T}}, \ldots, \boldsymbol{r}_{\mathrm{DMC}}^{(I,L)\,\mathrm{T}}]^{\mathrm{T}},$$

$$\boldsymbol{w} = [\boldsymbol{w}^{(1,1)\,\mathrm{T}}, \boldsymbol{w}^{(1,2)\,\mathrm{T}}, \ldots, \boldsymbol{w}^{(1,L)\,\mathrm{T}}, \ldots, \boldsymbol{w}^{(i,l)\,\mathrm{T}}, \ldots, \boldsymbol{w}^{(I,L)\,\mathrm{T}}]^{\mathrm{T}}.$$

By combining the different antennas the received signal stemming from SMCs is

$$\boldsymbol{r}_{\mathrm{SMC}} = \sum_{k=1}^{K} \boldsymbol{s}(\boldsymbol{\theta}_k)\alpha_k = \boldsymbol{S}(\boldsymbol{\Theta})\boldsymbol{\alpha} \tag{2.15}$$

where $\boldsymbol{s}(\boldsymbol{\theta}) = \left[\boldsymbol{s}^{(1,1)}(\boldsymbol{\theta})^{\mathrm{T}}, ..., \boldsymbol{s}^{(1,L)}(\boldsymbol{\theta})^{\mathrm{T}}, ..., \boldsymbol{s}^{(i,l)}(\boldsymbol{\theta})^{\mathrm{T}}, ..., \boldsymbol{s}^{(I,L)}(\boldsymbol{\theta})^{\mathrm{T}}\right]^{\mathrm{T}}$, and $\boldsymbol{S}(\boldsymbol{\Theta}) = \left[\boldsymbol{S}^{(1,1)}(\boldsymbol{\Theta})^{\mathrm{T}}, \ldots, \boldsymbol{S}^{(1,L)}(\boldsymbol{\Theta})^{\mathrm{T}}, \ldots, \boldsymbol{S}^{(i,l)}(\boldsymbol{\Theta})^{\mathrm{T}}, \ldots, \boldsymbol{S}^{(I,L)}(\boldsymbol{\Theta})^{\mathrm{T}}\right]^{\mathrm{T}}$.

The stochastic part of the received signal is described by the DMC plus AWGN, i.e., $\boldsymbol{r}_{\mathrm{DMC}} + \boldsymbol{w}$. It is easy to show that this random process is zero-mean and has the following covariance matrix:

$$\boldsymbol{C} = \boldsymbol{C}_{\mathrm{DMC}} + \boldsymbol{C}_{\mathrm{AWGN}}. \tag{2.16}$$

The covariance matrix for the AWGN $\boldsymbol{C}_{\mathrm{AWGN}} = \sigma_{\mathrm{w}}^2 \boldsymbol{I}$, with variance $\sigma_{\mathrm{w}}^2 = N_0/T_{\mathrm{s}}$. The covariance matrix for the DMC process for antenna pairs (i,l) and (i',l') is in general given by

$$
\begin{aligned}
\left[\boldsymbol{C}_{\mathrm{DMC}}\right]_{i,l,i',l'} =& \mathbb{E}\left[\boldsymbol{r}_{\mathrm{DMC}}^{(i,l)} \boldsymbol{r}_{\mathrm{DMC}}^{(i',l')\,\mathrm{H}}\right] \\
=& \int\int\int S_{\mathrm{DMC}}(\tau, \boldsymbol{\Omega}_{\mathrm{TX}}, \boldsymbol{\Omega}_{\mathrm{RX}}; \boldsymbol{p}_{\mathrm{TX}}, \boldsymbol{p}_{\mathrm{RX}}) \\
&\times \boldsymbol{s}^{(i,l)}(\tau, \boldsymbol{\Omega}_{\mathrm{TX}}, \boldsymbol{\Omega}_{\mathrm{RX}}; \Delta\boldsymbol{p}_{\mathrm{TX}}^{(i)}, \Delta\boldsymbol{p}_{\mathrm{RX}}^{(l)}) \\
&\times \boldsymbol{s}^{(i',l')}(\tau, \boldsymbol{\Omega}_{\mathrm{TX}}, \boldsymbol{\Omega}_{\mathrm{RX}}; \Delta\boldsymbol{p}_{\mathrm{TX}}^{(i)}, \Delta\boldsymbol{p}_{\mathrm{RX}}^{(l)})^{\mathrm{H}} d\tau ds_1(\boldsymbol{\Omega}_{\mathrm{TX}}) ds_1(\boldsymbol{\Omega}_{\mathrm{RX}}),
\end{aligned} \tag{2.17}
$$

where we used the uncorrelated scattering assumption in the delay, the direction-of-departure and the direction-of-arrival domains for (2.17).

While (2.17) delivers an accurate description of the DMC process if the uncorrelated scattering assumptions hold, the difficulty is that the DMC process is unknown and has to be estimated. Therefore, we often apply the following assumptions for the description of the DMC process:

(i) we employ the wideband aperture function for the DMC

(ii) we assume a separable delay - direction-of-departure - direction-of-arrival power spectrum, i.e.,

$$S_{\mathrm{DMC}}(\tau, \boldsymbol{\Omega}_{\mathrm{TX}}, \boldsymbol{\Omega}_{\mathrm{RX}}; \boldsymbol{p}_{\mathrm{TX}}, \boldsymbol{p}_{\mathrm{RX}}) = P_{\mathrm{DMC}} S_{\mathrm{DMC}}(\tau) S_{\mathrm{DMC}}(\boldsymbol{\Omega}_{\mathrm{TX}}) S_{\mathrm{DMC}}(\boldsymbol{\Omega}_{\mathrm{RX}}), \tag{2.18}$$

where P_{DMC} describes the power of the DMC with respect to the SMCs, and $S_{\mathrm{DMC}}(\tau)$, $S_{\mathrm{DMC}}(\boldsymbol{\Omega}_{\mathrm{TX}})$, and $S_{\mathrm{DMC}}(\boldsymbol{\Omega}_{\mathrm{RX}})$ are the delay power spectrum (DPS), the direction of departure power spectrum (DODPS), and

the direction of arrival power spectrum (DOAPS), respectively and integrate to 1.

(iii) we neglect correlations across antenna elements.

The first two assumptions lead to the Kronecker mode decomposition, i.e.,

$$\boldsymbol{C}_{\text{DMC}} = P_{\text{DMC}}\boldsymbol{C}_I \otimes \boldsymbol{C}_L \otimes \boldsymbol{C}_N, \tag{2.19}$$

with $\otimes$ as the Kronecker product, and

$$\boldsymbol{C}_I = \int S_{\text{DMC}}(\boldsymbol{\Omega}_{\text{TX}})\boldsymbol{s}_I(\boldsymbol{\Omega}_{\text{TX}})\boldsymbol{s}_I^{\text{H}}(\boldsymbol{\Omega}_{\text{TX}})ds_1(\boldsymbol{\Omega}_{\text{TX}}) \tag{2.20}$$

$$\boldsymbol{C}_L = \int S_{\text{DMC}}(\boldsymbol{\Omega}_{\text{RX}})\boldsymbol{s}_L(\boldsymbol{\Omega}_{\text{RX}})\boldsymbol{s}_L^{\text{H}}(\boldsymbol{\Omega}_{\text{RX}})ds_1(\boldsymbol{\Omega}_{\text{RX}}) \tag{2.21}$$

$$\boldsymbol{C}_N = \int S_{\text{DMC}}(\tau)\boldsymbol{s}_N(\tau)\boldsymbol{s}_N^{\text{H}}(\tau)d\tau, \tag{2.22}$$

where

$$\boldsymbol{s}_I(\boldsymbol{\Omega}_{\text{TX}}) = [e^{j2\pi f_c/c\boldsymbol{\Omega}_{\text{TX}}^{\text{T}}\Delta\boldsymbol{p}_{\text{TX}}^{(1)}} \ldots e^{j2\pi f_c/c\boldsymbol{\Omega}_{\text{TX}}^{\text{T}}\Delta\boldsymbol{p}_{\text{TX}}^{(I)}}]^{\text{T}} \tag{2.23}$$

$$\boldsymbol{s}_L(\boldsymbol{\Omega}_{\text{RX}}) = [e^{j2\pi f_c/c\boldsymbol{\Omega}_{\text{RX}}^{\text{T}}\Delta\boldsymbol{p}_{\text{RX}}^{(1)}} \ldots e^{j2\pi f_c/c\boldsymbol{\Omega}_{\text{RX}}^{\text{T}}\Delta\boldsymbol{p}_{\text{RX}}^{(L)}}]^{\text{T}} \tag{2.24}$$

$$\boldsymbol{s}_N(\tau) = [s_{\text{TX}}(-\tau) \ldots s_{\text{TX}}((N-1)T_{\text{s}} - \tau)]^{\text{T}}. \tag{2.25}$$

The Kronecker mode decomposition enables computationally less demanding inversion of the covariance matrix, needed for sophisticated estimators. The third assumption leads to eye-matrices for $\boldsymbol{C}_I$ and $\boldsymbol{C}_L$. This assumption is correct, if the individual antenna elements are spaced by $\frac{\lambda_c}{2}$ for three dimensional propagation [65], a uniform DODPS/DOAPS and a uniform linear array. For horizontal only propagation, the correlations in $\boldsymbol{C}_I$ and $\boldsymbol{C}_L$ follow a zero-order Bessel function of the first kind [65, 94]. The first zero occurs at approximately $0.4\lambda_c$, meaning that antennas spaced by $0.4\lambda_c$ show no correlation. However, the following antenna, i.e., $0.8\lambda_c$ apart from the first antenna, will be correlated.

As we consider single-snapshot based estimation in this thesis, the sample covariance matrix will be rank deficient and not invertible. Thus, we parametrize the ADPS and in turn the covariance matrix by a parameter vector $\boldsymbol{\eta}$, i.e., $\boldsymbol{C}(\boldsymbol{\eta})$.

Finally, under the made assumptions, the likelihood function of the model reads

$$f(\boldsymbol{r}|\boldsymbol{\Theta}, \boldsymbol{\alpha}, \boldsymbol{\eta}) = \frac{1}{\pi^{NIL}\det(\boldsymbol{C}(\boldsymbol{\eta}))}e^{(\boldsymbol{r}-\boldsymbol{S}(\boldsymbol{\Theta})\boldsymbol{\alpha})^{\text{H}}\boldsymbol{C}(\boldsymbol{\eta})^{-1}(\boldsymbol{r}-\boldsymbol{S}(\boldsymbol{\Theta})\boldsymbol{\alpha})}, \tag{2.26}$$

with $\det(\cdot)$ as the determinant of a matrix. This function is the basis for the subsequent chapters, for the derivation of fundamental performance bounds in Chapter 3, for the derivation of estimators in Chapter 4 and for the derivation of a joint estimation and detection of SMCs in Chapter 5.

2.4   Detour: A slightly different point of view

Another possibility to arrive at the multiple-input multiple-output signal model given by (2.6) is to start from a received signal described solely by the delay[14],

---

[14]This description is quite general, as it does not make the plane wave assumption. Furthermore, an array is not yet introduced, meaning that all correlations are expressed solely via the delay domain.

i.e.,

$$r(t) = \sum_{i=1}^{\infty} \bar{\alpha}_i s(t - \bar{\tau}_i(\boldsymbol{p}_{\mathrm{TX}}, \boldsymbol{p}_{\mathrm{RX}})) + n(t) \tag{2.27}$$

$$= \underbrace{\sum_{k=1}^{K} \bar{\alpha}_k s(t - \tau_k(\boldsymbol{p}_{\mathrm{TX}}, \boldsymbol{p}_{\mathrm{RX}}))}_{\text{SMCs: } r_{\mathrm{SMC}}(t)} + \underbrace{\sum_{k=K+1}^{\infty} \bar{\alpha}_k s(t - \tau_k(\boldsymbol{p}_{\mathrm{TX}}, \boldsymbol{p}_{\mathrm{RX}}))}_{\text{non-specular waves - DMC: } r_{\mathrm{DMC}}(t)} + \underbrace{n(t)}_{\text{AWGN}} ,$$

$$\tag{2.28}$$

where $s(t - \tau(\boldsymbol{p}_{\mathrm{TX}}, \boldsymbol{p}_{\mathrm{RX}})) = s_{\mathrm{TX}}(t - \tau(\boldsymbol{p}_{\mathrm{TX}}, \boldsymbol{p}_{\mathrm{RX}}))\mathrm{e}^{-j2\pi f_c \tau(\boldsymbol{p}_{\mathrm{TX}}, \boldsymbol{p}_{\mathrm{RX}})}$. The first term in (2.28) describes the SMCs, the second term comprises an infinite number[15] of non-specular waves leading to the DMC and the third term is the AWGN.

To uncover the influence of the direction of arrival and the direction of departure, we assume that within a region around $\boldsymbol{p}_{\mathrm{TX}}$ and $\boldsymbol{p}_{\mathrm{RX}}$ the plane-wave far-field condition holds and that within this region the same plane waves arrive. As before, we place a coordinate system with its origin at $\boldsymbol{p}_{\mathrm{TX}}$ and another coordinate system at $\boldsymbol{p}_{\mathrm{RX}}$. Thus, an antenna placed $\Delta\boldsymbol{p}_{\mathrm{RX}}$ apart from $\boldsymbol{p}_{\mathrm{RX}}$ receives the following SMCs from a transmitting antenna placed $\Delta\boldsymbol{p}_{\mathrm{TX}}$ apart from $\boldsymbol{p}_{\mathrm{TX}}$

$$r_{\mathrm{SMC}}(t, \Delta\boldsymbol{p}_{\mathrm{TX}}, \Delta\boldsymbol{p}_{\mathrm{RX}}) = \sum_{k=1}^{K} \bar{\alpha}_k s(t - \tau_k + \boldsymbol{\Omega}_{\mathrm{TX},k}^{\mathrm{T}} \Delta\boldsymbol{p}_{\mathrm{TX}}/c + \boldsymbol{\Omega}_{\mathrm{RX},k}^{\mathrm{T}} \Delta\boldsymbol{p}_{\mathrm{RX}}/c).$$

$$\tag{2.29}$$

By sampling (2.29) in the temporal and spatial domain (2.12) is obtained.

The delay of the non-specular waves can be split-up in a similar way leading to

$$r_{\mathrm{DMC}}(t, \Delta\boldsymbol{p}_{\mathrm{TX}}, \Delta\boldsymbol{p}_{\mathrm{RX}}) = \sum_{k=K+1}^{\infty} \bar{\alpha}_k s(t - \tau_k + \boldsymbol{\Omega}_{\mathrm{TX},k}^{\mathrm{T}} \Delta\boldsymbol{p}_{\mathrm{TX}}/c + \boldsymbol{\Omega}_{\mathrm{RX},k}^{\mathrm{T}} \Delta\boldsymbol{p}_{\mathrm{RX}}/c)$$

$$\tag{2.30}$$

Comparing (2.30) with the DMC term in (2.6), the connection between the two approaches is clearly seen.

2.5 Single-SMC Channel Model

With the channel and signal model given above, it is often not possible to derive closed-form expressions for, e.g., the fundamental limits in Chapter 3 or the detection performance in Chapter 5. Thus, we introduce the single-SMC in DMC and AWGN channel model. This SMC can be the LOS as in [N3], [T1] or any other reflection leading to an SMC. The signal is still described by (2.14), where the description of the SMC part reduces to a single component, meaning $K = 1$.

In [T1], we analyze the ranging performance of a single-input single-output (SISO) system. Thus, the channel is described by a LOS plus DMC model.

---

[15]Often this sum is modeled to consist of a certain number of terms. As this number is unknown, we used infinity for simplicity.
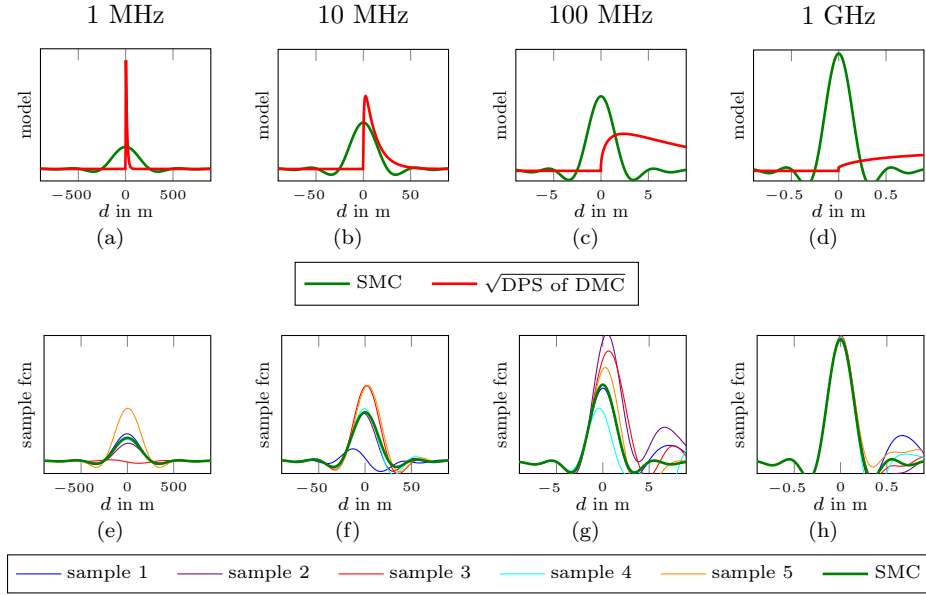
Figure 2.3: Model and sample functions of signal model given in (2.31) for a wide range of bandwidths neglecting AWGN. The upper row depicts the SMC (here the LOS, ──) and the square root of the DPS of the DMC (──), while the lower row highlights five sample functions (──,──,──,──,──) and for comparsion the unaltered SMC(──). The columns show different bandwidth starting from 1 MHz ((a) and (e)) up to 1 GHz ((d) and (h)).

An example of a system following this model is a narrowband system with a dominant LOS component. The sampled received signal is given by[16]

$$\boldsymbol{r} = \boldsymbol{s}_{\mathrm{TX}}(\tau)\alpha + \boldsymbol{r}_{\mathrm{DMC}} + \boldsymbol{w}. \tag{2.31}$$

The DMC term does not depend on the directions of departure and arrival anymore[17], leading to a description based solely on the delay, i.e., the delay power spectrum $S_{\mathrm{DMC}}(\tau)$.

Fig. 2.3 illustrates the signal model (top row) and some sample realizations (bottow row) neglecting AWGN for a wide range of bandwidths. For the simulation of the DMC, we utilized a DPS with a double-exponential shape [41, 59].[18] In the UWB case (Fig. 2.3d and 2.3h), the LOS component is clearly separated from the DMC process and neither fading nor pulse distortion occurs. By decreasing the bandwidth, the interference between the LOS component and the DMC process increases and leads to fading and distortion of the received pulse. For low bandwidth, the complete DMC process interferes with the LOS component, leading to a flat fading scenario without significant distortion.

---

[16]This is a sampled version of (2.28). It can also be seen as (2.14) without an array, meaning that $I = L = 1$ and $\Delta \boldsymbol{p}_{\mathrm{TX}}^{(1)} = \boldsymbol{0}$ and $\Delta \boldsymbol{p}_{\mathrm{RX}}^{(1)} = \boldsymbol{0}$, hence, not depending on the direction of departure and direction of arrival.

[17]In fact, the DMC is still influenced by the direction of departure and arrival, but it cannot be observed with the chosen aperture.

[18]The parameters and the function can be found in [T1].

20

2.6 RFID system model

Classical passive ultra-high frequency (UHF) RFID systems have been designed to replace bar-codes. Such systems are narrowband and thus do not allow accurate and robust ranging/positioning. However, several techniques have been proposed to increase the bandwidth and allow for more accurate ranging/positioning. Basically, two approaches have been investigated: (i) increasing the bandwidth at the tag [22, 23, 34] or (ii) increasing the bandwidth at the transmitter side [5, 7, 32] [N11]. The first approach uses a customized RFID tag scattering back a code division multiple access (CDMA) according to a suitable pseudorandom time-hopping sequence. The second approach modulates the transmitted continuous wave signal with a CDMA sequence, which is in turn scattered back by the addressed tag. The advantage of this approach is that it can work with standard off-the-shelf RFID tags.[19]

Here, we consider a system with M RFID readers operating at known positions $\boldsymbol{p}_m$. Each reader is equipped with L_m closely-spaced antennas that can be used to transmit and receive wideband signals. An RFID label is placed at unknown position $\boldsymbol{p}$. The according MIMO system is depicted in Fig. 2.4. The transmission from a TX reader antenna via the label to an RX reader antenna can be described by the backscatter channel. It consists of the downlink channel from the TX reader to the RFID label and the uplink channel from the RFID label to the RX reader. The backscatter channel can then be described via the convolution of the two constituent channels, the downlink and the uplink channels. The backscatter channel is also called pinhole channel, as all waves (modulated by the RFID label) have to converge at a pinhole (the label). In Fig. 2.4 two different backscatter channels are highlighted depending on the involved constituent channels: (i) a monostatic channel, consisting of the same two constituent channels, and (ii) a bistatic channel connecting two different readers, consisting of two uncorrelated constituent channels. Furthermore, static clutter is highlighted, stemming from the direct transmission between a reader with itself or between two different readers without converging at the pinhole. This static clutter can be canceled from the received signal, by means of different signaling and pre-processing schemes [5, 7, 23].

The two constituent channels, the downlink $h(\tau, \boldsymbol{\Omega}_{\mathrm{TX}}; \boldsymbol{p}_m, \boldsymbol{p})$ and the uplink $h(\tau, \boldsymbol{\Omega}_{\mathrm{RX}}; \boldsymbol{p}_{m'}, \boldsymbol{p})$, are modeled with a single-SMC in DMC channel as in Section 2.5, i.e.,

$$
\begin{aligned}
h(\tau, \boldsymbol{\Omega}_{\mathrm{TX}}; \boldsymbol{p}_m, \boldsymbol{p}) &= \alpha_m \delta(\tau - \tau_m)\delta(\boldsymbol{\Omega}_{\mathrm{TX}} - \boldsymbol{\Omega}_{\mathrm{TX},m}) \\
&\quad + h_{\mathrm{DMC}}(\tau, \boldsymbol{\Omega}_{\mathrm{TX}}; \boldsymbol{p}_m, \boldsymbol{p}) \tag{2.32}
\end{aligned}
$$

$$
\begin{aligned}
h(\tau, \boldsymbol{\Omega}_{\mathrm{RX}}; \boldsymbol{p}_{m'}, \boldsymbol{p}) &= \alpha_{m'} \delta(\tau - \tau_{m'})\delta(\boldsymbol{\Omega}_{\mathrm{RX}} - \boldsymbol{\Omega}_{\mathrm{RX},m'}) \\
&\quad + h_{\mathrm{DMC}}(\tau, \boldsymbol{\Omega}_{\mathrm{RX}}; \boldsymbol{p}_{m'}, \boldsymbol{p}). \tag{2.33}
\end{aligned}
$$

Note that the downlink and the uplink channel do not depend on $\boldsymbol{\Omega}_{\mathrm{RX}}$ and $\boldsymbol{\Omega}_{\mathrm{TX}}$, respectively, as the RFID label is assumed to consist of a single antenna. By

---

[19]A different approach are (often active) UWB RFID tags [10, 17]. These tags are capable of transmitting a UWB pulse, meaning that the received signal does only include the uplink channel from the tag to the receiver.
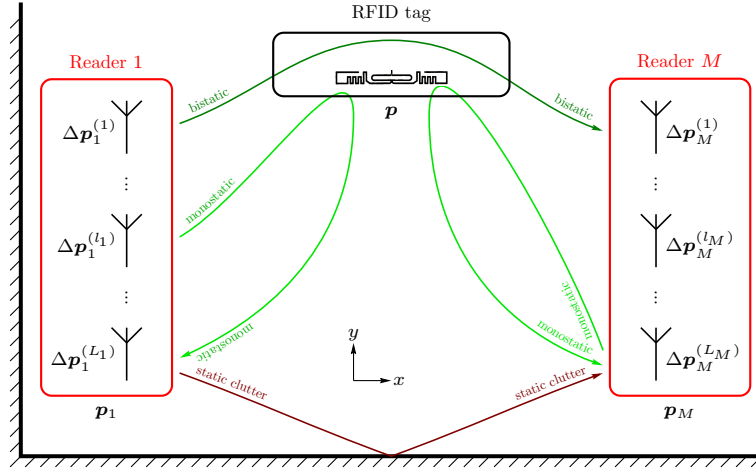
Figure 2.4: RFID setup including the RFID label at unknown position $\boldsymbol{p}$ and two readers at position $\boldsymbol{p}_1$ and $\boldsymbol{p}_M$ equipped with L_1 and L_M closely spaced antennas, respectively.

convolving the two constituent channels, the backscatter channel is

$$
\begin{aligned}
h_{\mathrm{BS}}(\tau, &\boldsymbol{\Omega}_{\mathrm{TX}}, \boldsymbol{\Omega}_{\mathrm{RX}}; \boldsymbol{p}_m, \boldsymbol{p}_{m'}, \boldsymbol{p}) = \hspace{3cm} (2.34) \\
& \alpha_m \alpha_{m'} \delta(\tau - \tau_m - \tau_{m'}) \delta(\boldsymbol{\Omega}_{\mathrm{TX}} - \boldsymbol{\Omega}_{\mathrm{TX},m}) \delta(\boldsymbol{\Omega}_{\mathrm{RX}} - \boldsymbol{\Omega}_{\mathrm{RX},m'}) \\
& + \alpha_m \delta(\boldsymbol{\Omega}_{\mathrm{TX}} - \boldsymbol{\Omega}_{\mathrm{TX},m}) h_{\mathrm{DMC}}(\tau, \boldsymbol{\Omega}_{\mathrm{RX}}; \boldsymbol{p}_{m'}, \boldsymbol{p}) \\
& + \alpha_{m'} \delta(\boldsymbol{\Omega}_{\mathrm{RX}} - \boldsymbol{\Omega}_{\mathrm{RX},m'}) h_{\mathrm{DMC}}(\tau, \boldsymbol{\Omega}_{\mathrm{TX}}; \boldsymbol{p}_m, \boldsymbol{p}) \\
& + \int h_{\mathrm{DMC}}(\lambda, \boldsymbol{\Omega}_{\mathrm{TX}}; \boldsymbol{p}_m, \boldsymbol{p}) h_{\mathrm{DMC}}(\tau - \lambda, \boldsymbol{\Omega}_{\mathrm{RX}}; \boldsymbol{p}_{m'}, \boldsymbol{p}) d\lambda
\end{aligned}
$$

The first term in (2.34) shows the part based solely on the LOS components of the two constituent channels. The second and third terms are the convolutions of the LOS components of the up- and downlink with the DMC of the down- and uplink, respectively. The fourth term in (2.34) represents the convolution of the DMC terms of the two constituent channels. The backscatter channel can be described by a single SMC plus DMC model (as described in Section 2.5), by subsuming the last three terms in (2.34) into $h_{\mathrm{DMC,m,m'}}(\tau, \boldsymbol{\Omega}_{\mathrm{TX}}, \boldsymbol{\Omega}_{\mathrm{RX}}; \boldsymbol{p}_m, \boldsymbol{p}_{m'}, \boldsymbol{p})$.

The sampled received signal for the backscatter channel can be obtained by equation (2.14). To this end, we define the SMC term by means of its combined complex amplitude $\alpha_{m,m'} = \alpha_m \alpha_{m'}$ and its dispersion parameters $\boldsymbol{\theta}_{m,m'} = [\tau_m + \tau_{m'}, \varphi_{\mathrm{D},m}, \varphi_{\mathrm{A},m'}]^{\mathrm{T}}$. Additionally, we place local coordinate systems with origins at the transmit reader position $\boldsymbol{p}_m$ and the receive reader position $\boldsymbol{p}_{m'}$ as in Section 2.2, and sample the resulting received signal as in Section 2.3.[20]

2.7 Concluding Remarks

This chapter has introduced the channel and signal models used within this thesis. The channel consists of two major building blocks:

---

[20]Of course, one has to take into consideration that $\boldsymbol{p}_m \equiv \boldsymbol{p}_{\mathrm{TX}}$, $\boldsymbol{p}_{m'} \equiv \boldsymbol{p}_{\mathrm{RX}}$, $l_m \equiv i$ and $l_{m'} \equiv l$, $\boldsymbol{\theta}_{\mathrm{m,m'}} \equiv \boldsymbol{\theta}_1$, and $K = 1$.

2.7. CONCLUDING REMARKS

- **Specular multipath components (SMC)**, containing position-related information, i.e., the delay, the DoD, and the DoA, because these parameters can be derived from the positions of the transmitters and receivers. Examples for SMCs are the LOS as well as reflections at flat surfaces.

- **Dense multipath component (DMC)**, consisting of a continuum of weak multipath components. The DMC acts (in this thesis) mainly as an interference with respect to the position-related information contained in the SMCs. The multipath components generating the DMC are non-specular waves stemming from, e.g., diffuse reflection at rough surfaces; in short *everything that is not resulting in an SMC is part of the DMC.*

The received signal is sampled in the temporal and spatial domains leading to a MIMO signal model. The likelihood function for the sampled received signal is characterized by a complex normal distribution which is the basis for the subsequent chapters. In Chapter 3, a closed-form solution is analyzed for the CRLB of a single-SMC in DMC model and for the RFID setup. Chapter 4 uses the likelihood function to derive ML estimators and Chapter 5 jointly infers the number of SMCs that can be reliably detected.

23

d = 25.2 m

24

d = 50.4 m

Chapter 3

Fundamental limits for position-related parameter estimation in dense multipath environments

Fundamental limits play an essential role in assessing the performance of an estimator. One such fundamental limit is the CRLB, placing a lower bound on the variance of any unbiased estimator [42, 100]. Compared to other lower bounds, e.g., the Ziv-Zakai bound [111] or Barankin-type bounds [55], the CRLB is the easiest to determine. Furthermore, by investigating the inverse of the CRLB, i.e., the Fisher information, properties of the system and signal model can be assessed.

The derivation of the CRLB is straightforward and has already been derived for a channel and signal model comprised of a multitude of SMCs [78] including the DMC [50, 71]. However, due to the overlap of SMCs it is difficult to gain any meaningful insight regarding the influence of individual signal and system parameters on the estimation of position-related quantities.

Thus, in this chapter, we highlight, on the basis of the single-SMC in DMC channel model (cf. Section 2.5), a closed-form solution for the delay estimation problem. This enables insight on the influence of channel and signal parameters onto the achievable ranging performance in DMC channels [N3], [T1]. Again, note that as soon two or more SMCs start to overlap, the closed-form solution will not hold anymore and one has to numerically evaluate the CRLB [35, 50, 71, 78], [N4, N5]. Next, we focus on the passive RFID MIMO system and derive the CRLB for the delay, the DoD and the DoA [T2], [N4]. Finally, we transform the CRLB on the channel parameters into the CRLB on the position, enabling insight on reader and antenna placement.

3.1   Limits on channel parameters estimation

Having the likelihood function in (2.26), we can derive the achievable performance to estimate the dispersion parameters $\boldsymbol{\Theta}$ by the CRLB. To this end, we

stack the parameters governing the likelihood function into a single parameter vector $\boldsymbol{\psi} = [\boldsymbol{\Theta}^{\mathrm{T}}, \mathfrak{R}\boldsymbol{\alpha}^{\mathrm{T}}, \mathfrak{I}\boldsymbol{\alpha}^{\mathrm{T}}, \boldsymbol{\eta}^{\mathrm{T}}]^{\mathrm{T}}$, where $\mathfrak{R}\boldsymbol{\alpha}$ and $\mathfrak{I}\boldsymbol{\alpha}$ are the real and imaginary parts of the complex amplitude. The (i,j)th element of the Fisher information matrix (FIM) $\boldsymbol{\mathcal{I}}(\boldsymbol{\psi})$, the inverse of the CRLB, is given for the Gaussian model as [42]

$$
\begin{aligned}
[\boldsymbol{\mathcal{I}}(\boldsymbol{\psi})]_{ij} =& 2\mathfrak{R}\Big[\frac{\partial\boldsymbol{\mu}^{\mathrm{H}}(\boldsymbol{\psi})}{\partial\psi_i}\boldsymbol{C}^{-1}(\boldsymbol{\psi})\frac{\partial\boldsymbol{\mu}(\boldsymbol{\psi})}{\partial\psi_j}\Big] \\
&+ \mathrm{Tr}\Big[\boldsymbol{C}^{-1}(\boldsymbol{\psi})\frac{\partial\boldsymbol{C}(\boldsymbol{\psi})}{\partial\psi_i}\boldsymbol{C}(\boldsymbol{\psi})\frac{\partial\boldsymbol{C}^{-1}(\boldsymbol{\psi})}{\partial\psi_j}\Big],
\end{aligned}
\tag{3.1}
$$

where $\boldsymbol{\mu}(\boldsymbol{\psi})$ and $\boldsymbol{C}(\boldsymbol{\psi})$ are the mean vector and the covariance matrix, respectively. The second part in (3.1) captures the potential influence of the covariance matrix on the estimation of parameter $\boldsymbol{\psi}$. In this chapter, we assume that the covariance matrix, or the parameters of the covariance matrix are known.[1]

The FIM and subsequently the CRLB can always be evaluated numerically. However, this makes it difficult to assess the influence of specific model and system parameters. In the following, we will discuss two special cases, the SISO ranging performance in Section 3.1.1 and the ranging and angulation performance for a MIMO-RFID system in Section 3.1.2.

3.1.1 SISO channel

To analyze the ranging performance of a SISO radio channel, we utilize the single-SMC channel model introduced in (2.31) in Section 2.5. Furthermore, we assume that the parameters governing the covariance matrix of the model are known. Thus, the parameter vector reduces to $\boldsymbol{\psi} = [\tau, \mathfrak{R}\alpha, \mathfrak{I}\alpha]^{\mathrm{T}}$, where $\mathfrak{R}\alpha$ and $\mathfrak{I}\alpha$ are the real and imaginary parts of the complex amplitude, respectively. The FIM is given as [N3] [T1]

$$
\boldsymbol{\mathcal{I}}(\boldsymbol{\psi}) = \begin{bmatrix} \mathcal{I}_{\tau,\tau} & \mathcal{I}_{\tau,\mathfrak{R}\alpha} & \mathcal{I}_{\tau,\mathfrak{I}\alpha} \\ \mathcal{I}_{\mathfrak{R}\alpha,\tau} & \mathcal{I}_{\mathfrak{R}\alpha,\mathfrak{R}\alpha} & 0 \\ \mathcal{I}_{\mathfrak{I}\alpha,\tau} & 0 & \mathcal{I}_{\mathfrak{I}\alpha,\mathfrak{I}\alpha} \end{bmatrix}.
\tag{3.2}
$$

We assume that the complex amplitude does not hold any position-related information[2] and model it as nuisance parameter. Thus, the ranging performance can be described by the equivalent Fisher information (EFI) for the delay estimation problem

$$
\mathcal{I}(\tau) = \big[[\boldsymbol{\mathcal{I}}^{-1}(\boldsymbol{\psi})]_{1,1}\big]^{-1}.
\tag{3.3}
$$

Finally, the ranging error bound is defined as the square root of the inverse of the EFI, i.e.,

$$
\mathcal{R}(\tau) = \sqrt{\mathcal{I}(\tau)^{-1}}.
\tag{3.4}
$$

---

[1] In [N3] we included the effect of a delay dependent covariance matrix and found that only at very small bandwidth the DPS effects the estimation of the delay.

[2] The amplitude does not follow a simple path-loss model, as we assumed that the beam-patterns of the antennas are unknown and included in the complex amplitude. Thus, it does not hold position-related information.

3.1. LIMITS ON CHANNEL PARAMETERS ESTIMATION

By neglecting the DMC term, (2.31) reduces to an AWGN-only model. This leads to the well known EFI for the delay estimation in AWGN, given as [42, 100]

$$\mathcal{I}_{\text{AWGN}}(\tau) = 8\pi^2\beta^2\text{SNR}. \tag{3.5}$$

In (3.5) the signal to noise ratio (SNR) is given as $\text{SNR} = \frac{\alpha^2\|\boldsymbol{s}_{\text{TX}}(\tau)\|^2 T_{\text{s}}}{N_0}$ and the effective (mean-square) bandwidth of the transmit pulse $\beta^2 = \frac{\|\dot{\boldsymbol{s}}_{\text{TX}}(\tau)\|^2}{4\pi^2\|\boldsymbol{s}_{\text{TX}}(\tau)\|^2}$, where $\dot{\boldsymbol{s}}_{\text{TX}}(\tau)$ is the sampled derivative of the transmit pulse with respect to τ.

By considering the DMC in the derivation, the REB reads [N3] [T1]

$$\mathcal{I}(\tau) = 8\pi^2\beta^2\gamma(\tau)\text{SINR}(\tau)\sin^2(\phi(\tau)) \tag{3.6}$$

$$= 8\pi^2\beta^2\widetilde{\text{SINR}}(\tau), \tag{3.7}$$

with the whitening gain $\gamma(\tau) = \frac{\beta_w^2(\tau)}{\beta^2}$, the effective (mean-square) bandwidth of the whitened pulse $\beta_w^2(\tau) = \frac{\|\dot{\boldsymbol{s}}_{\text{TX}}(\tau)\|_{\mathcal{H}}^2}{4\pi^2\|\boldsymbol{s}_{\text{TX}}(\tau)\|_{\mathcal{H}}^2}$, the effective signal to interference plus noise ratio (SINR) $\widetilde{\text{SINR}}(\tau) = \gamma(\tau)\text{SINR}(\tau)\sin^2(\phi(\tau))$, the $\text{SINR}(\tau) = \frac{|\alpha|^2\|\boldsymbol{s}_{\text{TX}}(\tau)\|_{\mathcal{H}}^2 T_{\text{s}}}{N_0}$, and $\phi(\tau)$ as the angle between $\boldsymbol{s}_{\text{TX}}(\tau)$ and $\dot{\boldsymbol{s}}_{\text{TX}}(\tau)$ in a Hilbert space $\mathcal{H}$ defined by an orthonormal expansion of the covariance matrix $\boldsymbol{C}(\boldsymbol{\eta})$. The inner product of $\boldsymbol{x}$ and $\boldsymbol{y}$ in this Hilbert space is given as

$$\langle \boldsymbol{x}, \boldsymbol{y} \rangle_{\mathcal{H}} = \frac{N_0}{T_{\text{s}}} \boldsymbol{y}^{\text{H}} \boldsymbol{C}(\boldsymbol{\eta})^{-1} \boldsymbol{x} \tag{3.8}$$

and the induced norm by $\|\boldsymbol{x}\|_{\mathcal{H}}^2 = \langle \boldsymbol{x}, \boldsymbol{x} \rangle_{\mathcal{H}}$. Comparing the two norms, $\|\boldsymbol{x}\|_{\mathcal{H}}^2$ and $\|\boldsymbol{x}\|^2$, it is clear that in the AWGN-only case both norms coincide, because the inverse covariance matrix reduces to T_{s}/N_0. Utilizing the Woodbury matrix identity, it is easy to show that the DMC reduces the induced norm given by (3.8) compared to $\|\boldsymbol{x}\|^2$, leading to $\text{SINR}(\tau) \leq \text{SNR}$. While (3.7) allows for an easy comparison to the AWGN only case (3.5) as all terms are combined into the effective SINR, (3.6) allows for more detailed insights:

- The whitening/equalization gain $\gamma(\tau)$ is defined as the ratio of the effective bandwidths of the whitened and non-whitened pulses. It has to be mentioned that the whitening/equalization operation by the multiplicaton with the inverse of the covariance matrix does not only whiten the signal in the spectrum, but also equalize it in the delay domain, as the DMC process is non-stationary.

- The factor $\sin^2(\phi(\tau))$ is the cost for estimating the nuisance parameter α. Common pulses (even or odd waveforms) are orthogonal to their derivatives. Thus, the estimation of the nuisance parameter α is 'cost-free' in AWGN. However, due to the non-stationary nature of the DMC, the whitening operation with the inverse of the covariance matrix makes the pulse asymmetric.

- The DMC acts as an interference for delay estimation as it increases the effective noise floor after the equalization with the inverse of the covariance matrix. This is easy to recognize in the extreme case of a constant delay power spectrum and a transmit pulse with blockspectrum: the only effect of the DMC in this case is that it increases the noise floor, leading to a reduced component SNR.

27
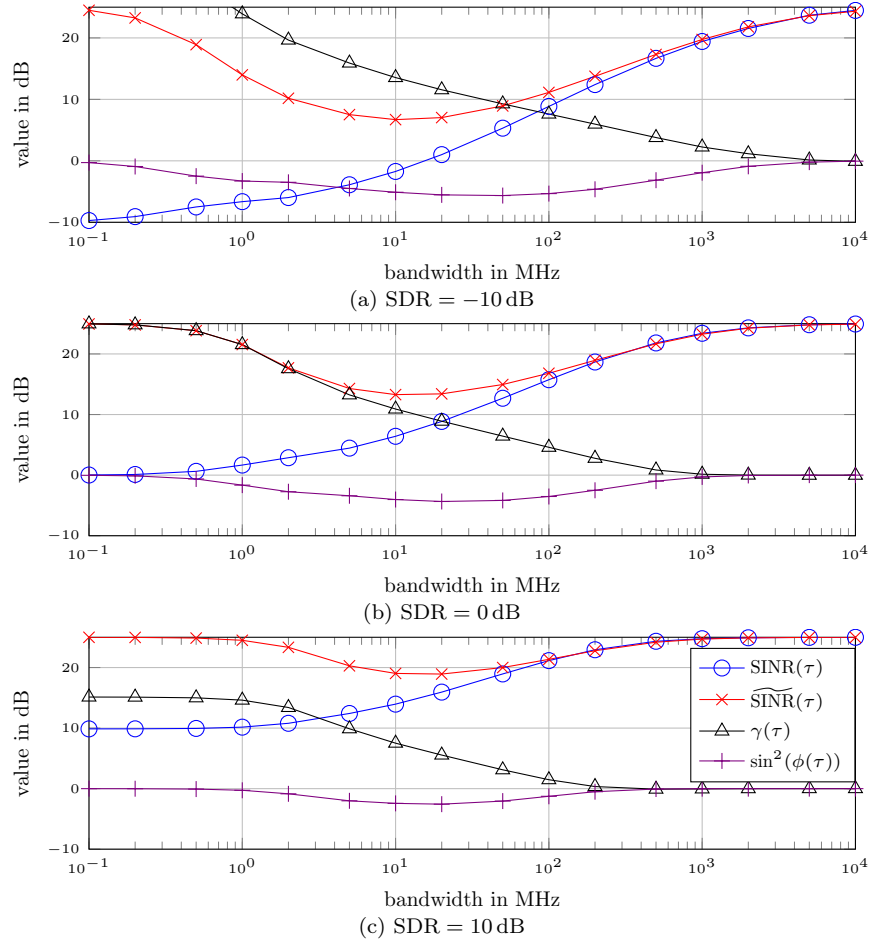
Figure 3.1: Parameters governing the EFI for delay estimation given in (3.6) and (3.7) over a wide range of bandwidth: $\text{SINR}(\tau)$ ($-\!\circ\!-$), $\widetilde{\text{SINR}}(\tau)$ ($-\!\times\!-$), whitening gain $\gamma(\tau)$ ($-\!\triangle\!-$) and loss factor $\sin^2(\phi(\tau))$ ($-\!\!+\!\!-$).

In Fig. 3.1 we illustrate the parameters governing the EFI for the delay estimation problem, i.e., $\text{SINR}(\tau)$ ($-\!\circ\!-$), $\widetilde{\text{SINR}}(\tau)$ ($-\!\times\!-$), whitening/equalization gain $\gamma(\tau)$ ($-\!\triangle\!-$) and loss factor $\sin^2(\phi(\tau))$ ($-\!\!+\!\!-$), over a wide range of bandwidth for the LOS component. For the evaluation, we utilized a root-raised cosine pulse with roll-off factor of 0.6 and pulse duration of $1/B$, with B as bandwidth.The DPS follows a double exponential function with parameters defined in [T1]. The SNR $= 25\,\text{dB}$ and the three subplots highlight the influence of the specular to dense ratio (SDR) defined as $\text{SDR} = \frac{\|\alpha \boldsymbol{s}_{\text{TX}}(\tau)\|^2}{P_{\text{DMC}}/T_{\text{s}}}$. Fig. 3.1a, 3.1b, and 3.1c refer to SDR $-10\,\text{dB}$, $0\,\text{dB}$, and $10\,\text{dB}$, respectively.

In the flat fading case, i.e., for narrow bandwidth, the $\text{SINR}(\tau)$ tends towards the SDR, while in the UWB case, i.e., for large bandwidth, the $\text{SINR}(\tau)$ approaches the SNR. The effective $\widetilde{\text{SINR}}(\tau)$ follows the $\text{SINR}(\tau)$ at large bandwidth, but it also tends towards the SNR at narrow bandwidth. We interpret

28

3.1. LIMITS ON CHANNEL PARAMETERS ESTIMATION
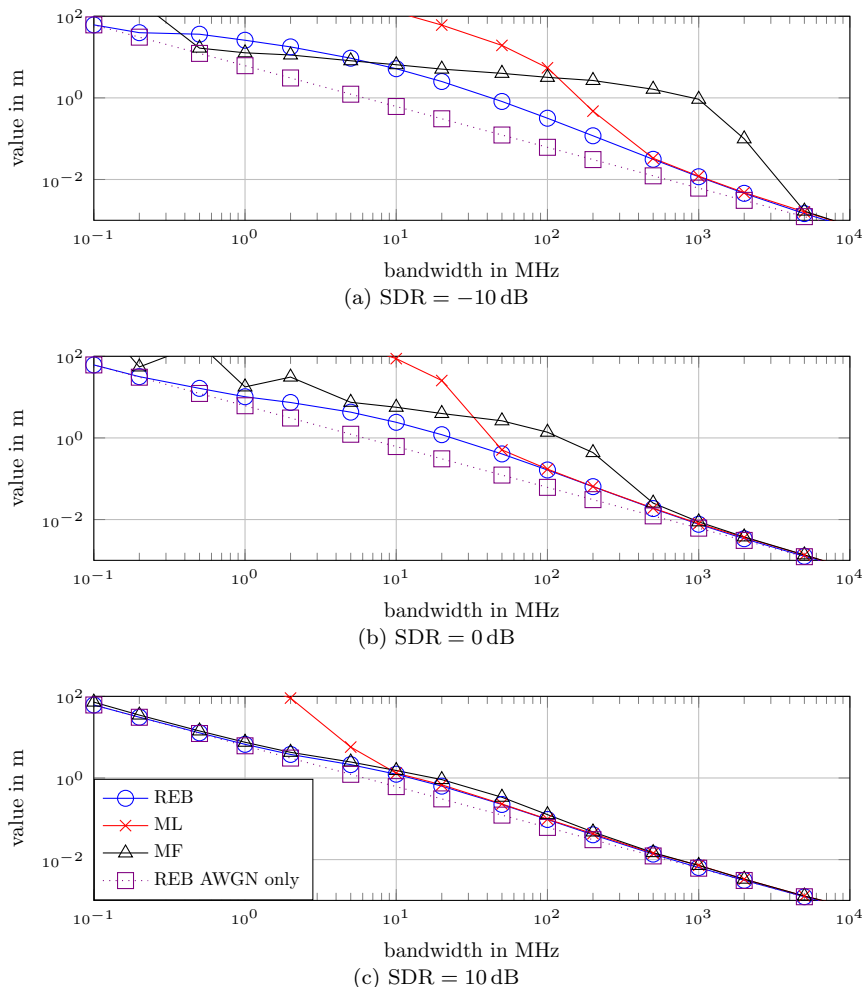
Figure 3.2: REB (—⊖—), REB for AWGN only (⋯□⋯) and simulated range estimation error standard deviation for ML (—✕—) and MF (—△—) estimator over a wide range of bandwidth.

the behavior of the SINR(τ) and the effective $\widetilde{\text{SINR}}(\tau)$ as describing the amplitude fading and the pulse distortion, respectively. At large bandwidth neither amplitude fading nor pulse distortion occur. Moving to smaller bandwidth, pulse distortion and amplitude fading set in, leading to decreased values for the SINR(τ) and $\widetilde{\text{SINR}}(\tau)$. By decreasing the bandwidth even more, the complete DMC interferes with the LOS component, leading to the flat fading case. In this case, no pulse distortion occurs and the $\widetilde{\text{SINR}}(\tau)$ approaches the SNR again, while the SINR(τ) tends towards the Rician K factor. The loss factor $\sin^2(\phi(\tau))$ is coupled with the asymmetry of the whitened pulse and reduces the achievable gain of the whitening operation.

In Fig. 3.2, we illustrate the REB (—⊖—) and the REB for AWGN-only (⋯□⋯). Fig. 3.2a, 3.2b, and 3.2c refer again to SDR -10 dB, 0 dB, and 10 dB, respectively. According to (3.5) the REB in the AWGN-only case scales quadratically

with the inverse of the bandwidth and linearly with the SNR. It serves as a comparison to highlight the influence of the DMC acting as interference for the ranging. The REB considering the influence of the DMC approaches the AWGN-only case at narrow and large bandwidths, where the effective $\widetilde{\mathrm{SINR}}(\tau)$ approaches the SNR. At intermediate bandwidth, the REB deviates from the AWGN-only bound due to the interference by the DMC process and is larger the lower the SDR is. Furthermore, the standard deviations of the ranging errors for two simulated estimators are included in Fig. 3.2: (i) an ML estimator (—✕—) considering the noise covariance matrix, and (ii) a naïve MF estimator (—△—) convolving the received signal with the template pulse. The MF estimator deviates from the bound already at high bandwidth, but it approaches the bound again at very low bandwidth. The ML estimator shows large outliers at low bandwidth, but is able to approach the bound at intermediate and high bandwidth. Both effects can be attributed to the whitening/equalization operation by the inverse covariance matrix: (i) The $\mathrm{SINR}(\tau)$ reflects the component SNR after the whitening/equalization operation and it is coupled with the detection of the LOS component. This will be further investigated in Chapter 5. This effect leads to the outliers at low bandwidth as the $\mathrm{SINR}(\tau)$ falls below this *detection threshold*. (ii) However, the accuracy is coupled with the effective $\widetilde{\mathrm{SINR}}(\tau)$, which is increased by the whitening/equalization operation. Thus, the ML estimator is able to approach the bound at intermediate bandwidth, where the MF estimator already deviates from the bound [N3], [T1].

To end this section, we want to highlight again that the underlying model is the single-SMC-in-DMC channel. As soon as two or more SMCs start to overlap, the EFI in (3.7) will be an upper bound on the information contained in the SMC under investigation and for an exact analysis, the CRLB has to be evaluated numerically. However, for SMCs with a spacing of about twice the pulse duration between each other, numerical analysis shows that the above expressions deliver accurate results.

3.1.2 Backscatter channel

In comparison to the SISO channel, the RFID setup with closely-spaced antennas enables classical array processing, exploiting phase information between array antenna elements. Thus, the parameter vector governing the likelihood function is given by $\boldsymbol{\psi}_{m,m'} = [\tau_{m,m'}, \varphi_{\mathrm{D},m}, \varphi_{\mathrm{A},m'}, |\alpha_{m,m'}|, \varphi_{\alpha_{m,m'}}]$ for reader combination m and m', with $|\alpha_{m,m'}|$ and $\varphi_{\alpha_{m,m'}}$ as the absolute value and the phase of the complex amplitude, respectively. For easier readability, we will drop the indices m and m' and reintroduce them where necessary.

In Appendix A.1, the covariance matrix of the DMC process is derived for a bistatic 2-reader RFID setup using the following assumptions: (i) the wideband model for the aperture function, (ii) a separable ADPS, and (iii) uniformly distributed DODPS and DOAPS. The FIM for the RFID channel parameters is

3.1. LIMITS ON CHANNEL PARAMETERS ESTIMATION

given as

$$
\mathbfcal{I}(\boldsymbol{\psi}) =
\begin{bmatrix}
\mathcal{I}_{\tau,\tau} & \mathcal{I}_{\tau,\varphi_{\mathrm{D}}} & \mathcal{I}_{\tau,\varphi_{\mathrm{A}}} & \mathcal{I}_{\tau,|\alpha|} & \mathcal{I}_{\tau,\varphi_{\alpha}} \\
\mathcal{I}_{\varphi_{\mathrm{D}},\tau} & \mathcal{I}_{\varphi_{\mathrm{D}},\varphi_{\mathrm{D}}} & \mathcal{I}_{\varphi_{\mathrm{D}},\varphi_{\mathrm{A}}} & \mathcal{I}_{\varphi_{\mathrm{D}},|\alpha|} & \mathcal{I}_{\varphi_{\mathrm{D}},\varphi_{\alpha}} \\
\mathcal{I}_{\varphi_{\mathrm{A}},\tau} & \mathcal{I}_{\varphi_{\mathrm{A}},\varphi_{\mathrm{D}}} & \mathcal{I}_{\varphi_{\mathrm{A}},\varphi_{\mathrm{A}}} & \mathcal{I}_{\varphi_{\mathrm{A}},|\alpha|} & \mathcal{I}_{\varphi_{\mathrm{A}},\varphi_{\alpha}} \\
\mathcal{I}_{|\alpha|,\tau} & \mathcal{I}_{|\alpha|,\varphi_{\mathrm{D}}} & \mathcal{I}_{|\alpha|,\varphi_{\mathrm{A}}} & \mathcal{I}_{|\alpha|,|\alpha|} & \mathcal{I}_{|\alpha|,\varphi_{\alpha}} \\
\mathcal{I}_{\varphi_{\alpha},\tau} & \mathcal{I}_{\varphi_{\alpha},\varphi_{\mathrm{D}}} & \mathcal{I}_{\varphi_{\alpha},\varphi_{\mathrm{A}}} & \mathcal{I}_{\varphi_{\alpha},|\alpha|} & \mathcal{I}_{\varphi_{\alpha},\varphi_{\alpha}}
\end{bmatrix} . \tag{3.9}
$$

The definitions of the individual entries can be found in Appendix A.2. As for the SISO setup, we can define the REB as the square root of the inverse of the $(1,1)$ element of the CRLB. In a similar fashion, we define the angulation error bound (AEB) for the AoD [35,52], [N4], i.e.,[3]

$$
\mathcal{A}(\varphi_{\mathrm{D}}) = \sqrt{\mathcal{I}^{-1}(\varphi_{\mathrm{D}})}, \tag{3.10}
$$

where the EFI on the angulation problem is given as

$$
\mathcal{I}(\varphi_{\mathrm{D}}) = \left[[\boldsymbol{\mathcal{I}}^{-1}(\boldsymbol{\psi})]_{2,2}\right]^{-1}. \tag{3.11}
$$

However, the spatial correlations of the covariance matrix prevent insight beyond numerical analysis. Thus, we neglect the spatial correlations of the covariance matrix, considering only the block-diagonal structure, leading to the following reduced FIM

$$
\boldsymbol{\mathcal{I}}_{\mathrm{nc}}(\boldsymbol{\psi}) =
\begin{bmatrix}
\mathcal{I}_{\mathrm{nc},\tau,\tau} & 0 & 0 & \mathcal{I}_{\mathrm{nc},\tau,|\alpha|} & 0 \\
0 & \mathcal{I}_{\mathrm{nc},\varphi_{\mathrm{D}},\varphi_{\mathrm{D}}} & 0 & 0 & 0 \\
0 & 0 & \mathcal{I}_{\mathrm{nc},\varphi_{\mathrm{A}},\varphi_{\mathrm{A}}} & 0 & 0 \\
\mathcal{I}_{\mathrm{nc},|\alpha|,\tau} & 0 & 0 & \mathcal{I}_{\mathrm{nc},|\alpha|,|\alpha|} & 0 \\
0 & 0 & 0 & 0 & \mathcal{I}_{\mathrm{nc},\varphi_{\alpha},\varphi_{\alpha}}
\end{bmatrix} . \tag{3.12}
$$

For this case, the dispersion parameters decouple, meaning that they do not influence the achievable performance of one another [N4, N6]. This enables the derivation of closed-form expressions for the ranging and angulation capabilities for the RFID setup.

The EFI for the AoD[4] is given as

$$
\mathcal{I}(\varphi_{\mathrm{D},m}) = \frac{8\pi^2 f_{\mathrm{c}}^2}{c^2} L_{m'} \mathrm{SINR}(\tau_{m,m'}) \sum_{l=1}^{L_m} \left(\frac{\partial \boldsymbol{\Omega}_{\mathrm{TX},m}^{\mathrm{T}}}{\partial \varphi_{\mathrm{D},m}} \Delta \boldsymbol{p}_m^{(l)}\right)^2. \tag{3.13}
$$

It scales linearly with the antennas at the RX and the $\mathrm{SINR}(\tau_{m,m'})$, and scales quadratically with the center frequency. The last term in (3.13) captures the scaling with respect to the array geometry and depends additionally on the value of the AoD. It is interesting to note that while the CRLB for the delay and AoD decouple, the EFI on the AoD still depends on the delay via the $\mathrm{SINR}(\tau_{m,m'})$, i.e., the component SNR after the whitening/equalization operation with the covariance matrix. In an AWGN-only model, the EFI for the AEB is the same, except that the $\mathrm{SINR}(\tau_{m,m'})$ is replaced by the SNR.

---

[3]We will only define the AEB for the AoD. The definition of the AEB for the AoA follows accordingly.

[4]Again, the EFI for the AoA is defined accordingly.

The EFI for the delay estimation is given as

$$\mathcal{I}(\tau_{m,m'}) = 8\pi^2\beta^2\widetilde{\text{SINR}}(\tau_{m,m'})L_m L_{m'}. \tag{3.14}$$

Compared to the SISO setup, the EFI for the delay scales linearly with the number of antennas of the TX and RX. As the FIM on the delay and AoD and AoA decouple, the same gain is achieved by a non-phase coherent setup [T2]. It is important to note that the pinhole nature of the backscatter channel increases the influence of the DMC with respect to the SISO channel, meaning that the SDR is reduced. This reduction in SDR leads to a decreased $\text{SINR}(\tau_{m,m'})$. In [6] it is shown that

$$\text{SDR}_{\text{BS}} = \frac{\text{SDR}_{\text{DL}}\text{SDR}_{\text{UL}}}{1 + \text{SDR}_{\text{DL}} + \text{SDR}_{\text{UL}}}, \tag{3.15}$$

with SDR_{DL} and SDR_{UL} as the SDR of the downlink and the uplink channel, respectively. It is clear from (3.15) that $\text{SDR}_{\text{BS}} < \min(\text{SDR}_{\text{DL}}, \text{SDR}_{\text{UL}})$, meaning that strong LOS conditions are necessary for accurate and robust ranging with backscatter channels.

Here, we have to mention that (3.13) and (3.14) are valid for bistatic reader setups, meaning $m \neq m'$. For a monostatic setup, the information is reduced in two ways: (i) The blocks in the DMC process covariance matrix are increased by a factor of up to 2 , leading to a reduced $\text{SINR}(\tau_{m,m})$ and $\widetilde{\text{SINR}}(\tau_{m,m})$. This reduction can be as high as 2 in the extreme case of negligible AWGN [T2] (see also (A.24) vs. (A.18)). (ii) Due to channel reciprocity, the received signal from antenna l to antenna l' and the reverse channel are the same (up to the AWGN) and thus only one should be considered.[5]

In Fig. 3.3 the influence of considering (——, (a), (c), (e)) or neglecting (——, (b), (d), (f)) the spatial correlations in the covariance matrix on the REB and AEB is depicted over a wide range of bandwidth. For the simulation, we used 4-ary linear arrays with a spacing of 0.4λ, oriented along the x-axis, at the TX reader and the RX reader, positioned at $\boldsymbol{p}_{\text{TX}} \equiv \boldsymbol{p}_m = [0,0]^{\text{T}}\text{m}$ and $\boldsymbol{p}_{\text{RX}} \equiv \boldsymbol{p}_{m'} = [5,0]^{\text{T}}\text{m}$, respectively. As the CRLB depends on the AoD and AoA, the RFID label was placed on a uniform rectangular grid between $[0,2]^{\text{T}}\text{m}$ and $[5,5]^{\text{T}}\text{m}$ with a spacing of half a meter in x and y directions, leading to 77 positions.[6] The results depicted in Fig. 3.3 are thus root mean square averaged over the label's position. The transmitted pulse is a root-raised cosine pulse with a roll-off factor of 0.6 and a pulse duration according to $1/B$, with B as bandwidth, at a carrier frequency of $f_{\text{c}} = 900\,\text{MHz}$. We set $\text{SNR} = 25\,\text{dB}$ and the SDR of the downlink and uplink are set such that $\text{SDR}_{\text{BS}} = 0\,\text{dB}$. The DODPS and DOAPS are assumed uniformly distributed, while the DPS of the downlink and the uplink follows the same double-exponential function used in the experiment to produce Fig. 3.2. The onsets of the DPSs are set equal to the LOS delays of the constituent channels. To compare the CRLB to the performance of standard estimators, at each RFID label position, 100 realizations of the DMC and AWGN process are drawn.

Solid lines with circle markers depict the REB/AEB (—⊖—) for the range, the AoD and the AoA in Figs. 3.3 (a) & (b), (c) & (d) and (e) & (f), respectively.

---

[5]By taking the mean of the two measurements it would be possible to reduce the AWGN for these measurements.

[6]A comparable setup is shown in Fig. 3.4.

3.1. LIMITS ON CHANNEL PARAMETERS ESTIMATION
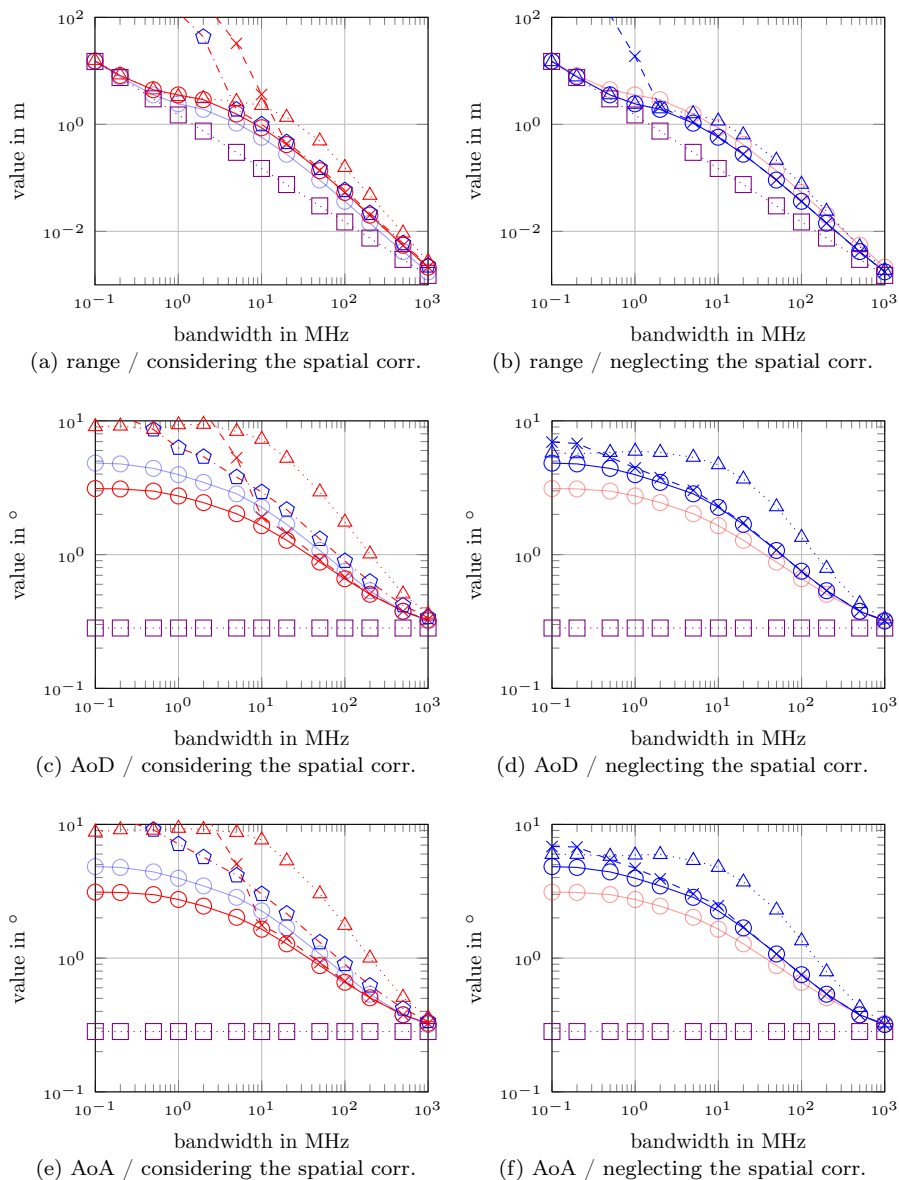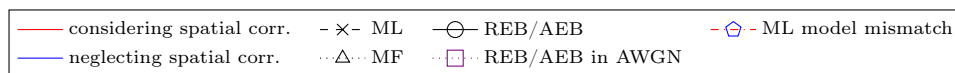
Figure 3.3: REB ((a) and (b)), and AEB for the AoD ((c) and (d)), and AoA ((e) and (f)) (—⊖—) including standard deviations of ML (- ✕ -) and MF (···△···) estimators for the two different covariance models, including spatial correlations (——, (a), (c), (e)) and neglecting spatial correlations (——, (b), (d), (f)). For comparison, the REB and AEB for an AWGN model (···□···) are included. Finally, a mismatched 'ML' estimator is added to analyze the effect of neglecting the spatial correlations only in the estimator (- ⬠ -).

33

Different colors show the two different covariance models, i.e., red lines use the spatially correlated covariance matrix (——, see Appendix A.2.1), while blue lines use the block-diagonal covariance matrix (——, see Appendix A.2.2). As for the SISO setup in Section 3.1.1, we compare the bounds to ML estimators (- ✕ -) making use of the inverse of the known covariance matrix and naïve MF estimators (⋯△⋯).

Fig. 3.3 (a) & (b) show that the influence of the spatial correlations is negligible at the highest bandwidth and increases slightly towards smaller bandwidth. For very narrow bandwidth, both the REB considering and neglecting the spatial correlations approach the REB in AWGN (⋯□⋯), as for the SISO setup. The ML estimators for both the model including the spatial correlations and the model neglecting the spatial correlations approach their respective bound at high bandwidth and deviate from the bound at $10\,\mathrm{MHz}$ and $1\,\mathrm{MHz}$, respectively. An interesting observation is made, by employing the covariance matrix neglecting the spatial correlations (block diagonal matrix) to the data generated including the correlations (- ⬠ -). We called this estimator 'ML model mismatch'. Of course this is not an ML estimator anymore, as it uses the mismatched covariance matrix. However, the estimator approaches the bound at high bandwidth, just as the ML estimator, and it deviates at comparable bandwidth as the ML estimator.

Fig. 3.3 (c) & (d) and (e) & (f) present the AEB[7]. Compared to the REB the spatial correlations included in the covariance matrix, increase the Fisher information, leading to a decreased AEB compared to the case neglecting the correlations. The ML estimators perform similar as for the REB. However, the 'ML model mismatch' estimator (- ⬠ -) is not able to approach the AEB (—○—), as it does not exploit the correlations in the covariance matrix. Nevertheless, it still performs better than the MF estimator. Furthermore, the 'ML model mismatch' estimator does not show the high risk of outliers to considerably smaller bandwidth than the ML estimator. We interpret this effect in the following way: (i) if the covariance matrix including the spatial correlations is utilized for the whitening/equalization operation, the resulting signal afterwards is an AWGN-only model with a reduced SNR, given by the $\mathrm{SINR}(\tau_{m,m'})$ (see discussion around Fig. 3.1 and Fig. 3.2). If this SNR is below a threshold, the estimated value will be uniformly distributed within its support. (ii) if the covariance matrix neglecting the spatial correlations is utilized for the whitening/equalization operation, the resulting signal afterwards will still include certain correlations which can be utilized by the estimator.

The above discussion shows that neglecting the spatial correlations within the covariance matrix does not significantly reduce the accuracy and robustness of an estimator. In Chapter 4 we will develop estimators on the basis of this finding. These estimators will also include the parameters of the covariance matrix which have been assumed known for the above derivations and simulations. If these additional parameters do not decouple from the above parameters, the presented CRLBs will be increased.

---

[7]As we used a symmetric setup (same array at the TX and RX), the AEB for the AoD equals the AEB for the AoA. Thus, we will only mention AEB as a general term, meaning either one.

3.2 Limits on position estimation

As mentioned in Chapter 2, some of the channel parameters, e.g., the delay, as well as the directions, depend on the position of the TX and RX. Remember that $h(\tau, \boldsymbol{\Omega}_{\mathrm{TX}}, \boldsymbol{\Omega}_{\mathrm{RX}}; \boldsymbol{p}_{\mathrm{TX}}, \boldsymbol{p}_{\mathrm{RX}})$ is parametrized by the position of the TX and RX. If we now want, e.g., to know the performance limits of estimating the position of the RX for known TX position, we can apply the chain rule [42, 51, 78, 100] on the FIM on the channel parameters and derive the equivalent Fisher information matrix (EFIM) for the RX position. To this end, we separate the individual parameters in $\boldsymbol{\psi}$ into position-related and nuisance parameters and define parameter vector $\boldsymbol{\xi} = [\boldsymbol{p}_{\mathrm{RX}}, \text{nuisance parameters in } \boldsymbol{\psi}]$. The FIM on parameter vector $\boldsymbol{\xi}$ is then given as

$$\boldsymbol{\mathcal{I}}(\boldsymbol{\xi}) = \boldsymbol{J}\boldsymbol{\mathcal{I}}(\boldsymbol{\psi})\boldsymbol{J}^{\mathrm{T}}, \tag{3.16}$$

where $\boldsymbol{J}$ is the Jacobian matrix, relating the variations in parameters of $\boldsymbol{\psi}$ to $\boldsymbol{\xi}$ and its elements are given as

$$[\boldsymbol{J}]_{i,j} = \frac{\partial \psi_i}{\partial \xi_j}. \tag{3.17}$$

Finally, the position error bound (PEB) is defined as

$$\mathcal{P}(\boldsymbol{p}_{\mathrm{RX}}) = \sqrt{\mathrm{Tr}\{\boldsymbol{\mathcal{I}}^{-1}(\boldsymbol{p}_{\mathrm{RX}})\}} \tag{3.18}$$

with the EFIM on the position estimation for 2-dimensional positioning as

$$\mathcal{I}(\boldsymbol{p}_{\mathrm{RX}}) = \left[[\boldsymbol{\mathcal{I}}^{-1}(\boldsymbol{\xi})]_{1:2,1:2}\right]^{-1}. \tag{3.19}$$

In the following, we will highlight this process focusing on the non-phase-coherent RFID setup of Section 2.6. For non-phase-coherent observations, beamforming cannot be applied and only the ranging information is available [T2]. The EFIM on the position of the RFID label can then be found as [T2]

$$\boldsymbol{\mathcal{I}}(\boldsymbol{p}) = \sum_{m=1}^{M} \mathcal{I}(\tau_{m,m})\boldsymbol{h}_{m,m}\boldsymbol{h}_{m,m}^{\mathrm{T}} + \sum_{m=1}^{M-1} \sum_{m'=m+1}^{M} \mathcal{I}(\tau_{m,m'})\boldsymbol{h}_{m,m'}\boldsymbol{h}_{m,m'}^{\mathrm{T}}, \tag{3.20}$$

where the influence of the geometry is described by $\boldsymbol{h}_{m,m'} = \frac{1}{c}(\boldsymbol{e}_m + \boldsymbol{e}_{m'})$ with $\boldsymbol{e}_m$ as unit vector pointing from the mth reader position $\boldsymbol{p}_m$ towards the RFID label's position $\boldsymbol{p}$. In (3.20), the first and second term highlight the contributions of monostatic and bistatic reader measurements, respectively. As the channel from reader m to reader m' and its reverse channel are the same (up to the AWGN), we consider only one of the bistatic measurements[8].

In Fig. 3.4[9] 2-fold standard deviation ellipses are depicted for different label positions (∗) in a halfplane. Two RFID readers, each equipped with either 1 or 2

---

[8]Again, the influence of the AWGN could be reduced by averaging.

[9]This figure is nearly the same as Fig. 4 in [T2]. However, in [T2] we assumed that monostatic measurements can be fully correlated (originating and ending at the same antenna) or uncorrelated (originating and ending at different antennas). In this work, according to (2.34), we are assuming that the DMC process only depends on the reader position $\boldsymbol{p}_m$ and not on the individual antenna position $\boldsymbol{p}_m^{(l)}$. Thus, the gain for the monostatic measurements is slightly decreased compared to the results in [T2].
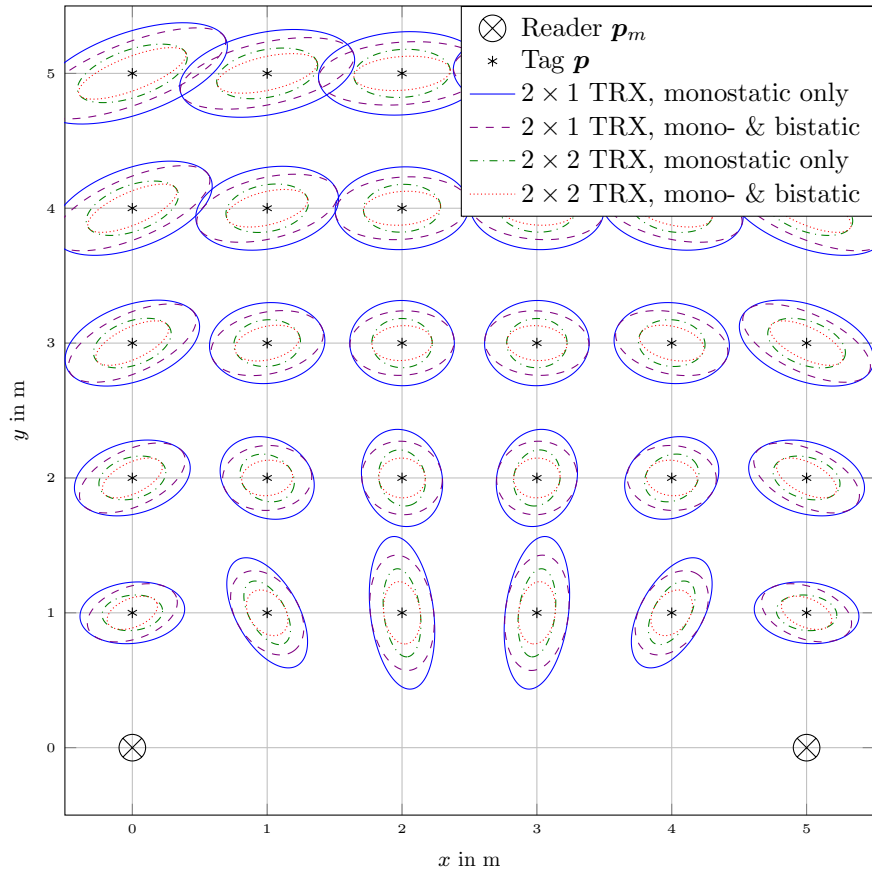
Figure 3.4: PEB depicted via 2-fold standard deviation error ellipses for a bandwidth of 50 MHz for different MIMO constellations: monostatic only without an array (——), mono- and bistatic without an array (‐ ‐ ‐), monostatic only with a 2-ary array (‐ · ‐ ·), mono- and bistatic with a 2-ary array (·········).

antennas for transmitting and receiving, are depicted by $\bigotimes$. For the two monostatic only setups (——, ‐ · ‐ ·), no time synchronization (per sample) is needed between the two readers, as only backscatter channels are used that originate and end at the same reader. According to (3.20), monostatic measurements add information only in the radial directions, corresponding to circles around the readers. Bistatic measurements add information mainly in the orthogonal axis, which corresponds to the normal direction to an ellipse with the two involved readers in its foci. This is highlighted in Fig. 3.4 by looking at the two scenarios including bistatic measurements (‐ ‐ ‐, ·········). By increasing the number of readers, according to (3.20), the monostatic part is applied M times, while the bistatic term is applied $\frac{M(M-1)}{2}$ times.

36

3.3 Concluding Remarks

In this chapter, we highlighted the fundamental limits for estimation of positon-related parameters from radio channel measurements in DMC channels. From a system point of view, the main limiting factors are the bandwidth and the array apertures.

- The EFI for the REB scales slightly super-quadratically with bandwidth (starting at intermediate bandwidths). This is a combination of quadratic scaling directly related to the bandwidth (also seen in AWGN) plus the effect of less interference of the DMC. Furthermore, the EFI for the REB scales linearly in the number of array elements at the transmitter and receiver [T1, T2], [N3].

- The EFI for the AEB is increased by increasing the bandwidth as less DMC interferes. In an AWGN-only setup, the AEB does not scale with bandwidth and only the array apertures are relevant. This scaling with respect to the array apertures applies in DMC interfered channels as well. However, its scaling behavior is more complicated than for the REB, as the EFI for the AEB is influenced by the array geometry and the AoD/AoA. In the special case of a ULA with wavelength half spacing, the array aperture scales the EFI for the AEB with a factor of $\frac{L(L-1)^2}{48}$. In general, larger array apertures increase the EFI for the AEB [N4], and even aliased arrays can be employed at the cost of additional ambiguities [N5].

With respect to positioning of RFID labels from range-only measurements, we have shown that monostatic measurements deliver information in radial direction, while bistatic measurements provide information orthogonal to an ellipse with the readers in its focal points [T2].

Regarding the channel, high SDR are beneficial for ranging and angulation, because the SINR is at least equal to the SDR. This is especially true for RFID setups as the SDR for the backscatter channel is at most the minimum of the two SDRs of the constituent channels. While the SDR cannot be influenced directly, our analysis shows that by increasing the bandwidth the influence of the DMC, and hence the SDR, on the SINR is diminished.

Within this chapter, it is assumed that the covariance matrix, i.e., the parameters of the DMC and AWGN process, is/are known. If the covariance matrix is not known, the EFI on a specific SMC parameter, e.g. τ, is influenced in two ways: (i) the information is increased if the covariance matrix depends on the parameter (see also (3.1) and [N3]) and (ii) the information is decreased if the cross-element is non-zero (if the SMC parameter does not decouple from the covariance matrix estimation) [42].

In realistic scenarios, the covariance matrix (or its parameters) will not be known and needs to be estimated concurrently with the dispersion parameters. Thus, in the following chapter we will drop the need of a known covariance matrix and present methods to estimate the parameters of the SMC and DMC jointly.

d = 23.1 m

d = 46.2 m

Chapter 4

Estimation in dense multipath environments

In the previous chapter, the CRLBs for position-related parameters have been analyzed and compared to two estimators: (i) an MF and (ii) an ML approach. While the MF estimator deviates form the bound at rather high bandwidth, the ML estimator is able to approach the bound down to a much lower bandwidth. However, the likelihood model in Chapter 3 assumed a known DMC-plus-AWGN covariance matrix. For actual measurements, this is certainly unrealistic and the parameters of the DMC and AWGN processes need to be estimated according to the likelihood model given in Chapter 2.

Therefore, estimators are needed which are capable of estimating the parameters of the SMC and the DMC-plus-AWGN process from a single or a few measurement snapshot(s). In Section 2.2, the relationship of the signal model and its Fourier transform has been highlighted. With this relationship in mind, the estimation of the dispersion parameters is basically a line-spectral estimation (LSE) problem [47, 87, 89]. As LSE problems occur in many different fields of research, e.g., sonar, radar, speech analysis, and channel estimation [89], numerous methods tackling LSE have been derived. Two main classes of approaches are subspace methods and maximum likelihood methods.

Subspace methods analyze the signal and/or noise subspace obtained by an eigenvalue decomposition of the signal covariance matrix $\boldsymbol{C}_{\mathrm{signal}} = \mathbb{E}\left[\boldsymbol{r}\boldsymbol{r}^{\mathrm{H}}\right]$. Examples of subspace methods are multiple signal classification (MUSIC) [69, 75], or estimation of signal parameters via rotational invariance technique (ESPRIT) [49, 72]. All subspace based methods rely on the assumption that the subspace spanned by the noise eigenvectors (only AWGN) is orthogonal to the subspace spanned by the spectral lines, the SMCs, and that the number of lines is smaller than the number of samples N [87]. By including the DMC process, the white noise assumption is violated, degrading the performance of subspace based methods [87]. Furthermore, subspace based methods need an estimate of the signal covariance matrix as input. As we want to employ our estimators on single-snapshot observations, the sample-based covariance matrix does not suffice. Methods like forward-backward smoothing could be applied, however, these degrade the estimation accuracy and resolution ability [47, 77, 109].

Maximum likelihood (ML) methods rely on the likelihood function given in

39

Section 2.3 and try to maximize the likelihood function with respect to its parameters. The benefit of ML based approaches is that they can be applied without a direct estimate of the signal covariance matrix and are capable of estimating the parameters of the SMCs from a single snapshot [47, 87]. Furthermore, they are less sensitive to violations of the statistical assumption of white noise [87, 88, 91] and it is also possible to derive estimators including the parameters of the DMC process [71]. Unfortunately, the derived cost-functions are highly multimodal, meaning that the initialization of the algorithms are paramount to converge towards the global optimum [87, 90]. ML estimators are distinguished in two categories defined by the underlying model of the complex amplitudes of the SMCs: (i) deterministic maximum likelihood (DML) [30, 47, 71, 87, 90] and (ii) stochastic maximum likelihood (SML) [14, 15, 40, 63, 92, 101]. The former assumes that the complex amplitudes are deterministic unknowns, while the latter assumes an underlying stochastic model. In classic array signal processing literature [47, 87, 102], the properties of the asymptotic behavior of DML and SML estimators have been investigated and are well understood if the number of snapshots is large [102] compared to the number of components (DML) or the number of sensors (SML). In [70] the asymptotic consistency and normality for the DML estimator has been proven for a single-snapshot scenario if the number of sensors grows large.

Given the likelihood function of Section 2.3, direct maximization of the likelihood function with respect to all parameters is computationally demanding. Thus, we resort to approximative schemes, e.g., variational inference [13] whose concept is discussed in Section 4.1. By separating the unknown parameter vector into disjoint subsets, the mean field approximation [64] is introduced in Section 4.1.1. Finally, we will present in Sections 4.2 and 4.3 two application examples using the concept of variational inference for ranging and direct positioning, respectively.

4.1 Variational Inference

Given a likelihood function $f(\boldsymbol{r}|\boldsymbol{\psi})$, with $\boldsymbol{\psi}$ as parameter vector and $\boldsymbol{r}$ as observed received signal, we want to estimate the probability distribution function (pdf) $f(\boldsymbol{\psi}|\boldsymbol{r})$ for some prior distribution $f(\boldsymbol{\psi})$. Unfortunately, the posterior pdf is often intractable due to the integration in the model evidence term in the denominator of the Bayes rule. Thus, we have to resort to approximative inference schemes. One possible pathway is variational inference, having its origins in the *calculus of variations* [13]. Variational inference, sometimes also called variational Bayesian inference or just variational Bayes, is a deterministic approximation scheme and tries to approximate the posterior pdf by some proxy pdf, i.e.,

$$q(\boldsymbol{\psi}|\boldsymbol{r}) \approx f(\boldsymbol{\psi}|\boldsymbol{r}). \tag{4.1}$$

The aim of variational Bayes is to minimize the Kullback-Leibler divergence (KLD) from the posterior to the proxy pdf, i.e.,

$$\mathrm{KL}\big(q(\boldsymbol{\psi}|\boldsymbol{r})\|f(\boldsymbol{\psi}|\boldsymbol{r})\big) = \mathbb{E}_{q(\boldsymbol{\psi}|\boldsymbol{r})}\left[\log\left(\frac{q(\boldsymbol{\psi}|\boldsymbol{r})}{f(\boldsymbol{\psi}|\boldsymbol{r})}\right)\right]. \tag{4.2}$$

Due to the intractable posterior pdf this is not possible, but it is easy to show that the logarithm of the constant model evidence can be decomposed into [13, 16]

$$\log(f(\boldsymbol{r})) = \mathcal{L}\big(q(\boldsymbol{\psi}|\boldsymbol{r})\big) + \mathrm{KL}\big(q(\boldsymbol{\psi}|\boldsymbol{r})\|f(\boldsymbol{\psi}|\boldsymbol{r})\big), \tag{4.3}$$

with the variational lower bound functional as

$$\mathcal{L}\big(q(\boldsymbol{\psi}|\boldsymbol{r})\big) = \mathbb{E}_{q(\boldsymbol{\psi}|\boldsymbol{r})}\left[\log\left(\frac{f(\boldsymbol{\psi},\boldsymbol{r})}{q(\boldsymbol{\psi}|\boldsymbol{r})}\right)\right]. \tag{4.4}$$

The optimal pdf $q^*(\boldsymbol{\psi}|\boldsymbol{r})$ is the one minimizing the KLD given in (4.2). By definition $\mathrm{KL}(q\|f) \geq 0$ for valid pdfs, thus, minimizing the KLD is equivalent to maximizing the variational lower bound (4.4), as the model evidence is constant with respect to $q(\boldsymbol{\psi}|\boldsymbol{r})$. Compared to the KLD, the variational lower bound contains the tractable joint pdf $f(\boldsymbol{\psi},\boldsymbol{r})$, and not the posterior pdf.

Minimizing the KLD from the posterior to the proxy pdf is not the only possible way of finding an approximation of the posterior. Another possibility is to minimize the KLD from the proxy to the posterior pdf, leading to expectation propagation algorithms [8, 13]. For multimodal posterior pdfs, the expectation propagation algorithm tries to include all the modes of the posterior while variational Bayes focuses the probability mass of the proxy pdf at regions of the true posterior with high probability mass [13, 16, 58].

4.1.1 Mean Field Approximation

Until now, we have not restricted the proxy pdf in any way. For inference problems with a large number of parameters, an often used approximation is (structured) mean field [13]. For the structured mean field approximation, one splits the parameter vector in subsets[1], $\boldsymbol{\psi} = [\boldsymbol{\psi}_1, ..., \boldsymbol{\psi}_P]$ and postulates that the proxy pdf factorizes with respect to these subsets, i.e.,

$$q(\boldsymbol{\psi}|\boldsymbol{r}) = \prod_{p=1}^{P} q(\boldsymbol{\psi}_p|\boldsymbol{r}). \tag{4.5}$$

Inserting (4.5) into (4.4) and evaluating the variational lower bound with respect to a single subset $\boldsymbol{\psi}_p$ while keeping the other parameters (not in this subset) fixed leads to [13, 16]

$$\mathcal{L}\big(q(\boldsymbol{\psi}|\boldsymbol{r})\big) = \mathbb{E}_{q(\boldsymbol{\psi}_p|\boldsymbol{r})}\left[\log\left(\frac{\exp\left\{\mathbb{E}_{q(\boldsymbol{\psi}_{\bar{p}}|\boldsymbol{r})}[\log(f(\boldsymbol{\psi},\boldsymbol{r}))]\right\}}{q(\boldsymbol{\psi}_p|\boldsymbol{r})}\right)\right] + \mathrm{const}, \tag{4.6}$$

with $q(\boldsymbol{\psi}_{\bar{p}}|\boldsymbol{r}) = \prod_{i\neq p} q(\boldsymbol{\psi}_i|\boldsymbol{r})$. Assuming that the optimal solution is achievable, it is possible to derive the unconstrained factor update as

$$q^*(\boldsymbol{\psi}_p|\boldsymbol{r}) = \frac{\exp\left\{\mathbb{E}_{q(\boldsymbol{\psi}_{\bar{p}}|\boldsymbol{r})}[\log(f(\boldsymbol{\psi},\boldsymbol{r}))]\right\}}{\int \exp\left\{\mathbb{E}_{q(\boldsymbol{\psi}_{\bar{p}}|\boldsymbol{r})}[\log(f(\boldsymbol{\psi},\boldsymbol{r}))]\right\} d\boldsymbol{\psi}_p}, \tag{4.7}$$

---

[1]If all individual parameters factorize it is often referred as mean field approximation, while for non-fully factorized subsets the term structured mean field approximation is used.

41

The denominator in (4.7) assures that $q^*(\boldsymbol{\psi}_p|\boldsymbol{r})$ is a valid pdf. By restricting the proxy pdf to a certain family of pdfs, we need to maximize (4.6) with this constraint. This will be performed below for the ML solution. As (4.6) or (4.7) are only for one subset of parameters, and depend on all other subsets of parameters, we have to iterate (in any order) over the subsets to converge towards a local maximum of the variational lower bound. This means that we need initial values for all subsets except the pth. The optimization is guaranteed to converge towards a local maxima of the variational lower bound [13]. However, convergence of mean field variational inference is only guaranteed to a local, but not to a global maximum.

Maximum Likelihood Solution   To find ML solutions with variational inference, we employ a uniform prior $f(\boldsymbol{\psi})$ and constrain the pdfs of the individual subsets to point estimates, i.e., $q(\boldsymbol{\psi}_p) = \delta(\boldsymbol{\psi}_p - \bar{\boldsymbol{\psi}}_p)$ with $\bar{\boldsymbol{\psi}}_p$ arbitrary. The solution to the maximization of (4.6) is then

$$\hat{\boldsymbol{\psi}}_p = \arg\max_{\boldsymbol{\psi}_p} \left(\log(f(\boldsymbol{r}, \boldsymbol{\psi}_p, \hat{\boldsymbol{\psi}}_{\bar{p}})) \right), \tag{4.8}$$

where $\hat{\boldsymbol{\psi}}_{\bar{p}}$ are the point estimates of all other parameters except $\boldsymbol{\psi}_p$. Remember that with the mean field approximation we have to iterate over the individual subsets to converge to a local maximum of the variational lower bound.

In [13, 16] it is shown that expectation maximization algorithms can be derived by variational inference and a structured mean-field approximation. To this end, the parameter vector is split into the hidden variables and the unknown parameters and a structured mean-field approximation between these two subsets is postulated. By employing the unconstrained factor update (4.7) for the hidden variables and point estimates for the unknown parameters, the update equations of the expectation maximization algorithm can be derived.

4.2   Application Example 1: Maximum Likelihood Ranging

In [T3] we utilized the above framework to derive an ML ranging estimator for a MIMO backscatter channel including the parameters of the DMC and AWGN processes. The signal model consists of a single SMC, i.e., the LOS, plus the DMC and AWGN processes. The parameter vector in this contribution is given as $\boldsymbol{\psi} = [\tau_{m,m'}, \varphi_{\mathrm{D},m,m'}, \varphi_{\mathrm{A},m,m'}, \alpha_{m,m'}, \boldsymbol{\eta}_{m,m'}]^{\mathrm{T}}$, with $\boldsymbol{\eta}_{m,m'}$ as the parameters of the DMC and AWGN processes, governing the covariance matrix. We split the parameter vector into the subsets $\boldsymbol{\psi}_1 = [\tau_{m,m'}, \varphi_{\mathrm{D},m,m'}, \varphi_{\mathrm{A},m,m'}]^{\mathrm{T}}$, $\boldsymbol{\psi}_2 = \alpha_{m,m'}$, and $\boldsymbol{\psi}_3 = \boldsymbol{\eta}_{m,m'}$ and apply the mean-field approximation to derive the iterative update equations (see Appendix of [T3] for details).

In [T3] we analyzed the algorithm with synthetic and measured data, enabling comparison to the REB derived in Section 3.1.2. The measurements were performed using lab-grade equipment at two scenarios, a laboratory and an industrial setup.

In Fig. 4.1 we compare the proposed algorithm to the REB (see Sec. 3.1.2), and the MF and ML[2] estimators. The proposed algorithm can be utilized with

---

[2]This is again the ML estimator with knowledge of the covariance matrix. For the mea-

4.2. APPLICATION EXAMPLE 1: MAXIMUM LIKELIHOOD RANGING

(a) Synthetic Data

(b) Measured Data
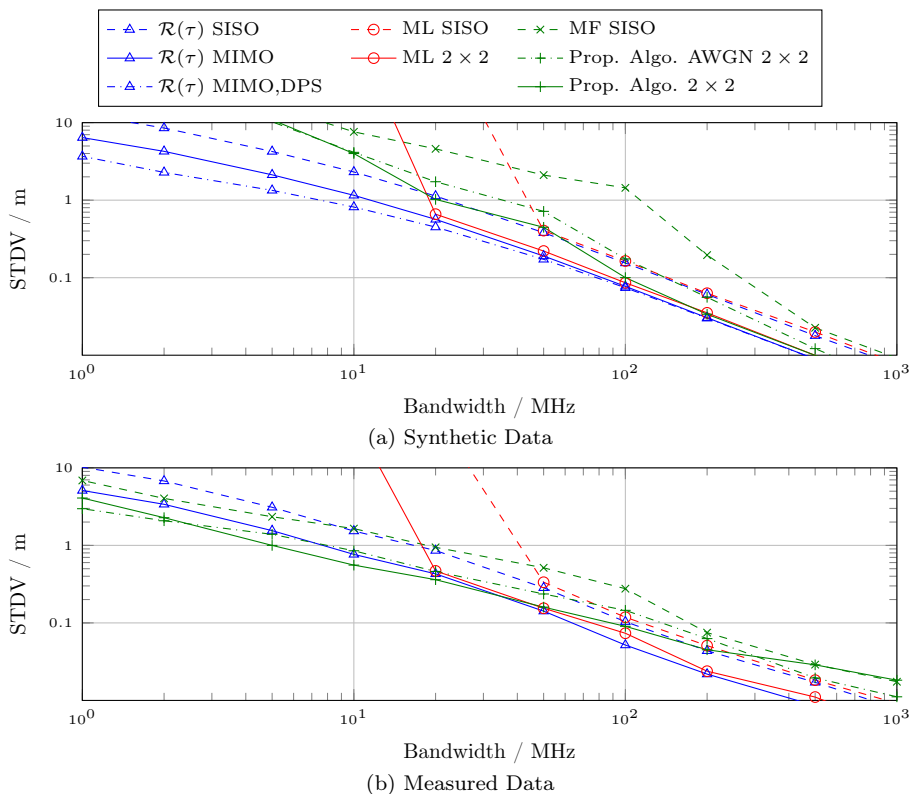
Figure 4.1: REB for SISO (- ▵ -), MIMO (—▵—) and MIMO including the effect of the DPS (-·▵·-), and range estimation standard deviations of a SISO MF estimator (- ✳ -), a SISO ML estimator (- ⊖ -), a MIMO ML estimator (—⊖—), the proposed MIMO AWGN only estimator (-·+·-), and the proposed MIMO estimator including the DMC (—+—) for simulated data (a) and measured data (b). To generate (a), the DPS of the downlink and uplink have been modeled with a double exponential DPS [41] leading to the following channel parameters: $K_{\mathrm{LOS}} = 0.2\,\mathrm{dB}$, $\tau_{\mathrm{RMS}} = 18.4\,\mathrm{ns}$.

two different settings for the covariance matrix, (i) the DMC-plus-AWGN model, and (ii) an AWGN-only setting, neglecting the DMC process. The latter can be seen as a MIMO MF implementation.

For Fig. 4.1a, we utilized realistic synthetic data, generated according to two channel parameters gathered from the measurements, namely the Rician K-factor for the LOS and the root-mean-square delay spread of the backscatter channel [T3]. The proposed estimator including the parameters of the DMC process (—+—) is able to approach the REB at a bandwidth down to 100 MHz. For smaller bandwidths, it starts to deviate from the REB, although not as drastically as the ML estimator. The algorithm is of an iterative nature, and during the initialization, we start by performing a grid search of the LOS parameters

---

sured data, we used a genie-aided covariance matrix estimation utilizing the highest available bandwidth. For details please refer to [T3].

in AWGN only. This is in fact the proposed algorithm with the AWGN-only setting (- · + · -). The subsequent estimation of the parameters of the DMC process underestimates the power in the DMC, because at small bandwidth most of the DMC interferes with the LOS (see Fig. 2.3), therefore, most of the power in the DMC is included in the LOS estimate. Thus, the proposed estimator tends toward an MF implementation at low bandwidths.

For the measured data, we need to perform certain pre-processing steps to be able to depict the REB and the ML estimator. In fact, we need to *know* the covariance matrix. Thus, we utilized the full bandwidth of the measurement equipment (1 GHz) and a 5×5 grid around the measured position to estimate the covariance matrix [T3]. The REB (- △ - and —△—) and ML estimators (- ⊖ - and —⊖—) perform similar as for the synthetic data. The proposed estimator (—+—) shows a rather large standard deviation at the highest bandwidth. This is probably the effect of the DMC estimation, as the AWGN-only estimator (- · + · -) performs better. Another explanation is that the single SMC in DMC-plus-AWGN model does not hold at this high bandwidth and multiple SMCs should be considered (see Chapter 5). However, at smaller bandwidth ($50 - 100$ MHz), the consideration of the DMC process in the algorithm benefits the ranging accuracy considerably. A very interesting effect can be seen at very low bandwidth (below 20 MHz), as all three practical estimators (without the need to know the covariance matrix), perform better than their respective REB. Two explanations come to mind: (i) the covariance matrix needed to compute the REB is wrong (remember that we used a genie-aided estimator at the highest bandwidth), or (ii) the power in the DMC which completely interferes with the LOS component at low bandwidths, *helps* with estimating the LOS component. This effect is depicted for the synthetic data[3] by the REB MIMO, DPS curve (- · △ · -), considering the effect of the onset on the estimation of the LOS delay [N3].

4.3 Application Example 2: Direct Positioning

Positioning via radio channels is often achieved in a two-way process: first position-related parameters are extracted from received signals which are in turn used by dedicated positioning algorithms [39, 110]. Here, we want to present a direct positioning algorithm, meaning that we model the effect of the unknown position directly within the received signal [T4]. Again, we consider a passive RFID setup where the aim is to infer the unknown position of an RFID tag. However, compared to [T3], the measurements have been performed with actual RFID tags and a software-defined-radio testbed capable of extending the utilized bandwidth to 25 MHz. The RFID tags are powered up by a classic UHF RFID protocol. By superimposing a low power broadband reference signal onto the interrogator's signal during tag-to-reader communication, a wideband backscatter measurement can be achieved [7, 31], [N11]. As standard UHF-RFID tags are developed for narrowband operation only, severe distortions would occur due to the antenna. Thus, a dual-frequency tag has been developed. In addition to the normal UHF antenna, the tag employs a 2.45 GHz antenna scattering back

---

[3]For the measured data, this is not possible as the derivative of the DPS is needed.

4.3. APPLICATION EXAMPLE 2: DIRECT POSITIONING

synchronously with the UHF backscatter modulation. The superimposed wide-band signal is thus transmitted in the 2.45 GHz band, enabling higher transmit power and a more flat antenna response at the RFID tag [31].

Fig. 4.2b depicts the floorplan of the laboratory where measurements have been performed. TX1 (○) and RX1 (∗) depict the positions of the UHF antennas for powering up and communicating with the passive tag. The positions of the TX and RX antennas for positioning are shown by □ and ×, respectively and denoted as TX2-TX4 and RX2-RX4. As TX3 & TX4 and RX3 & RX 4 are closely spaced, coherent processing is possible. The tag has been placed within the colored area on a uniform grid. A white color means that at this position, the tag did not receive enough power from the UHF communication, hence, it did not respond and thus no positioning is possible.

As we employ a rather low bandwidth, we model the channel as a LOS-plus-DMC channel. Furthermore, we directly model the influence of the unknown RFID tag position $\boldsymbol{p}$ onto the channel. This enables the direct estimation of the position without the need to first estimate the channel parameters and subsequently estimating the position. Given the direct modeling of the position on the received signal, the likelihood is given as [T4]

$$f(\boldsymbol{r}|\boldsymbol{p}, \boldsymbol{\eta}, \boldsymbol{\alpha}) = \frac{\mathrm{e}^{-(\boldsymbol{r}-\boldsymbol{S}(\boldsymbol{p})\boldsymbol{A}\boldsymbol{\alpha})^{\mathrm{H}}\boldsymbol{C}(\boldsymbol{\eta},\boldsymbol{p})^{-1}(\boldsymbol{r}-\boldsymbol{S}(\boldsymbol{p})\boldsymbol{A}\boldsymbol{\alpha})}}{\pi^{NJ}\det(\boldsymbol{C}(\boldsymbol{\eta}, \boldsymbol{p}))}, \qquad (4.9)$$

where $\boldsymbol{r} \in \mathbb{C}^{NJ \times 1}$ is the stacked received signal, $\boldsymbol{S}(\boldsymbol{p}) \in \mathbb{C}^{NJ \times J}$ is the position dependent signal matrix, $\boldsymbol{A} \in \{0, 1\}^{J \times K}$ is an association matrix enabling the coherent processing of closely-spaced backscatter channels, and $\boldsymbol{\alpha} \in \mathbb{C}^{K \times 1}$ are complex amplitudes[4]. The total number of channels is J while K models the number of reader TX and RX pairs. The number of samples in the temporal domain is denoted by N. For the above setup, $J = 9$ and $K = 4$ or $K = 9$ if the closely-spaced antennas are used coherently or not, respectively. This means that for the coherent version the number of complex amplitudes is 4 while for the non-coherent version 9 complex amplitudes have to be estimated. Furthermore, in (4.9), the covariance matrix does not only depend on the shape parameters of the DMC and the AWGN variance, expressed by $\boldsymbol{\eta}$, but also on the position of the RFID label. Actually, we assume that the shape of the DPS of the DMC process does not depend on the position of the transmitting and receiving antenna. However, we shifted the onset of the DPS with respect to the LOS delay of the j-th channel, while the LOS delay depends directly on the position of the RFID tag and the TX and RX antenna positions. Furthermore, we assume that the DMC is uncorrelated for the different antenna combinations, leading to a block-diagonal covariance matrix.

On the basis of the likelihood model, we developed an iterative ML estimator based on the mean-field approximation $f(\boldsymbol{p}, \boldsymbol{\alpha}, \boldsymbol{\eta}|\boldsymbol{r}) \approx q(\boldsymbol{p}, \boldsymbol{\alpha}|\boldsymbol{r})q(\boldsymbol{\eta}|\boldsymbol{r})$ and derive update equations for the different subsets of parameters [T4].

To be able to highlight the benefit of considering the DMC process in the estimation, we neglected the DMC process, leading to an AWGN-only model. Depending on the association matrix and the employed covariance matrix model, four different estimators are proposed:

- NC-AWGN: By setting the association matrix to a diagonal matrix, thus $K = J$, each antenna is treated as an individual reader. This means

---

[4]For the exact definitions please refer to [T4].
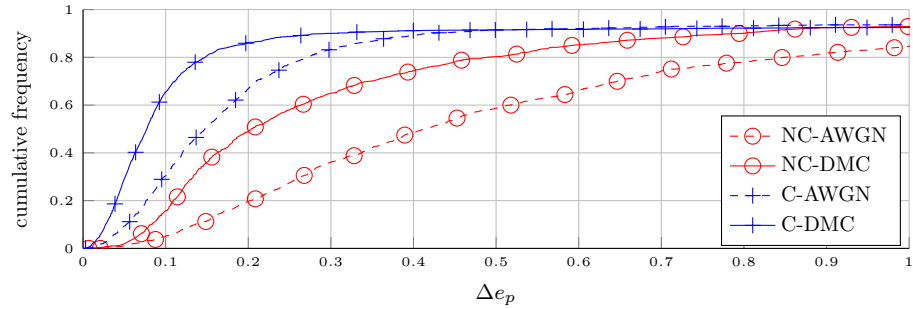
(a) Cumulative frequency of the position error for the proposed algorithms NC-AWGN (- ⊖ -), NC-DMC (—⊖—), C-AWGN (- + -), and C-DMC (—+—).
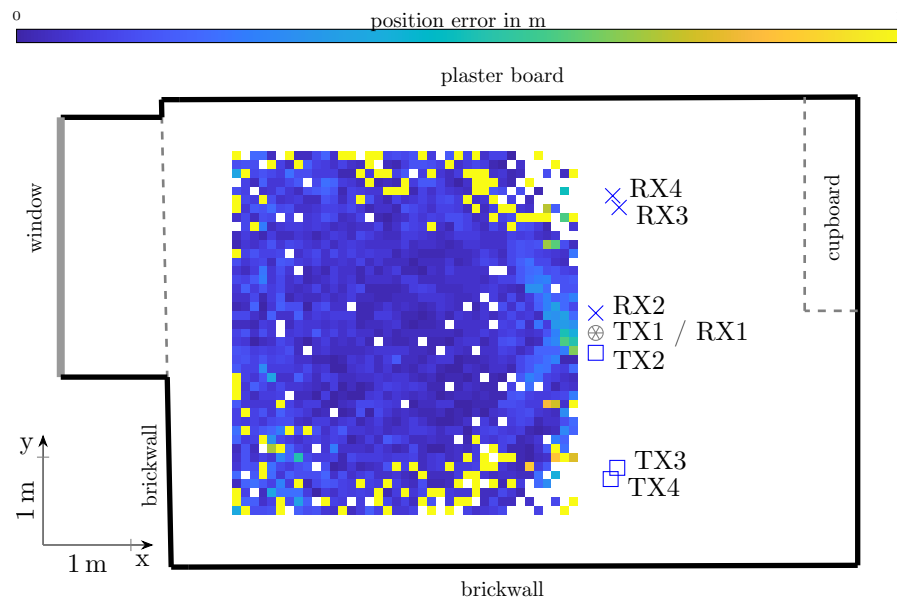
(b) Position error over the entire measurement scenario for the C-DMC algorithm.

Figure 4.2: Results for the direct positioning algorithm.

that the likelihoods for the different channels factorize and a non-coherent combining of the measurements is realized. Furthermore, by neglecting the DMC, an AWGN only model is employed and the algorithm is comparable to a classical MF [85, 103].

- NC-DMC: Here, the association matrix is still a diagonal matrix, but the parameters of the DMC process are estimated. This is possible as we assume that the parameters of the DMC process are the same over the complete room, i.e., we can observe the DMC process with all channels.

- C-AWGN: This algorithm uses closely-spaced antennas coherently, by estimating only a single complex amplitude for channels involving these antennas. Here, the association matrix is a tall rectangular matrix, where each row has only a single non-zero element. The non-zero element *picks* the related complex amplitude. This coherent combining of channels can be

seen as beamforming, as the relative phase between the antenna elements is considered. Thus, the AoD and/or AoA are included in the estimation of the position together with the delay. Again, this estimator uses the AWGN-only model.

- C-DMC: This variant of the estimator employs coherent processing and estimates the parameters of the DMC process.

Fig. 4.2 shows the results obtained by applying the four different variants of the algorithm on the measured data. Fig. 4.2a presents the cumulative frequency of the position errors. As expected, the coherent variants of the algorithm perform better than the non-coherent versions. This is explained by the additional position-related information stemming from the inherent beamforming. The algorithms including the DMC in the estimation also perform consistently better than the AWGN-only algorithms. Unfortunately, all algorithms show about 10 % outliers[5] which can be attributed to the initialization of the algorithms and the non-optimal placement of the antennas. This can be seen by looking at Fig. 4.2b which presents the position errors of the individual measurements. Most of the outliers occur in the bottom and top quarter of the measured grid. During the initialization, side modes of the evaluated likelihood function occur opposite the correct positions. The subsequent update procedure is then unable to recover the correct maximum. This could be improved by utilizing better antenna placement or a swarm like updating procedure, updating not only the maximum found during initialization but rather a number of local maxima.

4.4 Concluding Remarks

In this chapter we have shown that the estimation of position-related parameters from radio channel measurements benefits from considering the DMC process. In Section 4.2, the DMC process is seen purely as an interference to the estimation procedure. By including the parameters of the DMC process in the estimation algorithm, it is possible to approach the CRLB for ranging in DMC-plus-AWGN channels [T3]. In Section 4.3 we highlighted the possibility of exploiting the underlying position-related parameters within the DMC process for a direct positioning algorithm [T4].

Both application examples assume a deterministic complex amplitude, and can thus be categorized as DML estimators, using the single-SMC-in-DMC-plus-AWGN model. As the target bandwidth for this RFID application is below 100 MHz and the array apertures are not very large, this model simplification seems appropriate. However, as can be seen in Fig. 4.1, the estimator is not able to approach the CRLB for the highest bandwidths, for measured data.

For these high bandwidths, the model should be changed to include a multitude of SMCs. With this multi-SMC model in mind, a so far not discussed problem arises: How many SMCs can be estimated reliably from the given observed data?

---

[5]The measurements where the tag did not respond are not considered as these are not attributed to the algorithm but rather the UHF communication.

d = 21.6 m

d = 43.2 m

Chapter 5

Towards joint estimation and detection of specular multipath components

In the previous chapter, maximum likelihood estimators were introduced for the single-SMC-plus-DMC channel model. We have seen that for narrow to intermediate bandwidths, this model can be used to develop accurate range and position estimators. However, for large bandwidths, the model may be too simple and a more sophisticated model, including a multitude of SMCs, has to be used. This makes the problem more challenging, as not only the number of unknowns is increased, but also the number of SMCs needs to be inferred.

The classical methods introduced in Chapter 4, including the subspace based and the maximum likelihood methods, do not estimate the number of SMCs, but only estimate their parameters. Thus, these methods need to be augmented by another method which estimates the number of components, often on the basis of information theoretic criteria (see [53, 93] and references therein). These approaches are computationally intensive as they need to compute the parameters for each considered model order and they tend to be positively biased for non-asymptotic regions [53].

Another approach for joint estimation of the number of SMCs and their parameters are Bayesian methods [33, 66, 97, 99, 105, 106], including sparse Bayesian learning (SBL) introduced in Section 5.1. Early sparse Bayesian learning (SBL) methods utilized a fixed dictionary approach for the estimation of the dispersion parameters [79, 99], meaning that a known dictionary matrix S, based on a grid of parameter values, is used. This of course leads to leakage effects, thus, the found solution is not as sparse as possible [19]. By including the dispersion parameters into the estimation procedure, super-resolution algorithms have been developed for LSE [9, 37, 80, 82].[1]

However, the inherent sparsity promoting criteria of the Bayesian methods

---

[1]Note that categorization of these methods is difficult, as the term SBL is not defined rigorously. Classic SBL methods utilize a Gaussian-Gamma prior structure and (if at all) compute point estimates of the dispersion parameters, thus [9, 33, 37, 66], using different prior structures, are not classic SBL methods. Additionally, [9] estimates pdfs for the dispersion parameters.

still lead to a positive model bias [36,80,84]. In [80,82] it is proposed to increase the sparsity-inducing threshold depending on the probability of estimating artifacts. In [T5] we follow this idea and derive an adapted threshold to reduce the positive model bias by controlling the probability of artifacts. This approach is highlighted in Section 5.2. Furthermore, we show that the probability of false alarm for the single-SMC-in-DMC channel arrives at the same formula [N7]. In essence, the probability of artifacts / false alarms is based on a continuous search for the maximum value of a periodogram. Thus, we are interested in the excursion probability of said periodogram, or in more general terms of a χ^2-random field [1,2]. In [62] and [95] this theory is used to derive a detection threshold for a sinusoid and a complex exponential model, respectively. Both use a DML estimator and a one-dimensional dispersion parameter, meaning that it is valid for the delay estimation problem or for an azimuth angle estimation problem using a ULA. In comparison, in [T5] we extend the formulation to a SIMO setup, i.e., the joint delay and azimuth angle estimation problem and utilize more general array geometries.

In classic detection theory [43, Ch. 7], [54] the probability of false alarm is often analyzed using a bin-based approach. This approach is derived by analyzing the maximum of a discrete periodogram at the Fourier frequencies, hence it conceals the super-resolution capabilities of the employed estimation algorithms. Thus, the theoretical probability of false alarm is too small given a threshold, or vice versa, a threshold computed from a bin-based probability of false alarm is too small. To characterize the operation of the developed estimation and detection algorithm, the probability of detection is approximated by using the single-SMC model in Section 5.3. Finally, in Section 5.4 we apply the algorithm to a UWB SIMO data set to estimate the parameters of the DMC-plus-AWGN process and the parameters and the number of the SMCs.

5.1 Sparse Bayesian Learning

Sparse Bayesian learning (SBL) [33, 66, 97, 99, 105, 106] is a Bayesian method closely related to the relevance-vector machine (RVM) [98, 99]. While the RVM uses kernel basis functions, purely defined by the data set, SBL extends the concept to arbitrary basis functions, e.g. a Fourier basis [16]. SBL starts with the model given by[2]

$$\boldsymbol{r} = \boldsymbol{S}(\boldsymbol{\Theta})\boldsymbol{\alpha} + \boldsymbol{r}_{\mathrm{DMC}} + \boldsymbol{w}. \tag{5.1}$$

For SBL an estimator is designed by assuming that M SMCs can be estimated, where we have to ensure that $M \geq K$, where K is the *true* number of SMCs. Usually, M is selected to be as large as the number of observed samples, i.e., in our case $I \times L \times N$. The SBL estimator is designed to set the complex amplitudes of certain SMCs (or, as we will see shortly, their variances) to zero. This process disables these SMCs, meaning that the estimator induces sparsity. It does so,

---

[2]In classic machine learning literature [13,99], the used variables are $\boldsymbol{y} \equiv \boldsymbol{r}$, $\boldsymbol{\Phi}(\boldsymbol{x}) \equiv \boldsymbol{S}(\boldsymbol{\Theta})$, $\boldsymbol{w} \equiv \boldsymbol{\alpha}$, and $\boldsymbol{n} \equiv \boldsymbol{w}$. To keep the notation uncluttered and consistent, we keep the notation of the previous chapters.

by using the following probabilistic model

$$\begin{aligned} f(\boldsymbol{r}, \boldsymbol{\Theta}, \boldsymbol{\alpha}, \boldsymbol{\eta}, \boldsymbol{\gamma}) &\propto f(\boldsymbol{r}|\boldsymbol{\Theta}, \boldsymbol{\alpha}, \boldsymbol{\eta}, \boldsymbol{\gamma}) f(\boldsymbol{\Theta}, \boldsymbol{\alpha}, \boldsymbol{\eta}, \boldsymbol{\gamma}) \\ &\propto f(\boldsymbol{r}|\boldsymbol{\Theta}, \boldsymbol{\alpha}, \boldsymbol{\eta}) f(\boldsymbol{\Theta}) f(\boldsymbol{\alpha}|\boldsymbol{\gamma}) f(\boldsymbol{\gamma}) f(\boldsymbol{\eta}), \end{aligned} \tag{5.2}$$

where $\boldsymbol{\gamma}$ are so-called hyperparameters[3]. These hyperparameters regulate the width of the conditional distribution $f(\boldsymbol{\alpha}|\boldsymbol{\gamma})$ and are assigned a certain prior distribution $f(\boldsymbol{\gamma})$. In our work, we use a Gaussian prior model, i.e.,

$$f(\boldsymbol{\alpha}, \boldsymbol{\gamma}) = f(\boldsymbol{\alpha}|\boldsymbol{\gamma}) f(\boldsymbol{\gamma}), \tag{5.3}$$

where $f(\boldsymbol{\alpha}|\boldsymbol{\gamma}) = \prod_{m=1}^{M} \mathcal{CN}(\alpha_m|0, \gamma_m^{-1})$, with $\mathcal{CN}(x|\mu_x, \sigma_x^2)$ as complex normal distribution with mean μ_x and variance σ_x^2. Furthermore, we select a flat prior for the hyperparameters, i.e., $f(\boldsymbol{\gamma}) \propto 1$. Hence, the larger hyperparameter γ_m is, the smaller the variance for the complex amplitude α_m, meaning that said amplitude is close to zero with a high probability. In fact, the above setting is the same prior structure as for the RVM [99]. This prior setting is of course not the only one possible. In [66], settings on the basis of Gaussian scale mixtures are introduced, leading to Bessel-K models for the conditional distribution of the complex amplitudes. This Bessel-K model includes the most prominent settings used for SBL, including the ℓ_1-norm penalty [96] and the RVM setting [99]. Another possibility for the prior structure is a Bernoulli-Gaussian prior model[4] [9,18,38,45], which uses Bernoulli random variables to disable the SMCs.

Having specified the probabilistic model, the estimator needs to infer the dispersion parameters $\boldsymbol{\Theta}$, the complex amplitudes $\boldsymbol{\alpha}$, the hyperparameters $\boldsymbol{\gamma}$, and the parameters of the DMC and AWGN process $\boldsymbol{\eta}$. This can be achieved via Type-I or Type-II maximiziation [12,33,104]. Type-I maximization proceeds from (5.2) by marginalizing the hyperparameters and maximizing with respect to the complex amplitudes. In contrast, Type-II maximization marginalizes the complex amplitudes and maximizes with respect to the hyperparameters. Empirical results show that Type-II performs consistently better than Type-I [33], thus, we proceed by marginalizing the complex amplitudes leading to the marginalized likelihood function

$$\begin{aligned} f(\boldsymbol{r}|\boldsymbol{\Theta}, \boldsymbol{\eta}, \boldsymbol{\gamma}) &= \int f(\boldsymbol{r}|\boldsymbol{\Theta}, \boldsymbol{\alpha}, \boldsymbol{\eta}) f(\boldsymbol{\alpha}|\boldsymbol{\gamma}) d\boldsymbol{\alpha} \\ &\propto \det(\boldsymbol{C}(\boldsymbol{\Theta}, \boldsymbol{\eta}, \boldsymbol{\gamma}))^{-1} \mathrm{e}^{-\boldsymbol{r}^{\mathrm{H}} \boldsymbol{C}(\boldsymbol{\Theta}, \boldsymbol{\eta}, \boldsymbol{\gamma})^{-1} \boldsymbol{r}}, \end{aligned} \tag{5.4}$$

where $\boldsymbol{C}(\boldsymbol{\Theta}, \boldsymbol{\eta}, \boldsymbol{\gamma}) = C(\boldsymbol{\eta}) + \boldsymbol{S}(\boldsymbol{\Theta}) \boldsymbol{\Gamma}^{-1} \boldsymbol{S}(\boldsymbol{\Theta})^{\mathrm{H}}$ with $\boldsymbol{\Gamma} = \mathrm{diag}(\boldsymbol{\gamma})$ as diagonal matrix [13].

The marginalized likelihood in (5.4) is now the same/closely related to the probabilistic model used for SML[5] [14]. Note that in [14] the same model is used, while [15,40,63,92,101] use an arbitrary source covariance matrix, i.e., $\boldsymbol{\Gamma}$ is not just diagonal. The main difference of SML and the SBL-based estimation is the following: In SML the number of SMCs is known, while for SBL the

---

[3]The likelihood in (5.2) does not depend directly on it.

[4]Using our above definition for SBL, this prior structure should rather be called Bayesian learning.

[5]For a short discussion on the traits of SML please refer to Chapter 4 and the references therein.
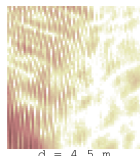
number of SMCs is fixed to some value M and the components are disabled via the complex amplitude/hyperparameter.

In [T5] we apply variational inference (see also Section 4.1) to derive update expressions for the dispersion parameters, the parameters of the DMC-plus-AWGN processes and the hyperparameters. Here, we want to highlight only the iterative update of the hyperparameters $\boldsymbol{\gamma}$ (please refer to [T5] for details on the update of the other parameters). We follow [16, 27, 79, 97], leading to a sequential update of the individual entries in γ_m. In short, all parameters are fixed to their current estimate, while only γ_m is updated. Doing so, yields the two stationary points [27]

$$\hat{\gamma}_m = \begin{cases} (|\rho(\boldsymbol{\theta}_m)|^2 - \zeta(\boldsymbol{\theta}_m))^{-1} & , \frac{|\rho(\boldsymbol{\theta}_m)|^2}{\zeta(\boldsymbol{\theta}_m)} > 1 \\ \infty & , \frac{|\rho(\boldsymbol{\theta}_m)|^2}{\zeta(\boldsymbol{\theta}_m)} \leq 1 \end{cases} , \tag{5.5}$$

where $\rho(\boldsymbol{\theta}_m)$ and $\zeta(\boldsymbol{\theta}_m)$ are, respectively, the posterior estimates of the mean and variance for the mth SMC's complex amplitude. Clearly, if the hyperparameter, being the precision of the complex amplitude, is set to ∞, the corresponding complex amplitude is 0. This leads effectively to a pruning of the mth SMC, thus leading to a sparse solution.

5.2 Probability of Artifacts / Probability of False Alarm

However, numerical experiments show that the SBL algorithm with the condition $\frac{|\rho(\boldsymbol{\theta}_m)|^2}{\zeta(\boldsymbol{\theta}_m)} > 1$ still produces artifacts [36, 80, 84]. These artifacts are components with finite hyperparameter that cannot be attributed to any true SMC. In [T5] we follow [81, 82] and increase the built-in condition, i.e., $\frac{|\rho(\boldsymbol{\theta}_m)|^2}{\zeta(\boldsymbol{\theta}_m)} > \kappa$, with κ as a modified threshold.

The probability of artifacts is defined as [81], [T5]

$$P_{\mathrm{A}}(\kappa) = \mathbb{P}\left[\exists m \in \{1, \ldots, M\} : \hat{\boldsymbol{\theta}}_m \in \Theta \setminus \Theta^{(r)} \wedge \hat{\gamma}_m < \infty\right] \tag{5.6}$$

$$\approx \mathbb{P}\left[\sup_{\boldsymbol{\theta} \in \Theta} \frac{|\boldsymbol{s}(\theta)^{\mathrm{H}} \boldsymbol{C}^{-1}(\boldsymbol{r}_{\mathrm{DMC}} + \boldsymbol{w})|^2}{\boldsymbol{s}(\theta)^{\mathrm{H}} \boldsymbol{C}^{-1} \boldsymbol{s}(\theta)} > \kappa\right]. \tag{5.7}$$

In (5.6) an artifact is defined to have a finite hyperparameter and its estimated dispersion parameters are outside a neighborhood around the true value, i.e., $\Theta^{(r)} \triangleq \cup_k B_r(\boldsymbol{\theta}_k)$, where $B_r(\boldsymbol{\theta})$ is the open ball of radius centered at $\boldsymbol{\theta} \in \Theta$, with Θ being the support of the dispersion parameters [T5], e.g., $\Theta = [0, T) \times [0, 2\pi)$ for a horizontal-only propagation SIMO configuration [T5]. To arrive at (5.7) we need to conjecture the asymptotic efficiency of SML estimators for single-snapshot measurement[6] and that the implemented iterative algorithm inherits this property [T5].

Here, we want to highlight a different way to arrive at a comparable formula as (5.7), on the basis of detection theory [43] [N7]. As in the previous chapters, we employ the single-SMC-in-DMC-plus-AWGN model and assume that the

---

[6]This has been proven for a DML estimator [70] but not for SML estimators.

5.2. PROBABILITY OF ARTIFACTS / FALSE ALARM

covariance matrix is known. Thus, the likelihood function is given as

$$f(\boldsymbol{r}|\boldsymbol{\theta}, \alpha) = \frac{1}{\pi^{NIL} \det(\boldsymbol{C})} \mathrm{e}^{(\boldsymbol{r} - \boldsymbol{s}(\boldsymbol{\theta})\alpha)^{\mathrm{H}} \boldsymbol{C}^{-1}(\boldsymbol{r} - \boldsymbol{s}(\boldsymbol{\theta})\alpha)}, \tag{5.8}$$

where the unknown parameters are the dispersion parameters $\boldsymbol{\theta}$ and the complex amplitude α.

The detection problem can then be formulated as the question: Does the current observation include an SMC (hypothesis $\mathcal{H}_1$) or not (hypothesis $\mathcal{H}_0$)? The generalized likelihood ratio test [43] is given as

$$L_{\mathrm{G}}(\boldsymbol{r}) = \sup_{\boldsymbol{\theta}, \alpha}(f(\boldsymbol{r}|\boldsymbol{\theta}, \alpha)). \tag{5.9}$$

By concentrating the likelihood with respect to α and taking the logarithm on both sides, we arrive at the test statistic

$$T(\hat{\boldsymbol{\theta}}) = \sup_{\boldsymbol{\theta}} \frac{|\boldsymbol{s}(\theta)^{\mathrm{H}} \boldsymbol{C}^{-1} \boldsymbol{r}|^2}{\boldsymbol{s}(\theta)^{\mathrm{H}} \boldsymbol{C}^{-1} \boldsymbol{s}(\theta)} \underset{\mathcal{H}_0}{\overset{\mathcal{H}_1}{\gtrless}} \kappa. \tag{5.10}$$

The probability of false alarm is then given as

$$P_{\mathrm{FA}}(\kappa) = \mathbb{P}\left[T(\hat{\boldsymbol{\theta}}) > \kappa; \mathcal{H}_0\right] \tag{5.11}$$

$$= \mathbb{P}\left[\sup_{\boldsymbol{\theta}} \frac{|\boldsymbol{s}(\boldsymbol{\theta})^{\mathrm{H}} \boldsymbol{C}^{-1}(\boldsymbol{r}_{\mathrm{DMC}} + \boldsymbol{w})|^2}{\boldsymbol{s}(\boldsymbol{\theta})^{\mathrm{H}} \boldsymbol{C}^{-1} \boldsymbol{s}(\boldsymbol{\theta})} > \kappa\right]. \tag{5.12}$$

Clearly, the right hand sides of (5.7) and (5.12) coincide. However, we want to emphasize that the two descriptions are different: While for the probability of artifacts an SBL-based approach is used, enabling the estimation of multiple SMCs, the probability of false alarm is derived for the detection of a single SMC on the basis of a DML estimator.

To find a numerical value for the probability of false alarm, we have to analyze the excursion probability that the maximum of the χ^2-random process[7]

$$u(\boldsymbol{\theta}) = \frac{|\boldsymbol{s}(\boldsymbol{\theta})^{\mathrm{H}} \boldsymbol{C}^{-1}(\boldsymbol{r}_{\mathrm{DMC}} + \boldsymbol{w})|^2}{\boldsymbol{s}(\boldsymbol{\theta})^{\mathrm{H}} \boldsymbol{C}^{-1} \boldsymbol{s}(\boldsymbol{\theta})} \tag{5.13}$$

exceeds the threshold κ [1, 2, 108]. For large κ it is possible to approximate the excursion probability with the expected Euler characteristic [2], i.e.,

$$\mathbb{P}\left[\sup_{\boldsymbol{\theta} \in \Theta} u(\boldsymbol{\theta}) > \kappa\right] \simeq \mathbb{E}\left[\varphi(A_\kappa(u, \Theta))\right], \tag{5.14}$$

where $\simeq$ means that the ratio of the two sides tends to 1 asymptotically in κ [2]. Furthermore in (5.14) the Euler characteristic $\varphi(A)$ of excursion set $A_\kappa(u, \Theta) = \{\boldsymbol{\theta} \in \Theta : u(\boldsymbol{\theta}) > \kappa\}$ is defined. The Euler characteristic is

$$\varphi(A) = \begin{cases} 0, & \text{if } A = \emptyset \\ 1, & \text{if } A \neq \emptyset \end{cases}. \tag{5.15}$$

---

[7]Actually, $u(\boldsymbol{\theta})$ is a χ^2-random process with component variance of $\frac{1}{2}$. To arrive at a standard χ^2-random process $u(\boldsymbol{\theta})$ is multiplied by 2 [T5].
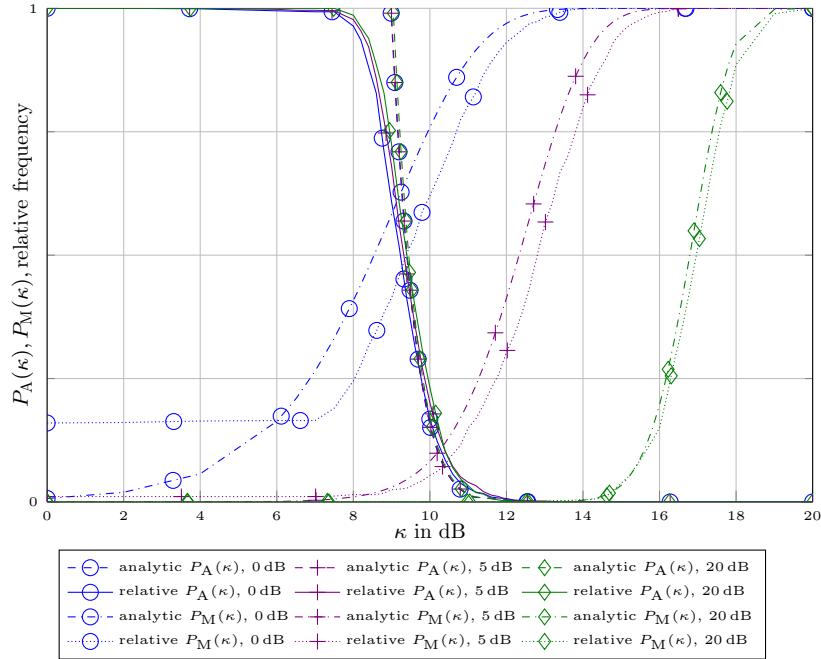
Figure 5.1: Operating characteristics of the algorithm for the estimation of a single SMC for three different values of SNR $= [5, 10, 20]$ dB with estimated noise covariance matrix. The SDR $= -5$ dB, leading to an $\mathrm{SINR}(\tau) = [-1.8, 2.2, 6.7]$ dB. The analytic probability of artifact $P_\mathrm{A}(\kappa)$ (-⊖-,-+-,-◇-) and the analytic probability of missed detection $P_\mathrm{M}(\kappa)$ (-⊖-,-+-,-◇-) are compared to the relative frequency of artifacts (—⊖—,—+—,—◇—) and the relative frequency of missed detection (⋯⊖⋯,⋯+⋯,⋯◇⋯) for 1000 realizations, respectively.

In [T5] we apply the above theory to derive the probability of artifact for horizontal-only propagation for a SIMO setup. This means that the dispersion parameter $\boldsymbol{\theta}$ includes the delay and the azimuth AoA. In [N7] we extend the framework to the full MIMO setup, using a 5-dimensional dispersion parameter. The derivation shows that the arrays need to be centro-symmetric with respect to the center of gravity of the array, i.e., $\boldsymbol{p}^{(l)} = -\boldsymbol{p}^{(l')}$ for the RX array. Arrays which fulfill this requirement are, e.g., rectangular, quadratic or cubic arrays. Note that (5.12) can be used to compute a threshold κ given a certain false alarm probability. This leads to a constant false-alarm rate detector [43].

5.3   Probability of missed detection

To obtain a full description of the operating characteristics[8], we need to specify the probability of missed detection, defined as the complementary probability

---

[8]We do not want to use the term *receiver operating characteristic*, as we use the probability of missed detection and not the probability of detection.

of the probability of detection [81] [T5]. For the single-SMC case, it is given as

$$P_{\mathrm{M}}(\kappa) = 1 - \mathbb{P}\left[T(\hat{\boldsymbol{\theta}}) > \kappa \wedge \hat{\boldsymbol{\theta}} \in \Theta^{(r)}; \mathcal{H}_1\right] \tag{5.16}$$

$$= \mathbb{P}\left[T(\hat{\boldsymbol{\theta}}) < \kappa \vee \hat{\boldsymbol{\theta}} \notin \Theta^{(r)}; \mathcal{H}_1\right] \tag{5.17}$$

$$\approx \mathbb{P}\left[u(\tilde{\boldsymbol{\theta}}) < \kappa; \mathcal{H}_1\right]. \tag{5.18}$$

According to (5.17) a missed detection occurs either if the test statistic does not exceed the threshold, i.e., no SMC is detected, or if the estimated parameter value is not in the neighborhood of the true parameter value. For the approximation in (5.18) we assume that the estimated parameter value $\hat{\boldsymbol{\theta}}$ converges towards the true parameter value $\tilde{\boldsymbol{\theta}}$. This can be argued for large bandwidths and apertures with the consistency of the DML estimator [11, 70].

Clearly, $2u(\tilde{\boldsymbol{\theta}})$ is distributed according to a non-central χ^2 distribution with non-centrality parameter $\lambda = 2|\tilde{\alpha}|^2 \boldsymbol{s}(\tilde{\boldsymbol{\theta}}) \boldsymbol{C}^{-1} \boldsymbol{s}(\tilde{\boldsymbol{\theta}})$. Thus, the missed detection can be approximated by

$$P_{\mathrm{M}}(\kappa) \approx \int_0^{\kappa} \mathrm{e}^{-x-\lambda/2} I_0(\sqrt{2\lambda x}) dx, \tag{5.19}$$

where $I_0(\cdot)$ is the modified Bessel function of the first kind. It is interesting to take a closer look at the non-centrality parameter λ. By neglecting the spatial correlations, the covariance matrix $\boldsymbol{C}$ reduces to a block diagonal structure, and the non-centrality parameter $\lambda = 2IL\mathrm{SINR}(\tau)$, where $\mathrm{SINR}(\tau)$ is defined in Sec. 3.1.1. This means that the probability of missed detection (and hence the probability of detection) are directly related to the $\mathrm{SINR}(\tau)$.

Fig. 5.1[9] compares the analytic probability of artifacts and missed detection to the relative frequency of artifacts and missed detection from a Monte-Carlo experiment using synthetic data, respectively. While the relative frequency of artifacts matches its analytic counterpart well, the relative frequency of missed detection shows a floor for small thresholds κ and small SNR. This floor is explained by the fact that the developed algorithm [T5] is set up (for this experiment) to estimate a maximum of 10 SMCs. Thus, for small SNR and small theshold, the algorithm is not capable with this setup to detect and estimate the SMC. Furthermore, the algorithm is too confident with respect to detection of the SMC. While the theoretical probability of missed detection is computed on the basis of the distribution of the test statistic at the true parameter value, the relative frequency of missed detection has to consider a certain neighborhood around the true parameter value to classify a detection. For this experiment, if any estimated component falls within 5 times the square root of the CRLB it is counted as a detection. Thus, as the algorithm employs an $\arg\max$ (searching for the continuous parameter), it is over confident.

5.4 Application Example 3: Channel parameter estimation using UWB measurements

In [T5] we apply the developed algorithm to the data measured in the room presented in Fig. 2.1, which was also used to generate the flipbooks. The trans-

---

[9]Please note that the algorithm developed in [T5] is used. For the channel and signal definitions, please refer to [T5].
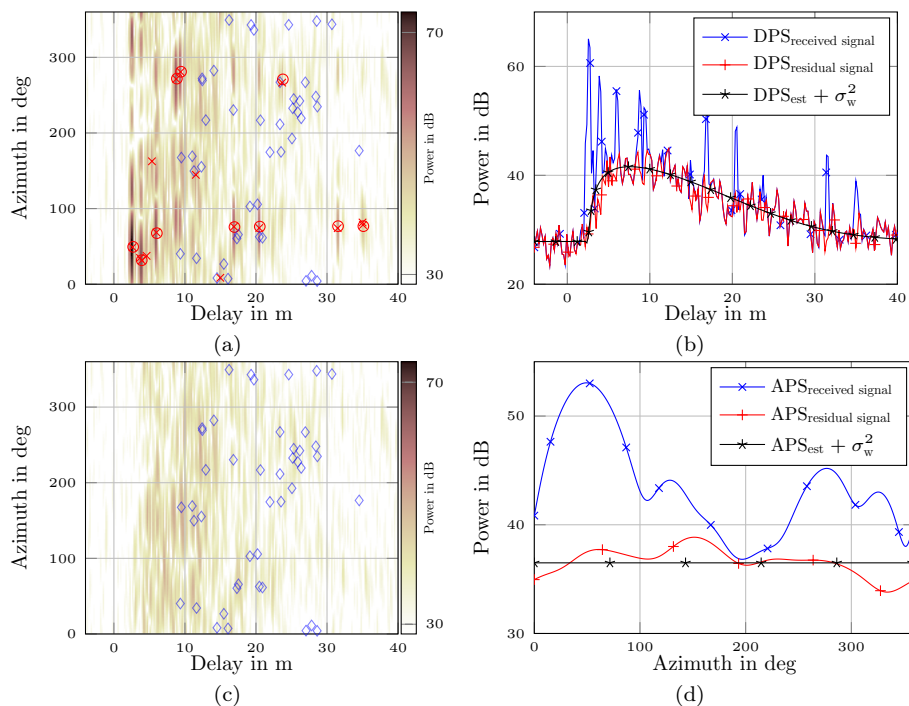
Figure 5.2: Estimation using a UWB signaling scheme: (a): Estimated ADPS of the received signal including the estimated SMCs ($\times$), associated predicted SMCs ($\circ$) and non-associated predicted SMCs ($\diamond$). (b): Estimated DPS of the received signal ($-\!\times\!-$), the residual signal ($-\!+\!-$), and the estimated parametrized DPS plus AWGN ($-\!\star\!-$). (c): Estimated ADPS of the residual signal and non-associated predicted SMCs ($\diamond$) (d): Estimated DOAPS for the same signals as in (b).

mitter is positioned at $\boldsymbol{p}_{\mathrm{TX}}$ and a 3×3 virtual receiver array with $2\,\mathrm{cm}$ spacing is used at $\boldsymbol{p}_{\mathrm{RX}}$. The employed antennas have a beampattern focusing most of their energy in the horizontal plane[10] and showing approximately isotropic radiation patterns [46]. A root-raised-cosine pulse with pulse duration of $1\,\mathrm{ns}$ and roll-off factor of 0.6 is used to filter the measured data to an effective bandwidth of $1\,\mathrm{GHz}$. For the algorithm, the probability of artifacts is set to $1\,\%$ and the threshold κ is computed online.

The results are depicted in Fig. 5.2. Fig. 5.2a illustrates the ADPS of the received signal including the estimated SMCs ($\times$). Using a simple optical ray-tracer we predict SMCs on the basis of the geometry of the setup up to fifth order reflections. These SMCs are depicted by $\circ$ and $\diamond$. To associate estimated SMCs to predicted SMCs we use a frequentist approach: we compute the CRLB of the estimated delay and AoA and associate a predicted SMC if both its delay and AoA fall within 5 times the square root of the CRLB. Clearly, most of the estimated SMCs are associated to predicted SMCs ($\circ$) and can thus be explained by the geometry of the setup. The non-associated SMCs ($\diamond$) are shown in both,

---

[10]This is the main reason to consider horizontal only propagation and restrict the DoA to the azimuth AoA and neglect the elevation AoA.

Fig. 5.2a and Fig. 5.2c, where the latter illustrates the ADPS of the residual signal, obtained by subtracting the estimated SMCs. In theory, this residual signal contains only the DMC and the AWGN. The strong peaks have vanished and we conclude that the non-associated SMCs are either not detectable or not present in the signal. Note again that the predicted SMCs are purely due to geometric considerations and do not include any effects as blocking by furniture or reflection coefficients. Fig. 5.2b depicts the DPS of the received signal (—×—), the residual signal (——) and the estimated parametrized DMC-plus-AWGN model (—*—). Clearly, the estimated parametrized DPS and the DPS of the residual signal match well. Finally, Fig. 5.2d shows the DOAPS for the same signals as Fig. 5.2b. The residual DOAPS is already quite flat over the azimuth range.

5.5   Concluding Remarks

This chapter discusses the problem of jointly inferring the parameters and the number of SMCs. This joint estimation and detection problem can be tackled by using sparsity enforcing priors for the complex amplitudes leading to inherent sparsification of the SMCs [9, 27, 38, 82, 99, 106]. However, using the inherent sparsity promoting threshold still leads to a high number of estimation artifacts [80]. Thus, in [T5] we derive the probability of estimating artifacts for a SIMO setup, by analyzing the excursion probability of a χ^2-random field [2]. In turn, the probability of artifacts can be used to adapt the threshold, which almost eliminates the positive model-order bias. In the supplementary material to [T5] it is shown how the threshold can be applied to state-of-the-art DML estimators [71], leading to comparable performances.

Of course, the probability of estimating artifacts describes only one half of the detection problem. Therefore, the probability of missed detection is derived for the single-SMC-in-DMC channel. It shows that this probability is directly linked to the SINR of the SMC-in-DMC.

Finally, the developed algorithm is applied to UWB data. The parameters of the estimated SMCs are compared to geometry-related predicted SMCs and most of the estimated SMCs can be associated to related predicted SMCs. This property of the algorithm enables accurate positioning but also tracking of position-related parameters [N8, N9] which could be used for environment and channel modeling [68, 107].

d = 20.1 m

d = 40.2 m

Chapter 6

Conclusion

The indoor radio channel can be characterized by a multitude of multipath components (MPCs). These MPCs are split into the specular multipath components (SMCs), electromagnetic waves that are resolvable with the measurement aperture, and the dense multipath component (DMC), electromagnetic waves that overlap and/or have low power and can not be resolved at the receiver (RX). This radio channel led to three research questions, restated here for convenience, and answered in the following:

RQ 1: *How accurate can position-related parameters be estimated in dense multipath environments and how do system parameters influence these estimation problems?*

In [T1, T2], [N3–N5] the ranging error bound (REB) and angulation error bound (AEB), i.e., the Cramér Rao lower bound (CRLB) for the delay and angle estimation problem, respectively, have been derived and analyzed. It shows that the accuracy of position-related parameters strongly depends on the bandwidth. For additive white Gaussian noise (AWGN) only channels, i.e., neglecting the DMC, the accuracy of the delay estimation profits from higher bandwidths, it scales reciprocal with bandwidth. The angular estimation accuracy is not influenced by the bandwidth in AWGN-only channels. However, for channels including the DMC, the bandwidth plays a vital role in estimation accuracy for both, the delay and the angular estimation problem [T1, T2] [N3–N5]. Additionally, the number of antennas benefits the accuracy of both estimation problems [T2] [N3, N4]. However, the accuracy can only be achieved, if the parameters of the DMC process are available to the estimator. Hence,

RQ 2: *Is it possible to increase the robustness and accuracy of the estimation of position-related parameters by concurrently estimating the parameters of the DMC process using multiple-input multiple-output (MIMO) systems?*

In [T3, T4] deterministic maximum likelihood (DML) estimators are developed for ranging and direct positioning utilizing single-snapshot multi-antenna measurements. Analysis of the developed algorithms highlight that the answer to RQ 2 depends strongly on the employed algorithm and the system parameters. If a large enough number of measurements is available due to multi-antenna systems, snapshot-based estimation of the parameters of the DMC process seems possible [T3–T5] [71]. For wideband systems, the single-SMC-in-DMC channel is an appropriate model to infer position-related parameters and the position itself. It is important to note that by decreasing the bandwidth, the equalization

with the inverse covariance matrix of the DMC and AWGN model leads to outliers. This threshold region is similar to the classic SNR threshold region, due to the fact that for decreasing bandwidth the component SNR, i.e., the SINR of the SMC in DMC decreases as well. The developed algorithms navigate around this problem as the scheduling leads to a matched filter (MF) approximation for narrow bandwidths. For ultra-wideband (UWB) systems, the single-SMC model does not suffice and we have to increase the model complexity by adding additional SMCs to approach the theoretical performance limits. Consequently, we have to estimate the number of SMCs, leading to the third research question:

RQ 3: *Is it possible to reliably infer the number of SMCs and their parameters in unknown DMC environments?*

In [T5] a detection threshold is derived within a sparse Bayesian learning algorithm to detect the number of resolvable SMCs, leading to a *yes, if* answer to RQ 3: Yes, it is possible to reliably detect SMCs if the SINRs are above a threshold and the SMCs are spaced sufficiently with respect to the measurement aperture. In [T5] we show empirically that for sufficiently spaced SMCs, i.e., above the Nyquist respectively the Rayleigh resolution, the detection probability for the single-SMC channel is a good approximation for the multi-SMC-in-DMC channel. Furthermore, for very narrow spacings, i.e., well below the Nyquist and Rayleigh resolution, the developed algorithm only estimates a single SMC. Hence, the algorithm is conservative with respect to the number of SMCs which is a desired behavior for positioning purposes. In [T5], the algorithm is employed by fixing the probability of artifacts and adapting the sparsity threshold.

Outlook on possible future research topics: The DML estimators developed for the radio frequency identification (RFID) setup assume that the SMC, i.e., the line-of-sight (LOS), is present in the signal. Due to the favorable conditions in the measurement setup, this assumptions is factual. In real-world scenarios, e.g., a fashion store or a warehouse, non-line-of-sight measurements will be encountered frequently. It would be important to study such non-line-of-sight scenarios and apply the theory of detection to add a degree of reliability and robustness to the estimated parameters.

Furthermore, the algorithms in this thesis are all developed based on single-snapshot measurements. Of course, the radio channel between a transmitter (TX) and RX does not change fundamentally, as long as the measurement update rate is high enough with respect to changes in the environment. Algorithms, tracking the estimates over multiple snapshots could not only speed up the initialization procedures of the algorithms, but also make the algorithms more robust with respect to noisy measurements [74, 83].

Another avenue for improvement is the fact that the estimates of the dispersion parameters are point estimates. By searching for closed-form solutions [9] or using sampling-based approaches [4], a probability distribution of the dispersion parameters can be estimated. Handing these distributions to the subsequent positioning algorithms, a (more) Bayesian treatment of the positioning problem is achieved, increasing the robustness and reliability of the solution [21].

Finally, I want to conclude with respect to the hypothesis of this thesis:
Position-related parameters in DMC environments can be estimated accurately and robustly by combining MIMO radio transmissions and reliable estimation techniques.

60

Appendices

d = 19.5 m

d = 39.0 m

Appendix A

Derivation of the CRLB for the backscatter channel

A.1 Covariance Matrix including spatial correlations

The sampled received signal at antenna l' at RX reader m', due to a transmission at antenna l at TX reader m, assuming the wideband aperture function (2.7), is given as (see also (2.11))

$$r_{m,m'}^{(l,l')} = \alpha_m \alpha_{m'} s_{\mathrm{TX}}(\tau_{m,m'}) e^{j2\pi \frac{f_c}{c} \boldsymbol{\Omega}_{\mathrm{TX},m}^{\mathrm{T}} \Delta \boldsymbol{p}_m^{(l)}} e^{j2\pi \frac{f_c}{c} \boldsymbol{\Omega}_{\mathrm{RX},m'}^{\mathrm{T}} \Delta \boldsymbol{p}_{m'}^{(l')}} \tag{A.1}$$

$$+ \alpha_m e^{j2\pi \frac{f_c}{c} \boldsymbol{\Omega}_{\mathrm{TX},m}^{\mathrm{T}} \Delta \boldsymbol{p}_m^{(l)}} \int \int h_{\mathrm{DMC}}(\tau - \tau_m, \boldsymbol{\Omega}_{\mathrm{RX}}; \boldsymbol{p}_{m'}, \boldsymbol{p}) s_{\mathrm{TX}}(\tau)$$

$$\times e^{j2\pi \frac{f_c}{c} \boldsymbol{\Omega}_{\mathrm{RX}}^{\mathrm{T}} \Delta \boldsymbol{p}_{m'}^{(l')}} d\tau ds_1(\boldsymbol{\Omega}_{\mathrm{RX}}) \tag{A.2}$$

$$+ \alpha_{m'} e^{j2\pi \frac{f_c}{c} \boldsymbol{\Omega}_{\mathrm{RX},m'}^{\mathrm{T}} \Delta \boldsymbol{p}_{m'}^{(l')}} \int \int h_{\mathrm{DMC}}(\tau - \tau_{m'}, \boldsymbol{\Omega}_{\mathrm{TX}}; \boldsymbol{p}_m, \boldsymbol{p}) s_{\mathrm{TX}}(\tau)$$

$$\times e^{j2\pi \frac{f_c}{c} \boldsymbol{\Omega}_{\mathrm{TX}}^{\mathrm{T}} \Delta \boldsymbol{p}_m^{(l)}} d\tau ds_1(\boldsymbol{\Omega}_{\mathrm{TX}}) \tag{A.3}$$

$$+ \int \int \int \int h_{\mathrm{DMC}}(\lambda, \boldsymbol{\Omega}_{\mathrm{TX}}; \boldsymbol{p}_m, \boldsymbol{p}) h_{\mathrm{DMC}}(\tau - \lambda, \boldsymbol{\Omega}_{\mathrm{RX}}; \boldsymbol{p}_{m'}, \boldsymbol{p})$$

$$\times s_{\mathrm{TX}}(\tau) e^{j2\pi \frac{f_c}{c} \boldsymbol{\Omega}_{\mathrm{TX}}^{\mathrm{T}} \Delta \boldsymbol{p}_m^{(l)}} e^{j2\pi \frac{f_c}{c} \boldsymbol{\Omega}_{\mathrm{RX}}^{\mathrm{T}} \Delta \boldsymbol{p}_{m'}^{(l')}} d\lambda d\tau ds_1(\boldsymbol{\Omega}_{\mathrm{TX}}) ds_1(\boldsymbol{\Omega}_{\mathrm{RX}}) \tag{A.4}$$

$$+ \boldsymbol{w}_{m,m'}^{(l,l')} \tag{A.5}$$

The term given by (A.1) describes the part based solely on the LOSs of the two constituent channels, the terms (A.2), (A.3), (A.4) can be combined to describe the DMC part of the backscatter channel, i.e., $r_{\mathrm{DMC},m,m'}^{(l,l')}$ and (A.5) describes the AWGN measurement noise. Stacking the received signals for reader pair (m, m') results in the received signal

$$\boldsymbol{r}_{m,m'} = \left[\boldsymbol{r}_{m,m'}^{(1,1)\,\mathrm{T}}, \ldots, \boldsymbol{r}_{m,m'}^{(1,L_{m'})\,\mathrm{T}}, \ldots, \boldsymbol{r}_{m,m'}^{(L_m,1)\,\mathrm{T}}, \ldots, \boldsymbol{r}_{m,m'}^{(L_m,L_{m'})\,\mathrm{T}} \right]^{\mathrm{T}} \in \mathbb{C}^{NL_m L_{m'} \times 1}. \tag{A.6}$$

The covariance matrix of the received signal from TX reader m to RX reader m' is given by[1]

$$\boldsymbol{C}_{m,m'} = \boldsymbol{C}_{\text{DMC},m,m'} + \boldsymbol{C}_{\text{AWGN},m,m'} \ \in \mathbb{C}^{NL_mL_{m'} \times NL_mL_{m'}}, \tag{A.7}$$

assuming the AWGN and DMC process are uncorrelated. The covariance matrix of the stacked AWGN vector $\boldsymbol{w}$ is given as $\boldsymbol{C}_{\text{AWGN},m,m'} = \sigma_w^2 \boldsymbol{I}$ and the covariance matrix with respect to the three terms describing the backscatter DMC process is $\boldsymbol{C}_{\text{DMC},m,m'}$. The $N \times N$ subblock, describing the covariance of the DMC part of the backscatter channel indexed by antenna pair (l, l') and antenna pair (l'', l''') is given as

$$[\boldsymbol{C}_{\text{DMC},m,m'}]_{l,l',l'',l'''} = \mathbb{E}\left[\boldsymbol{r}_{\text{DMC},m,m'}^{(l,l')} \boldsymbol{r}_{\text{DMC},m,m'}^{(l'',l''')\,\text{H}} \right]. \tag{A.8}$$

Inserting the three terms (A.2), (A.3), and (A.4) in (A.8) leads to nine terms:

$$[\boldsymbol{C}_{\text{DMC},m,m'}]_{l,l',l'',l'''} =$$

$$|\alpha_m|^2 e^{j2\pi \frac{f_c}{c} \boldsymbol{\Omega}_{\text{TX},m}^{\text{T}} \Delta \boldsymbol{p}_m^{(l)}} e^{-j2\pi \frac{f_c}{c} \boldsymbol{\Omega}_{\text{TX},m}^{\text{T}} \Delta \boldsymbol{p}_m^{(l'')}} \int\int\int\int \boldsymbol{s}_{\text{TX}}(\tau) \boldsymbol{s}_{\text{TX}}^{\text{H}}(\tau')$$

$$\times \mathbb{E}\left[h_{\text{DMC}}(\tau - \tau_m, \boldsymbol{\Omega}_{\text{RX}}; \boldsymbol{p}_{m'}, \boldsymbol{p}) h_{\text{DMC}}^*(\tau' - \tau_m, \boldsymbol{\Omega}_{\text{RX}}'; \boldsymbol{p}_{m'}, \boldsymbol{p}) \right]$$

$$\times e^{j2\pi \frac{f_c}{c} \boldsymbol{\Omega}_{\text{RX}}^{\text{T}} \Delta \boldsymbol{p}_{m'}^{(l')}} e^{-j2\pi \frac{f_c}{c} \boldsymbol{\Omega}_{\text{RX}}'^{\text{T}} \Delta \boldsymbol{p}_{m'}^{(l''')}} d\tau d\tau' ds_1(\boldsymbol{\Omega}_{\text{RX}}) ds_1(\boldsymbol{\Omega}_{\text{RX}}') \tag{A.9}$$

$$+ \alpha_m \alpha_{m'}^* e^{j2\pi \frac{f_c}{c} \boldsymbol{\Omega}_{\text{TX},m}^{\text{T}} \Delta \boldsymbol{p}_m^{(l)}} e^{-j2\pi \frac{f_c}{c} \boldsymbol{\Omega}_{\text{RX},m'}^{\text{T}} \Delta \boldsymbol{p}_{m'}^{(l''')}} \int\int\int\int \boldsymbol{s}_{\text{TX}}(\tau) \boldsymbol{s}_{\text{TX}}^{\text{H}}(\tau')$$

$$\times \mathbb{E}\left[h_{\text{DMC}}(\tau - \tau_m, \boldsymbol{\Omega}_{\text{RX}}; \boldsymbol{p}_{m'}, \boldsymbol{p}) h_{\text{DMC}}^*(\tau' - \tau_{m'}, \boldsymbol{\Omega}_{\text{TX}}; \boldsymbol{p}_m, \boldsymbol{p}) \right]$$

$$\times e^{j2\pi \frac{f_c}{c} \boldsymbol{\Omega}_{\text{RX}}^{\text{T}} \Delta \boldsymbol{p}_{m'}^{(l')}} e^{-j2\pi \frac{f_c}{c} \boldsymbol{\Omega}_{\text{TX}}^{\text{T}} \Delta \boldsymbol{p}_m^{(l'')}} d\tau d\tau' ds_1(\boldsymbol{\Omega}_{\text{RX}}) ds_1(\boldsymbol{\Omega}_{\text{TX}}) \tag{A.10}$$

$$+ \alpha_m e^{j2\pi \frac{f_c}{c} \boldsymbol{\Omega}_{\text{TX},m}^{\text{T}} \Delta \boldsymbol{p}_m^{(l)}} \int\int\int\int\int\int \boldsymbol{s}_{\text{TX}}(\tau) \boldsymbol{s}_{\text{TX}}^{\text{H}}(\tau')$$

$$\times \mathbb{E}\left[h_{\text{DMC}}(\tau - \tau_m, \boldsymbol{\Omega}_{\text{RX}}; \boldsymbol{p}_{m'}, \boldsymbol{p}) h_{\text{DMC}}^*(\lambda, \boldsymbol{\Omega}_{\text{TX}}; \boldsymbol{p}_m, \boldsymbol{p}) \right.$$

$$\left. \times h_{\text{DMC}}^*(\tau' - \lambda, \boldsymbol{\Omega}_{\text{RX}}'; \boldsymbol{p}_{m'}, \boldsymbol{p}) \right] e^{j2\pi \frac{f_c}{c} \boldsymbol{\Omega}_{\text{RX}}^{\text{T}} \Delta \boldsymbol{p}_{m'}^{(l')}} e^{-j2\pi \frac{f_c}{c} \boldsymbol{\Omega}_{\text{TX}}^{\text{T}} \Delta \boldsymbol{p}_m^{(l'')}}$$

$$\times e^{-j2\pi \frac{f_c}{c} \boldsymbol{\Omega}_{\text{RX}}'^{\text{T}} \Delta \boldsymbol{p}_{m'}^{(l''')}} d\tau d\tau' d\lambda ds_1(\boldsymbol{\Omega}_{\text{RX}}) ds_1(\boldsymbol{\Omega}_{\text{TX}}) ds_1(\boldsymbol{\Omega}_{\text{RX}}') \tag{A.11}$$

$$+ \alpha_{m'} \alpha_m^* e^{j2\pi \frac{f_c}{c} \boldsymbol{\Omega}_{\text{RX},m'}^{\text{T}} \Delta \boldsymbol{p}_{m'}^{(l')}} e^{-j2\pi \frac{f_c}{c} \boldsymbol{\Omega}_{\text{TX},m}^{\text{T}} \Delta \boldsymbol{p}_m^{(l'')}} \int\int\int\int \boldsymbol{s}_{\text{TX}}(\tau) \boldsymbol{s}_{\text{TX}}^{\text{H}}(\tau')$$

$$\times \mathbb{E}\left[h_{\text{DMC}}(\tau - \tau_{m'}, \boldsymbol{\Omega}_{\text{TX}}; \boldsymbol{p}_m, \boldsymbol{p}) h_{\text{DMC}}^*(\tau' - \tau_m, \boldsymbol{\Omega}_{\text{RX}}; \boldsymbol{p}_{m'}, \boldsymbol{p}) \right]$$

$$\times e^{j2\pi \frac{f_c}{c} \boldsymbol{\Omega}_{\text{TX}}^{\text{T}} \Delta \boldsymbol{p}_m^{(l)}} e^{-j2\pi \frac{f_c}{c} \boldsymbol{\Omega}_{\text{RX}}^{\text{T}} \Delta \boldsymbol{p}_{m'}^{(l''')}} d\tau d\tau' ds_1(\boldsymbol{\Omega}_{\text{TX}}) ds_1(\boldsymbol{\Omega}_{\text{RX}}) \tag{A.12}$$

$$+ |\alpha_{m'}|^2 e^{j2\pi \frac{f_c}{c} \boldsymbol{\Omega}_{\text{RX},m'}^{\text{T}} \Delta \boldsymbol{p}_{m'}^{(l')}} e^{-j2\pi \frac{f_c}{c} \boldsymbol{\Omega}_{\text{RX},m'}^{\text{T}} \Delta \boldsymbol{p}_{m'}^{(l''')}} \int\int\int\int \boldsymbol{s}_{\text{TX}}(\tau) \boldsymbol{s}_{\text{TX}}^{\text{H}}(\tau')$$

$$\times \mathbb{E}\left[h_{\text{DMC}}(\tau - \tau_{m'}, \boldsymbol{\Omega}_{\text{TX}}; \boldsymbol{p}_m, \boldsymbol{p}) h_{\text{DMC}}^*(\tau' - \tau_{m'}, \boldsymbol{\Omega}_{\text{TX}}'; \boldsymbol{p}_m, \boldsymbol{p}) \right]$$

$$\times e^{j2\pi \frac{f_c}{c} \boldsymbol{\Omega}_{\text{TX}}^{\text{T}} \Delta \boldsymbol{p}_m^{(l)}} e^{-j2\pi \frac{f_c}{c} \boldsymbol{\Omega}_{\text{TX}}'^{\text{T}} \Delta \boldsymbol{p}_m^{(l'')}} d\tau d\tau' ds_1(\boldsymbol{\Omega}_{\text{TX}}) ds_1(\boldsymbol{\Omega}_{\text{TX}}') \tag{A.13}$$

---

[1] Please note, that we analyze a two reader problem. For an M reader problem, the derivation of the covariance matrix is even more involved, as the cross-covariance between TX reader m and RX reader m' and TX reader m and RX reader m'' is non-zero.

$$+ \, \alpha_{m'} e^{j2\pi \frac{f_c}{c} \mathbf{\Omega}_{\mathrm{RX},m'}^{\mathrm{T}} \Delta \boldsymbol{p}_{m'}^{(l')}} \int \int \int \int \int \int \boldsymbol{s}_{\mathrm{TX}}(\tau) \boldsymbol{s}_{\mathrm{TX}}^{\mathrm{H}}(\tau')$$

$$\times \, \mathbb{E}\left[h_{\mathrm{DMC}}(\tau - \tau_{m'}, \mathbf{\Omega}_{\mathrm{TX}}; \boldsymbol{p}_m, \boldsymbol{p}) h_{\mathrm{DMC}}^*(\lambda, \mathbf{\Omega}'_{\mathrm{TX}}; \boldsymbol{p}_m, \boldsymbol{p}) \right.$$

$$\times h_{\mathrm{DMC}}^*(\tau' - \lambda, \mathbf{\Omega}_{\mathrm{RX}}; \boldsymbol{p}_{m'}, \boldsymbol{p}) \Big] e^{j2\pi \frac{f_c}{c} \mathbf{\Omega}_{\mathrm{TX}}^{\mathrm{T}} \Delta \boldsymbol{p}_m^{(l)}} e^{-j2\pi \frac{f_c}{c} \mathbf{\Omega}_{\mathrm{RX}}^{\mathrm{T}} \Delta \boldsymbol{p}_{m'}^{(l''')}}$$

$$\times \, e^{-j2\pi \frac{f_c}{c} \mathbf{\Omega}_{\mathrm{TX}}'^{\mathrm{T}} \Delta \boldsymbol{p}_m^{(l'')}} \, d\tau d\tau' d\lambda ds_1(\mathbf{\Omega}_{\mathrm{TX}}) ds_1(\mathbf{\Omega}_{\mathrm{RX}}) ds_1(\mathbf{\Omega}'_{\mathrm{TX}}) \quad (\text{A.14})$$

$$+ \, \alpha_m^* e^{-j2\pi \frac{f_c}{c} \mathbf{\Omega}_{\mathrm{TX},m}^{\mathrm{T}} \Delta \boldsymbol{p}_m^{(l'')}} \int \int \int \int \int \int \boldsymbol{s}_{\mathrm{TX}}(\tau) \boldsymbol{s}_{\mathrm{TX}}^{\mathrm{H}}(\tau')$$

$$\times \, \mathbb{E}\left[h_{\mathrm{DMC}}(\lambda, \mathbf{\Omega}_{\mathrm{TX}}; \boldsymbol{p}_m, \boldsymbol{p}) h_{\mathrm{DMC}}(\tau - \lambda, \mathbf{\Omega}_{\mathrm{RX}}; \boldsymbol{p}_{m'}, \boldsymbol{p}) \right.$$

$$\times h_{\mathrm{DMC}}^*(\tau' - \tau_m, \mathbf{\Omega}'_{\mathrm{RX}}; \boldsymbol{p}_{m'}, \boldsymbol{p}) \Big] e^{j2\pi \frac{f_c}{c} \mathbf{\Omega}_{\mathrm{TX}}^{\mathrm{T}} \Delta \boldsymbol{p}_m^{(l)}} e^{j2\pi \frac{f_c}{c} \mathbf{\Omega}_{\mathrm{RX}}^{\mathrm{T}} \Delta \boldsymbol{p}_{m'}^{(l')}}$$

$$\times \, e^{-j2\pi \frac{f_c}{c} \mathbf{\Omega}_{\mathrm{RX}}'^{\mathrm{T}} \Delta \boldsymbol{p}_{m'}^{(l''')}} \, d\tau d\tau' d\lambda ds_1(\mathbf{\Omega}_{\mathrm{RX}}) ds_1(\mathbf{\Omega}_{\mathrm{TX}}) ds_1(\mathbf{\Omega}'_{\mathrm{RX}}) \quad (\text{A.15})$$

$$+ \, \alpha_{m'}^* e^{-j2\pi \frac{f_c}{c} \mathbf{\Omega}_{\mathrm{RX},m'}^{\mathrm{T}} \Delta \boldsymbol{p}_{m'}^{(l''')}} \int \int \int \int \int \int \boldsymbol{s}_{\mathrm{TX}}(\tau) \boldsymbol{s}_{\mathrm{TX}}^{\mathrm{H}}(\tau')$$

$$\times \, \mathbb{E}\left[h_{\mathrm{DMC}}(\lambda, \mathbf{\Omega}_{\mathrm{TX}}; \boldsymbol{p}_m, \boldsymbol{p}) h_{\mathrm{DMC}}(\tau - \lambda, \mathbf{\Omega}_{\mathrm{RX}}; \boldsymbol{p}_{m'}, \boldsymbol{p}) \right.$$

$$\times h_{\mathrm{DMC}}^*(\tau' - \tau_{m'}, \mathbf{\Omega}'_{\mathrm{TX}}; \boldsymbol{p}_m, \boldsymbol{p}) \Big] e^{j2\pi \frac{f_c}{c} \mathbf{\Omega}_{\mathrm{TX}}^{\mathrm{T}} \Delta \boldsymbol{p}_m^{(l)}} e^{j2\pi \frac{f_c}{c} \mathbf{\Omega}_{\mathrm{RX}}^{\mathrm{T}} \Delta \boldsymbol{p}_{m'}^{(l')}}$$

$$\times \, e^{-j2\pi \frac{f_c}{c} \mathbf{\Omega}_{\mathrm{TX}}'^{\mathrm{T}} \Delta \boldsymbol{p}_m^{(l'')}} \, d\tau d\tau' d\lambda ds_1(\mathbf{\Omega}_{\mathrm{TX}}) ds_1(\mathbf{\Omega}_{\mathrm{RX}}) ds_1(\mathbf{\Omega}'_{\mathrm{TX}}) \quad (\text{A.16})$$

$$+ \int \int \int \int \int \int \int \int \boldsymbol{s}_{\mathrm{TX}}(\tau) \boldsymbol{s}_{\mathrm{TX}}^{\mathrm{H}}(\tau')$$

$$\times \, \mathbb{E}\left[h_{\mathrm{DMC}}(\lambda, \mathbf{\Omega}_{\mathrm{TX}}; \boldsymbol{p}_m, \boldsymbol{p}) h_{\mathrm{DMC}}(\tau - \lambda, \mathbf{\Omega}_{\mathrm{RX}}; \boldsymbol{p}_{m'}, \boldsymbol{p}) \right.$$

$$\times \, h_{\mathrm{DMC}}^*(\lambda', \mathbf{\Omega}'_{\mathrm{TX}}; \boldsymbol{p}_m, \boldsymbol{p}) h_{\mathrm{DMC}}^*(\tau' - \lambda', \mathbf{\Omega}'_{\mathrm{RX}}; \boldsymbol{p}_{m'}, \boldsymbol{p}) \Big]$$

$$\times \, e^{j2\pi \frac{f_c}{c} \mathbf{\Omega}_{\mathrm{TX}}^{\mathrm{T}} \Delta \boldsymbol{p}_m^{(l)}} e^{j2\pi \frac{f_c}{c} \mathbf{\Omega}_{\mathrm{RX}}^{\mathrm{T}} \Delta \boldsymbol{p}_{m'}^{(l')}} e^{-j2\pi \frac{f_c}{c} \mathbf{\Omega}_{\mathrm{TX}}'^{\mathrm{T}} \Delta \boldsymbol{p}_m^{(l'')}} e^{-j2\pi \frac{f_c}{c} \mathbf{\Omega}_{\mathrm{RX}}'^{\mathrm{T}} \Delta \boldsymbol{p}_{m'}^{(l''')}}$$

$$\times \, d\tau d\tau' d\lambda d\lambda' ds_1(\mathbf{\Omega}_{\mathrm{TX}}) ds_1(\mathbf{\Omega}_{\mathrm{RX}}) ds_1(\mathbf{\Omega}'_{\mathrm{TX}}) ds_1(\mathbf{\Omega}'_{\mathrm{RX}}). \quad (\text{A.17})$$

For a bistatic setup, i.e., $m \neq m'$, and assuming uncorrelated constituent channels , i.e., $\mathbb{E}\left[h_{\mathrm{DMC}}(\tau - \tau_{m'}, \mathbf{\Omega}_{\mathrm{TX}}; \boldsymbol{p}_m, \boldsymbol{p}) h_{\mathrm{DMC}}(\tau - \tau_m, \mathbf{\Omega}_{\mathrm{RX}}; \boldsymbol{p}_{m'}, \boldsymbol{p})^* \right] = 0$, only (A.9), (A.13), and (A.17) are non-zero. The terms (A.10) and (A.12) are zero due to the uncorrelatedness of the constituent channels, and the terms (A.11), (A.14), (A.15), and (A.16) are zero due to the zero-mean assumption. For seperable delay power spectra (see also (2.18)) , (A.8) reduces to [6, 57]

$$[\boldsymbol{C}_{\mathrm{DMC},m,m'}]_{l,l',l'',l'''} =$$
$$|\alpha_m|^2 e^{j2\pi \frac{f_c}{c} \mathbf{\Omega}_{\mathrm{TX},m}^{\mathrm{T}} (\Delta \boldsymbol{p}_m^{(l)} - \Delta \boldsymbol{p}_m^{(l'')})} P_{\mathrm{DMC},m'} \boldsymbol{C}_{\mathrm{DMC},m'}(\tau_m) c_{m'}(l', l''')$$
$$+ |\alpha_{m'}|^2 e^{j2\pi \frac{f_c}{c} \mathbf{\Omega}_{\mathrm{RX},m'}^{\mathrm{T}} (\Delta \boldsymbol{p}_{m'}^{(l')} - \Delta \boldsymbol{p}_{m'}^{(l''')})} P_{\mathrm{DMC},m} \boldsymbol{C}_{\mathrm{DMC},m}(\tau'_m) c_m(l, l'')$$
$$+ P_{\mathrm{DMC},m} P_{\mathrm{DMC},m'} \boldsymbol{C}_{\mathrm{DMC},m,m'} c_m(l, l'') c_{m'}(l', l'''). \quad (\text{A.18})$$

The delay covariance matrices of the downlink and uplink channel are given as

$$\boldsymbol{C}_{\mathrm{DMC},m}(\tau_{m'}) = \int S_{\mathrm{DMC},m}(\tau - \tau_{m'}) \boldsymbol{s}_{\mathrm{TX}}(\tau) \boldsymbol{s}_{\mathrm{TX}}(\tau)^{\mathrm{H}} d\tau, \text{ and} \quad (\text{A.19})$$

$$\boldsymbol{C}_{\mathrm{DMC},m'}(\tau_m) = \int S_{\mathrm{DMC},m'}(\tau - \tau_m) \boldsymbol{s}_{\mathrm{TX}}(\tau) \boldsymbol{s}_{\mathrm{TX}}(\tau)^{\mathrm{H}} d\tau, \quad (\text{A.20})$$

respectively. The angular direction of departure (DoD) and direction of arrival (DoA) covariance values are given as

$$c_m(l, l'') = \int S_{\text{DMC},m}(\boldsymbol{\Omega}_{\text{TX}}) e^{j2\pi \frac{f_c}{c} \boldsymbol{\Omega}_{\text{TX}}^{\text{T}} \Delta \boldsymbol{p}_m^{(l)}} e^{-j2\pi \frac{f_c}{c} \boldsymbol{\Omega}_{\text{TX}}^{\text{T}} \Delta \boldsymbol{p}_m^{(l'')}} ds_1(\boldsymbol{\Omega}_{\text{TX}}), \text{ and}$$
(A.21)

$$c_{m'}(l', l''') = \int S_{\text{DMC},m'}(\boldsymbol{\Omega}_{\text{RX}}) e^{j2\pi \frac{f_c}{c} \boldsymbol{\Omega}_{\text{RX}}^{\text{T}} \Delta \boldsymbol{p}_{m'}^{(l')}} e^{-j2\pi \frac{f_c}{c} \boldsymbol{\Omega}_{\text{RX}}^{\text{T}} \Delta \boldsymbol{p}_{m'}^{(l''')}} ds_1(\boldsymbol{\Omega}_{\text{RX}}),$$
(A.22)

respectively. Finally, the downlink-uplink covariance matrix is given as

$$\boldsymbol{C}_{\text{DMC},m,m'} = \int \int S_{\text{DMC},m}(\lambda) S_{\text{DMC},m'}(\tau - \lambda) \boldsymbol{s}_{\text{TX}}(\tau) \boldsymbol{s}_{\text{TX}}(\tau)^{\text{H}} d\tau d\lambda. \quad (A.23)$$

For a monostatic setup, i.e., $m = m'$, the terms (A.10) and (A.12) are also non-zero. This leads to

$$[\boldsymbol{C}_{\text{DMC},m,m}]_{l,l',l'',l'''} =$$
$$|\alpha_m|^2 e^{j2\pi \frac{f_c}{c} \boldsymbol{\Omega}_{\text{TX},m}^{\text{T}} (\Delta \boldsymbol{p}_m^{(l)} - \Delta \boldsymbol{p}_m^{(l'')})} P_{\text{DMC},m} \boldsymbol{C}_{\text{DMC},m}(\tau_m) c_m(l', l''')$$
$$+ |\alpha_m|^2 e^{j2\pi \frac{f_c}{c} \boldsymbol{\Omega}_{\text{TX},m}^{\text{T}} (\Delta \boldsymbol{p}_m^{(l)} - \Delta \boldsymbol{p}_m^{(l''')})} P_{\text{DMC},m} \boldsymbol{C}_{\text{DMC},m}(\tau_m) c_m(l', l'')$$
$$+ |\alpha_m|^2 e^{j2\pi \frac{f_c}{c} \boldsymbol{\Omega}_{\text{TX},m}^{\text{T}} (\Delta \boldsymbol{p}_m^{(l')} - \Delta \boldsymbol{p}_m^{(l'')})} P_{\text{DMC},m} \boldsymbol{C}_{\text{DMC},m}(\tau_m) c_m(l, l''')$$
$$+ |\alpha_m|^2 e^{j2\pi \frac{f_c}{c} \boldsymbol{\Omega}_{\text{TX},m}^{\text{T}} (\Delta \boldsymbol{p}_m^{(l')} - \Delta \boldsymbol{p}_m^{(l''')})} P_{\text{DMC},m} \boldsymbol{C}_{\text{DMC},m}(\tau_m) c_m(l, l'')$$
$$+ P_{\text{DMC},m}^2 \boldsymbol{C}_{\text{DMC},m,m} c_m(l, l'') c_m(l', l''')$$
$$+ P_{\text{DMC},m}^2 \boldsymbol{C}_{\text{DMC},m,m} c_m(l, l''') c_m(l', l''). \quad (A.24)$$

The term (A.17) leads to two terms (see [20] and [57]). In the monostatic setup and the case that the TX antenna is the RX antenna, the power of the DMC is doubled compared to a bistatic setup, i.e., uncorrelated constituent channels [6].

A.2 CRLB for the backscatter channel

As already mentioned in Section A.1, we consider a two-reader setup only, with reader m transmitting and reader m' receiving. The likelihood function governing the two-reader RFID setup is given by

$$f(\boldsymbol{r}_{m,m'}|\boldsymbol{\psi}) = \frac{1}{\pi^{NL_m L_{m'}} \det(\boldsymbol{C}_{m,m'}(\boldsymbol{\psi}_{m,m'}))}$$
$$\times e^{(\boldsymbol{r}_{m,m'} - \boldsymbol{\mu}_{m,m'}(\boldsymbol{\psi}))^{\text{H}} \boldsymbol{C}_{m,m'}(\boldsymbol{\psi}_{m,m'})^{-1} (\boldsymbol{r}_{m,m'} - \boldsymbol{\mu}_{m,m'}(\boldsymbol{\psi}))}, \quad (A.25)$$

where we assumed that the parameters governing the covariance matrix are known, i.e., we know the delay power spectrum (DPS), direction of departure power spectrum (DODPS) and direction of arrival power spectrum (DOAPS) of the constituent channels, except for its dependence on parameter vector $\boldsymbol{\psi}_{m,m'} = [\tau_{m,m'}, \varphi_{\text{D},m}, \varphi_{\text{A},m'}, |\alpha_{m,m'}|, \varphi_{\alpha_{m,m'}}]^{\text{T}}$. The mean value

$$\boldsymbol{\mu}_{m,m'}(\boldsymbol{\psi}) = \left[\boldsymbol{\mu}_{m,m'}^{(1,1)}(\boldsymbol{\psi})^{\text{T}}, \dots, \boldsymbol{\mu}_{m,m'}^{(1,L_{m'})}(\boldsymbol{\psi})^{\text{T}}, \dots, \boldsymbol{\mu}_{m,m'}^{(L_m,1)}(\boldsymbol{\psi})^{\text{T}}, \dots, \boldsymbol{\mu}_{m,m'}^{(L_m,L_{m'})}(\boldsymbol{\psi})^{\text{T}} \right]^{\text{T}},$$
(A.26)

where $\boldsymbol{\mu}_{m,m'}^{(l,l')}(\boldsymbol{\psi}) = |\alpha_{m,m'}|e^{j\varphi_{\alpha_{m,m'}}}\boldsymbol{s}_{\mathrm{TX}}(\tau_{m,m'})e^{j2\pi\frac{f_c}{c}\boldsymbol{\Omega}_{\mathrm{TX},m}^{\mathrm{T}}\Delta\boldsymbol{p}_m^{(l)}}e^{j2\pi\frac{f_c}{c}\boldsymbol{\Omega}_{\mathrm{RX},m'}^{\mathrm{T}}\Delta\boldsymbol{p}_{m'}^{(l')}}$.

A.2.1 Including spatial correlations

The individual Fisher information matrix (FIM) elements, considering the spatially correlated DMC covariance matrix ((A.18) or (A.24)), are given as (3.1)

$$[\boldsymbol{\mathcal{I}}(\boldsymbol{\psi})]_{ij} = 2\Re\left[\frac{\partial\boldsymbol{\mu}_{m,m'}^{\mathrm{H}}(\boldsymbol{\psi})}{\partial\psi_i}\boldsymbol{C}_{m,m'}(\boldsymbol{\psi})^{-1}\frac{\partial\boldsymbol{\mu}_{m,m'}(\boldsymbol{\psi})}{\partial\psi_j}\right]$$
$$+ \mathrm{Tr}\left[\boldsymbol{C}_{m,m'}(\boldsymbol{\psi})^{-1}\frac{\partial\boldsymbol{C}_{m,m'}(\boldsymbol{\psi})}{\partial\psi_i}\boldsymbol{C}_{m,m'}(\boldsymbol{\psi})^{-1}\frac{\partial\boldsymbol{C}_{m,m'}(\boldsymbol{\psi}))}{\partial\psi_j}\right],$$
$$= 2\Re\left[\sum_{l=1}^{L_m}\sum_{l'=1}^{L_{m'}}\sum_{l''=1}^{L_m}\sum_{l'''=1}^{L_{m'}}\frac{\partial\boldsymbol{\mu}_{m,m'}^{(l,l')}(\boldsymbol{\psi})}{\partial\psi_i}^{\mathrm{H}}[\boldsymbol{C}_{m,m'}(\boldsymbol{\psi})^{-1}]_{l,l',l'',l'''}\frac{\partial\boldsymbol{\mu}_{m,m'}^{(l'',l''')}(\boldsymbol{\psi})}{\partial\psi_j}\right],$$
$$+ \mathrm{Tr}\left[\boldsymbol{C}_{m,m'}(\boldsymbol{\psi})^{-1}\frac{\partial\boldsymbol{C}_{m,m'}(\boldsymbol{\psi})}{\partial\psi_i}\boldsymbol{C}_{m,m'}(\boldsymbol{\psi})^{-1}\frac{\partial\boldsymbol{C}_{m,m'}(\boldsymbol{\psi}))}{\partial\psi_j}\right], \qquad (\mathrm{A.27})$$

where $[\boldsymbol{C}_{m,m'}(\boldsymbol{\psi})^{-1}]_{l,l',l'',l'''}$ is the $N \times N$ subblock of the inverse covariance matrix indexed by antenna pair (l,l') and (l'',l'''). The partial derivatives of the mean value are given as

$$\frac{\partial\boldsymbol{\mu}_{m,m'}^{(l,l')}(\boldsymbol{\psi})}{\partial\tau_{m,m'}} = |\alpha_{m,m'}|e^{j\varphi_{\alpha_{m,m'}}}\dot{\boldsymbol{s}}_{\mathrm{TX}}(\tau_{m,m'})e^{j2\pi\frac{f_c}{c}\boldsymbol{\Omega}_{\mathrm{TX},m}^{\mathrm{T}}\Delta\boldsymbol{p}_m^{(l)}}$$
$$\times e^{j2\pi\frac{f_c}{c}\boldsymbol{\Omega}_{\mathrm{RX},m'}^{\mathrm{T}}\Delta\boldsymbol{p}_{m'}^{(l')}} \qquad (\mathrm{A.28})$$

$$\frac{\partial\boldsymbol{\mu}_{m,m'}^{(l,l')}(\boldsymbol{\psi})}{\partial\varphi_{\mathrm{D},m}} = |\alpha_{m,m'}|e^{j\varphi_{\alpha_{m,m'}}}\boldsymbol{s}_{\mathrm{TX}}(\tau_{m,m'})j2\pi\frac{f_c}{c}\frac{\partial\boldsymbol{\Omega}_{\mathrm{TX},m}^{\mathrm{T}}}{\partial\varphi_{\mathrm{D},m}}\Delta\boldsymbol{p}_m^{(l)}$$
$$\times e^{j2\pi\frac{f_c}{c}\boldsymbol{\Omega}_{\mathrm{TX},m}^{\mathrm{T}}\Delta\boldsymbol{p}_m^{(l)}}e^{j2\pi\frac{f_c}{c}\boldsymbol{\Omega}_{\mathrm{RX},m'}^{\mathrm{T}}\Delta\boldsymbol{p}_{m'}^{(l')}} \qquad (\mathrm{A.29})$$

$$\frac{\partial\boldsymbol{\mu}_{m,m'}^{(l,l')}(\boldsymbol{\psi})}{\partial\varphi_{\mathrm{A},m}} = |\alpha_{m,m'}|e^{j\varphi_{\alpha_{m,m'}}}\boldsymbol{s}_{\mathrm{TX}}(\tau_{m,m'})e^{j2\pi\frac{f_c}{c}\boldsymbol{\Omega}_{\mathrm{TX},m}^{\mathrm{T}}\Delta\boldsymbol{p}_m^{(l)}}$$
$$\times j2\pi\frac{f_c}{c}\frac{\partial\boldsymbol{\Omega}_{\mathrm{RX},m'}^{\mathrm{T}}}{\partial\varphi_{\mathrm{A},m'}}\Delta\boldsymbol{p}_{m'}^{(l')}e^{j2\pi\frac{f_c}{c}\boldsymbol{\Omega}_{\mathrm{RX},m'}^{\mathrm{T}}\Delta\boldsymbol{p}_{m'}^{(l')}} \qquad (\mathrm{A.30})$$

$$\frac{\partial\boldsymbol{\mu}_{m,m'}^{(l,l')}(\boldsymbol{\psi})}{\partial|\alpha_{m,m'}|} = e^{j\varphi_{\alpha_{m,m'}}}\boldsymbol{s}_{\mathrm{TX}}(\tau_{m,m'})e^{j2\pi\frac{f_c}{c}\boldsymbol{\Omega}_{\mathrm{TX},m}^{\mathrm{T}}\Delta\boldsymbol{p}_m^{(l)}}e^{j2\pi\frac{f_c}{c}\boldsymbol{\Omega}_{\mathrm{RX},m'}^{\mathrm{T}}\Delta\boldsymbol{p}_{m'}^{(l')}} \quad (\mathrm{A.31})$$

$$\frac{\partial\boldsymbol{\mu}_{m,m'}^{(l,l')}(\boldsymbol{\psi})}{\partial\varphi_{\alpha_{m,m'}}} = j|\alpha_{m,m'}|e^{j\varphi_{\alpha_{m,m'}}}\boldsymbol{s}_{\mathrm{TX}}(\tau_{m,m'})e^{j2\pi\frac{f_c}{c}\boldsymbol{\Omega}_{\mathrm{TX},m}^{\mathrm{T}}\Delta\boldsymbol{p}_m^{(l)}}$$
$$\times e^{j2\pi\frac{f_c}{c}\boldsymbol{\Omega}_{\mathrm{RX},m'}^{\mathrm{T}}\Delta\boldsymbol{p}_{m'}^{(l')}}, \qquad (\mathrm{A.32})$$

where $\frac{\partial\boldsymbol{\Omega}_{\mathrm{x},m}^{\mathrm{T}}}{\partial\varphi_{\mathrm{x},m}} = [-\sin(\varphi_{\mathrm{x},m}),\cos(\varphi_{\mathrm{x},m})]$ for $\mathrm{x} \in \{\mathrm{D},\mathrm{A}\}$. For the partial derivatives of the covariance matrix, we only consider the derivatives with respect to the angle of departure (AoD) and angle of arrival (AoA). Inspecting the covariance matrix ((A.18) or (A.24)) carefully, only the AoD and AoA appear directly in the covariance matrix (out of the previously defined parameter vector $\boldsymbol{\psi}_{m,m'}$).

While the delays and amplitudes of the constituent channels appear, the combined delay and amplitude do not appear and thus we neglect the trace term.[2] The partial derivatives of the $N \times N$ subblocks of the bistatic covariance matrix indexed by antenna pair (l, l') and (l'', l''') are given as

$$
\frac{\partial \left[\boldsymbol{C}_{\mathrm{DMC},m,m'}(\boldsymbol{\psi}) \right]_{l,l',l'',l'''}}{\partial \varphi_{\mathrm{D},m}} = j2\pi \frac{f_{\mathrm{c}}}{c} \frac{\partial \boldsymbol{\Omega}_{\mathrm{TX},m}^{\mathrm{T}}}{\partial \varphi_{\mathrm{D},m}} (\Delta \boldsymbol{p}_m^{(l)} - \Delta \boldsymbol{p}_m^{(l'')})
$$
$$
|\alpha_m|^2 \mathrm{e}^{j2\pi \frac{f_c}{c} \boldsymbol{\Omega}_{\mathrm{TX},m}^{\mathrm{T}} (\Delta \boldsymbol{p}_m^{(l)} - \Delta \boldsymbol{p}_m^{(l'')})} P_{\mathrm{DMC},m'} \boldsymbol{C}_{\mathrm{DMC},m'}(\tau_m) c_{m'}(l', l''') \qquad (\text{A.33})
$$
$$
\frac{\partial \left[\boldsymbol{C}_{\mathrm{DMC},m,m'}(\boldsymbol{\psi}) \right]_{l,l',l'',l'''}}{\partial \varphi_{\mathrm{A},m}} = j2\pi \frac{f_{\mathrm{c}}}{c} \frac{\partial \boldsymbol{\Omega}_{\mathrm{RX},m'}^{\mathrm{T}}}{\partial \varphi_{\mathrm{A},m'}} (\Delta \boldsymbol{p}_{m'}^{(l')} - \Delta \boldsymbol{p}_{m'}^{(l''')})
$$
$$
+ |\alpha_{m'}|^2 \mathrm{e}^{j2\pi \frac{f_c}{c} \boldsymbol{\Omega}_{\mathrm{RX},m'}^{\mathrm{T}} (\Delta \boldsymbol{p}_{m'}^{(l')} - \Delta \boldsymbol{p}_{m'}^{(l''')})} P_{\mathrm{DMC},m} \boldsymbol{C}_{\mathrm{DMC},m}(\tau_m') c_m(l, l'') \quad (\text{A.34})
$$

The partial derivatives, given above ((A.28)-(A.32)), combined with (A.27) suffices to numerically evaluate the FIM and subsequently the REB and AEB presented in Section 3.1.2.

A.2.2 Neglecting spatial correlations

To derive the analytic expressions presented in Section 3.1.2, we proceed by neglecting the spatial correlations within the DMC covariance matrix. This means that (A.8) is set to zero, except if $l = l''$ and $l' = l'''$, i.e., (A.7) reduces to a block-diagonal matrix. Thus, the individual FIM elements ((A.27)) are given by

$$
[\boldsymbol{\mathcal{I}}_{\mathrm{nc}}(\boldsymbol{\psi})]_{ij} = 2\Re \Big[\sum_{l=1}^{L_m} \sum_{l'=1}^{L_{m'}} \frac{\partial \boldsymbol{\mu}_{m,m'}^{(l,l')}(\boldsymbol{\psi})^{\mathrm{H}}}{\partial \psi_i} [\boldsymbol{C}_{m,m'}^{-1}]_{l,l',l,l'} \frac{\partial \boldsymbol{\mu}_{m,m'}^{(l,l')}(\boldsymbol{\psi})}{\partial \psi_j} \Big]. \qquad (\text{A.35})
$$

In the following we will derive the individual elements for the following assumptions: (i) the bistatic reader setup, i.e., $m \neq m'$, (ii) a real-valued transmit pulse, leading to a real-valued covariance matrix. By combining both assumptions (together with the fact that we neglect the spatial correlations), the subblocks in the covariance matrix (A.18) do not depend on the individual antenna positions anymore, hence to reduce notational complexity, we define $[\boldsymbol{C}_{m,m'}]_{l,l',l,l'} = \tilde{\boldsymbol{C}}_{m,m'}$. Inserting (A.28)-(A.32) in (A.35), the elements in (3.12) are given as

$$
\mathcal{I}_{\mathrm{nc},\tau_{m,m'},\tau_{m,m'}} = 2\Re \Big[\sum_{l=1}^{L_m} \sum_{l'=1}^{L_{m'}} |\alpha_{m,m'}|^2 \dot{\boldsymbol{s}}_{\mathrm{TX}}(\tau_{m,m'}) \tilde{\boldsymbol{C}}_{m,m'}^{-1} \dot{\boldsymbol{s}}_{\mathrm{TX}}(\tau_{m,m'}) \Big]
$$
$$
= 2 L_m L_{m'} |\alpha_{m,m'}|^2 \dot{\boldsymbol{s}}_{\mathrm{TX}}(\tau_{m,m'}) \tilde{\boldsymbol{C}}_{m,m'}^{-1} \dot{\boldsymbol{s}}_{\mathrm{TX}}(\tau_{m,m'}) \qquad (\text{A.36})
$$
$$
\mathcal{I}_{\mathrm{nc},\tau_{m,m'},\varphi_{\mathrm{D},m}} = 2\Re \Big[\sum_{l=1}^{L_m} \sum_{l'=1}^{L_{m'}} |\alpha_{m,m'}|^2 \dot{\boldsymbol{s}}_{\mathrm{TX}}(\tau_{m,m'}) \tilde{\boldsymbol{C}}_{m,m'}^{-1} \boldsymbol{s}_{\mathrm{TX}}(\tau_{m,m'})
$$
$$
\times j2\pi \frac{f_{\mathrm{c}}}{c} \frac{\partial \boldsymbol{\Omega}_{\mathrm{TX},m}^{\mathrm{T}}}{\partial \varphi_{\mathrm{D},m}} \Delta \boldsymbol{p}_m^{(l)} \Big] \qquad (\text{A.37})
$$

---

[2]Note that the delays and amplitudes of the constituent channels are combined with the onset and the power of the DPS, respectively in (A.18) or (A.24). While for the theoretical derivation we assume these parameter known, actual estimators will need to estimate these parameters and in fact will estimate the combination of the delays and amplitudes of the constituent channels with the onset and power of the DPS, respectively.

$$= 0$$

$$\mathcal{I}_{\mathrm{nc},\tau_{m,m'},\varphi_{\mathrm{A},m'}} = 2\Re\Big[\sum_{l=1}^{L_m}\sum_{l'=1}^{L_{m'}}|\alpha_{m,m'}|^2\dot{\boldsymbol{s}}_{\mathrm{TX}}(\tau_{m,m'})\tilde{\boldsymbol{C}}_{m,m'}^{-1}\boldsymbol{s}_{\mathrm{TX}}(\tau_{m,m'})$$

$$\times\, j2\pi\frac{f_{\mathrm{c}}}{c}\frac{\partial\boldsymbol{\Omega}_{\mathrm{RX},m'}^{\mathrm{T}}}{\partial\varphi_{\mathrm{A},m'}}\Delta\boldsymbol{p}_{m'}^{(l')}\Big] \tag{A.38}$$

$$= 0$$

$$\mathcal{I}_{\mathrm{nc},\tau_{m,m'},|\alpha_{m,m'}|} = 2\Re\Big[\sum_{l=1}^{L_m}\sum_{l'=1}^{L_{m'}}|\alpha_{m,m'}|\dot{\boldsymbol{s}}_{\mathrm{TX}}(\tau_{m,m'})\tilde{\boldsymbol{C}}_{m,m'}^{-1}\boldsymbol{s}_{\mathrm{TX}}(\tau_{m,m'})\Big]$$

$$= 2L_m L_{m'}|\alpha_{m,m'}|\dot{\boldsymbol{s}}_{\mathrm{TX}}(\tau_{m,m'})\tilde{\boldsymbol{C}}_{m,m'}^{-1}\boldsymbol{s}_{\mathrm{TX}}(\tau_{m,m'}) \tag{A.39}$$

$$\mathcal{I}_{\mathrm{nc},\tau_{m,m'},\varphi_{\alpha_{m,m'}}} = 2\Re\Big[\sum_{l=1}^{L_m}\sum_{l'=1}^{L_{m'}}j|\alpha_{m,m'}|^2\dot{\boldsymbol{s}}_{\mathrm{TX}}(\tau_{m,m'})\tilde{\boldsymbol{C}}_{m,m'}^{-1}\boldsymbol{s}_{\mathrm{TX}}(\tau_{m,m'})\Big]$$

$$\tag{A.40}$$

$$= 0$$

$$\mathcal{I}_{\mathrm{nc},\varphi_{\mathrm{D},m},\varphi_{\mathrm{D},m}} = 2\Re\Big[\sum_{l=1}^{L_m}\sum_{l'=1}^{L_{m'}}|\alpha_{m,m'}|^2\boldsymbol{s}_{\mathrm{TX}}(\tau_{m,m'})\tilde{\boldsymbol{C}}_{m,m'}^{-1}\boldsymbol{s}_{\mathrm{TX}}(\tau_{m,m'})$$

$$\times\,(2\pi\frac{f_{\mathrm{c}}}{c}\frac{\partial\boldsymbol{\Omega}_{\mathrm{TX},m}^{\mathrm{T}}}{\partial\varphi_{\mathrm{D},m}}\Delta\boldsymbol{p}_{m}^{(l)})^2\Big]$$

$$= \frac{8\pi^2 f_{\mathrm{c}}^2}{c^2}L_{m'}|\alpha_{m,m'}|^2\boldsymbol{s}_{\mathrm{TX}}(\tau_{m,m'})\tilde{\boldsymbol{C}}_{m,m'}^{-1}\boldsymbol{s}_{\mathrm{TX}}(\tau_{m,m'})$$

$$\times\sum_{l=1}^{L_m}(\frac{\partial\boldsymbol{\Omega}_{\mathrm{TX},m}^{\mathrm{T}}}{\partial\varphi_{\mathrm{D},m}}\Delta\boldsymbol{p}_{m}^{(l)})^2 \tag{A.41}$$

$$\mathcal{I}_{\mathrm{nc},\varphi_{\mathrm{D},m},\varphi_{\mathrm{A},m'}} = 2\Re\Big[\sum_{l=1}^{L_m}\sum_{l'=1}^{L_{m'}}|\alpha_{m,m'}|^2\boldsymbol{s}_{\mathrm{TX}}(\tau_{m,m'})\tilde{\boldsymbol{C}}_{m,m'}^{-1}\boldsymbol{s}_{\mathrm{TX}}(\tau_{m,m'})$$

$$\times\,4\pi^2\frac{f_{\mathrm{c}}^2}{c^2}\frac{\partial\boldsymbol{\Omega}_{\mathrm{TX},m}^{\mathrm{T}}}{\partial\varphi_{\mathrm{D},m}}\Delta\boldsymbol{p}_{m}^{(l)}\frac{\partial\boldsymbol{\Omega}_{\mathrm{RX},m'}^{\mathrm{T}}}{\partial\varphi_{\mathrm{A},m'}}\Delta\boldsymbol{p}_{m'}^{(l')}\Big] \tag{A.42}$$

$$= 0$$

$$\mathcal{I}_{\mathrm{nc},\varphi_{\mathrm{D},m},|\alpha_{m,m'}|} = 2\Re\Big[\sum_{l=1}^{L_m}\sum_{l'=1}^{L_{m'}}|\alpha_{m,m'}|\boldsymbol{s}_{\mathrm{TX}}(\tau_{m,m'})\tilde{\boldsymbol{C}}_{m,m'}^{-1}\boldsymbol{s}_{\mathrm{TX}}(\tau_{m,m'})$$

$$\times\,-j2\pi\frac{f_{\mathrm{c}}}{c}\frac{\partial\boldsymbol{\Omega}_{\mathrm{TX},m}^{\mathrm{T}}}{\partial\varphi_{\mathrm{D},m}}\Delta\boldsymbol{p}_{m}^{(l)}\Big] \tag{A.43}$$

$$= 0$$

$$\mathcal{I}_{\mathrm{nc},\varphi_{\mathrm{D},m},\varphi_{\alpha_{m,m'}}} = 2\Re\Big[\sum_{l=1}^{L_m}\sum_{l'=1}^{L_{m'}}|\alpha_{m,m'}|^2\boldsymbol{s}_{\mathrm{TX}}(\tau_{m,m'})\tilde{\boldsymbol{C}}_{m,m'}^{-1}\boldsymbol{s}_{\mathrm{TX}}(\tau_{m,m'})$$

$$\times\,2\pi\frac{f_{\mathrm{c}}}{c}\frac{\partial\boldsymbol{\Omega}_{\mathrm{TX},m}^{\mathrm{T}}}{\partial\varphi_{\mathrm{D},m}}\Delta\boldsymbol{p}_{m}^{(l)}\Big] \tag{A.44}$$

$$= 0$$

$$\mathcal{I}_{\mathrm{nc},\varphi_{\mathrm{A},m'},\varphi_{\mathrm{A},m'}} = 2\Re\Big[\sum_{l=1}^{L_m}\sum_{l'=1}^{L_{m'}}|\alpha_{m,m'}|^2\boldsymbol{s}_{\mathrm{TX}}(\tau_{m,m'})\tilde{\boldsymbol{C}}_{m,m'}^{-1}\boldsymbol{s}_{\mathrm{TX}}(\tau_{m,m'})$$
$$\times (2\pi\frac{f_{\mathrm{c}}}{c}\frac{\partial\boldsymbol{\Omega}_{\mathrm{RX},m'}^{\mathrm{T}}}{\partial\varphi_{\mathrm{A},m'}}\Delta\boldsymbol{p}_{m'}^{(l')})^2\Big]$$
$$= \frac{8\pi^2 f_{\mathrm{c}}^2}{c^2}L_m|\alpha_{m,m'}|^2\boldsymbol{s}_{\mathrm{TX}}(\tau_{m,m'})\tilde{\boldsymbol{C}}_{m,m'}^{-1}\boldsymbol{s}_{\mathrm{TX}}(\tau_{m,m'})$$
$$\times \sum_{l'=1}^{L_{m'}}(\frac{\partial\boldsymbol{\Omega}_{\mathrm{RX},m'}^{\mathrm{T}}}{\partial\varphi_{\mathrm{A},m'}}\Delta\boldsymbol{p}_{m'}^{(l')})^2 \tag{A.45}$$

$$\mathcal{I}_{\mathrm{nc},\varphi_{\mathrm{A},m'},|\alpha_{m,m'}|} = 2\Re\Big[\sum_{l=1}^{L_m}\sum_{l'=1}^{L_{m'}}|\alpha_{m,m'}|\boldsymbol{s}_{\mathrm{TX}}(\tau_{m,m'})\tilde{\boldsymbol{C}}_{m,m'}^{-1}\boldsymbol{s}_{\mathrm{TX}}(\tau_{m,m'})$$
$$\times -j2\pi\frac{f_{\mathrm{c}}}{c}\frac{\partial\boldsymbol{\Omega}_{\mathrm{RX},m'}^{\mathrm{T}}}{\partial\varphi_{\mathrm{A},m'}}\Delta\boldsymbol{p}_{m'}^{(l')}\Big] \tag{A.46}$$
$$= 0$$

$$\mathcal{I}_{\mathrm{nc},\varphi_{\mathrm{A},m'},\varphi_{\alpha_{m,m'}}} = 2\Re\Big[\sum_{l=1}^{L_m}\sum_{l'=1}^{L_{m'}}|\alpha_{m,m'}|^2\boldsymbol{s}_{\mathrm{TX}}(\tau_{m,m'})\tilde{\boldsymbol{C}}_{m,m'}^{-1}\boldsymbol{s}_{\mathrm{TX}}(\tau_{m,m'})$$
$$\times 2\pi\frac{f_{\mathrm{c}}}{c}\frac{\partial\boldsymbol{\Omega}_{\mathrm{RX},m'}^{\mathrm{T}}}{\partial\varphi_{\mathrm{A},m'}}\Delta\boldsymbol{p}_{m'}^{(l')}\Big] \tag{A.47}$$
$$= 0$$

$$\mathcal{I}_{\mathrm{nc},|\alpha_{m,m'}|,|\alpha_{m,m'}|} = 2\Re\Big[\sum_{l=1}^{L_m}\sum_{l'=1}^{L_{m'}}\boldsymbol{s}_{\mathrm{TX}}(\tau_{m,m'})\tilde{\boldsymbol{C}}_{m,m'}^{-1}\boldsymbol{s}_{\mathrm{TX}}(\tau_{m,m'})$$
$$= 2L_m L_{m'}\boldsymbol{s}_{\mathrm{TX}}(\tau_{m,m'})\tilde{\boldsymbol{C}}_{m,m'}^{-1}\boldsymbol{s}_{\mathrm{TX}}(\tau_{m,m'}) \tag{A.48}$$

$$\mathcal{I}_{\mathrm{nc},|\alpha_{m,m'}|,\varphi_{\alpha_{m,m'}}} = 2\Re\Big[\sum_{l=1}^{L_m}\sum_{l'=1}^{L_{m'}}j|\alpha_{m,m'}|\boldsymbol{s}_{\mathrm{TX}}(\tau_{m,m'})\tilde{\boldsymbol{C}}_{m,m'}^{-1}\boldsymbol{s}_{\mathrm{TX}}(\tau_{m,m'}) \tag{A.49}$$
$$= 0$$

$$\mathcal{I}_{\mathrm{nc},\varphi_{\alpha_{m,m'}},\varphi_{\alpha_{m,m'}}} = 2\Re\Big[\sum_{l=1}^{L_m}\sum_{l'=1}^{L_{m'}}|\alpha_{m,m'}|^2\boldsymbol{s}_{\mathrm{TX}}(\tau_{m,m'})\tilde{\boldsymbol{C}}_{m,m'}^{-1}\boldsymbol{s}_{\mathrm{TX}}(\tau_{m,m'})$$
$$= 2L_m L_{m'}|\alpha_{m,m'}|^2\boldsymbol{s}_{\mathrm{TX}}(\tau_{m,m'})\tilde{\boldsymbol{C}}_{m,m'}^{-1}\boldsymbol{s}_{\mathrm{TX}}(\tau_{m,m'}), \tag{A.50}$$

where (A.37), (A.38), (A.40), (A.42), (A.43), (A.44), (A.46), and (A.44) equate to zero as we chose the center of gravity as the reference point for the local coordinate system for the TX and RX arrays and (A.40), and (A.49) equate to zero as the term inside the real part is purly imaginary.

Due to the fact that the dispersion parameters decouple, it is straightforward to derive the AEB ((3.13)) and the REB ((3.14)) given in Section 3.1.2.

Chapter 7

Bibliography

[1] R. J. Adler and J. E. Taylor, *Random Fields and Geometry*. New York, NY, USA: Springer, 2007.

[2] R. J. Adler, J. E. Taylor, and K. J. Worsley, "Applications of random fields and geometry: Foundations and case studies," 2015.

[3] J. Andersen, J. Nielsen, G. Pedersen, G. Bauch, and M. Herdin, "Room electromagnetics," *IEEE Antennas Propag. Mag.*, vol. 49, no. 2, pp. 27–33, 2007.

[4] C. Andrieu and A. Doucet, "Joint Bayesian model selection and estimation of noisy sinusoids via reversible jump MCMC," *IEEE Trans. Signal Process.*, vol. 47, no. 10, pp. 2667–2676, Oct. 1999.

[5] D. Arnitz, U. Muehlmann, and K. Witrisal, "UWB ranging in passive UHF RFID: Proof of concept," *Electron. Lett.*, vol. 46, no. 20, pp. 1401–1402, Sep. 2010.

[6] ——, "Wideband characterization of backscatter channels: Derivations and theoretical background," *IEEE Trans. Antennas Propag.*, vol. 60, no. 1, pp. 257–266, Jan. 2012.

[7] H. Arthaber, T. Faseth, and F. Galler, "Spread-spectrum based ranging of passive UHF EPC RFID tags," *IEEE Commun. Lett.*, vol. 19, no. 10, pp. 1734–1737, Oct. 2015.

[8] M. Badiu, G. E. Kirkelund, C. N. Manchón, E. Riegler, and B. H. Fleury, "Message-passing algorithms for channel estimation and decoding using approximate inference," in *2012 IEEE International Symposium on Information Theory Proceedings*, 2012, pp. 2376–2380.

[9] M. A. Badiu, T. L. Hansen, and B. H. Fleury, "Variational Bayesian inference of line spectra," *IEEE Trans. Signal Process.*, vol. 65, no. 9, pp. 2247–2261, May 2017.

[10] M. Baghaei-Nejad, D. S. Mendoza, Z. Zou, S. Radiom, G. Gielen, Li-Rong Zheng, and H. Tenhunen, "A remote-powered rfid tag with 10mb/s UWB uplink and -18.5dbm sensitivity UHF downlink in 0.18μm CMOS," in *2009*
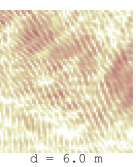
IEEE International Solid-State Circuits Conference - Digest of Technical Papers, 2009, pp. 198–199,199a.

[11] Z. D. Bai, X. R. Chen, P. R. Krishnaiah, Y. H. Wu, and L. C. Zhao, "Strong consistency of maximum likelihood parameter estimation of superimposed exponential signals in noise," *Theory of Probability & Its Applications*, vol. 36, no. 2, pp. 349–355, 1992.

[12] J. O. Berger, *Statistical decision theory and Bayesian analysis.* Springer Science & Business Media, 1985.

[13] C. M. Bishop, *Pattern Recognition and Machine Learning (Information Science and Statistics).* Secaucus, NJ, USA: Springer-Verlag New York, Inc., 2006.

[14] J. Böhme, "Estimation of source parameters by maximum likelihood and nonlinear regression," in *ICASSP'84. IEEE International Conference on Acoustics, Speech, and Signal Processing*, vol. 9. IEEE, 1984, pp. 271–274.

[15] Y. Bresler, "Maximum likelihood estimation of a linearly structured covariance with application to antenna array processing," in *Fourth Annual ASSP Workshop on Spectrum Estimation and Modeling.* IEEE, 1988, pp. 172–175.

[16] T. Buchgraber, "Variational sparse Bayesian learning: Centralized and distributed processing," Ph.D. dissertation, 2013.

[17] C. Carlowitz, M. Vossiek, A. Strobel, and F. Ellinger, "Precise ranging and simultaneous high speed data transfer using mm-wave regenerative active backscatter tags," in *2013 IEEE International Conference on RFID (RFID).* IEEE, 2013, pp. 253–260.

[18] F. Champagnat, Y. Goussard, and J. Idier, "Unsupervised deconvolution of sparse spike trains using stochastic approximation," *IEEE Trans. Signal Process.*, vol. 44, no. 12, pp. 2988–2998, 1996.

[19] Y. Chi, L. L. Scharf, A. Pezeshki, and A. R. Calderbank, "Sensitivity to basis mismatch in compressed sensing," *IEEE Trans. Signal Process.*, vol. 59, no. 5, pp. 2182–2195, 2011.

[20] G. Christakos, *Spatiotemporal random fields: theory and applications.* Elsevier, 2017.

[21] A. Conti, S. Mazuelas, S. Bartoletti, W. C. Lindsey, and M. Z. Win, "Soft information for localization-of-things," *Proc. IEEE*, vol. 107, no. 11, pp. 2240–2264, 2019.

[22] D. Dardari, "Pseudorandom active UWB reflectors for accurate ranging," *IEEE Commun. Lett.*, vol. 8, no. 10, pp. 608–610, Oct 2004.

[23] D. Dardari, R. D'Errico, C. Roblin, A. Sibille, and M. Z. Win, "Ultrawide bandwidth RFID: The next generation?" *Proc. IEEE*, vol. 98, no. 9, pp. 1570–1582, Sep. 2010.

[24] P. Davidson and R. Piché, "A survey of selected indoor positioning methods for smartphones," *IEEE Commun. Surveys Tuts.*, vol. 19, no. 2, pp. 1347–1370, Secondquarter 2017.

[25] DecaWave, *DW1000 User Manual, Version 2.05*, DecaWave, 2015.

[26] G. Durgin, *Space-Time Wireless Channels*, 1st ed.   USA: Prentice Hall Press, 2002.

[27] A. C. Faul and M. E. Tipping, "Analysis of sparse Bayesian learning," in *Advances in neural information processing systems*, 2002, pp. 383–389.

[28] B. H. Fleury, "First- and second-order characterization of direction dispersion and space selectivity in the radio channel," *IEEE Trans. Inf. Theory*, vol. 46, no. 6, pp. 2027–2044, Sep 2000.

[29] ——, "Lecture notes on "Array Signal Processing"," May-June 2019.

[30] B. H. Fleury, M. Tschudin, R. Heddergott, D. Dahlhaus, and K. I. Pedersen, "Channel parameter estimation in mobile radio environments using SAGE algorithm," *IEEE J. Sel. Areas Commun.*, vol. 17, no. 3, pp. 434–450, Mar. 1999.

[31] F. Galler, "Localization of passive UHF RFID tags," Ph.D. dissertation, Technische Universität Wien, 2019.

[32] F. Galler, T. Faseth, and H. Arthaber, "Implementation aspects of an SDR based EPC RFID reader testbed," in *2015 Int. EURASIP Workshop on RFID Technology (EURFID)*, Oct. 2015, pp. 94–97.

[33] R. Giri and B. Rao, "Type-I and Type-II Bayesian methods for sparse signal recovery using scale mixtures," *IEEE Trans. Signal Process.*, vol. 64, no. 13, pp. 3418–3428, July 2016.

[34] F. Guidi, "Study of ultra wide band modulated backscattering based RFID systems," Ph.D. dissertation, Ecole Polytechnique Paristech, Universita degli studi di Bologna, 2013.

[35] Y. Han, Y. Shen, X. P. Zhang, M. Z. Win, and H. Meng, "Performance limits and geometric properties of array localization," *IEEE Trans. Inf. Theory*, vol. 62, no. 2, pp. 1054–1075, Feb. 2016.

[36] T. L. Hansen, M. A. Badiu, B. H. Fleury, and B. D. Rao, "A sparse Bayesian learning algorithm with dictionary parameter estimation," in *2014 IEEE 8th Sensor Array and Multichannel Signal Processing Workshop (SAM)*, June 2014, pp. 385–388.

[37] T. L. Hansen, B. H. Fleury, and B. D. Rao, "Superfast line spectral estimation," *IEEE Trans. Signal Process.*, vol. PP, no. 99, pp. 1–1, 2018.

[38] T. Hansen, "Sparsity-based algorithms for line spectral estimation," Ph.D. dissertation, 2018.

[39] B. Hofmann-Wellenhof, H. Lichtenegger, and E. Wasle, *GNSS – Global Navigation Satellite Systems.*   Springer Press, 2008.

[40] A. G. Jaffer, "Maximum likelihood direction finding of stochastic sources: A separable solution," in *ICASSP-88., International Conference on Acoustics, Speech, and Signal Processing.* IEEE, 1988, pp. 2893–2896.

[41] J. Karedal, S. Wyne, P. Almers, F. Tufvesson, and A. F. Molisch, "A measurement-based statistical model for industrial ultra-wideband channels," *IEEE Trans. Wireless Commun.*, vol. 6, no. 8, pp. 3028–3037, Aug. 2007.

[42] S. Kay, *Fundamentals of Statistical Signal Processing: Estimation Theory.* Upper Saddle River, NJ, USA: Prentice Hall Signal Processing Series, 1993.

[43] ——, *Fundamentals of Statistical Signal Processing: Detection Theory.* Upper Saddle River, NJ, USA: Prentice Hall Signal Processing Series, 1998.

[44] R. A. Kennedy and P. Sadeghi, *Hilbert Space Methods in Signal Processing.* Cambridge University Press, 2013.

[45] J. Kormylo and J. Mendel, "Maximum likelihood detection and estimation of Bernoulli-Gaussian processes," *IEEE Trans. Inf. Theory*, vol. 28, no. 3, pp. 482–488, 1982.

[46] C. Krall, "Signal processing for ultra wideband transceivers," Ph.D. dissertation, Graz University of Technology, Austria, 2008.

[47] H. Krim and M. Viberg, "Two decades of array signal processing research: The parametric approach," *IEEE Signal Process. Mag.*, vol. 13, no. 4, pp. 67–94, Jul. 1996.

[48] J. Kulmer, "High-Accuracy Positioning Exploiting Multipath for Reducing the Infrastructure," Ph.D. dissertation, Graz University of Technology, 2019.

[49] S.-Y. Kung, K. S. Arun, and D. B. Rao, "State-space and singular-value decomposition-based approximation methods for the harmonic retrieval problem," *Journal of the Optical Society of America*, vol. 73, no. 12, pp. 1799–1811, 1983.

[50] E. Leitinger, "Cognitive Indoor Positioning and Tracking using Multipath Channel Information," Ph.D. dissertation, Graz University of Technology, 2016.

[51] E. Leitinger, P. Meissner, C. Rudisser, G. Dumphart, and K. Witrisal, "Evaluation of position-related information in multipath components for indoor positioning," *IEEE J. Sel. Areas Commun.*, vol. 33, no. 11, pp. 2313–2328, Nov. 2015.

[52] A. Mallat, J. Louveaux, and L. Vandendorpe, "UWB based positioning in multipath channels: CRBs for AOA and for hybrid TOA-AOA based methods," in *2007 IEEE International Conference on Communications*, June 2007, pp. 5775–5780.

[53] A. Mariani, A. Giorgetti, and M. Chiani, "Model order selection based on information theoretic criteria: Design of the penalty," *IEEE Trans. Signal Process.*, vol. 63, no. 11, pp. 2779–2789, Jun. 2015.

[54] Z. Marzi, D. Ramasamy, and U. Madhow, "Compressive channel estimation and tracking for large arrays in mm-wave picocells," *IEEE J. Sel. Topics Signal Process.*, vol. 10, no. 3, pp. 514–527, April 2016.

[55] R. McAulay and E. Hofstetter, "Barankin bounds on parameter estimation," *IEEE Trans. Inf. Theory*, vol. 17, no. 6, pp. 669–676, November 1971.

[56] P. Meissner, "Multipath-assisted indoor positioning," Ph.D. dissertation, Graz University of Technology, 2014.

[57] K. S. Miller, *Complex stochastic processes: an introduction to theory and application.* Addison Wesley Publishing Company, 1974.

[58] T. Minka, "Divergence measures and message passing," Tech. Rep., 2005.

[59] A. F. Molisch, "Ultrawideband propagation channels-theory, measurement, and modeling," *IEEE Trans. Veh. Technol.*, vol. 54, no. 5, pp. 1528–1545, Sep. 2005.

[60] ——, "Ultra-wide-band propagation channels," *Proc. IEEE*, vol. 97, no. 2, pp. 353–371, Feb. 2009.

[61] ——, *Wireless Communications.* Wiley-IEEE Press, 2005.

[62] B. Nadler and A. Kontorovich, "Model selection for sinusoids in noise: Statistical analysis and a new penalty term," *IEEE Trans. Signal Process.*, vol. 59, no. 4, pp. 1333–1345, April 2011.

[63] B. Ottersten, M. Viberg, P. Stoica, and A. Nehorai, *Exact and Large Sample Maximum Likelihood Techniques for Parameter Estimation and Detection in Array Processing.* Berlin, Heidelberg: Springer Berlin Heidelberg, 1993, pp. 99–151.

[64] G. Parisi, *Statistical field theory.* Addison-Wesley, 1988.

[65] A. Paulraj, R. Nabar, and D. Gore, *Introduction to Space-Time Wireless Communications*, 1st ed. USA: Cambridge University Press, 2008.

[66] N. L. Pedersen, C. N. Manchón, M.-A. Badiu, D. Shutin, and B. H. Fleury, "Sparse estimation using Bayesian hierarchical prior modeling for real and complex linear models," *Signal processing*, vol. 115, pp. 94–109, 2015.

[67] T. Pedersen, "Contributions in radio channel sounding, modeling, and estimation," Ph.D. dissertation, Aalborg University, 2009.

[68] T. Pedersen, "Stochastic multipath model for the in-room radio channel based on room electromagnetics," *IEEE Trans. Antennas Propag.*, vol. 67, no. 4, pp. 2591–2603, April 2019.

[69] V. F. Pisarenko, "The retrieval of harmonics from a covariance function," *Geophysical Journal International*, vol. 33, no. 3, pp. 347–366, 1973.

[70] C. R. Rao and L. Zhao, "Asymptotic behavior of maximum likelihood estimates of superimposed exponential signals," *IEEE Trans. Signal Process.*, vol. 41, no. 3, pp. 1461–1464, 1993.

[71] A. Richter, "Estimation of radio channel paramters: Models and algorithms," Ph.D. dissertation, Technische Universitaet Ilmenau, 2005.

[72] R. Roy and T. Kailath, "Esprit-estimation of signal parameters via rotational invariance techniques," *IEEE Trans. Acoust., Speech, Signal Process.*, vol. 37, no. 7, pp. 984–995, 1989.

[73] J. Salmi, "Contributions to measurement-based dynamic MIMO channel modeling and propagation parameter estimation," Ph.D. dissertation, Helsinki University of Technology, 2009.

[74] J. Salmi, A. Richter, and V. Koivunen, "Detection and tracking of mimo propagation path parameters using state-space approach," *IEEE Trans. Signal Process.*, vol. 57, no. 4, pp. 1538–1550, April 2009.

[75] R. Schmidt, "Multiple emitter location and signal parameter estimation," *IEEE Trans. Antennas Propag.*, vol. 34, no. 3, pp. 276–280, 1986.

[76] A. Shahmansoori, G. E. Garcia, G. Destino, G. Seco-Granados, and H. Wymeersch, "Position and orientation estimation through millimeter-wave MIMO in 5G systems," *IEEE Trans. Wireless Commun.*, vol. 17, no. 3, pp. 1822–1835, March 2018.

[77] T.-J. Shan, M. Wax, and T. Kailath, "On spatial smoothing for direction-of-arrival estimation of coherent signals," *IEEE Trans. Acoust., Speech, Signal Process.*, vol. 33, no. 4, pp. 806–811, 1985.

[78] Y. Shen and M. Z. Win, "Fundamental limits of wideband localization-part I: A general framework," *IEEE Trans. Inf. Theory*, vol. 56, no. 10, pp. 4956–4980, Oct. 2010.

[79] D. Shutin, T. Buchgraber, S. R. Kulkarni, and H. V. Poor, "Fast variational sparse Bayesian learning with automatic relevance determination for superimposed signals," *IEEE Trans. Signal Process.*, vol. 59, no. 12, pp. 6257–6261, Dec. 2011.

[80] D. Shutin and B. H. Fleury, "Sparse variational Bayesian SAGE algorithm with application to the estimation of multipath wireless channels," *IEEE Trans. Signal Process.*, vol. 59, no. 8, pp. 3609–3623, Aug 2011.

[81] D. Shutin, B. H. Fleury, and N. Schneckenburger, "Artifact suppression for super-resolution sparse Bayesian learning," 2018, submitted to IEEE Trans. Signal Process.

[82] D. Shutin and N. Schneckenburger, "Joint detection and super-resolution estimation of multipath signal parameters using incremental automatic relevance determination," *ArXiv e-prints*, Mar. 2015.

[83] D. Shutin and B. Vexler, "Sparse bayesian learning with dictionary refinement for super-resolution through time," in *2017 IEEE 7th International Workshop on Computational Advances in Multi-Sensor Adaptive Processing (CAMSAP)*. IEEE, 2017, pp. 1–5.

76

[84] D. Shutin, W. Wang, and T. Jost, "Incremental sparse Bayesian learning for parameter estimation of superimposed signals," in *10th International Conference on Sampling Theory and Applications*, no. 1, 2013, pp. 6–9.

[85] M. K. Simon, W. C. Lindsey, and S. M. Hinedi, *Digital communication techniques : signal design and detection*. Englewood Cliffs, New Jersey : PTR Prentice Hall, 1995.

[86] M. Steinbauer, A. F. Molisch, and E. Bonek, "The double-directional radio channel," *IEEE Antennas Propag. Mag.*, vol. 43, no. 4, pp. 51–63, 2001.

[87] P. Stoica and R. Moses, *Spectral Analysis of Signals*. Pearson Prentice Hall, 2005.

[88] P. Stoica and A. Nehorai, "Performance study of conditional and unconditional direction-of-arrival estimation," *IEEE Trans. Acoust., Speech, Signal Process.*, vol. 38, no. 10, pp. 1783–1795, 1990.

[89] P. Stoica, "List of references on spectral line analysis," *Signal Process.*, vol. 31, no. 3, pp. 329–340, Apr. 1993. [Online]. Available: https://doi.org/10.1016/0165-1684(93)90090-W

[90] P. Stoica, R. L. Moses, B. Friedlander, and T. Soderstrom, "Maximum likelihood estimation of the parameters of multiple sinusoids from noisy measurements," *IEEE Trans. Acoust., Speech, Signal Process.*, vol. 37, no. 3, pp. 378–392, 1989.

[91] P. Stoica and A. Nehorai, "Statistical analysis of two nonlinear least-squares estimators of sine-wave parameters in the colored-noise case," *Circuits, Systems and Signal Processing*, vol. 8, no. 1, pp. 3–15, 1989.

[92] ——, "On the concentrated stochastic likelihood function in array signal processing," *Circuits Syst. Signal Process.*, vol. 14, no. 5, pp. 669–674, Sep. 1995. [Online]. Available: https://doi.org/10.1007/BF01213963

[93] P. Stoica and Y. Selen, "Model-order selection: a review of information criterion rules," *IEEE Signal Process. Mag.*, vol. 21, no. 4, pp. 36–47, 2004.

[94] G. L. Stuber, *Principles of Mobile Communication*, 1st ed. USA: Kluwer Academic Publishers, 1996.

[95] F. Talebi and T. Pratt, "Model order selection for complex sinusoids in the presence of unknown correlated Gaussian noise," *IEEE Trans. Signal Process.*, vol. 63, no. 7, pp. 1664–1674, 2015.

[96] R. Tibshirani, "Regression shrinkage and selection via the lasso," *Journal of the Royal Statistical Society: Series B (Methodological)*, vol. 58, no. 1, pp. 267–288, 1996.

[97] M. E. Tipping and A. C. Faul, "Fast marginal likelihood maximisation for sparse Bayesian models," in *Proceedings of the Ninth International Workshop on Artificial Intelligence and Statistics*, C. M. Bishop and B. J. Frey, Eds., 2003, pp. 3–6.

[98] M. E. Tipping, "The relevance vector machine," in *Advances in neural information processing systems*, 2000, pp. 652–658.

[99] ——, "Sparse Bayesian learning and the relevance vector machine," *Journal of machine learning research*, vol. 1, no. Jun, pp. 211–244, 2001.

[100] H. L. Van Trees, *Detection, Estimation and Modulation, Part I.* Wiley Press, 1968.

[101] M. Viberg, B. Ottersten, and A. Nehorai, "Estimation accuracy of maximum likelihood direction finding using large arrays," in *Proc. 25th Asilomar Conf. Sig., Syst., Comput*, 1991, pp. 928–932.

[102] ——, "Performance analysis of direction finding with large arrays and finite data," *IEEE Trans. Signal Process.*, vol. 43, no. 2, pp. 469–477, 1995.

[103] M. Win and R. Scholtz, "Characterization of Ultra-Wide Bandwidth Wireless Indoor Channels: a Communication-Theoretic View," *IEEE J. Sel. Areas Commun.*, vol. 20, no. 9, pp. 1613 – 1627, Dec. 2002.

[104] D. P. Wipf, B. D. Rao, and S. Nagarajan, "Latent variable Bayesian models for promoting sparsity," *IEEE Trans. Inf. Theory*, vol. 57, no. 9, pp. 6236–6255, Sept. 2011.

[105] D. P. Wipf and S. S. Nagarajan, "A new view of automatic relevance determination," in *Advances in Neural Information Processing Systems 20*, J. C. Platt, D. Koller, Y. Singer, and S. T. Roweis, Eds. Curran Associates, Inc., 2008, pp. 1625–1632.

[106] D. P. Wipf and B. D. Rao, "Sparse Bayesian learning for basis selection," *IEEE Trans. Signal Process.*, vol. 52, no. 8, pp. 2153–2164, 2004.

[107] K. Witrisal, P. Meissner, E. Leitinger, Y. Shen, C. Gustafson, F. Tufvesson, K. Haneda, D. Dardari, A. F. Molisch, A. Conti, and M. Z. Win, "High-accuracy localization for assisted living: 5G systems will turn multipath channels from foe to friend," *IEEE Signal Process. Mag.*, vol. 33, no. 2, pp. 59–70, March 2016.

[108] K. J. Worsley, "Local maxima and the expected euler characteristic of excursion sets of χ^2, f and t fields," *Adv. Appl. Probab.*, vol. 26, no. 1, pp. 13–42, 1994. [Online]. Available: http://www.jstor.org/stable/1427576

[109] Yih-Min Chen, "On spatial smoothing for two-dimensional direction-of-arrival estimation of coherent signals," in *Proceedings of 1994 28th Asilomar Conference on Signals, Systems and Computers*, vol. 1, 1994, pp. 648–652 vol.1.

[110] R. Zekavat and R. M. Buehrer, *Handbook of Position Location: Theory, Practice and Advances*, 1st ed. Wiley-IEEE Press, 2011.

[111] J. Ziv and M. Zakai, "Some lower bounds on signal parameter estimation," *IEEE Trans. Inf. Theory*, vol. 15, no. 3, pp. 386–391, May 1969.

Part II

Included Papers

d = 16.8 m

d = 33.6 m

Bandwidth Dependence of the Ranging Error Variance in Dense Multipath

Stefan Hinteregger, Erik Leitinger, Paul Meissner, Josef Kulmer, and Klaus Witrisal

Abstract

It is well known that the time-of-flight ranging performance is heavy influenced by multipath propagation within a radio environment. This holds in particular in *dense* multipath channels as encountered in indoor scenarios. The signal bandwidth has a tremendous influence on this effect, as it determines whether the time resolution is sufficient to resolve the useful line-of-sight (LOS) signal component from interfering multipath.

This paper employs a geometry-based stochastic channel model to analyze and characterize the ranging error variance as a function of the bandwidth, covering the narrowband up to the UWB regimes. The Cramér-Rao lower bound (CRLB) is derived for this purpose. It quantifies the impact of bandwidth, SNR, and parameters of the multipath radio channel and can thus be used as an effective and accurate *channel model* (e.g.) for the cross-layer optimization of positioning systems. Experimental data are analyzed to validate our theoretical results.

1 Introduction

Positioning indoors is a challenging task. Existing systems like global navigation satellite systems (e.g GPS, Galileo) fail at indoor positioning due to the limited visibility of the satellites and the limited signal bandwidth. In indoor scenarios a multitude of multipath components (MPC) cause severe fading and pulse distortion of the received signals making the localization challenging.

Performance bounds for the ranging and positioning capabilities of a system allow for fundamental insight into system design considerations or cross-layer optimization. In [1,2] the Cràmer Rao lower bound has been investigated for radio and radar scenarios providing insight into the influence of system parameters like the signal to noise ratio (SNR) or the bandwidth.

Ultra-wideband (UWB) radio signals are considered to be most promising for indoor positioning because their fine time resolution allows to separate the arriving MPCs into individual components. To investigate performance bounds and capture the information included in the channel, a proper channel model is paramount. In [3] the stochastic IEEE 802.15.4a channel model has been used to derive the Cràmer Rao lower bound and the Ziv-Zakai bound for positioning indoors. By adding geometrically modeled components to the channel model using a so called geometry-based stochastic channel model, the additional information provided by specular multipath components can be quantified [4].

Since bandwidth is a scarce resource, minimal usage reduces the costs of a system drastically. By decreasing the bandwidth and moving to non-UWB radio signals the specular components (including the line of sight (LOS)) are no longer separated from other multipath components which are denoted as dense or diffuse multipath (DM). This DM leads to multipath effects such as amplitude fading and pulse distortion. For narrowband signals only amplitude fading occurs since the complete DM interferes with the LOS component, while for the UWB case the LOS component is well-separated from the DM. The bottom of Fig. 1 illustrates these cases and shows the pulse distortion and amplitude fading at bandwidths in between these "extreme cases".

In [5] we derived the Cràmer Rao lower bound (CRLB) on ranging and positioning for a channel consisting of the LOS component and dense multipath. Within this paper

- we analyze the CRLB for the ranging error for different channel parameters,

- derive an approximation for the CRLB, and

- validate the model and CRLB using measurement data.

2 Signal Model

We consider L measurements obtained from signal transmissions between an agent at an unknown position $\mathbf{p}$ and anchors at known positions $\mathbf{a}_\ell$. A unit energy pulse $s(t)$ is transmitted leading to the received signal

$$r(t) = \alpha_\ell s(t - \tau_\ell) + (s * \nu_\ell)(t) + w(t), \tag{1}$$

82
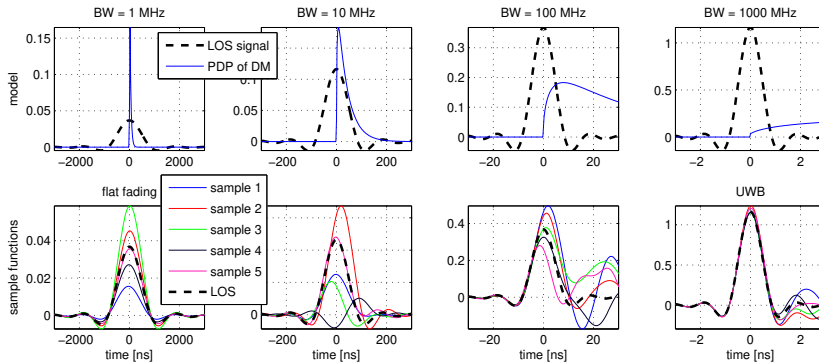
Figure 1: Model and sample functions illustrating the problem under investigation over a wide range of BWs (neglecting AWGN).

where $\alpha_\ell = |\alpha_\ell| e^{-j(2\pi f_c \tau_\ell + \varphi_0)}$ describes the complex amplitude of the deterministic line-of-sight (LOS) component with delay $\tau_\ell = \frac{1}{c}\|\mathbf{p} - \mathbf{a}_\ell\|$, where c denotes the speed of light, f_c is the carrier frequency and φ_0 is a random phase offset. The second term denotes the dense multipath (DM) which is modeled as a zero-mean complex Gaussian random process. By assuming uncorrelated scattering in the delay domain, the auto-correlation of the DM process is given as

$$K_\nu^{(\ell)}(t, u) = \mathbb{E}_\nu \left\{ \nu_\ell(t) \nu_\ell^*(u) \right\} = S_\nu^{(\ell)}(t - \tau_\ell) \delta(t - u), \tag{2}$$

where $S_\nu^{(\ell)}(t)$ is the power delay profile (PDP) of the DM process at position $\mathbf{p}$ as a function of the excess delay time. Quasi-stationarity in the spatial domain is assumed, meaning that the PDP does not change in the vicinity of the position $\mathbf{p}$. Finally, the third term in (1) models additive white Gaussian noise (AWGN).

The DM is modeled as double exponential function (cf. [6])

$$S_\nu^{(\ell)}(\tau) = \Omega_1 \frac{\gamma_{\text{dec}} + \gamma_{\text{rise}}}{\gamma_{\text{dec}}(\gamma_{\text{dec}} + \gamma_{\text{rise}}(1 - \chi))} (1 - \chi e^{-\tau/\gamma_{\text{rise}}}) e^{-\tau/\gamma_{\text{dec}}} \tag{3}$$

where Ω_1 is the total power of the DM, and γ_{rise}, γ_{dec}, and χ are shape parameters. The Rician K-factor for the LOS component is

$$K_{\text{LOS}} = \frac{|\alpha_\ell|^2}{\Omega_1}. \tag{4}$$

Fig. 1 illustrates the signal model and shows a few sample realizations of the received signal neglecting the AWGN. For high bandwidths (the UWB case) the DM process is clearly separated from the LOS component and neither fading nor distortion of the transmitted pulse occurs. By decreasing the bandwidth (BW) the interference between the transmitted pulse and the DM process increases and leads to fading and distortion of the received pulse. For low bandwidths the complete DM process interferes with the LOS component and only fading occurs. In the following the measurement index ℓ will be dropped.

3   Ranging Error Bound (REB)

In [5] we derived the REB, which is the square root of the inverse of the equivalent Fisher information (EFI) $\mathcal{R}(\tau) = \sqrt{\mathcal{I}_\tau^{-1}}$, the square root of the CRLB

$\mathrm{var}\{\hat{\tau}\} \geq \mathcal{I}_{\tau}^{-1}$ for the delay-estimation problem. This enables us to investigate the influence of the signal and environment model parameters onto the REB. Under the assumption that the AWGN and the DM are both Gaussian, the EFI for a single channel can be presented as

$$\mathcal{I}_{\tau} = 8\pi^2\beta^2\gamma\mathrm{SINR}\sin^2(\phi) = 8\pi^2\beta^2\widetilde{\mathrm{SINR}} \qquad (5)$$

where $\beta^2 = \|\dot{\mathbf{s}}_{\tau}\|^2 / (4\pi^2\|\mathbf{s}_{\tau}\|^2) = \int_f f^2|S(f)|^2\mathrm{d}f$ is the effective (mean square) bandwidth of the (energy-normalized) transmit pulse $s(t) \overset{\mathcal{F}}{\longleftrightarrow} S(f)$, $\mathbf{s}_{\tau}$ is the sampled transmit pulse shifted to τ, $\dot{\mathbf{s}}_{\tau}$ is its derivative, SINR is the signal-to-interference-plus-noise ratio (SINR) of the LOS component, γ is the so-called whitening gain, and $\sin^2(\phi)$ incorporates the estimation of the nuisance parameter α. The product of β^2, SINR, γ, and $\sin^2(\phi)$ thus provides the amount of information transmitted in the LOS component when influenced by DM and AWGN. For the derivation of (5), the inverse of the covariance matrix of DM plus AWGN is needed as a whitening operator. The SINR, the whitening gain γ, and $\sin^2(\phi)$ are also combined in the effective SINR, $\widetilde{\mathrm{SINR}}$ which can be expressed as [5]

$$\widetilde{\mathrm{SINR}} = \frac{|\alpha|^2}{N_0}\|\mathbf{s}_{\tau}\|^2 T_s \frac{\|\dot{\mathbf{s}}_{\tau}\|_{\mathcal{H}}^2}{\|\dot{\mathbf{s}}_{\tau}\|^2}\sin^2(\phi), \qquad (6)$$

where $T_{\mathrm{s}} = 1/f_{\mathrm{s}}$, f_{s} is the sampling frequency, $\|\cdot\|_{\mathcal{H}}^2$ denotes the weighted squared norm in a Hilbert space defined by the covariance $\mathbf{C}_{\mathrm{n}}/\sigma_{\mathrm{n}}^2$ (see Appendix A), and ϕ is the angle between $\mathbf{s}_{\tau}$ and its derivative $\dot{\mathbf{s}}_{\tau}$ in this Hilbert space. Appendix B introduces approximations for the previously defined parameters without the need to compute the inverse of the covariance matrix.

Fig. 2a illustrates the SINR, γ, $\sin^2(\phi)$, and $\widetilde{\mathrm{SINR}}$ over a wide range of bandwidths for three different K_{LOS} factors ($-10\,\mathrm{dB}$, $0\,\mathrm{dB}$, and $10\,\mathrm{dB}$). For low BWs the SINR tends towards the Rician K_{LOS} factor of the channel model and for high bandwidth it reaches the signal to noise ratio (SNR). The SINR reflects the amplitude fading of the LOS component. The $\widetilde{\mathrm{SINR}}$ follows the SINR at high bandwidth but reaches the SNR again at low bandwidth. The $\widetilde{\mathrm{SINR}}$ reflects the pulse distortion of the deterministic LOS component. At high BW neither fading nor distortion occurs and both the SINR and $\widetilde{\mathrm{SINR}}$ reach the SNR. By decreasing the BW, both amplitude fading and pulse distortion occur leading to decreased SINR and $\widetilde{\mathrm{SINR}}$. At very low BW only amplitude fading occurs since the complete DM process interferes with the pulse (cf. Fig. 1). The parameter $\sin^2(\phi)$ which can be attributed to the cost of estimating the nuisance parameter α reduces the achievable whitening gain. The lower the K_{LOS} factor the higher the cost for estimating the nuisance parameter.

In Fig. 2b the shape parameter γ_{rise} of the double exponential PDP (3) is varied. If γ_{rise}, which describes the onset behaviour of the PDP, is set to zero the double exponential PDP reduces to an exponentially decaying PDP. Thus, for high BW some amplitude fading and pulse distortion occur as well and the $\widetilde{\mathrm{SINR}}$ and SINR do not reach the SNR. The cost for estimating the nuisance parameter α is coupled with the pulse distortion. At low BW less pulse distortion occurs since the complete DM interferes with the LOS. In the region where the BW is approximately the inverse of the rms delay spread ($\tau_{\mathrm{rms}} = \{17.3, 16.1\}\,\mathrm{ns}$) the most pulse distortion occurs and the cost for estimating the nuisance parameter

84
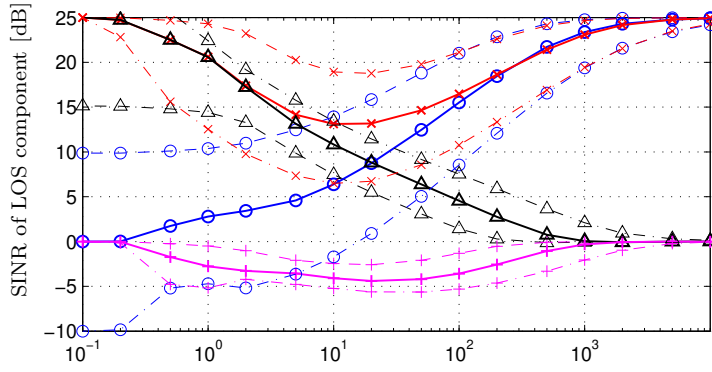
(a) K_{LOS}: dotted lines $10\,\text{dB}$, solid lines $0\,\text{dB}$, and chain dotted lines $-10\,\text{dB}$)
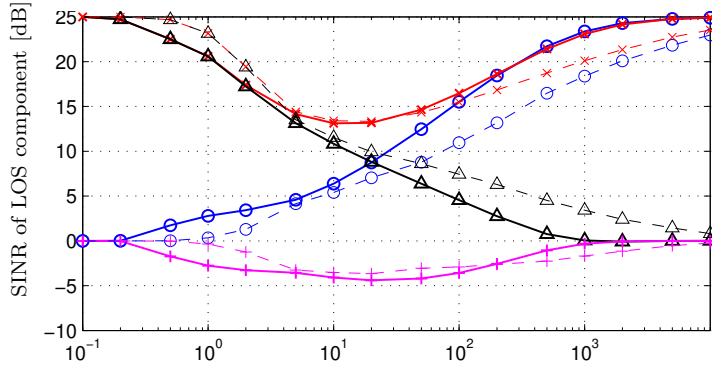
(b) γ_{rise}: solid lines $5\,\text{ns}$, and dotted lines $0\,\text{ns}$
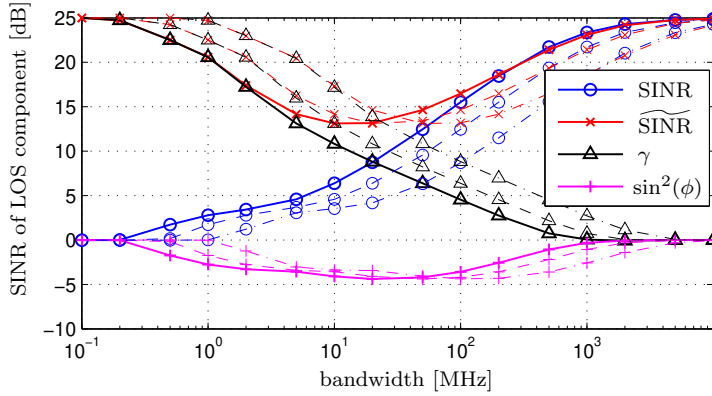
(c) γ_{rise} and γ_{dec}: solid lines $5\,\text{ns}$ and $20\,\text{ns}$, dotted lines $2.5\,\text{ns}$ and $10\,\text{ns}$, and chain dotted lines $1\,\text{ns}$ and $4\,\text{ns}$ respectively

Figure 2: SINR, $\widetilde{\text{SINR}}$, whitening gain γ, and $\sin^2(\phi)$ as a function of bandwidth and different channel parameters. If not stated otherwise: $\text{E}_{\text{LOS}}/N_0 = 25\,\text{dB}$, $K_{\text{LOS}} = 0\,\text{dB}$, $\gamma_{\text{dec}} = 20\,\text{ns}$, $\gamma_{\text{rise}} = 5\,\text{ns}$.

α is the highest.

By varying both the shape parameters γ_{rise} and γ_{dec} by the same factor, it can be shown, that the root mean square (rms) delay spread of the PDP is changed

85
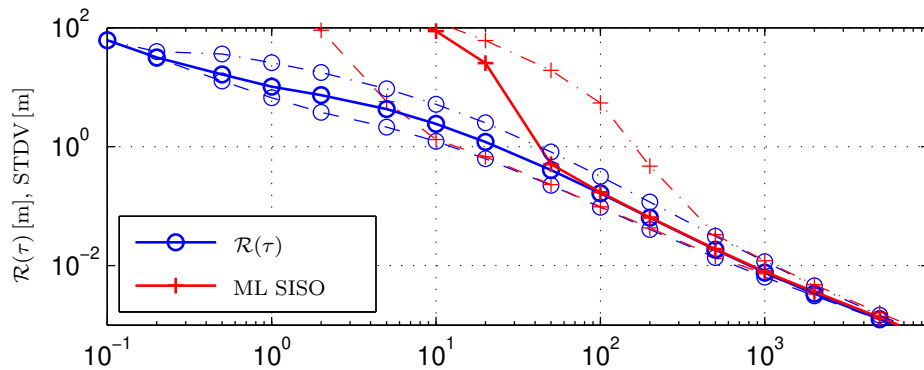
(a) REB and simulated range estimation error STDV for ML estimator
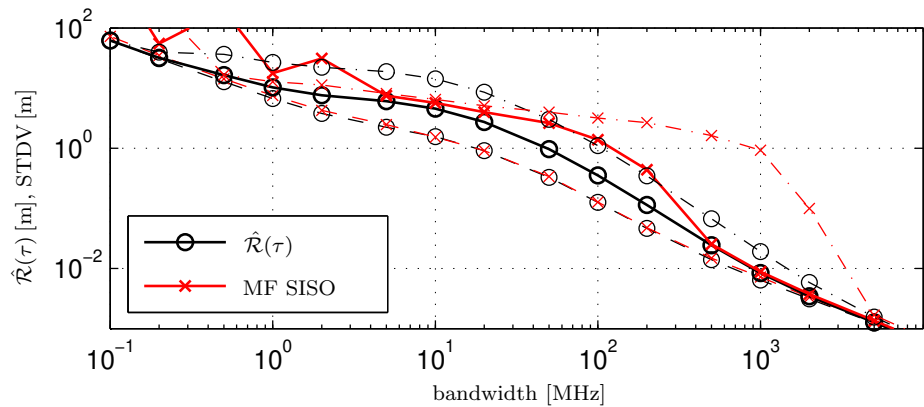
(b) Approx. REB and simulated range estimation error STDV for MF estimator

Figure 3: REB, approximated REB, and simulated range estimation error STDV for ML and MF estimator for different K_{LOS} factors (solid lines $10\,\mathrm{dB}$, dotted lines $0\,\mathrm{dB}$, and chain dotted lines $-10\,\mathrm{dB}$). Other channel parameters: $\mathrm{E}_{\mathrm{LOS}}/N_0 = 25\,\mathrm{dB}$, $\gamma_{\mathrm{dec}} = 20\,\mathrm{ns}$, $\gamma_{\mathrm{rise}} = 5\,\mathrm{ns}$.

by the same factor. Thus, in Fig. 2c the effect of different τ_{rms} is depicted. At low BW the $\widetilde{\mathrm{SINR}}$ is higher for smaller τ_{rms} since less pulse distortion occurs. At high BW, the lower τ_{rms} of the PDP, the higher the bandwidth needs to be for the same SINR and $\widetilde{\mathrm{SINR}}$.

In Fig. 3a the ranging error bound for three different K_{LOS}-factors ($10\,\mathrm{dB}$, $0\,\mathrm{dB}$, $-10\,\mathrm{dB}$) is depicted. Two different gains can be seen in Fig. 3a: An accuracy gain can be identified by looking at the REB at the same bandwidth. The higher the Rician K-factor, the lower the REB for the same bandwidth. The second gain, a detection gain, is depicted by the standard deviation (STDV) of the ranging error of a maximum likelihood (ML) estimator which uses the inverse of the covariance matrix of the DM plus AWGN random process as whitening. For a small K_{LOS} factor the estimator starts to deviate from the REB at higher bandwidth. The detection of the LOS is coupled with the SINR which reflects the SNR after the whitening operation. Hence, for higher K_{LOS} factors, the ML estimator deviates from the REB at lower BW.

In Fig. 3b the STDV of the ranging error of a "naïve" matched filter (MF)

86

estimator, which convolves the received signal with the transmitted pulse and searches for its maximum, is depicted along with the approximated values (Appendix B) for the REB. As long as the SINR is high enough, the MF estimator follows the approximation of the CRLB very well. Since the MF estimator projects the received signal onto the pulse, this estimator works in the signal space defined by the approximation for the inverse of the covariance matrix.

4 Validation

To validate the theoretical results in the previous section we performed measurements with an M-sequence correlative channel sounder by *Ilmsens*, which provides measurements over approx. the proposed UWB frequency range from 3.5 - 10.5 GHz. Out of this band we selected the desired bandwidth by filtering with a root raised cosine pulse with a pulse duration ranging from $0.25 \, \text{ns}$ to $10 \, \mu\text{s}$ with roll-off factor 0.5.

Fig. 4 shows the floorplan of the measurement scenario [7]. Measurements have been performed between an "agent" mounted on a 2D positioning table ($70 \, \text{cm}$ times $65 \, \text{cm}$ spaced by $1 \, \text{cm}$) to eight "anchors" arranged as two linear arrays spaced by $15 \, \text{cm}$. Instantaneous Rician K_{LOS} factors are shown for each measurement from the agent to Anchor 8. The K_{LOS} factor is higher in regions closer to the anchor and is on average $0.31 \, \text{dB}$. Instantaneous τ_{rms} are plotted in the lower right corner of Fig. 4 and is on average $17 \, \text{ns}$.

The covariance matrix of the dense multipath, needed for the whitening operation, has been estimated from a $2 \, \text{cm}$ spaced 5x5 grid around the current measurement by subtracting the LOS component from the received signal. The complex amplitudes $\hat{\alpha}_\ell$ of the LOS component have been estimated at the highest possible BW ($4 \, \text{GHz}$) and are used at lower BWs to subtract the LOS component. AWGN has been added to the measurements to get a desired E_{LOS}/N_0 of $25 \, \text{dB}$.

Fig. 5 shows the average values of the SINR, $\widetilde{\text{SINR}}$, γ, and $\sin^2(\phi)$ for 42 measurements. The agent positions have been placed on the grid in such a way that each measurement is used only once to minimize correlation effects between different realizations. The SINR shows the same behavior as the theory. At low BW it tends towards the K_{LOS} factor and at high BW it is bound by the E_{LOS}/N_0. The whitening gain as well as the effective SINR show similar behaviors as the theory. The synthetic data in Fig. 2a and Fig. 3a with $K_{\text{LOS}} = 0 \, \text{dB}$, $\gamma_{\text{rise}} = 5 \, \text{ns}$, and $\gamma_{\text{dec}} = 20 \, \text{ns}$ lead to a $\tau_{\text{rms}} = 17.3 \, \text{ns}$ and thus compares best to the measured data.

In Fig. 6 the REB and the STDV of the estimation error are shown for two estimators. The MF estimator works at BWs higher than $500 \, \text{MHz}$. At lower BWs a positive bias and outliers occur, which push the STDV of the MF estimator away from the theoretical bound. The ML estimator for a single-input, single-output (SISO) scenario starts to deviate from the REB at BWs below $100 \, \text{MHz}$. The accuracy gain due to proper handling of the pulse distortion is clearly visible. The synthetic data presented in Fig. 3a for comparable channel parameters (K_{LOS}, τ_{rms}) deviates at about $50 \, \text{MHz}$.

By using diversity at the anchor side, a single input, multiple output (SIMO) system can be realized. As shown in [5] additional uncorrelated measurements scale the effective SINR and the EFI linearly, thus the REB is scaled by the
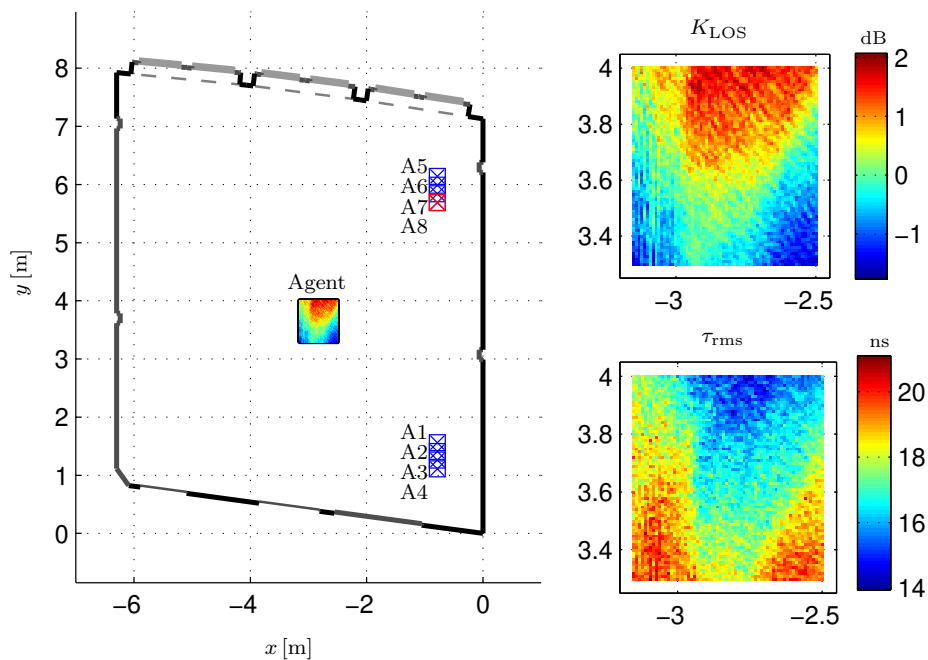
Figure 4: Floorplan of the validation scenario. Positioning of the agent has been performed with a 2D positioning table with 1 cm-spacing. Measurements have been performed from the agent to eight anchors (A1 to A8) aligned as two linear arrays with 15 cm-spacing. The plot shows the instantaneous Rician K_{LOS} factors in dB and the instantaneous rms delay spreads τ_{rms} factors in ns as a color coded map with respect to Anchor 8.
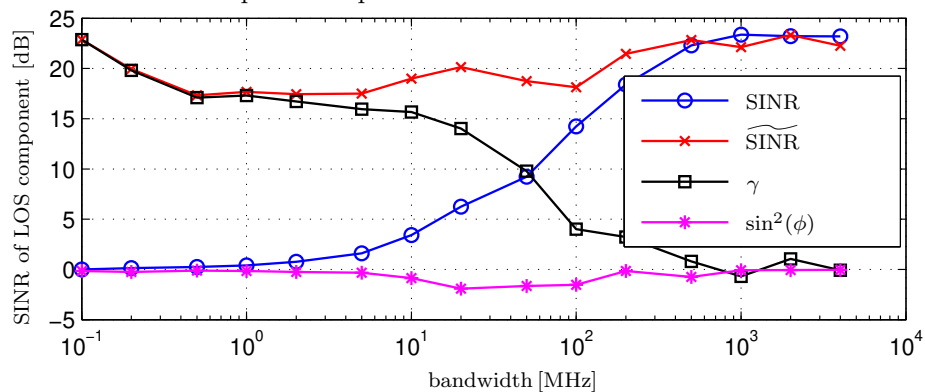
Figure 5: SINR, $\widetilde{\mathrm{SINR}}$, and whitening gain γ as a function of bandwidth for Anchor 8. Channel Parameters: $K_{\mathrm{LOS}} = 0.31\,\mathrm{dB}$, $\tau_{\mathrm{rms}} = 17.53\,\mathrm{ns}$

inverse of the square root of the number of receivers[1]. This factor of $1/2$ is seen in Fig. 6 for the 1x4-SIMO ML estimator. By additionally combining agent measurements a multiple input, multiple output (MIMO) system is obtained. Again, four measurements, have been combined to evaluate the ranging perfor-

---

[1]To obtain this diversity gain, the likelihood functions of individual measurements are added up, which corresponds to a non-coherent combining of measurements that require no phase coherence.
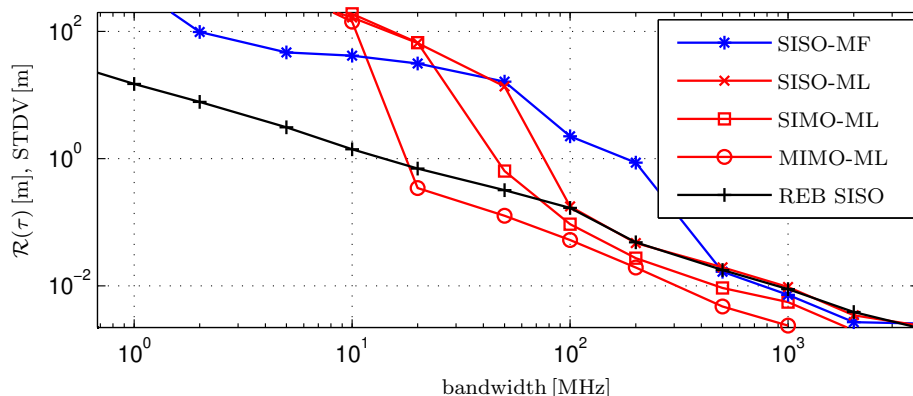
Figure 6: Ranging Error Bound and range estimation standard deviations of different estimators. Channel Parameters: $K_{\text{LOS}} = 0.31\,\text{dB}$, $\tau_{\text{rms}} = 17.53\,\text{ns}$

mance of the overall 4x4-MIMO system. The accuracy gain is another factor of 1/2 for the STDV in comparison to the 1x4-SIMO system. Furthermore, a detection gain is achieved by combining measurements. The detection of the LOS, which is coupled with the SINR is enhanced and the STDV of the estimation error follows the REB down to lower BW. With the 4x4 MIMO system a ranging STDV of 30 cm can be obtained at a BW of 20 MHz.

5 Conclusions and Outlook

The ranging error bound has been analyzed for LOS signals in dense multipath (DM), evaluating the impact of signal parameters and environmental model parameters like the K_{LOS} and τ_{rms} factor. A higher K_{LOS} and higher τ_{rms} factor of the power delay profile are preferred. The theoretical findings have been validated with real measurement data. Strong early reflections still pose a challenge for the ranging algorithm, specifically the estimation of the covariance matrix, but it is seen that diversity gain can overcome the need for ultra-wideband signals to obtain high-accuracy positions in dense multipath channels.

A Fisher Information for Delay Estimation

For a sampled received signal, the covariance matrix of AWGN and the DM is written as

$$\mathbf{C}_{\text{n}} = \sigma_{\text{n}}^2 \mathbf{I}_N + \mathbf{C}_{\text{c}} = \sigma_{\text{n}}^2 \mathbf{I}_N + \bar{\mathbf{S}}^{\text{H}} \mathbf{S}_{\nu} \bar{\mathbf{S}} \tag{A.1}$$

where $\bar{\mathbf{S}} = [\mathbf{s}_0, \cdots, \mathbf{s}_{N-1}]^{\text{T}} \in \mathbb{R}^{N \times N}$ is a signal matrix with $\mathbf{s}_i = [s((-i)T_{\text{s}}), \ldots, s((N-1-i)T_{\text{s}})]^{\text{T}}$ [4]. The elements of the covariance matrix of DM are

$$[\bar{\mathbf{S}}^{\text{H}} \mathbf{S}_{\nu} \bar{\mathbf{S}}]_{n,m} = \sum_{i=0}^{N-1} T_{\text{s}} S_{\nu}(iT_{\text{s}}) s((n-i)) s((m-i)). \tag{A.2}$$

The derivation of the EFI under non-stationary, non-white Gaussian noise, involves a whitening operation that is defined by the inverse of the covariance

89

matrix. By utilizing an eigenvector decomposition for the covariance matrix, and introducing the Fourier-weighted inner product in a Hilbert space defined by [5]

$$
\begin{aligned}
\frac{\langle \mathbf{x}, \mathbf{y} \rangle_{\mathcal{H}}}{\sigma_{\mathrm{n}}^2} &= \mathbf{y}^{\mathbf{H}} \mathbf{C}_{\mathrm{n}}^{-1} \mathbf{x} \\
&= \mathbf{y}^{\mathbf{H}} \mathbf{U} (\mathbf{\Lambda} + \sigma_{\mathrm{n}}^2 \mathbf{I}_N)^{-1} \mathbf{U}^{\mathrm{H}} \mathbf{x} \\
&= \frac{1}{\sigma_{\mathrm{n}}^2} \sum_{i=0}^{N-1} \frac{\mathbf{y}^{\mathrm{H}} \mathbf{u}_i \mathbf{u}_i^{\mathrm{H}} \mathbf{x}}{\lambda_i / \sigma_{\mathrm{n}}^2 + 1}
\end{aligned}
\tag{A.3}
$$

we can write the EFI as (cf. [5,8])

$$
\begin{aligned}
\mathcal{I}_\tau &= 2 \frac{|\alpha|^2}{\sigma_{\mathrm{n}}^2} \|\dot{\mathbf{s}}_\tau\|_{\mathcal{H}}^2 \sin^2(\phi) + \mathrm{tr}\left[\mathbf{C}_{\mathbf{n}}^{-1} \frac{\partial \mathbf{C}_{\mathbf{n}}}{\partial \tau} \mathbf{C}_{\mathbf{n}}^{-1} \frac{\partial \mathbf{C}_{\mathbf{n}}}{\partial \tau} \right] \\
&= 2 \frac{|\alpha|^2}{\sigma_{\mathrm{n}}^2} \|\dot{\mathbf{s}}_\tau\|_{\mathcal{H}}^2 \left(1 - \frac{|\langle \dot{\mathbf{s}}_\tau, \mathbf{s}_\tau \rangle_{\mathcal{H}}|^2}{\|\dot{\mathbf{s}}_\tau\|_{\mathcal{H}}^2 \|\mathbf{s}_\tau\|_{\mathcal{H}}^2} \right) + \mathrm{tr}\,[\bullet]
\end{aligned}
\tag{A.4}
$$

where the "$\mathrm{tr}\,[\bullet]$-part" is for the impact of unknown parameters of the DM process, e.g. the unknown arrival time of the DM. We argue in [5] that this part can be neglected.

Writing the SINR as

$$
\mathrm{SINR} = \frac{|\alpha|^2}{N_0} \|\mathbf{s}_\tau\|_{\mathcal{H}}^2 T_{\mathrm{s}}
\tag{A.5}
$$

the first part of (A.4 can be decomposed as in (5).

B   Approximated Inverse Covariance

Inspite of the different definitions, numeric evaluations are still needed to gain insight in the quantitative behavior of the introduced parameters. To address this issue, we introduce a decomposition of the covariance matrix into an orthonormal basis that allows the approximate numeric evaluation of the Hilbert norms. We decompose $\mathbf{C}_{\mathrm{n}}$ as

$$
\mathbf{C}_{\mathrm{n}} = [\mathbf{u}_1, \mathbf{u}_2, \mathbf{U}_0] \left[\begin{array}{cc} \begin{bmatrix} \eta & \rho \\ \rho^* & \eta' \end{bmatrix} & \mathbf{A} \\ \mathbf{A}^{\mathrm{H}} & \mathbf{\Lambda}_0 \end{array} \right] \begin{bmatrix} \mathbf{u}_1^{\mathrm{H}} \\ \mathbf{u}_2^{\mathrm{H}} \\ \mathbf{U}_0^{\mathrm{H}} \end{bmatrix}
\tag{B.1}
$$

choosing orthonormal basis vectors $\mathbf{u}_1 = \mathbf{s}_\tau / \|\mathbf{s}_\tau\|$ and $\mathbf{u}_2 = \dot{\mathbf{s}}_\tau / \|\dot{\mathbf{s}}_\tau\|$ in directions of the LOS pulse and its derivative. The coefficients η, η', and ρ describe the statistics of these two components of noise vector $\mathbf{n}$. They are computed from $\mathbf{C}_{\mathrm{n}}$, e.g. $\rho = \mathbf{u}_1^{\mathrm{H}} \mathbf{C}_{\mathrm{n}} \mathbf{u}_2$. Matrix $\mathbf{A}$ expresses the correlation of the noise in these two directions and the other coordinate axes (in $\mathbf{U}_0$).

Using the Schur complement and assuming that the correlations $\mathbf{A}$ are negligible, the inverse of $\mathbf{C}_{\mathrm{n}}$ is written as

$$
\mathbf{C}_{\mathrm{n}}^{-1} \approx [\mathbf{u}_1, \mathbf{u}_2, \mathbf{U}_0]
\tag{B.2}
$$
$$
\times \left[\begin{array}{cc} \begin{bmatrix} \eta' & -\rho \\ -\rho^* & \eta \end{bmatrix} \frac{1}{\eta\eta' - |\rho|^2} & \mathbf{X} \\ \mathbf{X}^{\mathrm{H}} & \mathbf{Z} \end{array} \right] \begin{bmatrix} \mathbf{u}_1^{\mathrm{H}} \\ \mathbf{u}_2^{\mathrm{H}} \\ \mathbf{U}_0^{\mathrm{H}} \end{bmatrix} .
$$

90

Using this approximation, it is straightforward to compute approximated values for the parameters defined in Appendix A. From (A.4), we obtain

$$\mathcal{I}_\tau^{(\mathrm{I})} \approx 2 \underbrace{\frac{\|\dot{\mathbf{s}}_\tau\|^2}{\|\mathbf{s}_\tau\|^2}}_{4\pi^2\beta^2} \underbrace{\frac{\eta}{\eta'}}_{\approx\gamma} \underbrace{\frac{|\alpha|^2\|\mathbf{s}_\tau\|^2\eta'}{\eta\eta' - |\rho|^2}}_{\approx\mathrm{SINR}} \underbrace{\left(1 - \frac{|\rho|^2}{\eta\eta'}\right)}_{\approx\sin^2(\phi)}. \tag{B.3}$$

From this, the SINR (A.5) times $\sin^2(\phi)$ can be written as

$$\sin^2(\phi)\mathrm{SINR} \approx |\alpha|^2\|\mathbf{s}_\tau\|^2 \frac{1}{\eta}$$

$$= |\alpha|^2 \frac{1}{N_0 + \sum_{i=0}^{N-1}[\boldsymbol{\varrho}_\mathbf{s}]_i^2 S_\nu(iT_\mathrm{s})T_\mathrm{s}}$$

where $\boldsymbol{\varrho}_\mathbf{s} = \bar{\mathbf{S}}\mathbf{s}_\tau T_\mathrm{s}$ is the autocorrelation sequence of waveform $s(t)$, whose norm is independent of T_s. This results shows that the interference power scales according to the inner product of the squared pulse ACF $\varrho^2(t)$ and the PDP $S_\nu(t)$. I.e., the greater the bandwidth, the better is the DM separated from the LOS component and the SINR converges towards the SNR. Using the results from (B.3), the effective SINR can be approximated by

$$\widetilde{\mathrm{SINR}} \approx |\alpha|^2\|\mathbf{s}_\tau\|^2 \frac{1}{\eta'} \tag{B.4}$$

References

[1] Y. Shen, S. Mazuelas, and M. Z. Win, "Network Navigation: Theory and Interpretation," *Selected Areas in Communications, IEEE Journal on*, vol. 30, no. 9, pp. 1823–1834, Oct. 2012.

[2] H. Godrich, A. Haimovich, and R. Blum, "Target Localization Accuracy Gain in MIMO Radar-Based Systems," *IEEE Trans. Inf. Theory*, vol. 56, no. 6, pp. 2783 –2803, June 2010.

[3] D. Dardari, A. Conti, U. Ferner, A. Giorgetti, and M. Z. Win, "Ranging With Ultrawide Bandwidth Signals in Multipath Environments," *Proc. IEEE*, vol. 97, no. 2, pp. 404–426, Feb. 2009.

[4] E. Leitinger, P. Meissner, C. Ruedisser, G. Dumphart, and K. Witrisal, "Evaluation of Position-related Information in Multipath Components for Indoor Positioning," *IEEE J. Sel. Areas Commun.*, vol. 33, no. 11, pp. 2313 – 2328, Nov. 2015.

[5] K. Witrisal, E. Leitinger, S. Hinteregger, and P. Meissner, "Bandwidth Scaling and Diversity Gain for Ranging and Positioning in Dense Multipath Channels," *Wireless Communications Letters, IEEE*, 2016.

[6] J. Karedal, S. Wyne, P. Almers, F. Tufvesson, and A. F. Molisch, "A Measurement-Based Statistical Model for Industrial Ultra-Wideband Channels," *IEEE Transactions on Wireless Communications*, 2007.

[7] P. Meissner, "Multipath-Assisted Indoor Positioning," Ph.D. dissertation, Graz University of Technology, 2014.

[8] S. Kay, *Fundamentals of Statistical Signal Processing: Estimation Theory.* Prentice Hall Signal Processing Series, 1993.

92

MIMO Gain and Bandwidth Scaling for RFID Positioning in Dense Multipath Channels

Stefan Hinteregger, Erik Leitinger, Paul Meissner, and Klaus Witrisal

Abstract

This paper analyzes the achievable ranging and positioning performance for two design constraints in a radio frequency identification (RFID) system: (*i*) the bandwidth of the transmit signal and (*ii*) the use of multiple antennas at the readers. The ranging performance is developed for correlated and uncorrelated constituent channels by utilizing a geometry-based stochastic channel model for the downlink and the uplink. The ranging error bound is utilized to compute the precision gain for a ranging scenario with multiple collocated transmit and receive antennas. The position error bound is then split into a monostatic and bistatic component to analyze the positioning performance in a multiple input, multiple output (MIMO) RFID system. Simulation results indicate that the ranging variance is approximately halved when utilizing uncorrelated constituent channels in a monostatic setup. It is shown that both the bandwidth and the number of antennas decrease the error variance roughly quadratically.

1   Introduction

RFID tags have penetrated every corner of our lifes, but are paramount in supply chain management and logistics. One major detriment of passive RFID technology is its unsatisfying localization capability. In numerous applications like sorting of goods, intelligent warehouses, flexible production, etc., a sub-meter or even sub-decimetre positioning would be needed.

A trend towards signals with higher bandwidth has been established, for both active and passive RFID tags, to achieve higher accuracy for localization purposes [1]. Dardari and coworkers have focused on ultrawide-bandwidth (UWB) tags with the capability to scatter back a spreading sequence for CDMA [2], while others have only adapted the readers and used existing tags for radar like scenarios (e.g. [3]).

Several researchers have analyzed performance bounds for ranging and positioning with ultra-wideband (UWB) radio signals [4,5]. In UWB settings, the channel is often modeled as a combination of specular reflections and so-called dense or diffuse multipath (DM) which comprises all other "energy producing" components [6] that cannot be resolved by the measurement aperture. By decreasing the bandwidth and thus going from UWB to conventional wideband radio signals the specular reflections cannot be isolated from the line-of-sight (LOS) component anymore, leading to a pulse distortion and fading effect. In [7] we analysed the ranging and positioning error bound for these conventional wideband radio signals in DM scenarios.

Besides using higher bandwidth, another way to increase the performance is to use multiple input, multiple output (MIMO) systems. For passive RFID tags the use of multiple antennas at the transmitter, tag and receiver have been analyzed with respect to the received power and bit error rate [8–11]. For ranging/positioning a MIMO-radar system can be employed using the geometric spread of the sensors and narrowband signals [12]. For classical outdoor radar applications the received signal consists of the backscattered LOS signal and additive white Gaussian noise (AWGN). Due to the previously introduced channel model the signal model for RFID radar systems operating indoors needs to be adapted leading to severe fading and distortions.

The main contributions of this paper are the following:

- We develop the ranging error variance for correlated and uncorrelated backscatter channels.

- We characterize the achievable ranging gain for multiple antennas in a monostatic setup.

- We discuss the position error bound for several readers leading to a MIMO RFID system.

The rest of this paper is organized as follows. Section 2 defines the system and signal model, which is used in Secton 3 to develop the ranging error variance for correlated and uncorrelated channels. Section 4 re-visits the relation between the range and the position estimation errors and demonstrates how diversity combining can be expressed in terms of monostatic and bistatic accuracy gains. Section 5 draws conclusions and presents an outlook.

94
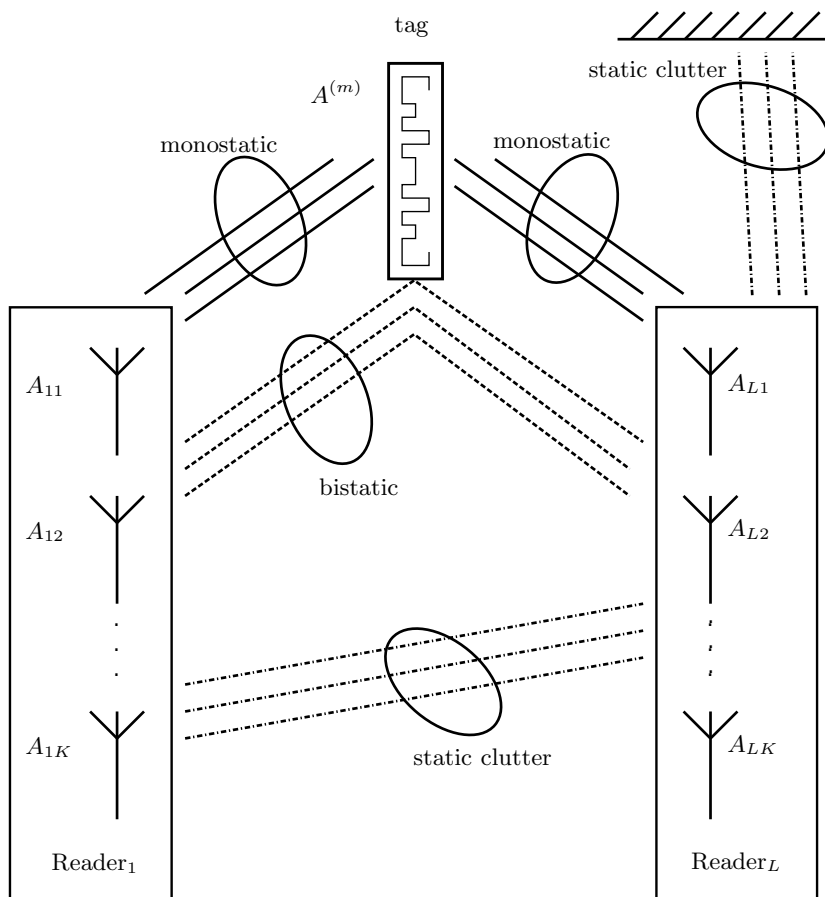
Figure 1: System Model of the MIMO RFID setup including monostatic, bistatic and multistatic scenarios

2 System and Channel Model

2.1 System Model

We consider L radio frequency identification (RFID) readers operating indoors at known positions $\mathbf{p}_\ell, \forall \ell \in \{1, \ldots, L\}$. Each reader consists of K closely-spaced antennas that can all be used to transmit and receive wideband signals (K TRX per reader). The signal $s(t)$ denotes the baseband equivalent transmit signal. The M RFID tags placed within the room at unknown positions $\mathbf{p}^{(m)}, \forall m \in \{1, \ldots, M\}$ scatter back the signal to the readers which in turn receive this signal. The according multiple input multiple output (MIMO) system model is depicted in Fig. 1.

The solid lines in Fig. 1 characterize monostatic links connecting antennas from reader ℓ via the tag with itself. Each monostatic link consists of two constituent channels, the downlink from one reader antenna $A_{\ell k}$ to the tag antenna $A^{(m)}$ and the uplink from the tag antenna $A^{(m)}$ back to the same reader but not necessarily the same antenna $A_{\ell k'}$. As we will see in Section 2.3 these channels

can be modelled as correlated or uncorrelated.

The dashed lines in Fig. 1 represent bistatic links connecting antennas from two different readers, $A_{\ell k}$ and $A_{\ell' k'}$, via the tag antenna $A^{(m)}$. Since the different readers are placed at different positions in the room, these channels will be modelled uncorrelated.

The dashed dotted lines in Fig. 1 depict static clutter that can be canceled from the received signal depending on the employed signaling scheme (cf. [3,13, 14]).

2.2 Channel Model

Each individual baseband radio channel between any reader antenna $A_{\ell k}$ and a tag antenna $A^{(m)}$ is modeled by a hybrid deterministic-stochastic channel model [15]

$$h_{\ell k}^{(m)}(\tau) = \alpha_{\ell k}^{(m)} \delta(\tau - \tau_{\ell k}^{(m)}) + \nu_{\ell k}^{(m)}(\tau), \tag{1}$$

where $\alpha_{\ell k}^{(m)}$ describes the complex amplitude of the deterministic line-of-sight (LOS) component with delay $\tau_{\ell k}^{(m)} = \frac{1}{c} \|\mathbf{p}^{(m)} - \mathbf{p}_{\ell k}\|$, with c as the speed of light. The second term on the right hand side in (1) denotes the dense multipath (DM) which models all other multipath components. This DM is modeled as a zero-mean complex Gaussian random process. We assume uncorrelated scattering (US) [16,17] along the delay axis τ for the DM process which means that the autocorrelation (ACF) of the DM is given as

$$K_\nu(\tau, u) = \mathbb{E}\left\{ \nu_{\ell k}^{(m)}(\tau) \nu_{\ell k}^{(m)}(u)^* \right\}$$
$$= S_{\nu,\ell k}^{(m)}(\tau - \tau_{\ell k}^{(m)}) \delta(\tau - u). \tag{2}$$

The power delay profile (PDP) $S_{\nu,\ell k}^{(m)}(\tau - \tau_{\ell k}^{(m)})$ is zero for $\tau < \tau_{\ell k}^{(m)}$ implying that the DM does not exist until the LOS component excites the channel. We also assume quasi-stationarity in the spatial domain, meaning that for one reader-tag configuration, the PDP does not change noticeably in the vicinity of the tag [18].

The following derivation of the backscatter channel model does not restrict the usage to a certain model for the PDP; different choices for the PDP could be an exponentially decreasing PDP or a double exponential PDP [19]. For easier readability only one tag is considered in the following, thus the tag index m will be dropped. This does not limit the system model since various multiple access schemes can be employed to handle multiple tags and to separate the signals from different readers [3,13,14].

2.3 Backscatter Channel Model

One backscatter channel is formed by concatenation of the respective uplink channel $h_{\ell k}$ with a downlink channel $h_{\ell' k'}$. This pinhole channel can be modelled by the convolution of the two constituent channels as

$$\begin{aligned} h_{\ell k, \ell' k'} &= (h_{\ell k} * h_{\ell' k'})(\tau) \\ &= \alpha_{\ell k} \alpha_{\ell' k'} \delta(\tau - \tau_{\ell k} - \tau_{\ell' k'}) \\ &\quad + \alpha_{\ell k} \nu_{\ell' k'}(\tau - \tau_{\ell k}) + \alpha_{\ell' k'} \nu_{\ell k}(\tau - \tau_{\ell' k'}) + \nu_{\ell k}(\tau) * \nu_{\ell' k'}(\tau). \end{aligned} \tag{3}$$

96

The first term in (3) shows the deterministic part of the backscatter channel. The second and third terms are the convolution of the DM of the downlink channel with the deterministic part of the uplink channel, and vice versa. Finally, the fourth term is the convolution of the two DM processes of the individual radio channels. By combining the last three terms in (3) to $\nu_{\ell k,\ell' k'}(\tau)$, the backscatter channel can be decomposed into a deterministic and a stochastic part resulting in a similar structure as for the individual channel in (1). The model in (3) assumes constant backscattering of the tag over the whole used bandwidth. This assumption does certainly not hold true for the UWB case, but the smaller the bandwidth gets, the less frequency dependent the radar cross section of a tag gets [20, 21].

Using the quasi-stationarity and the US assumption, the PDP of the backscatter channel is the second central moment of the DM process. Since the DM is described by a zero-mean Gaussian process, first and second moment give a complete description of the random process. In [22] the US assumption has been proven for a backscatter channel consisting of two US channels. Using $\nu_{\ell k,\ell' k'}(\tau)$ as the sum of the last three terms in (3), the PDP of the BS channel for two uncorrelated channels is [23]

$$
\begin{aligned}
S_{\nu,\ell k,\ell' k'}(\tau) &= \mathbb{E}\left\{\nu_{\ell k,\ell' k'}(\tau)\nu^*_{\ell k,\ell' k'}(\tau)\right\} \\
&= |\alpha_{\ell k}|^2 S_{\nu,\ell' k'}(\tau - \tau_{\ell k}) + |\alpha_{\ell' k'}|^2 S_{\nu,\ell k}(\tau - \tau_{\ell' k'}) \\
&\quad + S_{\nu,\ell k}(\tau) * S_{\nu,\ell' k'}(\tau).
\end{aligned}
\tag{4}
$$

For two fully correlated constituent channels, e.g. the downlink and the uplink are the same, the PDP is [22]

$$
\begin{aligned}
S_{\nu,\ell k,\ell k}(\tau) &= \mathbb{E}\left\{\nu_{\ell k,\ell k}(\tau)\nu^*_{\ell k,\ell k}(\tau)\right\} \\
&= 4|\alpha_{\ell k}|^2 S_{\nu,\ell k}(\tau - \tau_{\ell k}) + 2S_{\nu,\ell k}(\tau) * S_{\nu,\ell k}(\tau).
\end{aligned}
\tag{5}
$$

The power in the non-line-of-sight (NLOS) components is thus twice as high for fully correlated channels as for uncorrelated constituent channels. In comparison the power in the LOS component is the same for correlated and uncorrelated constituent channels.

2.4 Received Signal

RFID reader ℓ transmits a baseband pulse $s(t)$ via anntena k and the downlink channel $h_{\ell k}(\tau)$ to the tag. Assuming perfect backscattering by the tag, the signal is then fed via the uplink channel $h_{\ell' k'}(\tau)$ and antenna k' to RFID reader ℓ'. The received signal is given as

$$
\begin{aligned}
r(t) &= s(t) * h_{\ell k,\ell' k'}(t) + \omega(t) \\
&= \alpha_{\ell k}\alpha_{\ell' k'} s(t - \tau_{\ell k} - \tau_{\ell' k'}) + s(t) * \nu_{\ell k,\ell' k'}(t) + \omega(t),
\end{aligned}
\tag{6}
$$

where $\omega(t)$ is additive white Gaussian noise (AWGN) with a two-sided power spectral density of $N_0/2$.

3 Ranging Error Bound and Performance Gain

In [7] we derived the ranging error bound for dense multipath channels which is the inverse of the square root of the equivalent Fisher information (EFI) for
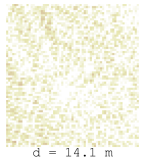
the delay estimation problem

$$\mathcal{R}(\tau) = \sqrt{\mathcal{I}_\tau^{-1}}. \tag{7}$$

The EFI for an AWGN channel (neglecting multipath) is well known [24] and can be presented in a canonical form as

$$\mathcal{I}_{\tau,\ell k,\ell'k'}^{\mathrm{AWGN}} = 8\pi^2\beta^2\mathrm{SNR}_{\ell k,\ell'k'} \tag{8}$$

where $\beta^2 = \frac{\|\dot{\mathbf{s}}_\tau\|^2}{(4\pi^2\|\mathbf{s}_\tau\|^2)} = \frac{\int_f f^2|S(f)|^2\mathrm{d}f}{\int_f |S(f)|^2\mathrm{d}f}$ is the effective (mean square) bandwidth of the (energy-normalized) transmit pulse $s(t) \overset{\mathcal{F}}{\longleftrightarrow} S(f)$, $\mathbf{s}_\tau$ is the sampled transmit pulse shifted to $\tau = \tau_{\ell k} + \tau_{\ell'k'}$, $\dot{\mathbf{s}}_\tau$ is its derivative, and $\mathrm{SNR}_{\ell k,\ell'k'} = \frac{|\alpha_{\ell k}\alpha_{\ell'k'}|^2}{N_0}\|\mathbf{s}_\tau\|^2 T_s$ is the signal to noise ratio with $T_\mathrm{s} = 1/f_\mathrm{s}$, f_s being the sampling frequency.

Adding the Gaussian DM, the EFI can be presented for a single backscatter channel in a canonical form as [4]

$$\mathcal{I}_{\tau,\ell k,\ell'k'} = 8\pi^2\beta^2\gamma\mathrm{SINR}_{\ell k,\ell'k'} \tag{9}$$

$$= 8\pi^2\beta^2\widetilde{\mathrm{SINR}}_{\ell k,\ell'k'}, \tag{10}$$

where SINR is the signal-to-interference-plus-noise ratio (SINR) of the LOS component, and γ is the so-called whitening gain. The product of β^2, SINR, and γ thus provides the amount of information transmitted in the LOS component when influenced by DM and AWGN. For the derivation of (9), the inverse of the covariance matrix of DM plus AWGN is needed as a whitening operator. The SINR and the whitening gain γ are also combined in the effective SINR, $\widetilde{\mathrm{SINR}}$ which can be expressed as (see the appendix)

$$\widetilde{\mathrm{SINR}}_{\ell k,\ell'k'} = \frac{|\alpha_{\ell k}\alpha_{\ell'k'}|^2}{N_0}\|\mathbf{s}_\tau\|^2 T_s \frac{\|\dot{\mathbf{s}}_\tau\|_{\mathcal{H}}^2}{\|\dot{\mathbf{s}}_\tau\|^2}\sin^2(\phi), \tag{11}$$

where $\|\cdot\|_{\mathcal{H}}^2$ denotes the weighted squared norm in a Hilbert space defined by the covariance $\mathbf{C}_\mathrm{n}/\sigma_\mathrm{n}^2$ (see the appendix), and ϕ is the angle between $\mathbf{s}_\tau$ and its derivative $\dot{\mathbf{s}}_\tau$ in this Hilbert space.

In Fig. 2 the SINR, $\widetilde{\mathrm{SINR}}$, and γ are shown for a monostatic setup for fully correlated and for uncorrelated constituent channels with solid and dashed lines respectively over a wide range of bandwidths (BW). The necessary distance between the downlink and uplink of the backscatter channel to be (at least partially) uncorrelated is characterized by the correlation distance which is defined as the distance at which the correlation of two channel impulse responses drops below a given value (e.g. 50 %). For uniformly distributed angle-of-arrivals the correlation distance is in the order of the wavelength λ [25]. The SINR is bound for high BW by the signal to noise ratio (SNR) and for low BW by the Rician K-factor of the backscatter channel.[1] For high bandwidths the effective SINR is also bound by the SNR, while for low bandwidths the $\widetilde{\mathrm{SINR}}$ achieves the SNR as well. The effective SINR is in fact a measure of the pulse distortion rather than the fading of the LOS component [7].

---

[1] For Fig. 2 the K_{LOS} factor for the constituent channels are chosen such that the backscatter channel has an overall K_{LOS} of 1 [22].

98
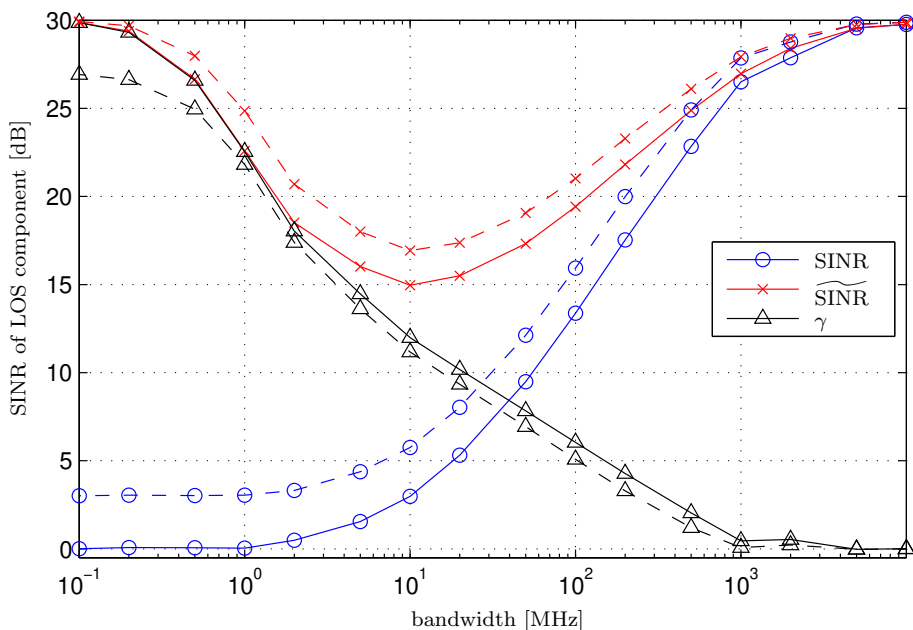
Figure 2: SINR, $\widetilde{\mathrm{SINR}}$, and whitening gain γ for a monostatic setup with correlated (solid line) and uncorrelated (dashed line) constituent channels. Constituent Channel Parameters: $K_{\mathrm{LOS}} = 6.4\,\mathrm{dB}$, $\gamma_{\mathrm{rise}} = 5\,\mathrm{ns}$, $\gamma_{\mathrm{dec}} = 20\,\mathrm{ns}$, $E_{\mathrm{LOS}}/N_0 = 30\,\mathrm{dB}$

The REB decreases linearly with the effective bandwidth in conformity with (10). According to Fig. 2 the effective SINR increases from about $10\,\mathrm{MHz}$ also with increasing bandwidth; thus the REB decreases slightly more than linearly with the bandwidth.

The gain in SINR achieved by using two closely-spaced antennas with un-correlated constituent channels in a monostatic setup is $3\,\mathrm{dB}$ for low BW and gets $0\,\mathrm{dB}$ for high BW, where the whitening gain is already negligible, since the LOS component is isolated from the DM and the channel is AWGN dominated. The gain for $\widetilde{\mathrm{SINR}}$ is highest in the medium BW region where the most pulse disortion occurs and is about $2\,\mathrm{dB}$. This gain for SINR and $\widetilde{\mathrm{SINR}}$ for uncorre-lated channels is explained by the additional power in the DM process according to Section 2.3.

Looking at a 1-dimensional positioning scenario, e.g. positioning on a con-veyor belt, where only ranging is needed, the EFI from (10) can be extended for one RFID reader with K antennas as

$$\mathcal{I}_{\tau,\ell K} = 8\pi^2\beta^2 \sum_{k=1}^{K} \sum_{k'=k}^{K} \widetilde{\mathrm{SINR}}_{\ell k, \ell k'}. \tag{12}$$

This equation holds for antenna arrays which are closely spaced with respect to the distance between the tag and the center point of the array. The second sum in (12) only indexes $K-k+1$ terms, since the channel from k to k' and the reverse channel from k' to k are the same (reciprocity) thus no new observation

99
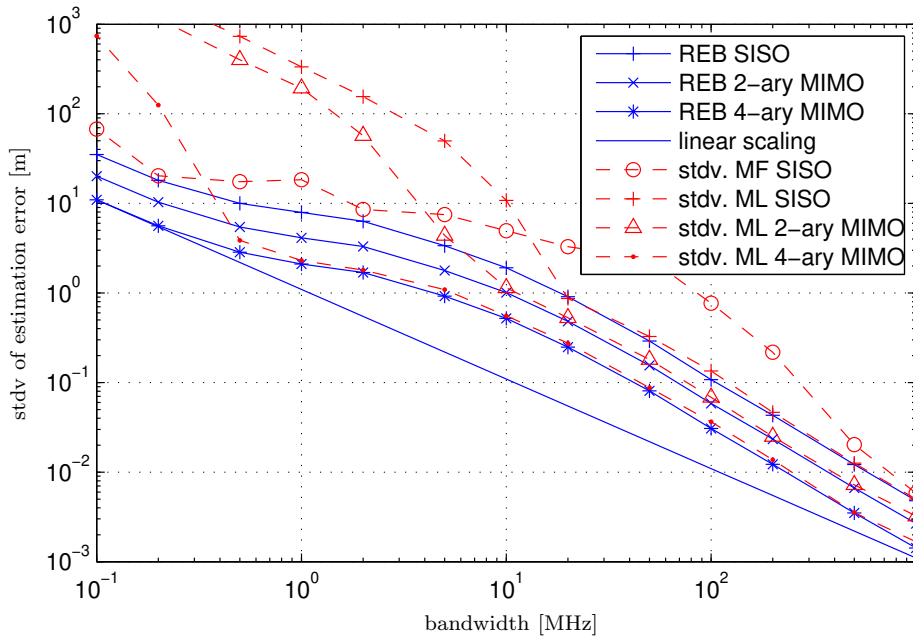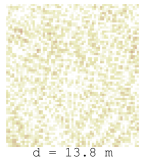
Figure 3: Ranging Error Bound for monostatic setup, 2-Array reader, 4-Array reader and standard deviations for different estimators. Constituent Channel Parameters: $K_{\text{LOS}} = 6.4\,\text{dB}$, $\gamma_{\text{rise}} = 5\,\text{ns}$, $\gamma_{\text{dec}} = 20\,\text{ns}$, $E_{\text{LOS}}/N_0 = 30\,\text{dB}$

of the DM process is obtained.

For an antenna array with K antennas, K fully correlated and $\sum_{k=1}^{K-1} k = \frac{K(K-1)}{2}$ uncorrelated backscatter channels are available, leading to a total effective SINR of

$$\begin{aligned}
\widetilde{\text{SINR}}_{\text{total}} &= K\widetilde{\text{SINR}}_{\ell k,\ell k} + \frac{K(K-1)}{2}\widetilde{\text{SINR}}_{\ell k,\ell k'} \\
&= \left(K + g_{\text{uncorr}}\frac{K(K-1)}{2} \right) \widetilde{\text{SINR}}_{\ell k,\ell k} \\
&\approx K^2\widetilde{\text{SINR}}_{\ell k,\ell k},
\end{aligned} \tag{13}$$

where g_{uncorr} is the gain in $\widetilde{\text{SINR}}$ for an uncorrelated versus a correlated measurement and is approximated as 2 for the final approximation.

In Fig. 3 the REB is depicted for different reader arrays. The gain due to the twofold antenna array and 4-ary antenna array is shown by the REB. From (12) and Fig. 3 it is clear that the REB scales slightly more than linearly with the bandwidth. According to (13) the number of antennas also scales the REB linearly. However, the gain for using uncorrelated constituent channels is smaller than 2, thus the gain for using additional antennas is smaller than for increasing the bandwidth.

By simulating a ranging scenario with one RFID reader with K antennas the REB can be evaluated. For the following simulations, a double exponential PDP is used to model the NLOS contributions by the DM process [19]. For ranging two different estimators are used, a classical matched filter (MF) and a

100

maximum likelihood (ML) estimator. The accuracy gain due to the whitening operation used for the ML estimator is especially noticeable for BW between 50 and 500 MHz. The better performance of the MF estimator at low BW can be explained by the fact, that the complete DM interferes with the LOS, thus the MF uses the power in the DM also for ranging. The ML estimator, in contrast, will suppress the DM process due to the whitening filter.

The accuracy gain for the K-ary array is also shown by the standard deviations of the estimator errors. Furthermore, a detection gain can be identified when inspecting the curves for the ML estimator for SISO and MIMO processing. The ML estimator achieves the REB at lower bandwidths since the detection of the LOS is enhanced, similarily as the bit error rate is decreased for MIMO processing in communication systems. While the detection gain is impressive at bandwidth below 10 MHz the limit for useable indoor positioning, assuming a ranging accuracy in the submeter range, is roughly in the range from 20 to 100 MHz.

4   Positioning Error Bound and Performance Gain

The position error bound (PEB) is the square root of the trace of the inverse EFI matrix (EFIM) on the position estimation error

$$\mathcal{P}\{\mathbf{p}\} = \sqrt{\text{tr}\{\boldsymbol{\mathcal{I}_p}^{-1}\}} \leq \sqrt{\mathbb{E}\left\{\|\mathbf{p} - \hat{\mathbf{p}}\|^2\right\}} \tag{14}$$

and can be computed from the EFI for the delay estimation with the chain rule as [4, 5]

$$\begin{aligned}
\boldsymbol{\mathcal{I}_p} = &\sum_{\ell=1}^{L}\sum_{k=1}^{K}\sum_{k'=k}^{K} \mathcal{I}_{\tau,\ell k,\ell k'}\mathbf{h}_{\ell k,\ell k'}\mathbf{h}_{\ell k,\ell k'}^{\mathbf{T}} \\
&+ \sum_{\ell=1}^{L-1}\sum_{\ell'=\ell+1}^{L}\sum_{k=1}^{K}\sum_{k'=1}^{K} \mathcal{I}_{\tau,\ell k,\ell' k'}\mathbf{h}_{\ell k,\ell' k'}\mathbf{h}_{\ell k,\ell' k'}^{\mathbf{T}},
\end{aligned} \tag{15}$$

where the first term accounts for the monostatic channels between an RFID reader with itself, and the second term relates to the bistatic channels between two different readers leading to a multistatic scenario (cf. Fig. 1). The geometry of the setup is expressed by $\mathbf{h}_{\ell k,\ell' k'}$ as (cf. [4, 5, 12])

$$\mathbf{h}_{\ell k,\ell' k'}^{(m)} = \frac{1}{c}(\mathbf{e}_{\ell k}^{(m)} + \mathbf{e}_{\ell' k'}^{(m)}), \tag{16}$$

where we included the index of the tag for completeness and $\mathbf{e}_{\ell k}^{(m)}$ is a unit vector in the direction between the m-th tag and the k-th antenna of the ℓ-th reader. Using the approximation that for closely spaced antennas the unit vector $\mathbf{e}_{\ell k}^{(m)} \approx \mathbf{e}_{\ell k'}^{(m)}, \forall k, k'$ and introducing $\mathbf{h}_{\ell,\ell'}$ for $\mathbf{h}_{\ell k,\ell' k'}^{(m)}$, (15) can be written with (13) as

$$\begin{aligned}
\boldsymbol{\mathcal{I}_p} \approx &\, 8\pi^2\beta^2 K^2 \sum_{\ell=1}^{L} \widetilde{\text{SINR}}_{\ell,\ell}\mathbf{h}_{\ell,\ell}\mathbf{h}_{\ell,\ell}^{\mathbf{T}} \\
&+ 8\pi^2\beta^2 K^2 \sum_{\ell=1}^{L-1}\sum_{\ell'=\ell+1}^{L} \widetilde{\text{SINR}}_{\ell,\ell'}\mathbf{h}_{\ell,\ell'}\mathbf{h}_{\ell,\ell'}^{\mathbf{T}}.
\end{aligned} \tag{17}$$

101
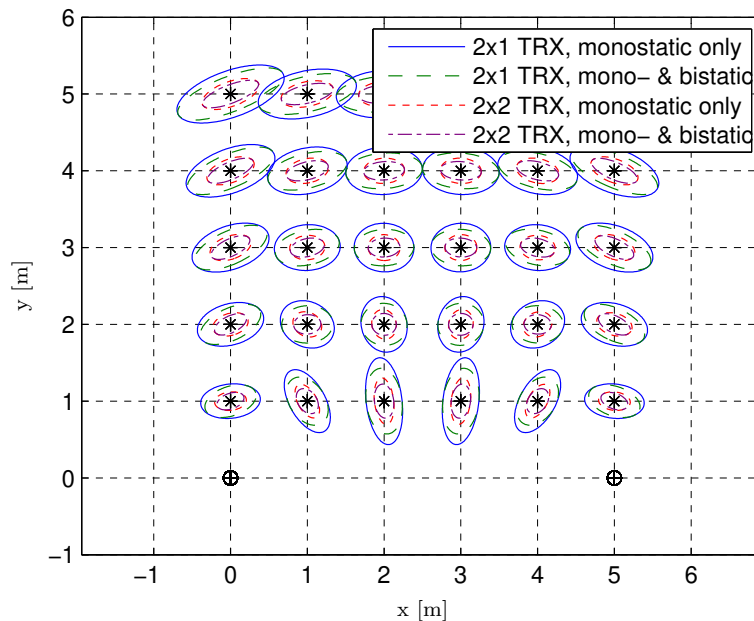
Figure 4: 2-fold standard deviation ellipses for a bandwidth of 50 MHz and different MIMO constellations. Constituent Channel Parameters: distance dependent K_{LOS} [22], $\gamma_{\mathrm{rise}} = 5\,\mathrm{ns}$, $\gamma_{\mathrm{dec}} = 20\,\mathrm{ns}$, $E_{\mathrm{LOS}}/N_0 = 30\,\mathrm{dB}$

By increasing the number of antennas per reader, the EFIM for the position error scales with the square of the number of antennas K in both the monostatic directions and the bistatic directions. Thus the PEB decreases linearly with respect to the number of antennas in the directions defined by $\mathbf{h}_{\ell,\ell}^{(m)}$ and $\mathbf{h}_{\ell,\ell'}^{(m)}$. Furthermore, by increasing the number of readers, the gain in monostatic directions is achieved L-times, while the gain in bistatic directions is applied $\frac{L(L-1)}{2}$-times.

In Fig. 4 the 2-fold standard deviation ellipses are depicted for different tag positions in a half plane. These ellipses can be computed from the inverse of the position EFIM $\boldsymbol{\mathcal{I}_\mathbf{p}}$. One RFID reader is positioned at $[0\ 0]^{\mathbf{T}}$ and another reader at $[5\ 0]^{\mathbf{T}}$. These readers are either equipped with one or two TRX, depending on the scenario. The first two scenarios (2x1TRX monostatic only, and 2x1TRX mono- and bistatic) use one TRX, while the latter two scenarios (2x2TRX monostatic only, and 2x2TRX mono- and bistatic) use two TRX at each reader. For the first and third scenario, no time synchronisation is needed between the RFID readers, since only backscatter channels are used that originate and end at the same reader.

Within these scenarios, the influence of the geometry is clearly visible. According to (16) monostatic measurements (Scenarios 1 and 3) add information only in the radial directions, corresponding to circles around the readers. Bistatic measurements (between two different readers) add information mainly in the orthogonal axis, which corresponds to the normal direction of an ellipse with the two readers in its foci. In Fig. 4 this directional information gain is

102
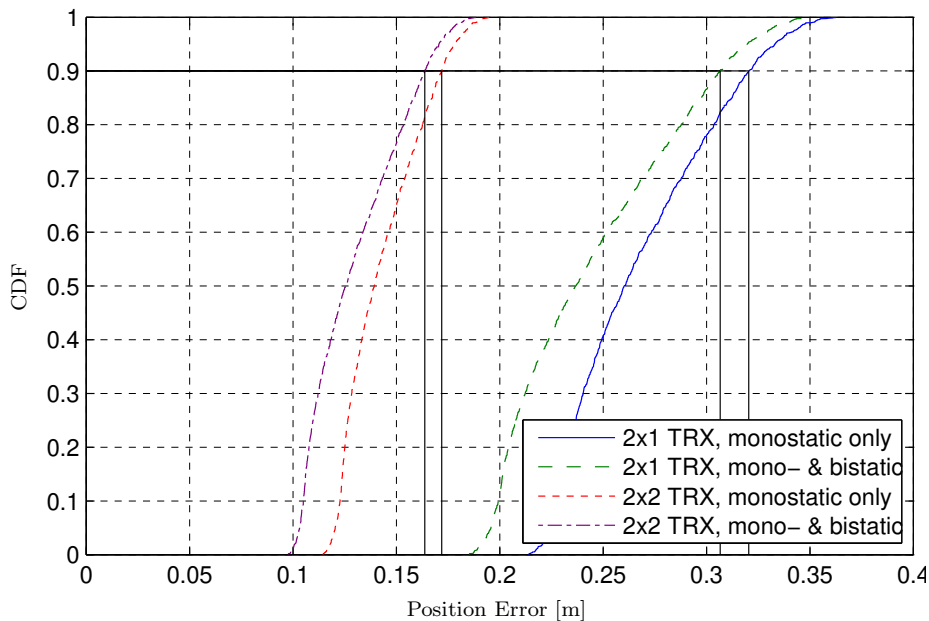
Figure 5: Cumulative Distribution Function of the Position Error Bound for a bandwidth of 50 MHz for a 10 cm spacing in a half plane and different MIMO constellations. Constituent Channel Parameters: distance dependent K_{LOS} [22], $\gamma_{\mathrm{rise}} = 5\,\mathrm{ns}$, $\gamma_{\mathrm{dec}} = 20\,\mathrm{ns}$, $E_{\mathrm{LOS}}/N_0 = 30\,\mathrm{dB}$

well visible since the ellipses for the mono- and bistatic scenarios are tangent to the monostatic scenarios in one direction, while an information gain is seen for the orthogonal direction.

By comparing the ellipses for Scenarios 1 and 2 with the Scenarios 3 and 4, respectively, the accuracy gain for additional antennas can be seen. The ellipses for Scenarios 3 and 4 have the same orientations as for Scenarios 1 and 2, and are K-times smaller.

To evaluate the overall potential positioning performance in the half plane, the PEB is displayed in Fig. 5 for a 10 cm spacing over the half plane. The gain by adding an additional antenna is about a factor of two like described by (17).

5   Conclusions and Outlook

The MIMO gain and bandwidth scaling have been analyzed for RFID positioning in dense multipath scenarios. The error standard deviation for additional antennas scales roughly linearly with respect to a single monostatic link. Increasing the bandwidth scales the standard deviation of each measurement slightly more than linearly, leading to a higher gain. Furthermore, additional antennas also show a detection gain enabling the usage of lower bandwidths. The next steps are to validate these findings by measurements and develop algorithms which are able to employ the theoretical findings.

A   Fisher Information for Delay Estimation

The EFI is defined as the second moment of the partial derivative of the log-likelihood function [24]. By sampling the received signal in (6) the likelihood function conditioned on the parameter vector $\boldsymbol{\psi} = [\tau, \Re\alpha, \Im\alpha]$ is defined as

$$f(\mathbf{r}|\boldsymbol{\psi}) \propto \exp\left\{-(\mathbf{r} - \mathbf{s}_\tau\alpha)^{\mathrm{H}}\mathbf{C}_{\mathrm{n}}^{-1}(\mathbf{r} - \mathbf{s}_\tau\alpha)\right\} \tag{A.1}$$

where the covariance matrix of DM and AWGN is

$$\mathbf{C}_{\mathrm{n}} = \sigma_{\mathrm{n}}^2\mathbf{I}_N + \mathbf{C}_{\mathrm{c}} = \sigma_{\mathrm{n}}^2\mathbf{I}_N + \bar{\mathbf{S}}^{\mathrm{H}}\mathbf{S}_{\nu,\ell k,\ell'k'}\bar{\mathbf{S}}, \tag{A.2}$$

where $\bar{\mathbf{S}} = [\mathbf{s}_0, \cdots, \mathbf{s}_{N-1}]^{\mathrm{T}} \in \mathbb{R}^{N \times N}$ is the *full* signal matrix with $\mathbf{s}_i = \left[s((-i)T_{\mathrm{s}}), \ldots, s((N-1-i)T_{\mathrm{s}})\right]^{\mathrm{T}}$ [4]. The elements of the covariance matrix are

$$[\bar{\mathbf{S}}^{\mathrm{H}}\mathbf{S}_{\nu\ell k,\ell'k'}\bar{\mathbf{S}}]_{n,m} = \sum_{i=0}^{N-1} T_{\mathrm{s}}S_{\nu\ell k,\ell'k'}(iT_{\mathrm{s}}) \times s((n-i)T_s)s((m-i)T_s). \tag{A.3}$$

The derivation of the FIM under non-stationary, non-white Gaussian noise, involves a whitening operation that is defined by the inverse of the covariance matrix. By utilizing an eigenvector decomposition for the covariance matrix, we introduce the Fourier weighted inner product in a Hilbert space defined [7] by

$$\begin{aligned}
\frac{\langle \mathbf{x}, \mathbf{y} \rangle_{\mathcal{H}}}{\sigma_{\mathrm{n}}^2} &= \mathbf{y}^{\mathbf{H}}\mathbf{C}_n^{-1}\mathbf{x} \\
&= \mathbf{y}^{\mathbf{H}}\mathbf{U}(\boldsymbol{\Lambda} + \sigma_{\mathrm{n}}^2\mathbf{I}_N)^{-1}\mathbf{U}^{\mathrm{H}}\mathbf{x} \\
&= \frac{1}{\sigma_{\mathrm{n}}^2}\sum_{i=0}^{N-1}\frac{\mathbf{y}^{\mathrm{H}}\mathbf{u}_i\mathbf{u}_i^{\mathrm{H}}\mathbf{x}}{\lambda_i/\sigma_{\mathrm{n}}^2 + 1}
\end{aligned} \tag{A.4}$$

to completely define the FIM. This yields the SINR of the LOS component as

$$\mathrm{SINR}_{\ell k\ell'k'} = \frac{|\alpha_{\ell k}\alpha_{\ell'k'}|^2}{N_0}\|\mathbf{s}_\tau\|_{\mathcal{H}}^2 T_s \sin^2(\phi), \tag{A.5}$$

where $\|\cdot\|_{\mathcal{H}}^2$ denotes the squared norm in the Hilbert space, and ϕ is the angle between $\mathbf{s}_\tau$ and its derivative $\dot{\mathbf{s}}_\tau$ in this Hilbert space. It can cleary be seen, that the SINR is directly influenced by the power of the DM which is reflected in the eigenvalues λ_i in the whitening operation. The whitening gain is

$$\gamma = \frac{\|\dot{\mathbf{s}}_\tau\|_{\mathcal{H}}^2\|\mathbf{s}_\tau\|^2}{\|\dot{\mathbf{s}}_\tau\|^2\|\mathbf{s}_\tau\|_{\mathcal{H}}^2}, \tag{A.6}$$

and the effective SINR is

$$\widetilde{\mathrm{SINR}}_{\ell k\ell'k'} = \frac{|\alpha_{\ell k}\alpha_{\ell'k'}|^2}{N_0}\|\mathbf{s}_\tau\|^2 T_s \frac{\|\dot{\mathbf{s}}_\tau\|_{\mathcal{H}}^2}{\|\dot{\mathbf{s}}_\tau\|^2}\sin^2(\phi). \tag{A.7}$$

104

References

[1] G. Li, D. Arnitz, R. Ebelt, U. Muehlmann, K. Witrisal, and M. Vossiek, "Bandwidth dependence of CW ranging to UHF RFID tags in severe multipath environments," in *2011 IEEE Int. Conf. RFID*, Apr. 2011, pp. 19–25.

[2] D. Dardari, A. Conti, U. Ferner, A. Giorgetti, and M. Z. Win, "Ranging with ultrawide bandwidth signals in multipath environments," *Proc. IEEE*, vol. 97, no. 2, pp. 404–426, Feb. 2009.

[3] H. Arthaber, T. Faseth, and F. Galler, "Spread-spectrum based ranging of passive UHF EPC RFID tags," *IEEE Commun. Lett.*, vol. 19, no. 10, pp. 1734–1737, Oct. 2015.

[4] E. Leitinger, P. Meissner, C. Rudisser, G. Dumphart, and K. Witrisal, "Evaluation of position-related information in multipath components for indoor positioning," *IEEE J. Sel. Areas Commun.*, vol. 33, no. 11, pp. 2313–2328, Nov. 2015.

[5] Y. Shen and M. Z. Win, "Fundamental limits of wideband localization-part I: A general framework," *IEEE Trans. Inf. Theory*, vol. 56, no. 10, pp. 4956–4980, Oct. 2010.

[6] A. Richter and R. S. Thoma, "Joint maximum likelihood estimation of specular paths and distributed diffuse scattering," in *IEEE Vehicular Technology Conf., VTC 2005-Spring*, 2005.

[7] K. Witrisal, E. Leitinger, S. Hinteregger, and P. Meissner, "Bandwidth scaling and diversity gain for ranging and positioning in dense multipath channels," *IEEE Wireless Commun. Lett.*, vol. 5, no. 4, pp. 396–399, Aug. 2016.

[8] M. A. Ingram, M. F. Demirkol, and D. Kim, "Transmit diversity and spatial multiplexing for RF links using modulated backscatter," in *Proceedings of the Int. Symp. on Signals, Systems and Electron., Tokyo*, Jul. 2001.

[9] J. D. Griffin and G. D. Durgin, "Gains for RF tags using multiple antennas," *IEEE Trans. Antennas Propag.*, vol. 56, no. 2, pp. 563–570, Feb. 2008.

[10] ——, "Multipath fading measurements for multi-antenna backscatter RFID at 5.8 GHz," in *2009 IEEE Int. Conf. RFID*, Apr. 2009, pp. 322–329.

[11] C. He, X. Chen, Z. J. Wang, and W. Su, "On the performance of MIMO RFID backscattering channels," *EURASIP Journal on Wireless Commun. and Networking*, vol. 2012, no. 1, p. 1–15, 2012.

[12] H. Godrich, A. M. Haimovich, and R. S. Blum, "Target localization accuracy gain in MIMO radar-based systems," *IEEE Trans. Inf. Theory*, vol. 56, no. 6, pp. 2783–2803, Jun. 2010.

[13] D. Dardari, R. D'Errico, C. Roblin, A. Sibille, and M. Z. Win, "Ultrawide bandwidth RFID: The next generation?" *Proc. IEEE*, vol. 98, no. 9, pp. 1570–1582, Sep. 2010.

[14] D. Arnitz, U. Muehlmann, and K. Witrisal, "UWB ranging in passive UHF RFID: Proof of concept," *Electron. Lett.*, vol. 46, no. 20, pp. 1401–1402, Sep. 2010.

[15] K. Witrisal and P. Meissner, "Performance bounds for multipath-assisted indoor navigation and tracking (MINT)," in *IEEE Int. Conf. Commun. (ICC)*, 2012.

[16] P. Bello, "Characterization of randomly time-variant linear channels," *IEEE Trans. Commun. Sys.*, vol. 11, no. 4, pp. 360 –393, Dec. 1963.

[17] A. F. Molisch, *Wireless Communications.* Wiley-IEEE Press, 2005.

[18] ——, "Ultra-wide-band propagation channels," *Proc. IEEE*, vol. 97, no. 2, pp. 353–371, Feb. 2009.

[19] J. Karedal, S. Wyne, P. Almers, F. Tufvesson, and A. F. Molisch, "A measurement-based statistical model for industrial ultra-wideband channels," *IEEE Trans. Wireless Commun.*, vol. 6, no. 8, pp. 3028–3037, Aug. 2007.

[20] P. V. Nikitin and K. V. S. Rao, "Theory and measurement of backscattering from RFID tags," *IEEE Antennas Propag. Mag.*, vol. 48, no. 6, pp. 212–218, Dec. 2006.

[21] D. Arnitz, U. Muehlmann, and K. Witrisal, "Tag-based sensing and positioning in passive UHF RFID: Tag reflection," in *3rd Int EURASIP workshop on RFID Technology*, 2010.

[22] ——, "Wideband characterization of backscatter channels: Derivations and theoretical background," *IEEE Trans. Antennas Propag.*, vol. 60, no. 1, pp. 257–266, Jan. 2012.

[23] E. Leitinger, P. Meissner, M. Frohle, and K. Witrisal, "Performance bounds for multipath-assisted indoor localization on backscatter channels," in *2014 IEEE Radar Conf.*, May 2014, pp. 0070–0075.

[24] S. Kay, *Fundamentals of Statistical Signal Processing: Estimation Theory.* Upper Saddle River, NJ, USA: Prentice Hall Signal Processing Series, 1993.

[25] D. Arnitz, U. Muehlmann, and K. Witrisal, "Characterization and modeling of UHF RFID channels for ranging and localization," *IEEE Trans. Antennas Propag.*, vol. 60, no. 5, pp. 2491–2501, May 2012.

Range Estimation and Performance Limits for UHF-RFID Backscatter Channels

Stefan Grebien, Josef Kulmer, Florian Galler, Michael Goller,
Erik Leitinger, Holger Arthaber, and Klaus Witrisal

Abstract

The accuracy of time-of-flight based ranging over UHF RFID backscatter channels is fundamentally limited by the available bandwidth and highly dependent on the channel characteristics. Comprehensive wideband channel measurements are presented and analyzed with respect to parameters which influence the potential ranging performance. The Cramér Rao lower bound on time-of-flight based ranging is evaluated and we study the influence of dense multipath on the bound. Based on a line-of-sight (LOS) plus dense multipath (DM) radio channel model, a multiple-input multiple-output (MIMO) ranging algorithm is developed, capable of iteratively estimating the LOS parameters and the statistics of the DM. The accuracy of the developed algorithm is compared to the performance bound. The results highlight the tradeoff between a higher bandwidth and spatial diversity for UHF RFID systems with respect to time-of-flight based ranging. In a 2×2 MIMO setup, an accuracy of about $0.5\,\mathrm{m}$ is achieved at a bandwidth of $50\,\mathrm{MHz}$.

1 Introduction

Accurate and robust ranging with ultra-high frequency (UHF) radio frequency identification (RFID) tags is a key-enabler for a variety of applications in production, supply chain management, and retail. Many of these require a sub-meter accuracy which is still an unsolved challenge. For time-of-flight (ToF) based ranging systems, the available bandwidth imposes a fundamental limit on the achievable accuracy.

A thorough characterization of the UHF-RFID channel is needed for developing robust ranging algorithms. For narrowband signals, the backscatter channel has been well analyzed with respect to fading statistics [1]. Several measurement campaigns [1–5] have studied the individual (*i.e.* up- and downlink) channels in both the narrowband and wideband regimes, but only some analyses have been performed of wideband parameters like the Rician K-factor for the line-of-sight (LOS) component or the root-mean-square (RMS) delay spread for the backscatter channel [2].

The application driven requirement of sub-meter ranging leads to a clear trend towards larger bandwidth systems in the UHF-RFID technology [6–8]. Ranging methods are heavily influenced by the wideband statistics of the backscatter channel. The achievable ranging performance has been analyzed for different scenarios. E.g., in ultra-wideband settings the Cramér Rao lower bound and the Ziv-Zakai bound have been derived [9,10]. The Cramér Rao lower bound in dense multipath (DM) channels has been studied in [11] for ToF-based ranging, and in [8] for a wideband UHF-RFID scenario.

To exploit the utmost ranging information from channel measurements, high accuracy channel estimators are necessary. Maximum likelihood estimators for superimposed signals are typically iterative algorithms, e.g., the expectation maximization (EM) algorithm [12] which evolved into space alternating EM schemes [13]. These algorithms assume separable superimposed signals in additive white Gaussian noise (AWGN). Measurements showed [4,14,15] that due to overlapping of the signals and a restricted measurement aperture an additional interference term, so-called DM, needs to be introduced in the channel model. This means that a high-performance channel estimator should consider this impairment [14].

Taking into account the requirements and the current state of the research, the main contributions of this paper are:[1]

- we develop a multiple-input multiple-output (MIMO) channel estimator capable of estimating the LOS parameters (delay, angle-of-departure, angle-of-arrival) and the statistics of the DM by utilizing a delay-sum beamformer, and

- we analyze measurements from two scenarios, apply the developed algorithm and analyze the ranging error bound for backscatter channels under DM, in single-input single-output (SISO) and MIMO setups.

---

[1] Parts of this journal paper have been presented at the IEEE RFID conference 2017 [16]. In Section 2 we adapted the channel model to be able to cope with the development of the MIMO range estimator, which is found in Section 3.2, and the ranging error bound for the MIMO setup in Section 3.3.2. Finally, we added simulation results in Section 6.1 and applied the developed algorithm to the measured data in Section 6.2.2.

108

The paper is organized as follows: Section 2 defines the problem and introduces the channel model. Section 3 develops range estimators for the SISO and MIMO setup and presents their Cramér Rao lower bounds. Section 4 describes the measurement setup and Section 5 analyzes the measured data. In Section 6 the algorithms are validated with simulated and measured data and Section 7 concludes the paper.

2 Problem Formulation

We investigate the backscatter channel consisting of a downlink channel from RFID reader ℓ to an RFID tag and an uplink from the tag to the RFID reader ℓ'.[2] Both RFID readers ℓ and ℓ' are equipped with K and K' closely spaced antennas respectively. Antennas with index k are assigned to reader ℓ located at $\mathbf{p}_{\ell k}$ and antennas with index k' belong to ℓ' at $\mathbf{p}_{\ell' k'}$. The tag is located at unknown position $\mathbf{p}$.

Each of the RFID reader antennas can be used to transmit and/or receive a wideband signal [6, 8]. The aim is to find the overall propagation delay of the backscatter channel between the transmitting RFID reader via the tag to the receiving RFID reader. Depending on the number of antennas used at the transmitting and receiving RFID reader, a SISO, a SIMO or a MIMO system can be analyzed.

2.1 Channel Model

The backscatter channel model between downlink antenna k and uplink antenna k' is modeled by a LOS plus DM model [2, 11]

$$h_{kk'}(\tau) = \alpha_{kk'}\delta(\tau - \tau_{kk'}) + \nu_{kk'}(\tau), \tag{1}$$

where $\delta(\tau)$ is the Dirac pulse, and the LOS is characterized by its complex-valued amplitude $\alpha_{kk'}$ and delay $\tau_{kk'}$. The LOS delay of the backscatter channel is equivalent to the Euclidean distance between the positions of the downlink antenna, the tag and the uplink antenna scaled by the speed of light c, such that $\tau_{kk'} = (\|\mathbf{p}_{\ell k} - \mathbf{p}\| + \|\mathbf{p} - \mathbf{p}_{\ell' k'}\|)/c$.

The term $\nu_{kk'}(\tau)$ in (1) models the DM consisting of all occurring multipath components (MPC), including reflections at flat surfaces and scattering at small objects. This DM is modeled as a zero-mean complex Gaussian random process, assuming uncorrelated scattering (US) along the delay axis τ [17]. Thus, the auto-correlation function of the DM is $\mathbb{E}\{\nu_{kk'}(\tau)[\nu_{kk'}(u)]^*\} = S_{\nu,kk'}(\tau - \tau_{kk'})\delta(\tau - u)$ with $S_{\nu,kk'}(\tau)$ as the power-delay-profile (PDP) of the DM which is zero for $\tau < 0$. This means, that some information about the LOS delay is encoded in the PDP of the DM. In this work we use a double exponential PDP [4] which includes five parameters $\mathbf{\Gamma} = [\tau_{\text{DM}}, P_{\text{DM}}, \gamma_{\text{fall}}, \gamma_{\text{rise}}, \chi]^T$, where τ_{DM} is the onset of the DM, P_{DM} describes the overall power of the DM, γ_{rise}, γ_{fall}, and χ are shape parameters of the DM.[3] We also assume quasi-stationarity in the spatial domain, meaning that for one reader / tag configuration, the PDP does not change noticeably in the vicinity of the tag [17]. The signal model does

---

[2]This can describe either a monostatic setup ($\ell = \ell'$) or a bistatic setup ($\ell \neq \ell'$).

[3]It is straightforward to use different PDPs, e.g. an exponential PDP, since only the parameter vector $\mathbf{\Gamma}$ has to be adjusted.
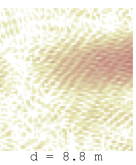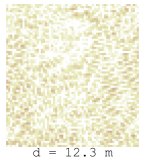
not include more than one tag. This does not limit the system operation to one tag, but rather implies the usage of multiple access schemes [6, 7] to separate multiple tags.

2.2 Received Signal

The received signal $r_{kk'}(t)$[4] at any antenna k' stemming from antenna k results as convolution of the transmitted baseband signal $s(t)$ and the overall backscatter channel described in (1) as

$$r_{kk'}(t) = \alpha_{kk'} s(t - \tau_{kk'}) \exp\left\{-j\left(2\pi f_c \tau_{kk'} + \varphi_0\right)\right\} + (s * \nu_{kk'})(t) + \omega(t), \quad (2)$$

where φ_0 is an unknown initial phase and $\omega(t)$ is AWGN with a two-sided power spectral density of $N_0/2$.

3 Range Estimation

Depending on the number of used antennas at the transmitting and receiving reader, different estimators are developed in the following section.

3.1 Single-Input Single-Output

The range measurement obtained between a transmit reader antenna, the tag, and a receive reader antenna is given by $d_{\mathrm{SISO}} = c\tau_{kk'}$, determining the unknown tag position $\mathbf{p}$ as a point on an ellipse. By sampling the received signal with $f_{\mathrm{s}} = 1/T_{\mathrm{s}}$, with T_{s} as sampling period, (2) can be written for the SISO model in vector notation as

$$\mathbf{r}_{kk'} = \alpha_{kk'} \mathbf{s}_{\tau_{kk'}} + \mathbf{n}_{\mathrm{c},kk'} + \boldsymbol{\omega}_{kk'} \quad (3)$$

where $\mathbf{s}_{\tau_{kk'}} = [s(-\tau_{kk'}), s(T_{\mathrm{s}} - \tau_{kk'}), \ldots, s((N-1)T_{\mathrm{s}} - \tau_{kk'})]^T e^{-j(2\pi f_c \tau_{kk'} + \varphi_0)}$, $\mathbf{n}_{\mathrm{c},kk'} = [(s*\nu_{kk'})(0), (s*\nu_{kk'})(T_{\mathrm{s}}), \ldots, (s*\nu_{kk'})((N-1)T_{\mathrm{s}})]^T$, and $\mathbf{r}_{kk'}$ and $\boldsymbol{\omega}_{kk'}$ are sampled versions of the received signal and the AWGN as vectors $\in \mathbb{C}^{N \times 1}$.

Given the deterministic unknown parameter vector $\boldsymbol{\theta}_{\mathrm{SISO}} = [\tau_{kk'}, \alpha_{kk'}]^T$, the likelihood function is given as

$$f(\mathbf{r}_{kk'} | \boldsymbol{\theta}_{\mathrm{SISO}}) \propto \exp\left\{(\mathbf{r}_{kk'} - \alpha_{kk'} \mathbf{s}_{\tau_{kk'}})^H \mathbf{C}_{kk'}^{-1}(\mathbf{r}_{kk'} - \alpha_{kk'} \mathbf{s}_{\tau_{kk'}})\right\}, \quad (4)$$

where $\mathbf{C}_{kk'} = \mathbf{S}^H \mathbf{S}_{\boldsymbol{\nu},kk'} \mathbf{S} + \frac{N_0}{T_{\mathrm{s}}} \mathbf{I} \in \mathbb{R}^{N \times N}$ is the covariance matrix with $\mathbf{S} = [\mathbf{s}_0, \ldots, \mathbf{s}_{(N-1)T_{\mathrm{s}}}]^T$ and $\mathbf{S}_{\boldsymbol{\nu},kk'} = \mathrm{diag}\{S_{\nu,kk'}(iT_{\mathrm{s}}) \cdot T_{\mathrm{s}}\}$ is a diagonal matrix containing the PDP.

To estimate the distance d_{SISO}, we apply: (i) a maximum likelihood (ML) estimator, and (ii) a naïve matched filter (MF) estimator. The ML estimator accounts for the influence of the DM expressed by the covariance matrix and thus requires the PDP of the DM and N_0 to be known.

---

[4]This model assumes perfect (frequency independent) backscattering of the tag over the whole bandwidth. This certainly does not hold when considering 'wideband' signals, but the smaller the bandwidth gets, the less frequency dependent the radar cross section of a tag gets [18]. It would be possible to include the frequency dependent behavior in the baseband pulse $s(t)$ [19], but in this work we want to focus on the influence of the channels, and thus neglect this effect.

110

3.1.1 ML estimator

The ML estimator for the delay estimation problem is found by maximizing the likelihood function (4) with respect to the parameter $\tau_{kk'}$.

$$\hat{d}_{\mathrm{SISO,ML}} = c \cdot \underset{\tau_{kk'}}{\mathrm{argmax}} \{ f(\mathbf{r}_{kk'} | \boldsymbol{\theta}_{\mathrm{SISO}}) \}. \tag{5}$$

The nuisance parameter $\alpha_{kk'}$ has to be estimated jointly with $\tau_{kk'}$ [20], which can be written as

$$\hat{\alpha}_{kk'}(\tau_{kk'}) = \frac{\mathbf{r}_{kk'}^H \mathbf{C}_{kk'}^{-1} \mathbf{s}_{\tau_{kk'}}}{\mathbf{s}_{\tau_{kk'}}^H \mathbf{C}_{kk'}^{-1} \mathbf{s}_{\tau_{kk'}}}. \tag{6}$$

3.1.2 MF estimator

The MF estimator simply correlates the received signal with the transmit pulse and searches for the maximum, i.e.

$$\hat{d}_{\mathrm{SISO,MF}} = c \cdot \underset{\tau_{kk'}}{\mathrm{argmax}} \{ \mathbf{r}_{kk'}^H \mathbf{s}_{\tau_{kk'}} \}. \tag{7}$$

This estimator ($\hat{d}_{\mathrm{SISO,MF}}$) would be optimal for a signal model without the DM [20, p. 192].

3.2 Multiple-Input Multiple-Output

To overcome the shortcoming of the SISO range estimation, namely the *need to know* the statistics of the DM plus AWGN, a SIMO or MIMO setup is necessary which enables the joint estimation of the LOS parameters and the parameters of the DM.[5]

The received signal in a MIMO setup is found by stacking the individual received signals between an RFID reader via the tag to an RFID reader. The received signal $\mathbf{r}$ reads

$$\mathbf{r} = \alpha \mathbf{s} + \mathbf{n}_{\mathrm{c}} + \boldsymbol{\omega} \quad \in \mathbb{C}^{NKK' \times 1}, \tag{8}$$

where $\mathbf{r} = [\mathbf{r}_{11}^T, ..., \mathbf{r}_{KK'}^T]^T$, $\mathbf{s} = [\mathbf{s}_{11}^T, ..., \mathbf{s}_{KK'}^T]^T$, $\mathbf{n}_{\mathrm{c}} = [\mathbf{n}_{\mathrm{c},11}^T, ..., \mathbf{n}_{\mathrm{c},KK'}^T]^T$, and $\boldsymbol{\omega} = [\boldsymbol{\omega}_{11}^T, ..., \boldsymbol{\omega}_{KK'}^T]^T$. We assume that the transmitting and receiving antennas are spaced closely enough such that the amplitude $\alpha = \alpha_{kk'} \forall k, k'$ is the same over all individual backscatter channels.

To reduce the $K \times K'$ large search space for the individual delays $\tau_{kk'}$, they are re-written as a sum of three terms: (i) a delay from the center of the transmitting array $\mathbf{p}_{\ell}$ via the tag to the center of the receiving array $\mathbf{p}_{\ell'}$, $\tau_{\ell\ell'} = \frac{1}{c}(\|\mathbf{p} - \mathbf{p}_{\ell}\|^2 + \|\mathbf{p} - \mathbf{p}_{\ell'}\|^2) = \frac{1}{c}d_{\mathrm{MIMO}}$, (ii) an additional delay $\Delta\tau_{\ell k} = -\frac{1}{c}(\Delta p_{x_{\ell k}} \cos(\varphi_{\mathrm{AoD}}) + \Delta p_{y_{\ell k}} \sin(\varphi_{\mathrm{AoD}}))$ as a function of the angle-of-departure φ_{AoD} and the known antenna position offsets $\Delta\mathbf{p}_{\ell k}$ given by the transmitter array geometry, and (iii) an additional delay $\Delta\tau_{\ell' k'} = -\frac{1}{c}(\Delta p_{x_{\ell' k'}} \cos(\varphi_{\mathrm{AoA}}) + \Delta p_{y_{\ell' k'}} \sin(\varphi_{\mathrm{AoA}}))$ as a function of the angle-of-arrival φ_{AoA} and the known

---

[5]In the following the MIMO estimator is developed which can be applied straightforwardly to a SIMO setup by neglecting the angle-of-departure that cannot be estimated by an RFID SIMO setup.

antenna position offsets $\Delta \mathbf{p}_{\ell' k'}$ given by the receiver array geometry.[6] The parameters of the LOS are combined into the vector $\boldsymbol{\psi} = [\tau_{\ell\ell'}, \varphi_{\mathrm{AoD}}, \varphi_{\mathrm{AoA}}]^T$

The according likelihood function for the received signal, given the unknown deterministic parameter vector $\boldsymbol{\theta}_{\mathrm{MIMO}} = [\boldsymbol{\psi}, \alpha, \boldsymbol{\eta}]^T$, is

$$f(\mathbf{r}|\boldsymbol{\theta}_{\mathrm{MIMO}}) = \frac{1}{\pi^{NKK}|\mathbf{C}(\boldsymbol{\eta})|} \exp\left\{ (\mathbf{r} - \alpha\mathbf{s}(\boldsymbol{\psi}))^H \mathbf{C}(\boldsymbol{\eta})^{-1} (\mathbf{r} - \alpha\mathbf{s}(\boldsymbol{\psi})) \right\}, \quad (9)$$

where we have introduced $\mathbf{s}(\boldsymbol{\psi})$ to show the dependence of the delay, and the two angles explicitly.[7] As for the amplitudes, we assume that the statistics of the DM process do not change for one reader / tag configuration, thus $\mathbf{C}_{kk'}(\boldsymbol{\eta}) \approx \tilde{\mathbf{C}}(\boldsymbol{\eta})$, with $\boldsymbol{\eta} = [N_0, \boldsymbol{\Gamma}]^T$ as the parameters describing the AWGN and the parameters of the DM process. The overall covariance matrix can now be written as a diagonal block matrix $\mathbf{C}(\boldsymbol{\eta}) = \mathrm{diag}(\tilde{\mathbf{C}}(\boldsymbol{\eta}), ..., \tilde{\mathbf{C}}(\boldsymbol{\eta}))$.[8]

The direct maximization of the likelihood function (9) to derive an ML estimator for $\boldsymbol{\theta}_{\mathrm{MIMO}}$ is difficult, since a maximization with respect to eleven parameters[9] would be necessary. To split the search space into smaller search spaces, a structured mean field variational approach is used which approximates the posterior of the parameters as

$$f(\boldsymbol{\theta}_{\mathrm{MIMO}}|\mathbf{r}) \approx q(\boldsymbol{\psi})q(\alpha)q(\boldsymbol{\eta}) = q(\boldsymbol{\theta}_{\mathrm{MIMO}}), \quad (10)$$

where we assumed that the DM process, the parameters of the LOS component, and the complex amplitudes are independent. As no prior information of the parameters is available, a uniform prior is used for the parameters, meaning that the parameter posterior is proportional to the likelihood. To find a close approximation for the parameter posterior we chose to minimize the Kullback-Leibler divergence from the parameter posterior $f(\boldsymbol{\theta}_{\mathrm{MIMO}}|\mathbf{r})$ towards $q(\boldsymbol{\theta}_{\mathrm{MIMO}})$. This can be accomplished [21] by maximizing the variational lower bound of q towards the joint probability density function $f(\boldsymbol{\theta}_{\mathrm{MIMO}}, \mathbf{r})$

$$\mathcal{L}(q) = \int q(\boldsymbol{\theta}_{\mathrm{MIMO}}) \log \frac{f(\boldsymbol{\theta}_{\mathrm{MIMO}}, \mathbf{r})}{q(\boldsymbol{\theta}_{\mathrm{MIMO}})} d\boldsymbol{\theta}_{\mathrm{MIMO}}. \quad (11)$$

By evaluating the variational lower bound for the individual subsets of parameters while keeping the other parameters fixed, using a point estimate for the parameters $q(\boldsymbol{\psi}) = \delta(\boldsymbol{\psi} - \hat{\boldsymbol{\psi}})$, an iterative local maximization of the variational lower bound can be found. In the appendix, the derivation of the maximization problems can be found for the different subsets. At each iteration step we update the LOS parameters delay, the angle-of-arrival (AoA), and the angle-of-departure (AoD) using the log likelihood in (9) conditioned on the LOS amplitude and covariance from the previous iteration

$$\hat{\boldsymbol{\psi}}^{\mathrm{new}} = \underset{\hat{\boldsymbol{\psi}}}{\mathrm{argmax}} \left\{ -\left(\mathbf{r} - \hat{\alpha}^{\mathrm{old}}\mathbf{s}(\hat{\boldsymbol{\psi}})\right)^H \mathbf{C}(\hat{\boldsymbol{\eta}}^{\mathrm{old}})^{-1} \left(\mathbf{r} - \hat{\alpha}^{\mathrm{old}}\mathbf{s}(\hat{\boldsymbol{\psi}})\right) \right\}, \quad (12)$$

---

[6] For (ii) and (iii) it is assumed that the distance between the tag and the transmitter/receiver array is large with respect to the array spacing.

[7] We could have modeled the parameter vector $\boldsymbol{\psi}$ also as a function of the unknown tag position $\mathbf{p}$, but as we are interested in ranging we estimate the delay $\tau_{\ell\ell'}$ directly.

[8] This diagonal block matrix assumes, that the DM at different antenna elements are uncorrelated. In Section 5 the spaced-distance-correlation-function for the DM is analyzed, which expresses these correlations.

[9] For the direct search, the real and imaginary part of the amplitude have to be searched for separately

112

Algorithm 1: Summary of the proposed algorithm.

Initialization:

- perform grid search for $\hat{\boldsymbol{\psi}} = \text{argmax}_{\boldsymbol{\psi}} \left\{ \mathbf{r}^H \mathbf{s}(\boldsymbol{\psi}) \right\}$

- estimate $\hat{N}_0$ according to (27) and initialize $\hat{\boldsymbol{\eta}} = [\hat{N}_0/2, \hat{\boldsymbol{\Gamma}}]^T$ (cf. Footnote 11) and $\hat{\alpha}$ acc. to (13)

Iterations:
do

    update $\hat{\boldsymbol{\psi}}$ according to (12)
    update $\hat{\alpha}$ according to (13)
    update $\hat{\boldsymbol{\eta}}$ according to (14)
while *not converged*;

---

followed by updating the LOS amplitude and the noise statistic parameters[10]

$$\hat{\alpha}^{\text{new}} = \frac{\mathbf{r}^H \mathbf{C}(\hat{\boldsymbol{\eta}}^{\text{old}})^{-1} \mathbf{s}(\hat{\boldsymbol{\psi}}^{\text{new}})}{\mathbf{s}(\hat{\boldsymbol{\psi}}^{\text{new}})^H \mathbf{C}(\hat{\boldsymbol{\eta}}^{\text{old}})^{-1} \mathbf{s}(\hat{\boldsymbol{\psi}}^{\text{new}})}, \tag{13}$$

$$\hat{\boldsymbol{\eta}}^{\text{new}} = \underset{\hat{\boldsymbol{\eta}}}{\text{argmax}} \left\{ -\log\left\{ |\mathbf{C}(\hat{\boldsymbol{\eta}})| \right\} \right.$$
$$\left. - \left(\mathbf{r} - \hat{\alpha}^{\text{new}} \mathbf{s}(\hat{\boldsymbol{\psi}}^{\text{new}}) \right)^H \mathbf{C}(\hat{\boldsymbol{\eta}})^{-1} \left(\mathbf{r} - \hat{\alpha}^{\text{new}} \mathbf{s}(\hat{\boldsymbol{\psi}}^{\text{new}}) \right) \right\}. \tag{14}$$

Due to the sequential nature of the algorithm it needs initial values for all parameters. These can be found for the LOS parameters by a grid search for the delay (spacing of T_s), the AoA and AoD (spaced by $5°$) with a matched filter delay-sum beamformer, for the AWGN parameters by estimating $\hat{N}_0$ according to (27) and using standard values for the DM parameters.[11] A summary of the algorithm is presented in Algorithm 1.

3.3 Ranging Error Bound $\mathcal{R}(\tau)$

3.3.1 REB for SISO processing

The Cramér Rao lower bound for the delay estimation problem for DM channels [11], called ranging error bound (REB), is given by the inverse of the square root of the equivalent Fisher information (EFI),

$$\mathcal{R}(\tau_{kk'}) = \sqrt{\mathcal{I}_{\tau_{kk'}}^{-1}}. \tag{15}$$

---

[10]As we are interested most in the LOS parameters we update these parameters first. Depending on the order of the update, the algorithm will sometimes converge to a different local maxima [21].

[11]As the DM can only start after the LOS arrived at the receiver, we set $\tau_{\text{DM,init}} = \hat{\tau}_{\ell,\ell'}$, we assume that the power in the DM is approximately half the overall noise power, use standard values [4] for $\gamma_{\text{rise}} = 20$ ns and $\gamma_{\text{fall}} = 8$ ns and initialize the shape parameter χ randomly in the interval $(0, 1)$.
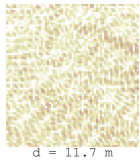
For a backscatter channel the EFI is

$$\mathcal{I}_{\tau_{kk'}} = 8\pi^2\beta^2\widetilde{\text{SINR}}_{kk'} + \text{tr}\left\{\mathbf{C}_{kk'}^{-1}\frac{\partial\mathbf{C}_{kk'}}{\partial\tau}\mathbf{C}_{kk'}^{-1}\frac{\partial\mathbf{C}_{kk'}}{\partial\tau}\right\}, \tag{16}$$

$$\approx 8\pi^2\beta^2\widetilde{\text{SINR}}_{kk'} \tag{17}$$

where $\beta^2 = \|\dot{\mathbf{s}}_{\tau_{kk'}}\|/(4\pi^2\|\mathbf{s}_{\tau_{kk'}}\|)$ is the effective (mean-square) bandwidth of the transmit pulse, $\dot{\mathbf{s}}_{\tau_{kk'}}$ is the derivative of $s(t - \tau_{kk'})$ with respect to t, and $\widetilde{\text{SINR}}_{kk'}$ is the effective signal-to-interference-plus-noise-ratio (SINR) [8]. The second term in (16) describes the additional delay information in the DM, as the onset of the DM coincides with the LOS delay.[12]

In particular, the effective SINR describes the useful ranging information of the LOS component when influenced by DM and AWGN and can be factored into three parameters [11]:

(i) the signal-to-interference-plus-noise-ratio $\text{SINR}_{kk'} = |\alpha_{kk'}|^2\mathbf{s}_{\tau_{kk'}}^H\mathbf{C}_{kk'}^{-1}\mathbf{s}_{\tau_{kk'}}$ which quantifies the signal-to-noise-ratio (SNR) after the square root of the covariance matrix has been applied as whitening filter,

(ii) the whitening gain $\gamma_{kk'} = \dfrac{\dot{\mathbf{s}}_{\tau_{kk'}}^H\mathbf{C}_{kk'}^{-1}\dot{\mathbf{s}}_{\tau_{kk'}}}{\mathbf{s}_{\tau_{kk'}}^H\mathbf{C}_{kk'}^{-1}\mathbf{s}_{\tau_{kk'}}}\dfrac{1}{4\pi^2\beta^2}$ which quantifies the bandwidth gain due to the knowledge of the PDP,

(iii) and $\sin^2(\varphi_{kk'})$ which is an information loss due to the estimation of the nuisance parameter $\alpha_{kk'}$.[13]

3.3.2 REB for MIMO processing

In [8] we have shown that the EFI is additive for individual measurements if the statistics of the DM are known and the antenna elements within one array are closely spaced, leading to

$$\mathcal{I}_{\tau_{\ell\ell'}} = \sum_{k=1}^{K}\sum_{k'=1}^{K'}\mathcal{I}_{\tau_{kk'}}, \text{ and} \tag{18}$$

$$\mathcal{I}_{\tau_{\ell\ell}} = \sum_{k=1}^{K}\sum_{k'=k}^{K}\mathcal{I}_{\tau_{kk'}} \tag{19}$$

for a bistatic (18) and a monostatic (19) setup respectively. For the algorithm developed in Section 3.2 this EFI is overrated, as the estimation process of the AoA, the AoD and the DM parameters are not accounted for in the derivation of (16) and (17). The estimation of additional parameters shows to be subtractive with respect to the EFI [20]. Thus, the REB computed from (18) or (19) is certainly a lower bound for Algorithm 1. While (19) and (18) are developed for non-coherent processing of the measurements, it is discussed in [11] that for the

---

[12]In (10) we assumed independence among $\tau_{kk'}$ and τ_{DM} yielding the compact algorithm in (12) and (14). This assumptions affects the information contained in $\tau_{kk'}$ and subsequently the potential performance of the estimator.

[13]$\varphi_{kk'}$ describes the angle between the whitened pulse and the whitened pulse derivative in a vector space. For common pulses and an AWGN model, $\varphi_{kk'} = 90°$. Due to the whitening this angle gets smaller than $90°$.

assumption of a uniformly distributed PDP in angular domain they also hold for coherent processing. Eq. (18) or (19) can be interpreted as the REB for a MIMO setup with knowledge of the PDP as well as the AoD and AoA.

In Section 6 we compare the performance of the derived ranging algorithms with the theoretical lower bound, obtained from the signal model, for both SISO and MIMO processing. Furthermore, we evaluate the impact of the estimated PDP, AoD and AoA on the REB for MIMO processing. Next, the measurement scenarios are described and basic channel parameters are analyzed.

4   Measurement Setup

The measurement data used in this work are obtained from a series of wideband measurements using an m-sequence channel sounder by Ilmsens [22], operating in the frequency range ($-10\,\mathrm{dB}$ cut-off) from 0.1 to 3.2 GHz. It has one transmitting (TX) and two receiving channels (RX), a sampling frequency of 6.95 GHz, thus a resolution of 4.31 cm. It uses a sequence length of 4095 chips and thus a maximum delay of 589.2 ns or 176.6 m. To measure up to four antennas per RX channel we use two RF switching matrices [23]. The cross-talk and the system-response of the measurement equipment are removed up to the antenna ports by a match-through calibration. This setup provides the flexibility to study different configurations, including SISO as well as MIMO setups.

A tapered slot antenna (also called Vivaldi antenna) with a 3 dB mainlobe width of approximately $90\,^\circ$ is used as reader antenna. Its wideband gain pattern is not completely independent of frequency but shows good properties in the frequency range from 0.75 to 1.5 GHz. The tag antenna is an elliptic dipole-like structure with an omnidirectional gain pattern similar to RFID tags. Again, the wideband pattern shows good properties in the same frequency range as the reader antennas.

A positioning table is used to accurately position the RFID tag in an automated way to obtain a large number of measurements with different tag positions. The positioning table spans a $0.68 \times 0.64\,\mathrm{m}$ grid with a spacing of 4 cm. For the individual measurement runs, the positioning table can be placed at different locations in the room in order to evaluate the desired coverage.

Measurement data have been acquired in two different scenarios: Scenario A is a standard laboratory hall at TU Wien that was chosen in order to evaluate a typical indoor lab / office environment. Scenario B is an industrial hall with a significant amount of metal fixtures. Both scenarios are described in more detail in the following sections.

4.1   Scenario A

In Fig. 1a and Fig. 2a the floorplan and a picture of the measurement scenario in the laboratory are depicted, respectively. The positioning table with the tag antenna is placed at two positions in the room (T1 & T2), while the reader antennas are set up as two linear arrays with antenna positions at $\mathbf{p}_1$ to $\mathbf{p}_4$ & $\mathbf{p}_5$ to $\mathbf{p}_8$. The back of the room holds a cabinet with laboratory equipment, while the other side of the room is occupied by a metal cabinet. Furthermore, the lab holds a set of aluminum profiles for linear axis movements that is placed
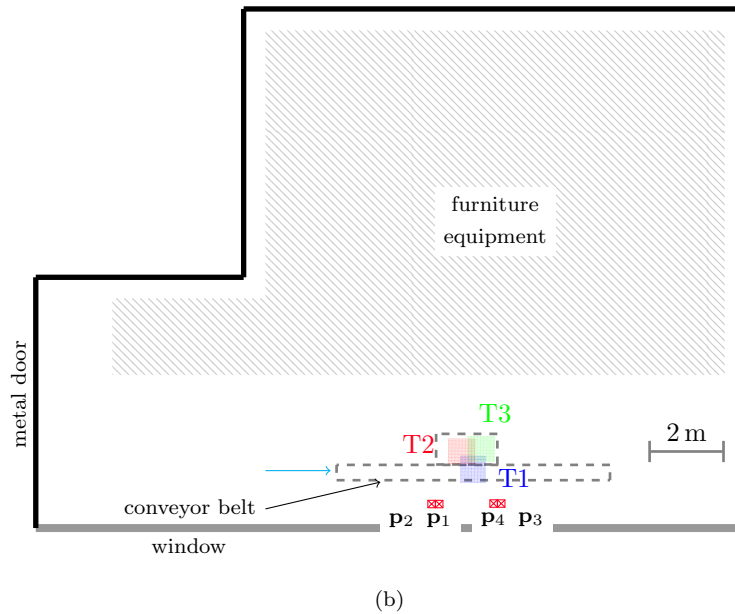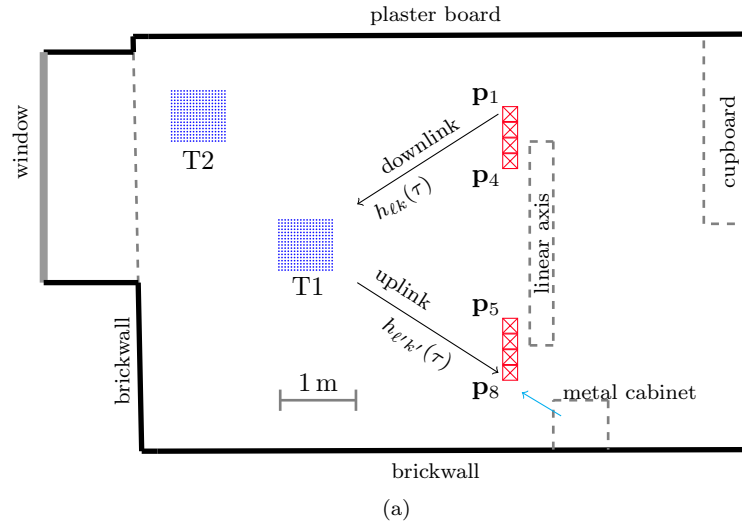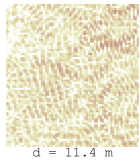
Figure 1: Floorplans of the two measurement scenarios. At each table position, 306 measurements are obtained with a spacing of $4\,\mathrm{cm}$ on a 17×18 grid. The cyan arrows depict the point of view of the photographs in Fig. 2.
(a) Scenario A: Laboratory at TU Wien with some furniture and a linear axis. Eight closely-spaced Vivaldi antennas arranged as two arrays ($\mathbf{p}_1$ to $\mathbf{p}_4$ & $\mathbf{p}_5$ to $\mathbf{p}_8$) and two different table positions (T1 & T2).
(b) Scenario B: Industrial setup with a conveyor belt, aluminum profiles, and many scatterers. Four closely-spaced Vivaldi antennas arranged as two arrays ($\mathbf{p}_1$ and $\mathbf{p}_2$ & $\mathbf{p}_3$ and $\mathbf{p}_4$) and three different table positions (T1, T2 & T3).

116
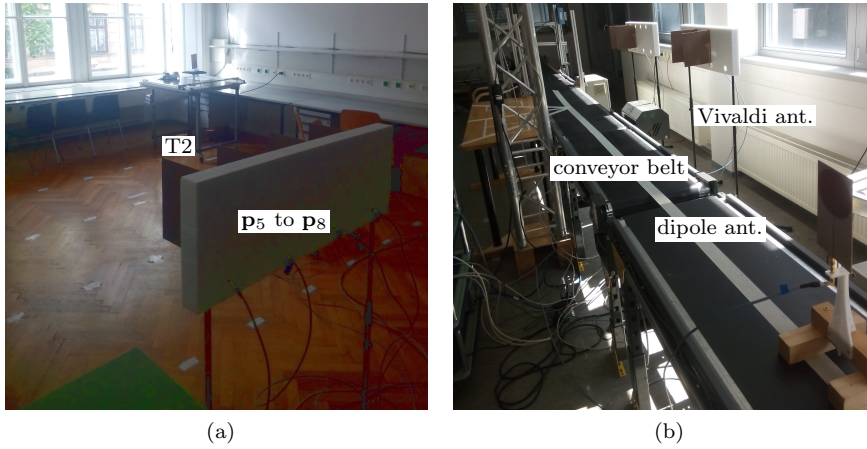
Figure 2: Pictures of the two measurement scenarios: (a) Scenario A, (b) Scenario B. The point of view with respect to the floorplan is shown with a cyan arrow in Fig. 1.

directly behind the antennas. All antennas are set up at a constant height of 1.3 m.

4.2 Scenario B

The second measurement campaign (see floorplan in Fig. 1b and picture in Fig. 2b) has been performed in an industrial hall with metal fixtures and a conveyor belt setup as typically found in manufacturing and logistics. The hall is approximately 18 by 12 m large and the facilities are used to analyze and study logistic processes and systems, e.g., for consignment / picking of goods. The positioning table is placed at three partly overlapping positions (T1, T2, T3) in three consecutive measurement runs and two readers, each having two antennas (at $\mathbf{p}_1$, $\mathbf{p}_2$ & $\mathbf{p}_3$, $\mathbf{p}_4$), are emulated. All antennas are set up at a constant height of 1.3 m.

4.3 Pre-Processing

The measurement setup in the two described scenarios includes a data processing pipeline comprising the following steps: First, the cross-talk and system-response are removed for calibration of the downlink and the uplink channel measurements. These measurements are subsequently convolved with each other to get the calibrated measurements of the backscatter channel [2]. Next, this backscatter signal is converted to baseband using a center frequency of $f_\mathrm{c} = 900\,\mathrm{MHz}$. Finally, the bandwidth is reduced by convolution with a root-raised-cosine pulse $s(t)$ with a pulse duration of $T_p = 1\,\mathrm{ns}$ and roll-off-factor of 0.6. The result of this pre-processing is called channel response (CR) $\mathbf{g}_{kk'}$ given by

$$\mathbf{g}_{kk'} = \alpha_{kk'}\mathbf{s}_{\tau_{kk'}} + \mathbf{n}_\mathrm{c}. \tag{20}$$

In contrast to the received signal model, the actual signal contains AWGN which is neglected in further considerations due to the high SNR of the employed

117

channel sounder.

Due to the large bandwidth, we can assume that the LOS can be resolved from the multipath components which enables us to estimate $\alpha_{kk'}$ by a projection $\hat{\alpha}_{kk'} = \mathbf{g}_{kk'}^H \mathbf{s}_{\tau_{kk',\mathrm{GM}}} T_s$ of the CR onto the baseband pulse at the true delay given by the geometric model $\tau_{kk',\mathrm{GM}} = (\|\mathbf{p}_{\ell k} - \mathbf{p}\| + \|\mathbf{p} - \mathbf{p}_{\ell' k'}\|)/c$. This estimate is used for the following channel analysis.

5   Channel Analysis

In order to investigate the properties of the backscatter channel with a focus on ranging and positioning, we consider the following three parameters for the analysis:

Rician K-factor of the LOS component   The ranging performance is highly influenced by the power ratio between the LOS component and all NLOS components [24]. This power ratio is comparable to the Rician K-factor in narrowband systems and is termed Rician K-factor of the LOS component K_{LOS}. Instantaneous K_{LOS} values are computed from individual CRs by $\hat{K}_{\mathrm{LOS},kk'} = \frac{\|\hat{\alpha}_{kk'} \mathbf{s}_{\tau_{kk',\mathrm{GM}}}\|^2}{\|\mathbf{g}_{kk'} - \hat{\alpha}_{kk'} \mathbf{s}_{\tau_{kk',\mathrm{GM}}}\|^2}$.

Root-mean-square delay spread τ_{RMS}   The rms delay spread quantifies the variance of the arrival times of MPCs with significant energy and is estimated from the second centralized moment of instantaneous normalized PDPs including the LOS component, i.e., $|\mathbf{g}_{kk'}|^2$.

Spaced-distance-correlation-function   For methods that exploit spatial diversity (e.g., beamforming, combining of measurements from closely-spaced antennas), uncorrelated measurements are usually preferred to get additional information [8]. We analyze the spaced-distance-correlation-function (SDCF) of the DM which expresses the percentage of correlation at a certain distance. To compute the SDCF for a specific backscatter channel and a specific grid point $\mathbf{p}_{\mathrm{c}}$, we find all points around $\mathbf{p}_{\mathrm{c}}$ on the grid with a certain distance (e.g. $16 \pm 2\,\mathrm{cm}$), $\mathcal{P}_c = \{\mathbf{p}_i : \|\mathbf{p}_i - \mathbf{p}_c\| = 16 \pm 2\,\mathrm{cm}\}$, shift the CRs along time domain such that the LOS delay coincides with the LOS of the center point $\mathbf{p}_c$, estimate the mean of the complex channel coefficients for the LOS component, subsequently subtract the LOS component, compute the correlation coefficients between the channel transfer functions of the DM at $\mathbf{p}_{\mathrm{c}}$ with all $\mathbf{p}_i$, and average over all points in $\mathcal{P}_c$. In Section 3.2 the overall covariance matrix is approximated with a diagonal block matrix. This means, that correlations between the individual antenna elements are neglected. The lower the SDCF for the DM is, the better this approximation holds.

We evaluate the described parameters for all individual channels and all backscatter channels, and discuss the results and their implications for the ranging problem (for the two scenarios described in Section 4). The channel-analysis results are shown in Fig. 3 as cumulative distribution functions (CDF). The left column shows the results for Scenario A and the right for Scenario B.
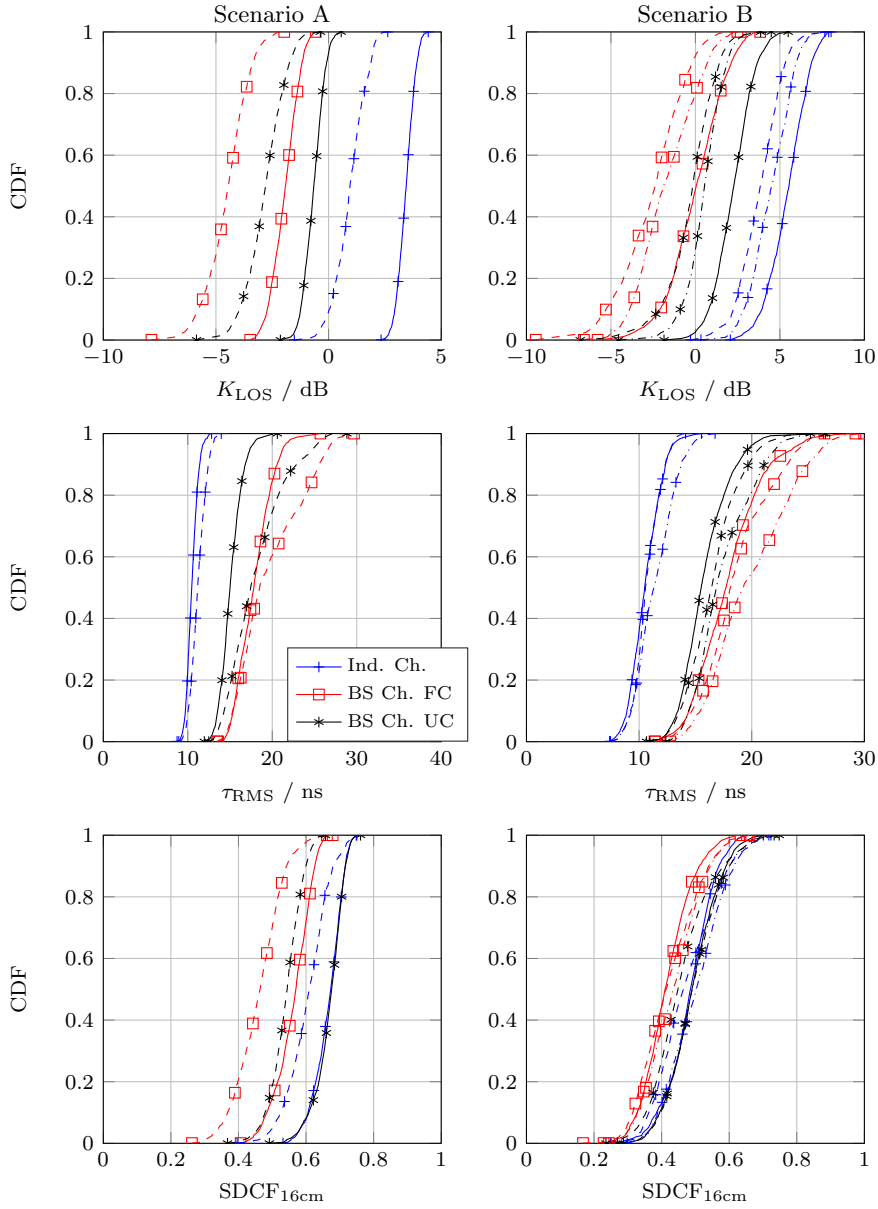
Figure 3: Cumulative distribution functions (CDF) of the three parameters (1$^\text{st}$ row K_LOS, 2$^\text{nd}$ row τ_RMS, 3$^\text{rd}$ row SDCF$_\text{16cm}$) for both individual (Ind.) and backscatter (BS) channels for Scenario A (left column) and Scenario B (right column). The different line types distinguish the table positions (solid lines: T1, dashed lines: T2, dash-dotted lines: T3). Additionally the BS channels are separated into fully correlated (FC) and uncorrelated channels (UC).

5.1 Analysis for Scenario A

Solid and dashed lines are table positions T1 and T2 respectively. The backscatter channel results, which are separated in fully correlated (FC - red and squares) channels (downlink =uplink / $\ell = \ell'$ and $k = k'$) and (partly) uncorrelated (UC - black and asterisks) channels ($\ell \neq \ell'$ or $k \neq k'$), and the individual (Ind. - blue and crosses) channel (downlinks/uplinks) results are depicted.

The K_{LOS} factor (in dB) for the individual channels is always positive for T1 (median of $4.2\,\mathrm{dB}$), while for T2 it is positive for $80\,\%$ of the measurements (median of $0.9\,\mathrm{dB}$). This reduction is explained by the larger distance to T2 since the power in the LOS component decreases faster than the power in the NLOS components. According to theory [2] the Rician K-factor for the LOS component of a backscatter channel is

$$K_{\mathrm{LOS},kk'} = \left(1 - \frac{\kappa}{2}\right) \frac{K_{\mathrm{LOS},k} K_{\mathrm{LOS},k'}}{1 + K_{\mathrm{LOS},k} + K_{\mathrm{LOS},k'}}, \tag{21}$$

with κ as correlation coefficient ranging from 0 to 1 for uncorrelated and fully correlated channels respectively, and $K_{\mathrm{LOS},k}$ and $K_{\mathrm{LOS},k'}$ as the Rician K-factor for the individual constituent channels. Equ. (21) shows that the backscatter K_{LOS} factor is dominated by the smaller of the two individual factors and that for fully correlated individual channels, a $3\,\mathrm{dB}$ loss is expected compared to uncorrelated channels. In Fig. 3, this loss is only $2\,\mathrm{dB}$ because the assumption of fully uncorrelated channels does not hold true within this set-up.

The RMS delay spread for the individual channels is slightly larger for T2 explained by the same reasoning as above, that the LOS component attenuates faster with increasing distance than the NLOS components. The RMS delay spread is larger for the backscatter channels since the delays are extended by the convolution of the channels. The FC data have a larger RMS delay spread than the UC data because the power in the NLOS component is increased up to a factor of two.

The median of the SDCF evaluated at a spacing of $16\,\mathrm{cm}$ is 0.7 for both individual and the uncorrelated backscatter channels, and below 0.4 to 0.5 for the fully correlated backscatter channels. With increasing distance (cmp. T1 and T2) the correlation of the DM is slightly reduced for both the individual and the backscatter channels by a value of approximately 0.1.

5.2 Analysis for Scenario B

Solid, dashed, and dash-dotted lines are table positions T1, T2, and T3 respectively. The results compare well to the data gathered in the laboratory. The K_{LOS} factor for individual channels again exceeds $0\,\mathrm{dB}$ (median of $5\,\mathrm{dB}$) and the results for the backscatter channel are slightly above the K_{LOS} factor obtained in the laboratory due to the shorter distances. The median of the RMS delay spread is $17\,\mathrm{ns}$ for the backscatter and $11\,\mathrm{ns}$ for the individual channels. The median of the SDCF evaluated at $16\,\mathrm{cm}$ is 0.4 for the FC backscatter and 0.5 for the individual and UC backscatter channels. The results for the different table positions are in general more homogeneous than for the laboratory scenario, since the table positions are partly overlapping.

120

6 Validation of the Algorithms

We finally validate the algorithms presented in Sec. 3 with simulated and measured data over a wide range of bandwidths.

6.1 Simulated Data

The algorithms are validated using simulated data, generated according to the estimated channel parameters (K_{LOS} and τ_{RMS}) from Section 5. Fig. 4 shows the REBs for the SISO (blue, solid line) and MIMO model (blue, dashed line) according to (17), as well as the REB for the MIMO model including the effect of the PDP (blue, dash-dotted line) according to (16). For Scenario A and Scenario B a 4×4 and 2×2 MIMO setup is used respectively. The effect of including the PDP dependent part in the REB is only relevant at lower bandwidths (BWs). Furthermore, the standard deviations for different estimators are depicted in Fig. 4:

- ML SISO (red solid, 'o'): The SISO ML estimator (5) is able to follow the REB to BWs in the range of $50 - 100$ MHz. At smaller BW the risk of large outliers is high, as the SINR, which determines the detectability of the LOS after whitening, is small.[14]

- MF SISO (green solid, '+'): The SISO MF estimator (7) does not consider the DM and deviates from the bound already at large BW. At small BW the MF estimator gets more robust than the ML, as the complete power of the PDP overlaps with the arrival of the LOS, and the estimator can *make use* of this power. However, the ranging precision is only in the range of the distance between the transmitting reader, the tag and the receiving reader (or higher).

- ML MIMO (red dashed, 'o'): In Section 3.3 it was argued that (18) is the REB for a MIMO setup with knowledge of the PDP and the AoD and AoA. To show that with this knowledge, the actual REB can be achieved, we use the following technique: We compute the log-likelihoods according to (4) (needing to know the DM) align them in time-domain with respect to the array positions (needing to know the AoD and AoA for the delay-sum beamformer) and take the sum over all array positions. In Fig. 4 two gains are seen for the ML MIMO estimator, (i) a precision gain at constant bandwidth, and (ii) a detection gain, as the estimator is able to follow the bound to smaller BWs compared to the ML SISO estimator.

- A1 MIMO (green dashed, '+'): The MIMO estimator applying Algorithm 1 is able to achieve the MIMO REB at large BWs. It deviates from the bound at larger BWs than the ML MIMO estimator, since the estimation of the parameters of the DM, the AoD and the AoA reduces the EFI. Interestingly, the estimator does not show the high level of outliers as the ML estimators. This can be argued in the following way: During the initialization of the algorithm, a grid search is performed which is closely related to an MF estimator. As the MF estimator does not take the DM process into account, some power of the DM process is included in the initial LOS estimate. The subsequent DM estimation procedure underestimates the power included in the DM. At small

---

[14]see dashed lines in Fig. 5 and explanation below.
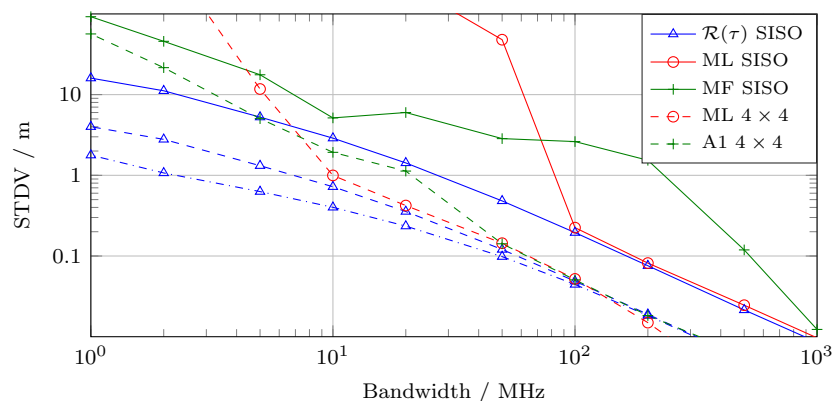
(a)
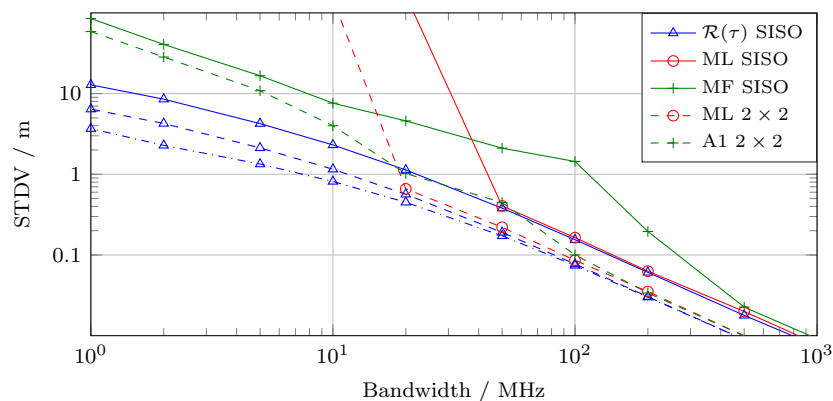
(b)

Figure 4: REB (blue, triangles) for SISO (solid), MIMO (dashed) according to (17) and MIMO including the effect of the PDP (dash dotted) according to (16), and range estimation standard deviations of the developed algorithms for simulated data (solid lines: SISO, dashed lines: MIMO). The PDP of the downlink and uplink have been modeled with a double exp. PDP [4] leading to the following channel parameters:

(a) Scenario A: $K_{\mathrm{LOS}} = -3\,\mathrm{dB}$, $\tau_{\mathrm{RMS}} = 18.6\,\mathrm{ns}$.

(b) Scenario B: $K_{\mathrm{LOS}} = 0.2\,\mathrm{dB}$, $\tau_{\mathrm{RMS}} = 18.4\,\mathrm{ns}$.

BWs (below $10\,\text{MHz}$) most of the DM interferes with the LOS component and thus most of the DM power is included in the LOS initialization. Thus, Algorithm 1 converges towards a matched filter implementation at small BW.

6.2 Measured Data

To be able to compute the REB, the associated parameters, and the ML estimators, the covariance matrix of the DM process needs to be estimated from the measured data.

6.2.1 Covariance Estimation

The covariance matrix is determined as follows.[15] At each table position, the overall 18×17 grid is reduced to smaller subgrids (5×5), leading to $N_{\text{sg}} = 9$ non-overlapping subgrids. This reduction of the grid is necessary since the covariance matrix of DM is position dependent. The following processing steps are conducted:

- Extract channel responses $\mathbf{g}_{kk',1\,\text{GHz}}$ at the largest possible bandwidth ($1\,\text{GHz}$) on a subgrid.

- Align the channel responses such that the LOS components arrive at the same time $\tau_{kk'}$.

- Estimate the complex channel coefficients $\hat{\alpha}_{kk'}$ with the projection of the CR onto the baseband pulse $\mathbf{s}_{\tau_{kk'}}$.

- Compute the mean value of the estimated complex channel coefficients $\bar{\hat{\alpha}}_{kk'}$.

- At the target bandwidth, extract channel responses $\mathbf{g}_{kk'}$, align the signals such that the LOS components arrive at the same time, subtract the LOS signal $\bar{\hat{\alpha}}_{kk'}\mathbf{s}_{\tau_{kk'}}$ and compute the covariance matrix of the resulting signals.

- To arrive at the covariance matrix for DM plus AWGN we need to add the noise variance N_0/T_{s} to the main diagonal. We define N_0 via the energy of the LOS component $E_{\text{LOS}} = |\bar{\hat{\alpha}}_{kk'}|^2 \|\mathbf{s}_{\tau_{kk'}}\|^2 T_{\text{s}}$. The SNR for the LOS component is set to $E_{\text{LOS}}/N_0 = 25\,\text{dB}$ for the following validation.

The resulting covariance matrix estimate is shown in Fig. 6 for a BW of $100\,\text{MHz}$. For the plot, the signals are shifted such that the LOS components arrive at $0\,\text{ns}$. The resulting estimate shows that the US assumption does not hold for the considered scenario. The off-diagonal terms stem from deterministic reflections at flat surfaces which are correlated via the room geometry.

6.2.2 Evaluation and Comparison to Simulated Data

To be able to apply the developed estimators to the acquired measurement data, we use the pre-processing steps laid out in Sec. 4.3 to derive the CRs at

---

[15]The estimation of the covariance matrix as described here is for the validation of the REB only. It is not a practical algorithm to be used in actual ranging / positioning applications due to its requirement of the LOS amplitudes.
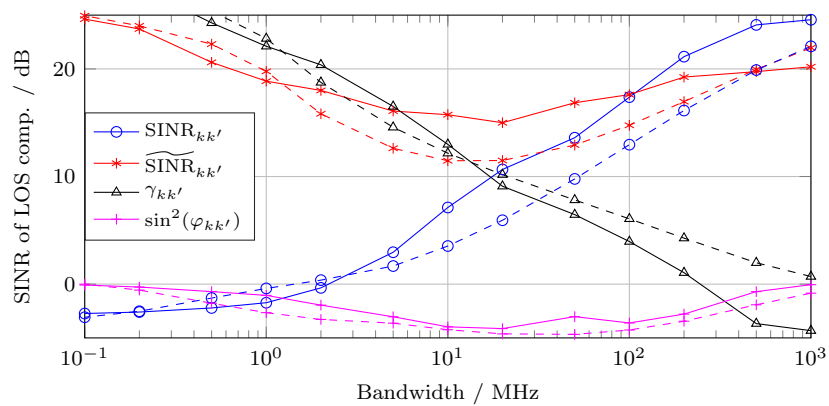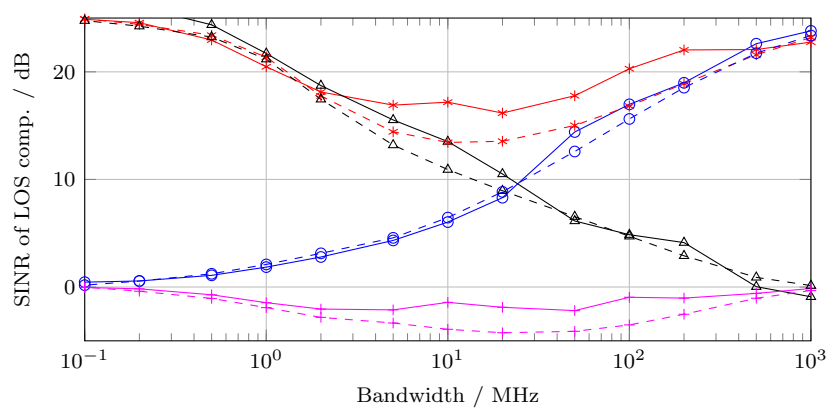
Figure 5: $\mathrm{SINR}_{kk'}$, $\widetilde{\mathrm{SINR}}_{kk'}$, whitening gain $\gamma_{kk'}$, and information loss $\sin^2(\varphi_{kk'})$ for measured (solid lines) and simulated data (dashed lines).
(a) Scenario A: measured data (solid lines / TX antenna at $\mathbf{p}_1$, table position T2, RX antenna at $\mathbf{p}_2$ / $K_{\mathrm{LOS}} = -3\,\mathrm{dB}$, $\tau_{\mathrm{RMS}} = 18.3\,\mathrm{ns}$) and simulated data (dashed lines / channel parameters see Fig. 4a).
(b) Scenario B: measured data (solid lines / TX antenna at $\mathbf{p}_2$, table position T3, RX antenna at $\mathbf{p}_4$ / $K_{\mathrm{LOS}} = 0.22\,\mathrm{dB}$, $\tau_{\mathrm{RMS}} = 18.2\,\mathrm{ns}$) and simulated data (dashed lines / channel parameters see Fig. 4b).

124
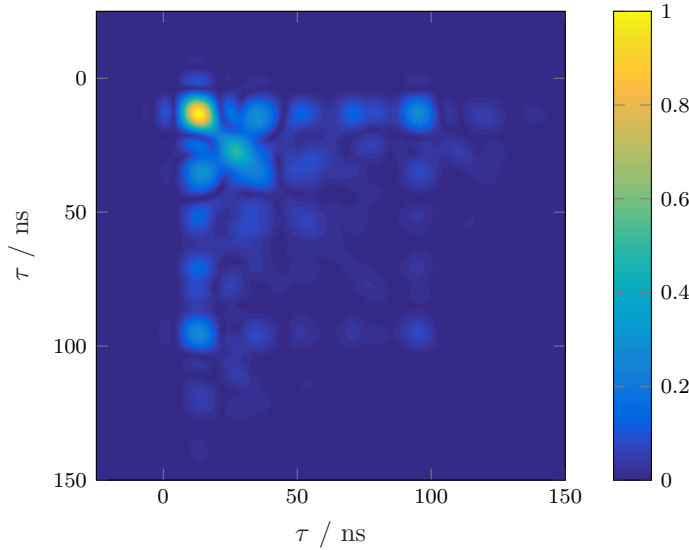
Figure 6: Estimated covariance matrix of DM at $B = 100\,\mathrm{MHz}$ for the backscatter channel from antenna 1 via tag 1 to antenna 1 measured in the laboratory scenario. For improved illustration, the absolute values scaled to the range 0-1 are shown.

the target bandwidth, and add AWGN (generated with the previously defined N_0) to obtain the received signal described in (3).

In Fig. 5, the $\mathrm{SINR}_{kk'}$, effective SINR $\widetilde{\mathrm{SINR}}_{kk'}$, whitening gain $\gamma_{kk'}$ and information loss $\sin^2(\varphi_{kk'})$ are shown for different bandwidths for both scenarios (solid lines). The SINR tends towards the SNR and towards the K_{LOS} factor for large and small bandwidth respectively. In comparison, the effective SINR is achieving the SNR also at small bandwidth. The $\mathrm{SINR}_{kk'}$ and $\widetilde{\mathrm{SINR}}_{kk'}$ describe the amplitude fading and the pulse distortion of the LOS component respectively [11]. At very large bandwidth neither pulse distortion nor amplitude fading occur as the DM is resolved from the LOS component. At small bandwidth only "flat" amplitude fading occurs as the complete DM overlaps with the LOS component. In-between these two extreme cases, both effects occur and deteriorate the ranging precision which is described by $\widetilde{\mathrm{SINR}}_{kk'}$. The two factors linking the $\mathrm{SINR}_{kk'}$ and $\widetilde{\mathrm{SINR}}_{kk'}$ are the whitening gain $\gamma_{kk'}$ and the information loss $\sin^2(\varphi_{kk'})$. In both scenarios, the comparison to simulated data (dashed lines) shows an excellent match over the entire considered bandwidth range. The main difference is the negative whitening gain at large bandwidths in Fig. 5a which is explained by a frequency dependent behavior of the antenna pattern. The useful bandwidth in this case is actually smaller than 1 GHz explaining the negative whitening gain. As the bandwidth gets smaller, the frequency dependent behavior vanishes and the simulated data fits the actual measurements. In Scenario B, this effect is not visible due to the different geometric setup.

In Fig. 7, the REB and the standard deviations of the introduced estimators are shown for a SISO and MIMO ranging scenario. The REB including the effect

Table 1: Summary of the achievable REB and standard deviations of the MF and A1 estimators for three different operating scenarios (SISO, 2x2 MIMO & 4x4 MIMO) at three different bandwidths (regulations of the ETSI (EU), FCC (US) and for operation in the 2.4 GHz ISM band) in m. The REB has been simulated with the parameters given in Fig. 5b for the SISO and 2×2 MIMO case and the parameters given in Fig. 5a for the 4×4 MIMO case.

	ETSI 3 MHz	FCC 26 MHz	ISM 83.5 MHz
REB SISO	3.68	0.70	0.19
MF SISO	3.47	0.86	0.35
REB MIMO 2x2	1.84	0.35	0.09
A1 MIMO 2x2	1.85	0.32	0.11
REB MIMO 4x4	0.86	0.19	0.06
A1 MIMO 4x4	2.08	0.52	0.18

of the PDP cannot be computed, as the US assumption (off-diagonal terms in the covariance matrix, cf. Fig. 6) is violated. The same four estimators as in Fig. 4 are analyzed:

- ML SISO (red solid, 'o'): The SISO ML estimator is able to follow the REB to BWs in the region of 50 MHz again and shows the high risk of outliers below this BW.

- MF SISO (green solid, '+'): The SISO MF estimator deviates from the REB at high BWs, and gets more robust than the ML at lower BWs, just as in the simulations. At BWs below 10 MHz, in Scenario B, it outperforms the REB which can be explained since the REB does not consider the second term in (16), leading in turn to a too high REB (cf. Fig. 4).

- ML MIMO (red dashed, 'o'): The MIMO ML estimator shows a similar behavior as in the simulations. In Fig. 7a, it starts to deviate from the bound at 50 MHz but does not show the high risk of outliers down to a BW of 10 MHz. This can be attributed to the off-diagonal terms in the covariance matrix (violation of US assumption).

- A1 MIMO (green dashed, '+'): The developed algorithm for the MIMO setup does not achieve the bound at very high BWs because the LOS-plus-DM channel model is not correct at these BWs. Here, a channel model consisting of more than one distinct specular component plus DM (a so-called geometry-based stochastic channel model [25]) should be employed. At a bandwidth below 100 MHz the algorithm starts to achieve the bound since the LOS plus DM model starts to fit the measured data better. At even lower BWs, the algorithm starts to outperform not only the MIMO ML estimator but also the REB for the MIMO case (in Scenario B). As Algorithm 1 tends towards an MF algorithm at small BWs it makes use of the DM process, hence it outperforms the MIMO ML estimator. The REB in Fig. 7 does not take the delay information of the DM process into account, which is the reason that the algorithm can outperform the REB.

In Table 1 an overview of the achievable ranging precision is listed for three different operating scenarios (Scenario B; SISO, 2x2 MIMO & Scenario A; 4x4 MIMO) at three different BW. The BW are chosen to fit into the ETSI

126
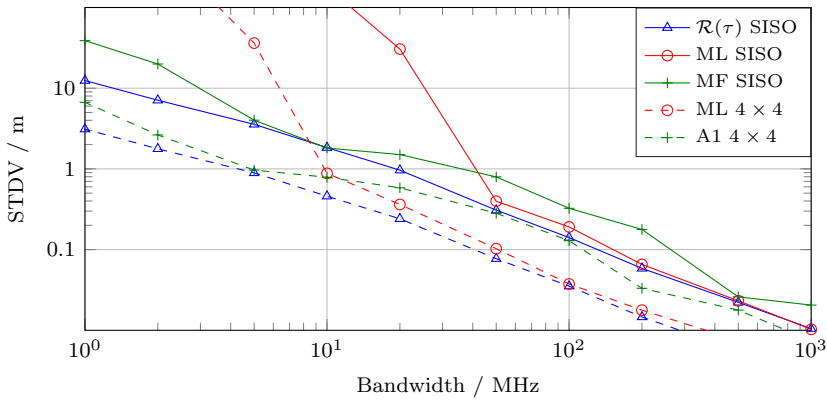
(a)
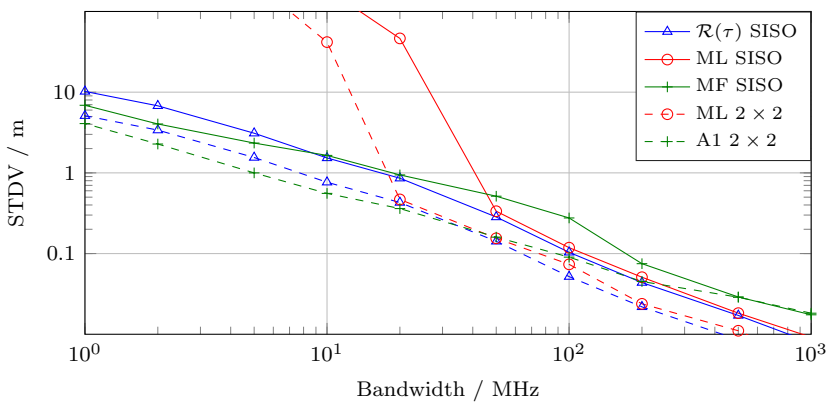
(b)

Figure 7: REB and range estimation standard deviations for measured data (solid lines: SISO, dashed lines: MIMO). The REB (blue, triangles) is depicted for the SISO and MIMO setup according to (17). Non-practical algorithms (need to know the PDP of the DM) are shown with 'o'. Practical algorithms are shown with '+'. (a) Scenario A, (b) Scenario B.

and FCC regulations for UHF RFID systems and the $2.4\,\mathrm{GHz}$ ISM band. At each BW the estimators, MF for the SISO case and A1 for the MIMO case, are compared to the REB. Interestingly, the estimator performs better for the 2×2 than the 4×4 MIMO setup. This can be explained by (i) the "better" channel parameters with respect to ranging of Scenario B [24] and (ii) the shortcomings of the algorithm: it does not take the correlations of the DM into account and assumes that the complex amplitudes as well as the DM are the same for all backscatter channels.[16] For a 2×2 setup, the ranging precision is 1.85, 0.35 and $0.11\,\mathrm{m}$ in the ETSI, the FCC and the ISM band respectively.

7 Conclusions

We analyzed channel measurements in the UHF-RFID frequency band, obtained in two different environments, a laboratory and an industrial hall. Wideband channel parameters have been analyzed, the Rician K-factor for the LOS component, the RMS delay spread, and the spaced distance correlation function. These parameters influence the achievable ranging performance which can be quantified with a Cramér Rao lower bound. This bound on the ranging error standard deviation has been validated with two algorithms which need to know the statistics of the DM with simulated data and measured data. Furthermore, two practical algorithms have been developed, (i) a naïve matched filter estimator for the SISO setup and (ii) an iterative algorithm for the MIMO setup capable of estimating the parameters of the LOS and the parameters of the DM. For a MIMO system the precision is below $20\,\mathrm{cm}$ at a bandwidth of $83.5\,\mathrm{MHz}$ which fits in the ISM band. Future research will focus on validating the developed algorithms with measurements including a real UHF-RFID tag.

This appendix derives the update equations for the MIMO algorithm presented in Section 3.2. Inserting the structured mean field approximation (10) into the variational lower bound given in (11) one can show that [21]

$$\mathcal{L}(q) = -\mathrm{KL}(q(\boldsymbol{\psi})||\tilde{f}(\boldsymbol{\psi})) + \mathrm{const.} \tag{22}$$

with KL as Kullback-Leibler divergence and

$$\tilde{f}(\boldsymbol{\psi}) = \frac{\exp(\mathbb{E}_{q(\boldsymbol{\eta})q(\alpha)}\{\log f(\boldsymbol{\theta}_{\mathrm{MIMO}}, \mathbf{r})\})}{\int \exp(\mathbb{E}_{q(\boldsymbol{\eta})q(\alpha)}\{\log f(\boldsymbol{\theta}_{\mathrm{MIMO}}, \mathbf{r})\})d\boldsymbol{\psi}}. \tag{23}$$

By choosing a point estimate for the parameters $q(\boldsymbol{\psi}) = \delta(\boldsymbol{\psi} - \hat{\boldsymbol{\psi}})$ we find from (22)

$$
\begin{aligned}
\hat{\boldsymbol{\psi}}^{\mathrm{new}} &= \underset{\hat{\boldsymbol{\psi}}}{\mathrm{argmin}} \left\{ \mathrm{KL}(\delta(\boldsymbol{\psi} - \hat{\boldsymbol{\psi}})||\tilde{f}(\boldsymbol{\psi})) \right\} = \underset{\hat{\boldsymbol{\psi}}}{\mathrm{argmax}} \left\{ \log \tilde{f}(\hat{\boldsymbol{\psi}}) \right\} \\
&= \underset{\hat{\boldsymbol{\psi}}}{\mathrm{argmax}} \left\{ \mathbb{E}_{q(\boldsymbol{\eta})q(\alpha)} \left\{ \log f(\hat{\boldsymbol{\psi}}, \boldsymbol{\eta}, \alpha, \mathbf{r}) \right\} \right\} \\
&= \underset{\hat{\boldsymbol{\psi}}}{\mathrm{argmax}} \left\{ \mathbb{E}_{q(\boldsymbol{\eta})q(\alpha)} \left\{ \log \left(f(\mathbf{r}|\hat{\boldsymbol{\psi}}, \boldsymbol{\eta}, \alpha) f(\hat{\boldsymbol{\psi}}) \right) \right\} \right\} + \mathrm{const.}
\end{aligned}
\tag{24}
$$

---

[16]As the antennas emulating an RFID reader are spaced by $20\,\mathrm{cm}$ these assumptions start to be violated.

We thus have to solve for the expectation operator in (24). This is done by choosing point estimates for the AWGN, the DM parameters $q(\boldsymbol{\eta}) = \delta(\boldsymbol{\eta} - \hat{\boldsymbol{\eta}})$, and the complex amplitudes $q(\alpha) = \delta(\alpha - \hat{\alpha})$. Since we have no prior information regarding the parameters, a uniform prior is chosen, leading to the update equation for the LOS parameters

$$\hat{\boldsymbol{\psi}}^{\text{new}} = \underset{\hat{\boldsymbol{\psi}}}{\arg\max} \left\{ - \left(\mathbf{r} - \hat{\alpha}\mathbf{s}(\hat{\boldsymbol{\psi}}) \right)^H \mathbf{C}(\hat{\boldsymbol{\eta}})^{-1} \left(\mathbf{r} - \hat{\alpha}\mathbf{s}(\hat{\boldsymbol{\psi}}) \right) \right\}.$$

By performing the same steps for the complex amplitude, (24) reads

$$
\begin{aligned}
\hat{\alpha}^{\text{new}} &= \underset{\hat{\alpha}}{\arg\max} \left\{ \mathbb{E}_{q(\boldsymbol{\eta})q(\boldsymbol{\theta})}\{\log\left(f(\mathbf{r}|\boldsymbol{\psi}, \boldsymbol{\eta}, \hat{\alpha})f(\hat{\alpha})\right)\} \right\} + \text{const.} \\
&= \underset{\hat{\alpha}}{\arg\max} \left\{ - \left(\mathbf{r} - \hat{\alpha}\mathbf{s}(\hat{\boldsymbol{\psi}}) \right)^H \mathbf{C}(\hat{\boldsymbol{\eta}})^{-1} \left(\mathbf{r} - \hat{\alpha}\mathbf{s}(\hat{\boldsymbol{\psi}}) \right) \right\}
\end{aligned}
\tag{25}
$$

As $\hat{\alpha}$ appears linearly in (25), the maximum can be found analytically as

$$\hat{\alpha}^{\text{new}} = \frac{\mathbf{r}^H \mathbf{C}(\hat{\boldsymbol{\eta}})^{-1}\mathbf{s}(\hat{\boldsymbol{\psi}})}{\mathbf{s}(\hat{\boldsymbol{\psi}})^H \mathbf{C}(\hat{\boldsymbol{\eta}})^{-1}\mathbf{s}(\hat{\boldsymbol{\psi}})}. \tag{26}$$

For the noise parameters, (24) reads

$$
\begin{aligned}
\hat{\boldsymbol{\eta}}^{\text{new}} &= \underset{\hat{\boldsymbol{\eta}}}{\arg\max} \left\{ \mathbb{E}_{q(\boldsymbol{\psi})q(\alpha)}\{\log\left(f(\mathbf{r}|\boldsymbol{\psi}, \hat{\boldsymbol{\eta}}, \alpha)f(\hat{\boldsymbol{\eta}})\right)\} \right\} + \text{const} \\
&= \underset{\hat{\boldsymbol{\eta}}}{\arg\max} \left\{ -\log\{|\mathbf{C}(\hat{\boldsymbol{\eta}})|\} - \left(\mathbf{r} - \hat{\alpha}\mathbf{s}(\hat{\boldsymbol{\psi}}) \right)^H \mathbf{C}(\hat{\boldsymbol{\eta}})^{-1} \left(\mathbf{r} - \hat{\alpha}\mathbf{s}(\hat{\boldsymbol{\psi}}) \right) \right\},
\end{aligned}
$$

where the last equality is again due to the assumption of a uniform prior for the noise parameters.

Finally, during the initialization of the algorithm it is assumed, that only AWGN is present to initialize the power spectral density N_0 and the power of the DM P_{DM}. By reducing the noise parameter vector to $\boldsymbol{\eta} = N_0$ only, and solving (24) again, an analytical solution can be found as

$$\hat{N}_0 = \frac{T_s \left(\mathbf{r} - \hat{\alpha}\mathbf{s}(\hat{\boldsymbol{\psi}}) \right)^H \left(\mathbf{r} - \hat{\alpha}\mathbf{s}(\hat{\boldsymbol{\psi}}) \right)}{NKK'}. \tag{27}$$

References

[1] J. D. Griffin and G. D. Durgin, "Gains for RF tags using multiple antennas," *IEEE Trans. Antennas Propag.*, vol. 56, no. 2, pp. 563–570, Feb. 2008.

[2] D. Arnitz, U. Muehlmann, and K. Witrisal, "Wideband characterization of backscatter channels: Derivations and theoretical background," *IEEE Trans. Antennas Propag.*, vol. 60, no. 1, pp. 257–266, Jan. 2012.

[3] M. S. Varela and M. G. Sanchez, "RMS delay and coherence bandwidth measurements in indoor radio channels in the UHF band," *IEEE Trans. Veh. Technol.*, vol. 50, no. 2, pp. 515–525, Mar. 2001.

[4] J. Karedal, S. Wyne, P. Almers, F. Tufvesson, and A. F. Molisch, "A measurement-based statistical model for industrial ultra-wideband channels," *IEEE Trans. Wireless Commun.*, vol. 6, no. 8, pp. 3028–3037, Aug. 2007.

[5] A. G. Dimitriou, S. Siachalou, A. Bletsas, and J. N. Sahalos, "A site-specific stochastic propagation model for passive UHF RFID," *IEEE Antennas Wireless Propag. Lett.*, vol. 13, pp. 623–626, 2014.

[6] H. Arthaber, T. Faseth, and F. Galler, "Spread-spectrum based ranging of passive UHF EPC RFID tags," *IEEE Commun. Lett.*, vol. 19, no. 10, pp. 1734–1737, Oct. 2015.

[7] D. Dardari, R. D'Errico, C. Roblin, A. Sibille, and M. Z. Win, "Ultrawide bandwidth RFID: The next generation?" *Proc. IEEE*, vol. 98, no. 9, pp. 1570–1582, Sep. 2010.

[8] S. Hinteregger, E. Leitinger, P. Meissner, and K. Witrisal, "MIMO gain and bandwidth scaling for RFID positioning in dense multipath channels," in *2016 IEEE Int. Conf. RFID*, May 2016, pp. 1–6.

[9] D. Dardari, A. Conti, U. Ferner, A. Giorgetti, and M. Z. Win, "Ranging with ultrawide bandwidth signals in multipath environments," *Proc. IEEE*, vol. 97, no. 2, pp. 404–426, Feb. 2009.

[10] Y. Shen and M. Z. Win, "Fundamental limits of wideband localization-part I: A general framework," *IEEE Trans. Inf. Theory*, vol. 56, no. 10, pp. 4956–4980, Oct. 2010.

[11] K. Witrisal, E. Leitinger, S. Hinteregger, and P. Meissner, "Bandwidth scaling and diversity gain for ranging and positioning in dense multipath channels," *IEEE Wireless Commun. Lett.*, vol. 5, no. 4, pp. 396–399, Aug. 2016.

[12] A. P. Dempster, N. M. Laird, and D. B. Rubin, "Maximum likelihood from incomplete data via the EM algorithm," *J, Roy. Statist., Ser. B*, vol. 39, no. 1, pp. 1–38, 1977.

[13] B. H. Fleury, M. Tschudin, R. Heddergott, D. Dahlhaus, and K. I. Pedersen, "Channel parameter estimation in mobile radio environments using SAGE algorithm," *IEEE J. Sel. Areas Commun.*, vol. 17, no. 3, pp. 434–450, Mar. 1999.

[14] A. Richter, "Estimation of radio channel paramters: Models and algorithms," Ph.D. dissertation, Technische Universitaet Ilmenau, 2005.

[15] D. Arnitz, U. Muehlmann, and K. Witrisal, "Characterization and modeling of UHF RFID channels for ranging and localization," *IEEE Trans. Antennas Propag.*, vol. 60, no. 5, pp. 2491–2501, May 2012.

[16] S. Hinteregger, J. Kulmer, M. Goller, F. Galler, H. Arthaber, and K. Witrisal, "UHF-RFID backscatter channel analysis for accurate wideband ranging," in *2017 IEEE Int. Conf. RFID*, May 2017, pp. 117–123.

130

[17] A. F. Molisch, "Ultra-wide-band propagation channels," *Proc. IEEE*, vol. 97, no. 2, pp. 353–371, Feb. 2009.

[18] P. V. Nikitin, K. V. S. Rao, and R. D. Martinez, "Differential RCS of RFID tag," *Electron. Lett.*, vol. 43, no. 8, pp. 431–432, 04 2007.

[19] F. Guidi, "Study of ultra wide band modulated backscattering based RFID systems," Ph.D. dissertation, Ecole Polytechnique Paristech, Universita degli studi di Bologna, 2013.

[20] S. Kay, *Fundamentals of Statistical Signal Processing: Estimation Theory.* Prentice Hall Signal Processing Series, 1993.

[21] C. M. Bishop, *Pattern Recognition and Machine Learning (Information Science and Statistics).* Secaucus, NJ, USA: Springer-Verlag New York, Inc., 2006.

[22] Ilmsens Channel Sounder. [Online]. Available: http://www.ilmsens.com

[23] Mini Circuits, RC-4SPDT-A18 and RC-1SP4T-A18. [Online]. Available: http://www.minicircuits.com

[24] S. Hinteregger, E. Leitinger, P. Meissner, J. Kulmer, and K. Witrisal, "Bandwidth dependence of the ranging error variance in dense multipath," in *2016 24th European Signal Processing Conf. (EUSIPCO)*, Aug. 2016, pp. 733–737.

[25] N. Michelusi, U. Mitra, A. F. Molisch, and M. Zorzi, "UWB sparse/diffuse channels, part I: Channel models and bayesian estimators," *IEEE Trans. Signal Process.*, vol. 60, no. 10, pp. 5307–5319, Oct. 2012.

d = 9.0 m

132

d = 18.0 m

Experimental Evaluation of a UHF-MIMO RFID System for Positioning in Multipath Channels

Stefan Grebien, Florian Galler, Daniel Neunteufel,
Ulrich Mühlmann, Stefan Johannes Maier,
Holger Arthaber, and Klaus Witrisal

Abstract

This paper presents an experimental evaluation of an ultra-high-frequency (UHF) multiple-input-multiple-output (MIMO) radio-frequency identification (RFID) system for positioning. To this end, we propose a set of novel parametric maximum likelihood direct-positioning algorithms capable of exploiting the coherent measurements performed by closely-spaced antennas and simultaneously exploiting the non-coherent measurements by widely-spaced antennas. The radio channel indoors for relatively small bandwidth can be characterized by a line-of-sight component plus a multitude of so-called dense multipath components (DMC). The proposed algorithm framework is able to consider the DMC, enabling more accurate positioning. We present an experimental RFID testbed, capable of performing wideband measurements up to 50 MHz bandwidth. This testbed is able to query the RFID tag at the UHF band while performing the position measurements in the 2.45 GHz band, supporting such wideband signal transmission. A dual-frequency RFID tag is presented, equipped with two antennas, scattering back synchronously at the UHF and 2.45 GHz bands. Utilizing the experimental UHF-MIMO RFID testbed we show that 80 % of the position errors are smaller 0.15 m if the DMC process is included in the algorithm.

1 Introduction

In passive ultra-high frequency (UHF)-radio frequency identification (RFID), the reader transmits a continuous wave (CW) signal which activates the tag. Once powered up, the tag receives commands from the reader and answers by switching the load of its antenna, known as backscatter modulation. The initial intention when developing the UHF-RFID technology was to replace bar codes to track goods by simply moving tagged objects through a gate. This application became so successful that the technology is now ubiquitous in retail, manufacturing, and supply-chain management.

Accurate positioning of RFID tags at decimeter level would open new applications, e.g., real-time recommender systems for brick-and-mortar stores, sorting of goods, or shelf-level navigation. Unfortunately, standard UHF-RFID systems utilize a bandwidth of several kHz only, making these systems classical narrow-band systems. This leads to one of the ultimate fontiers of RFID technology: *high-accuracy-positioning*.

It is well known that the estimation accuracy of the position in an additive white Gaussian noise (AWGN) channel can be improved by increasing the signal-to-noise ratio (SNR) and the signal bandwidth [1]. However, the indoor radio channel is characterized by a multitude of multipath components leading to so called dense multipath component (DMC). This DMC interferes with the position-information carried by the line of sight (LOS) component, thus hindering accurate positioning indoors [2,3]. This effect is even stronger for the pinhole channel experienced by a UHF-RFID system, as the backscatter channel consists of two concatenated multipath channels [4].

Thus, the signal-to-interference-ratio (SIR) introduced by the DMC, and not the SNR, ultimately dictates the performance of any RFID positioning system. The interference of the DMC can be influenced by two system parameters: (i) bandwidth, and (ii) diversity [4]. This has led to the trend to increase the bandwidth utilized in RFID systems [5–7] and to utilize multiple antennas at each reader [8–10], leading to a multiple-input multiple-output (MIMO) system.

In this paper we present a novel maximum-likelihood (ML) positioning technique which estimates besides the position, the parameters of the LOS, the DMC, and the AWGN. We analyze measurements from a UHF-MIMO-RFID testbed capable of utilizing up to 50 MHz and measuring up to 4 transmitter (TX) and receiver (RX) antennas coherently.

2 System and Signal Model

2.1 System Model

We consider L transmitting and L' receiving RFID readers, operating indoors at known positions $\boldsymbol{p}_l \in \mathbb{R}^2, \forall l \in \{1, ..., L\}$ and $\boldsymbol{p}_{l'} \in \mathbb{R}^2, \forall l' \in \{1, ..., L'\}$. Each reader is equipped with M_l and $M'_{l'}$ antennas, respectively, located at known positions $\boldsymbol{p}_{l,m_l} \in \mathbb{R}^2, \forall l \in \{1, ..., L\}, \forall m_l \in \{1, ..., M_l\}$ and $\boldsymbol{p}_{l',m'_{l'}} \in \mathbb{R}^2, \forall l' \in \{1, ..., L'\}, \forall m'_{l'} \in \{1, ..., M'_{l'}\}$. An RFID tag is located at unknown position $\boldsymbol{p} \in \mathbb{R}^2$. We consider a 2-dimensional positioning problem and assume that the RFID readers and tags are placed at the same height.

Such a scenario is illustrated in Fig. 1 which shows a floorplan of the room
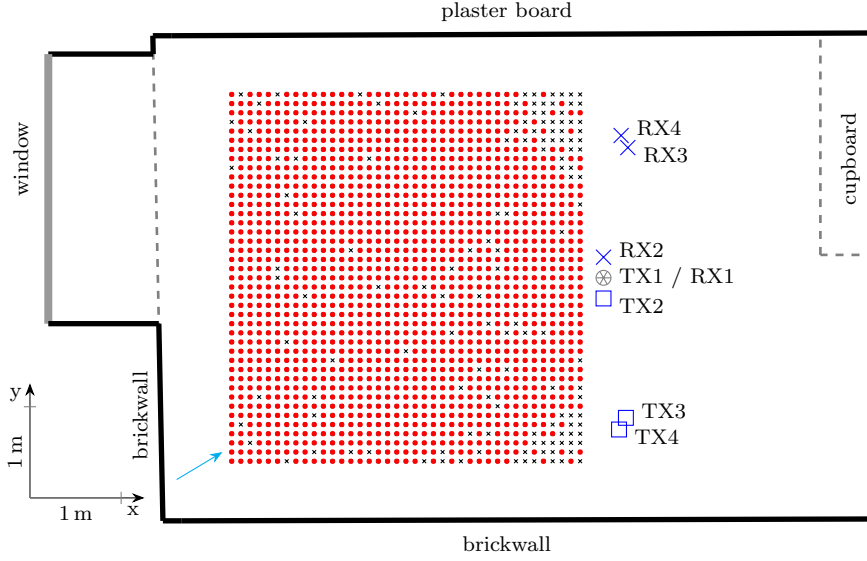
Figure 1: Floorplan of the laboratory where the measurements were performed, including the positions of the TX and RX UHF antennas ($\circ$, $*$), the TX and RX 2.4 GHz antennas ($\square$, $\times$), the positions where the tag did respond ($\cdot$), and the positions where the tag did not respond ($\cdot$). $\longrightarrow$ depicts the point of view of the photograph in Fig. 2a.

where measurements were taken (see also Sec. 4.3). This setup consists of 2 TX readers (TX2 and TX3 & TX4) and 2 RX readers (RX6 and RX7 & RX8). For a more detailed description of the setup, as well as the description of TX1 and RX1, please refer to Sec. 4.3.

2.2 Signal Model

The radio channel from the $\{l, m_l\}$-th transmitting antenna via the tag to the $\{l', m'_{l'}\}$-th receiving antenna is given by

$$h_{lm_l, l'm'_{l'}}(\tau; \boldsymbol{p}) = \alpha_{l,l'}\delta(\tau - \tau_{lm_l, l'm'_{l'}}(\boldsymbol{p})) + \nu_{lm_l, l'm'_{l'}}(\tau)$$
$$\equiv h_j(\tau; \boldsymbol{p}) = \alpha_k\delta(\tau - \tau_j(\boldsymbol{p})) + \nu_j(\tau), \tag{1}$$

where we introduced the unique mapping $j = f(l, m_l, l', m'_{l'}) \in \{1, ..., J\}$ with $J = \sum_l M_l \sum_{l'} M'_{l'}$ as the total number of channels and $k = g(l, l') \in \{1, ..., K\}$ with $K = LL'$ as the number of reader TX and RX pairs, to reduce notational complexity. We furthermore introduce the inverse mapping functions $\{l(j), m_l(j), l'(j), m'_{l'}(j)\} \triangleq f^{-1}(j)$ and $\{l(k), l'(k)\} \triangleq g^{-1}(k)$.

The first and second summand in (1) describe the LOS and the DMC, respectively. The LOS is characterized by the delay $\tau_j(\boldsymbol{p}) = \frac{1}{c}(\|\boldsymbol{p} - \boldsymbol{p}_{lm_l}\| + \|\boldsymbol{p}_{l'm'_{l'}} - \boldsymbol{p}\|)$ with c as speed of light and the complex amplitude α_k. It is assumed that the complex amplitudes only depend on the reader positions and not the individual antenna positions. The DMC $\nu_j(\tau)$ is modeled as a zero-mean Gaussian random process with auto-correlation function

$$\mathbb{E}[\nu_j(\tau)\nu^*_{j'}(\tau')] = S_\nu(\tau - \tau_j(\boldsymbol{p}))\delta(\tau - \tau')\delta[j - j'], \tag{2}$$

135
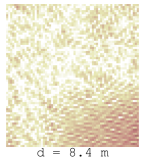
where $S_\nu(\tau)$ is the delay power spectrum (DPS). In (2) we assume that the DPS is uncorrelated in the delay domain and for different antenna combinations[1]. Furthermore, we assume that the shape of the DPS of the DMC process does not depend on the positions of the transmitting and receiving antennas.

Assume that the m_l-th antenna at the l-th TX reader transmits baseband signal $s(t)$ at a carrier frequency f_c which is scattered back by the RFID tag. The received signal $r_j(t)$ received by the $m'_{l'}$-th antenna of the l'-th RX-reader is

$$r_j(t) = \int s(t-\tau)\mathrm{e}^{-j2\pi f_c\tau}h_j(\tau;\boldsymbol{p})d\tau + w_j(t)$$
$$= \alpha_k s_j(t;\boldsymbol{p}) + \int s(t-\tau)\mathrm{e}^{-j2\pi f_c\tau}\nu_j(\tau)d\tau + w_j(t), \qquad (3)$$

where $s_j(t;\boldsymbol{p}) = s(t-\tau_j(\boldsymbol{p}))\mathrm{e}^{-j2\pi f_c\tau_j(\boldsymbol{p})}$ and $w_j(t)$ as measurement noise process modeled as independent AWGN with double-sided power spectral density $N_0/2$. The signal $s_j(t;\boldsymbol{p})$ incorporates directly the position of the tag as well as the TX and RX antenna positions.

In the receiver, the signals given in (3) are sampled with frequency $f_s = 1/T_s$. By stacking the J received signals of length $N = T/T_s$ with T as observation duration, we obtain the discrete-time signal model

$$\boldsymbol{r} = \boldsymbol{S}(\boldsymbol{p})\boldsymbol{A}\boldsymbol{\alpha} + \boldsymbol{w}_c + \boldsymbol{w} \in \mathbb{C}^{NJ\times 1}, \qquad (4)$$

where $\boldsymbol{r} = [\boldsymbol{r}_1^\mathrm{T} \cdots \boldsymbol{r}_J^\mathrm{T}]^\mathrm{T}$, $\boldsymbol{\alpha} = [\alpha_1 \cdots \alpha_K]^\mathrm{T} \in \mathbb{C}^{K\times 1}$,

$$\boldsymbol{S}(\boldsymbol{p}) = \begin{bmatrix} \boldsymbol{s}_1(\boldsymbol{p}) & \boldsymbol{0} & \cdots & \boldsymbol{0} \\ \boldsymbol{0} & \boldsymbol{s}_2(\boldsymbol{p}) & \cdots & \boldsymbol{0} \\ \cdots & \cdots & \cdots & \cdots \\ \boldsymbol{0} & \boldsymbol{0} & \cdots & \boldsymbol{s}_J(\boldsymbol{p}) \end{bmatrix} \in \mathbb{C}^{NJ\times J}, \qquad (5)$$

with $\boldsymbol{s}_j(\boldsymbol{p}) = [s_j(0;\boldsymbol{p})\ s_j(T_s;\boldsymbol{p}) \cdots s_j((N-1)T_s;\boldsymbol{p})]^\mathrm{T} \in \mathbb{C}^{N\times 1}$, $\boldsymbol{0}$ as a vector of zeros of same size and association matrix $\boldsymbol{A}$ with entries

$$[\boldsymbol{A}]_{j,k} = \begin{cases} 1 & \text{if } l(k) = l(j) \text{ and } l'(k) = l'(j) \\ 0 & \text{otherwise} \end{cases} \in \mathbb{N}^{J\times K}.$$

The advantage of this association matrix is that we can formulate an ML estimator for the position $\boldsymbol{p}$ which inherently applies coherent processing, i.e. beamforming, if a specific reader is equipped with more than one antenna. The details of this ML estimator can be found in Section 3.

Furthermore, in (4) we define the two vectors obtained by stacking and sampling the DMC $\boldsymbol{w}_c$ and AWGN $\boldsymbol{w}$. The (j,j)-th $N \times N$ subblock of the covariance matrix of the DMC process is

$$[\boldsymbol{C}_c(\boldsymbol{p},\boldsymbol{\vartheta})]_{j,j} = \int S_\nu(\tau - \tau_j(\boldsymbol{p});\boldsymbol{\vartheta})\boldsymbol{s}(\tau)\boldsymbol{s}(\tau)^\mathrm{H}d\tau, \qquad (6)$$

---

[1]Usually uncorrelated scattering in the delay and angular domains is assumed. This leads (in general) to spatial correlations of the DMC at different antennas. However, most state-of-the-art algorithms [11,12] have been developed for a spatially white DMC process, as assumed here.

where $\boldsymbol{s}(\tau) = [s(-\tau)\ s(T_\mathrm{s} - \tau)\ \cdots\ s((N-1)T_\mathrm{s} - \tau)]$ and we introduced a DPS $S_\nu(\tau; \boldsymbol{\vartheta})$ parametrized by vector $\boldsymbol{\vartheta}$. It is important to note that (6) shifts the onset of the DPS $S_\nu(\tau; \boldsymbol{\vartheta})$ to the delay of the LOS $\tau_j(\boldsymbol{p})$. The covariance matrix for the DMC and AWGN vector is

$$\boldsymbol{C}(\boldsymbol{\eta}, \boldsymbol{p}) = \boldsymbol{C}_\mathrm{c}(\boldsymbol{\vartheta}, \boldsymbol{p}) + \boldsymbol{C}_\mathrm{w} \in \mathbb{C}^{NL \times NL}, \tag{7}$$

where $\boldsymbol{C}_\mathrm{w} = \sigma_\mathrm{w}^2 \boldsymbol{I}$, with $\sigma_\mathrm{w}^2 = N_0 / T_\mathrm{s}$, $\boldsymbol{I}$ as the identity matrix of appropriate dimensions and we combined the parameters of the DPS and AWGN into $\boldsymbol{\eta} = [\sigma_\mathrm{w}^2\ \boldsymbol{\vartheta}^\mathrm{T}]^\mathrm{T}$.

Thus, the likelihood function of the model reads

$$f(\boldsymbol{r}|\boldsymbol{p}, \boldsymbol{\eta}, \boldsymbol{\alpha}) = \frac{\mathrm{e}^{-(\boldsymbol{r} - \boldsymbol{S}(\boldsymbol{p})\boldsymbol{A}\boldsymbol{\alpha})^\mathrm{H} \boldsymbol{C}(\boldsymbol{\eta}, \boldsymbol{p})^{-1} (\boldsymbol{r} - \boldsymbol{S}(\boldsymbol{p})\boldsymbol{A}\boldsymbol{\alpha})}}{\pi^{NJ} \det(\boldsymbol{C}(\boldsymbol{\eta}, \boldsymbol{p}))}, \tag{8}$$

with $\det(\cdot)$ as the determinant of a matrix.

In the derived algorithm, we use the following double-exponential parametric DPS [13]

$$S_\nu(\tau; \boldsymbol{\vartheta}) = \Omega \frac{\gamma_f + \gamma_r}{\gamma_f^2} \mathrm{e}^{-\tau/\gamma_f} (1 - \mathrm{e}^{-\tau/\gamma_r}) u(\tau), \tag{9}$$

with Ω as the power of the DMC process, γ_f and γ_r as fall and rise constant of the process, $u(\tau)$ as step function, and $\boldsymbol{\vartheta} = [\Omega\ \gamma_f\ \gamma_r]^\mathrm{T}$.

3 ML Algorithm

The likelihood function given in (8) is the basis for deriving an ML estimator for the position. The nuisance parameters, i.e., the complex amplitudes and the parameters of the DMC and AWGN have to be estimated as well.

In the following we will develop four ML estimators based on the utilized signal model: Depending on the association matrix, it is possible to utilize a non-coherent (NC) or coherent (C) combining of the measurements. Furthermore, by neglecting the DMC process, i.e., $\boldsymbol{C}_c = \boldsymbol{0}$ and thus $\eta = \sigma_\mathrm{w}^2$, an AWGN-only algorithm is obtained.

As a direct maximization of the likelihood function in (8) is not feasible, we apply variational Bayes and a structured mean-field approximation [14] to find point estimates of the position $\boldsymbol{p}$, the complex amplitudes $\boldsymbol{\alpha}$ and the parameters of the DMC and AWGN $\boldsymbol{\eta}$. To this end, we apply the following mean-field-approximation with respect to the posterior[2] distribution

$$f(\boldsymbol{p}, \boldsymbol{\alpha}, \boldsymbol{\eta}|\boldsymbol{r}) \approx q(\boldsymbol{p}, \boldsymbol{\alpha}|\boldsymbol{r}) q(\boldsymbol{\eta}|\boldsymbol{r}) = q(\boldsymbol{\theta}|\boldsymbol{r}), \tag{10}$$

where we assume that the position and the complex amplitudes are independent of the parameters of the DMC and AWGN process and introduced the overall parameter vector $\boldsymbol{\theta} = [\boldsymbol{p}^\mathrm{T} \boldsymbol{\alpha}^\mathrm{T} \boldsymbol{\eta}^\mathrm{T}]^\mathrm{T}$. We choose to minimize the Kullback-Leibler divergence from the posterior distribution $f(\boldsymbol{\theta}|\boldsymbol{r})$ to the approximating distribution $q(\boldsymbol{\theta}|\boldsymbol{r})$. This can be accomplished by maximizing the variational lower

---

[2]As we assume uniform priors for the parameters to estimate, the posterior is proportional to the likelihood.
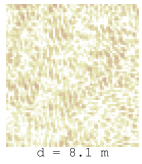
bound of the approximating distribution

$$\mathcal{L}(q) = \int q(\boldsymbol{\theta}|\boldsymbol{r}) \log \frac{f(\boldsymbol{\theta}, \boldsymbol{r})}{q(\boldsymbol{\theta}|\boldsymbol{r})} d\boldsymbol{\theta}. \tag{11}$$

By evaluating the variational lower bound for the individual subsets of parameters while keeping the other parameters fixed, an iterative local maximization of the variational lower bound can be found. In the next two paragraphs, we derive the update equations for the position, the complex amplitudes, and the parameters of the DMC and AWGN process by enforcing point estimates for the individual parameters.

Inferring the position and the complex amplitudes By keeping the parameters for the DMC and AWGN fixed, and evaluating the variational lower bound for the position and complex amplitudes, an iterative local maximization of the variational lower bound can be found [14]

$$\mathcal{L}(q) = -\mathrm{KL}(q(\boldsymbol{p}, \boldsymbol{\alpha}|\boldsymbol{r})||\tilde{f}(\boldsymbol{p}, \boldsymbol{\alpha})) + \mathrm{const} \tag{12}$$

where KL is the Kullback-Leibler divergence and

$$\tilde{f}(\boldsymbol{p}, \boldsymbol{\alpha}) \propto \exp(\mathbb{E}_{q(\boldsymbol{\eta}|\boldsymbol{r})}[\log f(\boldsymbol{p}, \boldsymbol{\alpha}, \boldsymbol{\eta}, \boldsymbol{r})]). \tag{13}$$

By choosing point estimates for the position and the complex amplitudes $q(\boldsymbol{p}, \boldsymbol{\alpha}|\boldsymbol{r}) = \delta(\boldsymbol{p} - \hat{\boldsymbol{p}})\delta(\boldsymbol{\alpha} - \hat{\boldsymbol{\alpha}})$, (12) is minimized if the point mass centers, denoted by $\hat{\boldsymbol{p}}^{\mathrm{new}}$ and $\hat{\boldsymbol{\alpha}}^{\mathrm{new}}$, are aligned with the mode of $\tilde{f}(\boldsymbol{p}, \boldsymbol{\alpha})$, leading to

$$\begin{aligned} \{\hat{\boldsymbol{p}}, \hat{\boldsymbol{\alpha}}\} &= \underset{\boldsymbol{p}, \boldsymbol{\alpha}}{\arg\max}(\mathbb{E}_{q(\boldsymbol{\eta}|\boldsymbol{r})}[\log f(\boldsymbol{p}, \boldsymbol{\alpha}, \boldsymbol{\eta}, \boldsymbol{r})]) \\ &= \underset{\boldsymbol{p}, \boldsymbol{\alpha}}{\arg\max}\big(-\log\det(\boldsymbol{C}(\hat{\boldsymbol{\eta}}, \boldsymbol{p})) \\ &\quad - (\boldsymbol{r} - \boldsymbol{S}(\boldsymbol{p})\boldsymbol{A}\boldsymbol{\alpha})^{\mathrm{H}}\boldsymbol{C}(\hat{\boldsymbol{\eta}}, \boldsymbol{p})^{-1}(\boldsymbol{r} - \boldsymbol{S}(\boldsymbol{p})\boldsymbol{A}\boldsymbol{\alpha})\big), \end{aligned} \tag{14}$$

where we assumed point estimates for the parameters of the DMC and AWGN process as well. By taking the partial derivative of (14) with respect to the complex amplitudes $\boldsymbol{\alpha}$, an analytic solution for $\hat{\boldsymbol{\alpha}}$ can be found as

$$\begin{aligned} \hat{\boldsymbol{\alpha}}(\boldsymbol{p}) =& [(\boldsymbol{S}(\boldsymbol{p})\boldsymbol{A})^{\mathrm{H}}\boldsymbol{C}(\hat{\boldsymbol{\eta}}, \boldsymbol{p})^{-1}(\boldsymbol{S}(\boldsymbol{p})\boldsymbol{A})]^{-1} \\ &\times (\boldsymbol{S}(\boldsymbol{p})\boldsymbol{A})^{\mathrm{H}}\boldsymbol{C}(\hat{\boldsymbol{\eta}}, \boldsymbol{p})^{-1}\boldsymbol{r}. \end{aligned} \tag{15}$$

Inserting (15) into (14), the update equation for the position estimate is found as

$$\begin{aligned} \hat{\boldsymbol{p}} = \underset{\boldsymbol{p}}{\arg\max}\big(&-\log\det(\boldsymbol{C}(\hat{\boldsymbol{\eta}}, \boldsymbol{p})) \\ &- (\boldsymbol{r} - \boldsymbol{S}(\boldsymbol{p})\boldsymbol{A}\hat{\boldsymbol{\alpha}}(\boldsymbol{p}))^{\mathrm{H}}\boldsymbol{C}(\hat{\boldsymbol{\eta}}, \boldsymbol{p})^{-1}(\boldsymbol{r} - \boldsymbol{S}(\boldsymbol{p})\boldsymbol{A}\hat{\boldsymbol{\alpha}}(\boldsymbol{p}))\big). \end{aligned} \tag{16}$$

Inferring the parameters of the DMC and AWGN process To find the update equation for the parameters of the DMC and AWGN process, we perform the same steps when deriving (14), leading to

$$\hat{\boldsymbol{\eta}} = \underset{\boldsymbol{\eta}}{\arg\max}(\mathbb{E}_{q(\boldsymbol{p}, \boldsymbol{\alpha}|\boldsymbol{r})}[\log f(\boldsymbol{p}, \boldsymbol{\alpha}, \boldsymbol{\eta}, \boldsymbol{r})])$$

138

$$= \arg\max_{\boldsymbol{\eta}}\big(- \log\det(\boldsymbol{C}(\boldsymbol{\eta}, \hat{\boldsymbol{p}})) \tag{17}$$
$$- (\boldsymbol{r} - \boldsymbol{S}(\hat{\boldsymbol{p}})\boldsymbol{A}\hat{\boldsymbol{\alpha}})^{\mathrm{H}}\boldsymbol{C}(\boldsymbol{\eta}, \hat{\boldsymbol{p}})^{-1}(\boldsymbol{r} - \boldsymbol{S}(\hat{\boldsymbol{p}})\boldsymbol{A}\hat{\boldsymbol{\alpha}})\big).$$

If only AWGN is considered, an analytic solution of (17) is found as

$$\hat{\sigma}_{\mathrm{w}}^2 = \frac{(\boldsymbol{r} - \boldsymbol{S}(\hat{\boldsymbol{p}})\boldsymbol{A}\hat{\boldsymbol{\alpha}})^{\mathrm{H}}(\boldsymbol{r} - \boldsymbol{S}(\hat{\boldsymbol{p}})\boldsymbol{A}\hat{\boldsymbol{\alpha}})}{NJ}. \tag{18}$$

Initialization of the algorithm A major challenge for every local maximization is to find a proper initialization scheme. In our setup, we initialize the position and the complex amplitudes by assuming the AWGN-only model and perform a grid search of the likelihood over the entire room. By inserting the AWGN only model into (14), (15) and (16) become independent of $\boldsymbol{C}$. Having initialized the position, the complex amplitudes and the variance of the AWGN samples, we initialize the parameters of the DMC and AWGN process with $\boldsymbol{\eta}^{\mathrm{init}} = [\hat{\sigma}_{\mathrm{w}}^2/2 \ \hat{\sigma}_{\mathrm{w}}^2/2 \ 20\mathrm{e}^{-9} \ 8\mathrm{e}^{-9}]^{\mathrm{T}}$ if the DMC is considered. Otherwise, we set $\eta^{\mathrm{init}} = \hat{\sigma}_{\mathrm{w}}^2$.

Proposed algorithms The introduced iterative optimization scheme together with the signal model enable a variety of different algorithms that will be explained in the following and compared in Sec. 5.

- NC-AWGN: By setting the association matrix $\boldsymbol{A}$ to a diagonal matrix, thus $J{=}K$, every antenna pair is treated as an individual reader. Another interpretation is that the likelihoods of the different antennas factorize and thus a NC combining of the different measurements is performed. Furthermore, during the update phase of the algorithm, (18) is used, meaning that the DMC is neglected. This is comparable to a classical matched-filter delay estimation [9].

- NC-DMC: For this setting, the association matrix $\boldsymbol{A}$ is still a diagonal matrix, but (17) is used during the update phase. This means that the parameters of the AWGN and DMC process are estimated. Usually, coherent measurements are needed to estimate the parameters of the DMC [11,12]. The assumption that the parameters of the DMC process do not change with respect to the TX and RX antennas enables in this version the estimation of the parameters of the DMC.

- C-AWGN: By combining antennas which are closely spaced (distance between antenna elements below the wavelength) into a single reader, thus only estimating a single amplitude α_k as a nuisance parameter and relating the phase shifts of the antenna to the position $\boldsymbol{p}$, a coherent addition of such channels is achieved. This inherently adds beamforming in an optimal sense to the algorithm. It means that for TX and RX readers with more than a single antenna, the angle-of-departure (AOD) and/or angle-of-arrival (AOA) are/is considered, respectively. Furthermore, for all reader pairs, the distance between the TX antenna, the tag and the RX antenna is included in the estimation process. For this distance estimate, additional antennas at readers increase the SNR during the estimation process. As for the NC-AWGN estimator, only AWGN is considered.

139
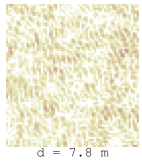
Algorithm 1: Summary of the proposed algorithms.

---

set the association matrix $\boldsymbol{A}$ according to the algorithm:

- NC-AWGN & NC-DMC: diagonal matrix

- C-AWGN & C-DMC: according to the scenario

Initialization:

- perform grid search for
  $\boldsymbol{p}^{\mathrm{init}} = \max\left\{-(\boldsymbol{r} - \boldsymbol{S}(\boldsymbol{p})\boldsymbol{A}\hat{\boldsymbol{\alpha}}(\boldsymbol{p}))^{\mathrm{H}}(\boldsymbol{r} - \boldsymbol{S}(\boldsymbol{p})\boldsymbol{A}\hat{\boldsymbol{\alpha}}(\boldsymbol{p}))\right\}$, with $\hat{\boldsymbol{\alpha}}(\boldsymbol{p})$
  according to (15).

- compute $\boldsymbol{\alpha}^{\mathrm{init}}(\boldsymbol{p}^{\mathrm{init}})$ according to (15)

- estimate $\hat{\sigma}_{\mathrm{w}}^2$ (18) and initialize $\boldsymbol{\eta}^{\mathrm{init}}$ according to the different algorithms:
  NC-AWGN, C-AWGN: $\eta^{\mathrm{init}} = \hat{\sigma}_{\mathrm{w}}^2$
  NC-DMC, C-DMC: $\boldsymbol{\eta}^{\mathrm{init}} = [\hat{\sigma}_{\mathrm{w}}^2/2 \ \hat{\sigma}_{\mathrm{w}}^2/2 \ 20\mathrm{e}^{-9} \ 8\mathrm{e}^{-9}]^{\mathrm{T}}$

Iterations:
do

update $\hat{\eta} \equiv \hat{\sigma}_{\mathrm{w}}^2$ according to (18) (NC-AWGN, C-AWGN) or $\hat{\boldsymbol{\eta}}$ (17)
(NC-DMC, C-DMC)
update $\hat{\boldsymbol{p}}$ and $\hat{\boldsymbol{\alpha}}$ according to (16) and (15)
while *not converged*;

- C-DMC: The fourth variant of the proposed algorithm does not only utilize the coherent processing introduced above, but also considers the DMC process. It has been shown that proper treatment of the DMC leads to a more accurate and robust distance, AOD, AOA and thus position estimation [4,15].

A summary of the proposed algorithms is presented in Algorithm 1.

4 Results

In this section, we present the utilized bandwidth extension with respect to classical UHF-RFID tags and introduce the testbed as well as a dual-frequency RFID tag used for measurements in a laboratory environment. Finally, we employ the developed ML algorithms to the measured data and show positioning results.

4.1 Bandwidth Extension for RFID tags

To be able to utilize a higher bandwidth and increase the positioning performance, a previously developed broadband system for backscatter tags is employed [6]. This method superimposes a low power broadband reference signal onto the interrogator's signal during tag-to-reader communication. The received signal by the interrogator is cyclically aligned and averaged over the same number of 'zero' and 'one' modulation bits of the tag. This process suppresses signal components of static echos and antenna coupling. Hence, the reference signal
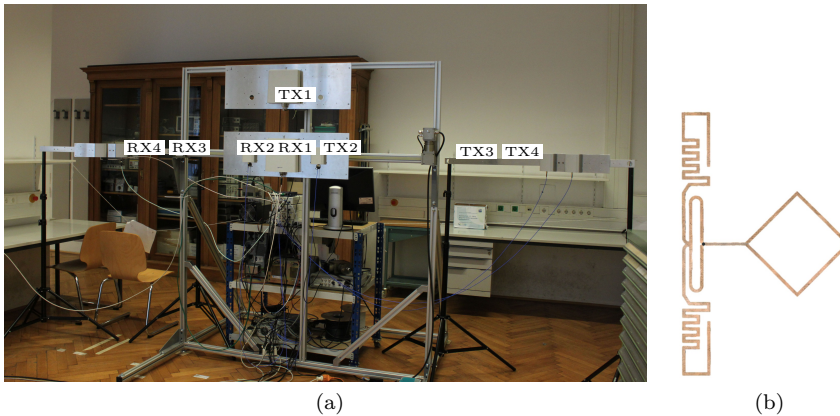
Figure 2: Picture of the measurement scenario (a) and picture of the dual-frequency RFID tag (b). The point of view with respect to the floorplan is shown with ⟶ in Fig. 1.

transmitted over the backscatter channel can be measured. In this work, a 255 bit long maximum length sequence with a chip rate of 25 MHz is used.

4.2 Architecture of the testbed

For the experimental research on the proposed positioning algorithms, an RFID reader testbed based on an off-the-shelf software defined radio (SDR) was developed. Among the wide range of different SDRs the Ettus research N210 with the SBX daughter board was chosen. The main reasons were the accessibility of the schematics, and the high sampling rate of 100 MHz. To be able to communicate with RFID tags, stringent timing requirements need to be met during the interrogation. Furthermore, for the positioning method under research, a large bandwidth and a high resolution of the received signal are necessary, which are limited by the Ethernet data rate when the standard GNU radio framework is used. A custom field programmable gate array (FPGA) design was developed to overcome these issues.

For this implementation, a light-weight electronic product code (EPC) decoder and encoder were developed. The decoder was designed to provide accurate information of the sub bit edges in the 100 MHz time domain, which is essential for the coherent adding explained in [6]. Furthermore, a logic was designed such that an arbitrary signal can be cyclically added to the EPC transmitter. A RX was developed such that the coherent adding is already done within the FPGA and the data needed to be transferred to a PC for post-processing is reduced.

Furthermore, to be able to perform research with multiple-input multiple-output (MIMO) systems a synchronization over the "MIMO link[3]" was developed [8].

UHF-RFID tags are designed for good sensitivity in a narrow frequency band in the range from $865 - 928$ MHz. This makes positioning with a wideband sig-

---

[3]A connector of the USRP enabling high speed data transfer and synchronization directly between two USRPs.
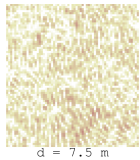
nal utilizing off-the-shelf UHF-RFID tags difficult since noticeable signal distortions occur[4]. Therefore, a dual-frequency tag was designed which can be seen in Fig. 2b. Its design is based on the UCODE 7 IC and in addition to the normal RFID operation in the UHF band, the tag employs a 2.45 GHz antenna, scattering back synchronously with the EPC backscatter modulation. This enables the extension of the tested to the 2.45 GHz band, conceptually described in [8]. The localization signal in the 2.45 GHz band was transmitted with an EIRP of 8 dBm. The maximum allowed power-level for tranmission in the 2.45 GHz band in the EU without listen before talk is 10 dBm [16]. Thereby, it is much higher than the allowed powerlevel in the UHF band. Another advantage is that the antenna employed for the localization of the RFID tag is designed to be wideband leading to fewer signal distortions.

4.3 Measurement Setup

The floorplan and a picture of the measurement setup are presented in Fig. 1 and in Fig. 2a, respectively. In Fig. 1 the TX and RX antennas are depicted by □ and ×, respectively. These antennas transmit and receive the localization sequence in the 2.45 GHz band, while the UHF reader, which powers up and queries the tag, is presented by the ○ and ∗ (placed on top of each other). The utilized antennas are six Huber&Suhner SPA-2400/75/0/V and two Huber&Suhner SPA-8090/78/8/0/V antennas for the 2.45 GHz and UHF bands, respectively.

All antennas were placed at a height of 1.45 m above the ground except for the UHF transmit antenna which was placed on a height of 2 m. The height difference of the UHF transmit antenna does not influence the positioning problem, as it is only used to power up the tag. The RFID tag was positioned on a grid with size 3.8×4 m with a spacing of 10 cm by an automated tag positioning system. This system uses four winches and high tensile strength lines connected to a suspended tag [8]. The measured positions are presented by ·, while the positions where the tag answered are represented by ·. Only the positions where the tag answered can be used for the positioning algorithms.

For the following results, only the antennas transmitting and receiving in the 2.45 GHz band have been used (presented by □ and × in Fig. 1). For the NC-AWGN and NC-DMC algorithms, all TX-RX antenna pairs are treated as individual readers, i.e., we have 3 TX and RX readers with 1 antenna per reader leadign to a total of $J = K = 9$ channels. For the C-AWGN and C-DMC algorithms, the antennas TX3 & TX4 and RX3 & RX4 are combined to form a reader. Thus, 2 TX and RX readers are utilized, either equipped with 2 or 1 antenna, leading to $J = 9$ channels and $K = 4$ TX-RX reader pairs.

5 Evaluation of the Algorithm

Fig. 3 illustrates the cumulative distribution functions (CDF) of the position error, defined as $P(\|\boldsymbol{p} - \hat{\boldsymbol{p}}\| \leq \Delta e_p)$, for the proposed algorithms. The NC-AWGN algorithm (- ⊚ -) shows the largest errors and the most outliers. Remember that the NC-AWGN algorithm does not make coherent use of the closely spaced antennas TX3 & TX4 and RX3 & RX4. The NC-DMC algorithm (—⊚—) which

---

[4]However, the presented testbed and algorithm work with off-the-shelf UHF-RFID tags.
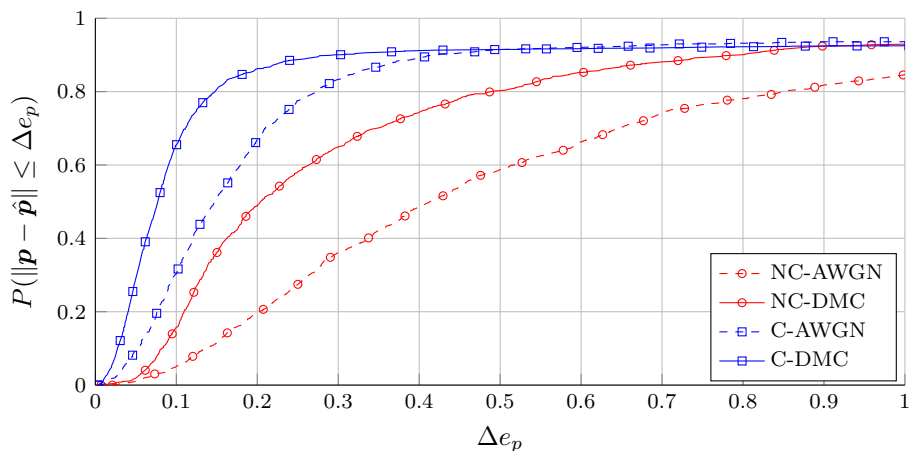
Figure 3: CDF of the position error for the proposed algorithms NC-AWGN
($-\circ-$), NC-DMC ($-\!\!\circ\!\!-$), C-AWGN ($-\square-$), and C-DMC ($-\!\!\square\!\!-$).

considers the DMC process increases the positioning accuracy significantly and
reduces the number of outliers. The coherent versions, C-AWGN ($-\square-$) and
C-DMC ($-\!\!\square\!\!-$), profit from the additional information in the coherent measure-
ments. 80 % of the position errors are below 0.28 and 0.15 m for the C-AWGN
and C-DMC algorithm, respectively.

In Fig. 4 the position error at the measured positions is presented in a color-
coded way for the C-DMC algorithm. The position error is capped at 1 m and
positions where the tag did not answer are presented in white.

As can be seen in Fig. 3 and Fig. 4, all proposed methods show about 10 %
outliers, meaning that the position error is larger 1 m. As can be seen, most of
the outliers do form a circle-like shape around the center of the measured grid.
This can be related to a poor geometry of the reader antennas as illustrated in
Fig. 4. Due to the backscatter channel, the 'small apertures' of the two arrays
formed by TX3 & TX4 and RX3 & RX4, and the non-ideal placement of the
additional readers TX2 and RX2, the evaluated likelihood function during the
initialization shows side-modes which are mirrored at a straight line from TX1
towards the window. Due to the DMC and AWGN process, such a side-mode
can be higher than the correct mode. As the consecutive iterative algorithm
optimizes locally, it cannot recover to find to the correct mode.

In Fig. 3, the advantage of considering the DMC process can clearly be seen.
Note that we assumed that the parameters of the DMC process do not change
for the different channels, but rather that only the onset of the DMC is shifted
(cmp. (6)). Usually, it is assumed that the DPS, given by (2), is stationary only
within a small local area [3, 13]. However, as the utilized bandwidth is 25 MHz,
the covariance matrix, given in (6), is quasi-stationary in a larger area [17].

6   Conclusions

In this work, we introduced a novel positioning algorithm for a dual-frequency
RFID tag, capable of estimating the position, the complex amplitude and the
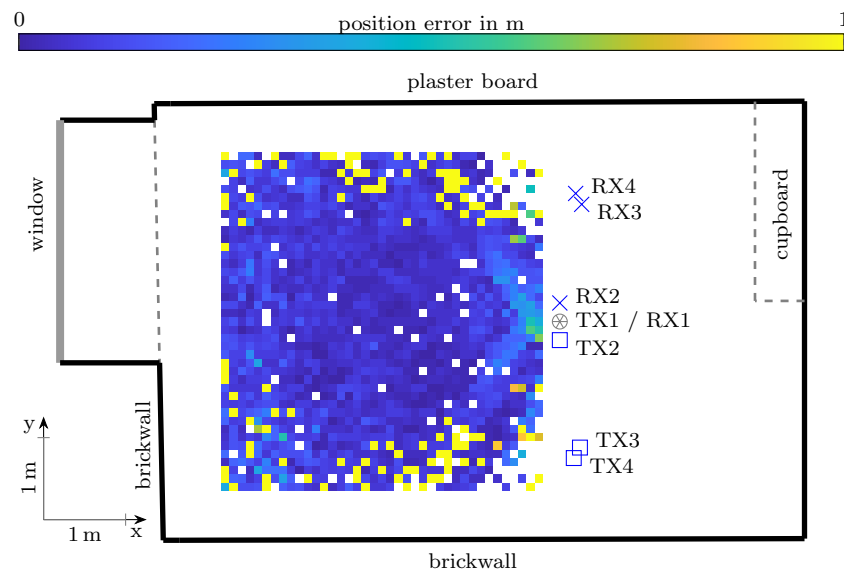
Figure 4: Position error over the entire measurement scenario for the C-DMC algorithm.

parameters of the DMC and AWGN process. By utilizing coherent processing of closely-spaced antennas, an ML estimator is proposed and analyzed. Furthermore, a UHF-MIMO experimental testbed is presented enabling coherent processing of up to 4 TX and RX antennas as well as a bandwidth extension of up to 50 MHz. It is shown that by considering the DMC 80 % of the position errors lie below 0.15 m for a bandwidth of 25 MHz.

References

[1] S. Kay, *Fundamentals of Statistical Signal Processing: Estimation Theory.* Upper Saddle River, NJ, USA: Prentice Hall Signal Processing Series, 1993.

[2] Y. Shen and M. Z. Win, "Fundamental limits of wideband localization-part I: A general framework," *IEEE Trans. Inf. Theory*, vol. 56, no. 10, pp. 4956–4980, Oct. 2010.

[3] K. Witrisal, E. Leitinger, S. Hinteregger, and P. Meissner, "Bandwidth scaling and diversity gain for ranging and positioning in dense multipath channels," *IEEE Wireless Commun. Lett.*, vol. 5, no. 4, pp. 396–399, Aug. 2016.

[4] S. Hinteregger, E. Leitinger, P. Meissner, and K. Witrisal, "MIMO gain and bandwidth scaling for RFID positioning in dense multipath channels," in *2016 IEEE Int. Conf. RFID*, May 2016, pp. 1–6.

[5] D. Dardari, R. D'Errico, C. Roblin, A. Sibille, and M. Z. Win, "Ultrawide bandwidth RFID: The next generation?" *Proc. IEEE*, vol. 98, no. 9, pp. 1570–1582, Sep. 2010.

[6] H. Arthaber, T. Faseth, and F. Galler, "Spread-spectrum based ranging of passive UHF EPC RFID tags," *IEEE Commun. Lett.*, vol. 19, no. 10, pp. 1734–1737, Oct. 2015.

[7] X. Hui, Y. Ma, and E. C. Kan, "Real-time code-division multi-tag localization with centimeter accuracy," in *2017 IEEE International Conference on RFID (RFID)*, May 2017, pp. 110–116.

[8] F. Galler, S. Grebien, T. Faseth, K. Witrisal, G. Magerl, and H. Arthaber, "Extension of an SDR UHF RFID testbed for MIMO and monostatic time of flight based ranging," *IEEE Journal of Radio Frequency Identification*, vol. 1, no. 1, pp. 32–38, March 2017.

[9] S. Grebien, J. Kulmer, F. Galler, M. Goller, E. Leitinger, H. Arthaber, and K. Witrisal, "Range estimation and performance limits for UHF-RFID backscatter channels," *IEEE Journal of Radio Frequency Identification*, vol. 1, no. 1, pp. 39–50, March 2017.

[10] M. Scherhäufl, M. Pichler, and A. Stelzer, "Maximum likelihood position estimation of passive uhf rfid tags based on evaluation of backscattered transponder signals," in *2016 IEEE Topical Conference on Wireless Sensors and Sensor Networks (WiSNet)*, Jan 2016, pp. 24–26.

[11] A. Richter and R. S. Thoma, "Joint maximum likelihood estimation of specular paths and distributed diffuse scattering," in *IEEE Vehicular Technology Conf., VTC 2005-Spring*, 2005.

[12] B. Hanssens, E. Tanghe, D. P. Gaillot, M. Liénard, C. Oestges, D. Plets, L. Martens, and W. Joseph, "An extension of the RiMAX multipath estimation algorithm for ultra-wideband channel modeling," *EURASIP Journal on Wireless Communications and Networking*, vol. 2018, no. 1, p. 164, Jun 2018. [Online]. Available: https://doi.org/10.1186/s13638-018-1177-3

[13] J. Karedal, S. Wyne, P. Almers, F. Tufvesson, and A. F. Molisch, "A measurement-based statistical model for industrial ultra-wideband channels," *IEEE Trans. Wireless Commun.*, vol. 6, no. 8, pp. 3028–3037, Aug. 2007.

[14] C. M. Bishop, *Pattern Recognition and Machine Learning (Information Science and Statistics)*.   Secaucus, NJ, USA: Springer-Verlag New York, Inc., 2006.

[15] T. Wilding, S. Grebien, U. Mühlmann, and K. Witrisal, "AoA and ToA accuracy in dense multipath channels," in *2018 IEEE ICL-GNSS*, June 2018.

[16] *ETSI EN 300 328 v2.1.1, Wideband transmission systems; Data transmission equipment operating in the 2.4 GHz ISM band and using wide band modulation techniques; Harmonised Standard covering the essential requirements of article 3.2 of Directive 2014/53/EU*, European Telecommunications Standards Institute Std.

[17] G. Steinböck, T. Pedersen, B. H. Fleury, W. Wang, and R. Raulefs, "Experimental validation of the reverberation effect in room electromagnetics," *IEEE Trans. Antennas Propag.*, vol. 63, no. 5, pp. 2041–2053, May 2015.

146

Super-Resolution Channel Estimation Including the Dense Multipath Component — A Sparse Variational Bayesian Approach

Stefan Grebien*, Erik Leitinger*, Klaus Witrisal, Bernard H. Fleury

* Have equally contributed as first authors.

Abstract

In this paper, we present a sparse Bayesian learning (SBL) algorithm for super-resolution estimation of single-input-multiple-output (SIMO) multipath channel parameters. The algorithm is developed for estimating the two-dimensional dispersion parameters, delay and angle of arrival (AoA), of the multipath components. SBL algorithms are well suited for estimating jointly the model order and parameters of superimposed signals. Specifically, the proposed algorithm is a Type-II SBL algorithm with a hierarchical Gaussian prior. It considers — beside the parameters of the specular multipath components (SMCs) — also the parameters of the dense multipath component (DMC) and noise. Typically, the DMC incorporates SMCs that cannot be resolved due to the finite aperture of the measurement equipment. The DMC can severely degrade the estimation accuracy of the dispersion parameters of SMCs, if not properly dealt with. We formulate a theoretical framework to derive a probability of estimating artifacts using non-stationary χ^2-random fields. The framework is used to adapt a threshold to counteract the trend of point-estimate-based SBL algorithms to overestimate the number of signal components, i.e., the model order. Using synthetic and real channel measurements, we show that the proposed algorithm has the ability to estimate the parameters of correctly detected SMCs and of the DMC with high accuracy. We compare our results with a state-of-the-art parametric Type-I maximum likelihood channel estimation algorithm and show the benefits of our proposed method.

147

1 Introduction

Future 5G wireless communication technologies and the Internet of Things (IoT) paradigm will be characterized by supporting a variety of services with high quality requirements, addressing performance metrics such as reliability, latency, data throughput, and resource-efficient use of the infrastructure [1, 2]. Spatial location information is expected to become an indispensable feature of these emerging wireless networks, considering that the user devices will have the capability of estimating accurately their locations and predicting relevant radio channel quality measures [3, 4]. The robustness of acquired location information strongly depends on the surrounding environment and hence multipath propagation [5–7]. To exploit efficiently the position-related information acquired from the multipath channels for localization [6–10], high performance multiantenna parametric channel estimators are needed. Note that in general, the estimation of multipath channel parameters can be cast as a line spectral estimation (LSE) problem [11–13].

1.1 State of the Art

Parametric channel models are in general represented by superimposed weighted Dirac delta distributions with distinct locations (atoms) in the respective domain (delay, angle, space, frequency). Usually, a finite measurement aperture leads to a model based on the convolution of the response of the measurement equipment with these atoms. Expectation-maximization algorithms (EM) [14] were suggested first to estimate parameters of superimposed signals. Next, space-alternating EM methods [15, 16] evolved and were used in the context of wideband radio channel data. In recent years, these estimators have been extended towards a channel model which includes a dense multipath component (DMC), multipath components that cannot be resolved by the finite measurement aperture [17]. Considering the DMC process can significantly improve the estimation accuracy of the locations of the atoms and their according weights [17]. However, all these estimators have in common that they do not incorporate the model order into the estimation problem directly, even though it has a pivotal role when estimating superimposed model parameters from real measured data. Traditionally, estimators are augmented by a separate model-order selection based on information theoretic criteria as for example the Akaike information criterion (AIC), the Bayesian information criterion (BIC), or the minimum description length (MDL) [18–20]. Yet, such approaches are computationally intensive as the information criteria need to be computed first for each model order candidate before a decision can be made. But more importantly, it has been shown that information-criterion-based model-order estimation tends to be positively biased in non-asymptotic regions of SNR and number of observed samples. Hence, artifacts that are induced by the estimators themselves are a pitfall of these procedures. A number of penalty terms have been proposed to correct this bias [21].

Another approach towards joint estimation of superimposed signal parameters and model-order selection has emerged within the field of sparse signal reconstruction (SSR) [22–24]. SSR aims at recovering a sparse weight vector in an underdetermined linear model with a known discrete dictionary (matrix) [25]. It solves an optimization problem with $L1$-norm regularization also

called basis pursuit denoising [26] or LASSO (least absolute shrinkage and selection operator) [24]. SSR can also be formulated within the Bayesian framework as maximum-a-posteriori (MAP) estimator using a sparsity promoting prior on the weight vector distribution [27]. From a (probabilistic) graphical model point of view, learning methods using hierarchical sparsity promoting priors (Laplacian or gamma priors) were coined with the name sparse Bayesian learning (SBL) [28–32]. In [33], Type-I and Type-II estimators of sparsity-promoting hyperpriors are discussed. Type-I estimators can be seen as maximum a posteriori (MAP) estimators using sparsity-inducing prior distributions and marginalizing over these priors while Type-II estimators maximize the evidence of the priors. All these methods have in common that they only consider a finite discretized dictionary to represent the signal parameters as for example the line spectral frequencies, i.e., the SMC parameters.

The main shortcoming of a finite discretized dictionary is the occurrence of aliased atom locations, which leads again to a positive model bias and inaccurate estimation of locations. Partly, this can be circumvented by increasing the granularity of the dictionary, but with a significant increase of computational cost and without removing the tendency of model bias especially in asymptotic regions. Extension of SSR to a continuous dictionary, which leads to super-resolution capabilities[1], as found in [34–39]. In there, the regularization term is the atomic norm or total variation norm. Many SBL algorithms as for example [12, 13, 40, 41] naturally include the estimation of atom's locations into the inference process and therefore support super resolution. These algorithms differ in some aspects as for example (i) the chosen sparsity-inducing hierarchical prior model, e.g. gamma-Gaussian [40, 41], Bernoulli-Gaussian [12, 13], (ii) the statistical structure of the location parameters, i.e. if they are modeled independently [12, 40] or joint [41], or (iii) whether the full posterior of the location parameters is inferred [12] or point estimates are acquired [13, 40, 41].

Instances of Type-II algorithms, as for example for reformulated automatic relevance determination (R-ARD) [27] and iterative R-ARD (IR-ARD) [42, 43], contain a threshold which is used to decide whether a signal atom is kept. In [27, 42, 43] it was shown that the model-order determination by thresholding still leads to a positive model bias. By considering the full posterior of the superimposed signal parameters, and in particular of the atom locations, a significant reduction of the positive model bias was achieved [12]. [2] In general, it was observed that reducing posterior pdfs of model parameters to point estimates has the tendency to induce a positive model-order bias. However, considering the full posterior pdfs of the model parameters comes typically at the cost of an increased complexity.

In [41], an adapted threshold was derived for detecting signal atoms for a Type-II maximum-likelihood (ML) SBL algorithm. This adaptation almost eliminates the positive model bias. Based on the fact that the detection is closely related to the extreme value distribution of the maximum of a periodogram and therefore of a random field [45, 46]. Using χ^2-random fields, an upper bound was derived on the probability of estimating artifacts (and on the according probability of missed detection of signal atoms) under the simplifying assumption of

---

[1]Super resolution in the context of optimization or inference means that an algorithm is capable of recovering signal locations beyond the sensing equipment's resolution.

[2]A Markov chain Monte Carlo implementation to infer the location parameters of superimposed signals jointly with model order selection can be found in [44].

non-overlapping signal atom artifacts in noise. Numerical analyses have shown that signal atom pruning using this adapted threshold leads to almost no positive model bias in medium and high SNR regions and tendency of underestimating the model order in low SNR regions. As comparison, in classical detection theory [47], the detection threshold is derived for a single signal atom with unknown frequency in noise by analyzing the maximum of a periodogram at the n Fourier frequencies. This leads to a (detection-)threshold that contains the probability of estimating artifacts (i.e. false alarm probability) and a $\log n$-term considering for the n Fourier frequencies, but not a random-field-theory-related $\log \log n$-term that considers for the $\arg\max$-function on the periodogram [41, 45, 46].

1.2   Contributions of the Paper

In this paper, we propose a Type-II ML SBL algorithm with a hierarchical Gaussian prior for single-input-multiple-output (SIMO) multipath channels considering also the parameters of the DMC process. It jointly estimates the two-dimensional dispersion parameters, delay and angle of arrival (AoA), of the SMCs, the parameters of the DMC and noise, and the number of SMCs (the model order). Furthermore, the probability of artifact is derived for this SIMO multipath channel model, which can be used to reduce the positive model bias substantially.

The contributions of this paper are the following:

- Development of a Type-II point-estimate-based SBL algorithm with a hierarchical Gaussian prior for SIMO multipath radio channels[3], which is applicable to colored non-stationary noise models, i.e. measurement noise plus a DMC are accounted for. The algorithm jointly estimates the delays and AoAs of the SMCs, the parameters of the DMC and noise processes, and the model order.

- Derivation of the probability of artifacts of the SIMO multipath channel model by using two-dimensional non-stationary χ^2-random fields [48, 49].

- In-depth analysis of the proposed algorithm and the derived adaptive threshold using synthetically generated channel measurements.

- Comparison with an equivalent Type-I point-estimate-based ML algorithm.

- Room-geometry-related analysis of the parameters of the SMCs estimated from real channel measurements acquired in an indoor environment.

The remainder of the paper is structured as follows: In Section 2 we introduce the signal model and the underlying statistical structure. Section 3 presents the statistical inference problem and the structure of the sparsity inducing hierarchical prior and Section 4 formulates the variational inference algorithm. In Section 5 the adapted threshold is derived for the pruning condition. Section 7 reports numerical results using synthetic and real channel measurements. Section 8 concludes the paper.

---

[3]The presented algorithm is designed for a multiple-input–single-output (MISO) and single-input–multiple-output (SIMO) system, but the extension to a multiple-input–multiple-output (MIMO) system is straightforward.

150

2 Signal Model

2.1 Channel Model

We consider an experimental setup with an ultra-wideband measurement equipment consisting of a transmitter and a receiver operating in an indoor environment. The transmitter is equipped with a single antenna, while an antenna array with colocated elements is mounted at the receiver. For the sake of simplicity we assume a two dimensional scenario with horizontal-only propagation.[4] We also postulate that the transmitter and the receiver are located sufficiently far away from each other and from objects in the environment that notably affect propagation, like walls, boards, etc. so that the plane-wave assumption is realistic.

The experimental setup allows for investigating dispersion in the radio channel in delay and angle of arrival (AoA) at the receiver site. The system response characterizing this mechanism is the delay-AoA spread function that we denote by $h(\tau, \varphi)$, with $\tau \in \mathbb{R}$ and $\varphi \in [-\pi, +\pi)$ being respectively the (relative) delay and AoA variables.[5] Obviously $h(\tau, \varphi)$ depends on the position of the transmitter and receiver in the environment. We make the common assumption that the time-frequency-space aperture of the sounding equipment is selected so that $h(\tau, \varphi)$ is nearly constant over it. This will be the case provided the propagation conditions remain practically the same over a region including the receive array. Furthermore, the electromagnetic properties of the objects, such as reflection and transmission coefficients, that significantly affect propagation are nearly constant over the observed frequency range. In this study we assume that the delay-AoA spread function consists of the superposition of a finite number, say K, of specular components and a dense (diffuse) component, i.e.

$$h(\tau, \varphi) = \sum_{k \in \mathcal{K}} \tilde{\alpha}_k \delta(\tau - \tilde{\tau}_k) \delta(\varphi - \tilde{\varphi}_k) + \nu(\tau, \varphi). \tag{1}$$

The kth specular multipath component (SMC), $k \in \mathcal{K} \triangleq \{1, \ldots, K\}$, is characterized by its amplitude $\tilde{\alpha}_k \in \mathbb{C}$, its (relative) delay $\tilde{\tau}_k \in \mathbb{R}$ and AoA $\tilde{\varphi}_k \in [-\pi, +\pi)$. We model the dense multipath component (DMC) $\nu(\tau, \varphi)$ as a complex circular (i.e. zero-mean) Gaussian random process [17, 51]. Furthermore, we assume uncorrelated scattering in which case the auto-correlation function of $\nu(\tau, \varphi)$ takes the form

$$\mathbb{E}[\nu(\tau', \varphi')\nu^*(\tau, \varphi)] = P(\tau, \varphi; \boldsymbol{\vartheta})\delta(\tau' - \tau)\delta(\varphi' - \varphi) \tag{2}$$

with the delay-AoA power spectrum $P(\tau, \varphi; \boldsymbol{\vartheta})$ [52] being entirely determined by a vector parameter $\boldsymbol{\vartheta}$ that we shall specify later. The rationale behind the selection of the model (1) is as follows. Specular components originate from electromagnetic wave propagation in the environment that is essentially non-dispersive, such as LOS propagation, specular reflection and transmission. SMCs are such specular components that can be resolved by the measurement equipment with its finite sounding aperture (in space and frequency). The DMC

---

[4]An extension to three dimensional scenarios with horizontal and vertical propagation is straightforward, but it would lead to a cumbersome notation and one would not gain any new insights.

[5]We adapt the terminology from [50].
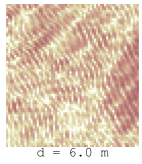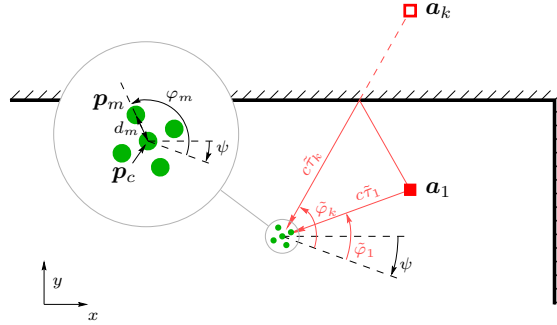
Figure 1: Layout of the array with its center of gravity at $\boldsymbol{p}_c$, element positions at $\boldsymbol{p}_m$, $m \in \mathcal{M}$, and reference orientation ψ. The mth position is characterized by the angle φ_m and the distance d_m with respect to $\boldsymbol{p}_c$. The 1st SMC originates from propagation along the line-of-sight path from the anchor at position $\boldsymbol{a}_1$ with angle $\tilde{\varphi}_1$ and distance $c\tilde{\tau}_1$. The kth SMC is incident with angle $\tilde{\varphi}_k$ and can be conceived as originating from a virtual anchor [6] at position $\boldsymbol{a}_k$ which is at distance $c\tilde{\tau}_k$ from $\boldsymbol{p}_c$. Constant c denotes the speed of light.

incorporates specular components that cannot be resolved and contributions originating from dispersive electromagnetic interactions, like diffuse scattering and diffraction. Thus, the model (1) depends on the sounding aperture or equivalently the resolution capability of the measurement equipment.

The number K of SMCs, their individual parameters $\tilde{\tau}_k$ and $\tilde{\varphi}_k$, $k \in \mathcal{K}$, and the vector parameter $\boldsymbol{\vartheta}$ characterizing the DMC are unknown. In this paper we propose an algorithm to estimate these parameters. We consider the following scenario: (1) the delay-AoA spread function $h(\tau, \varphi)$ has bounded support, i.e., without loss of generality $h(\tau, \varphi) = 0$ whenever $\tau \notin [0, T)$ and (2) the equipment is designed in such a way to ensure an aliasing-free estimation of $h(\tau, \varphi)$ over the domain $[0, T) \times [-\pi, \pi)$. Condition (1) is fullfilled provided $\tilde{\tau}_k \in [0, T)$, $k \in \mathcal{K}$ and $P(\tau, \varphi; \boldsymbol{\vartheta}) = 0$ whenever $\tau \notin [0, T)$. Thus, we can restrict the range of τ to $[0, T)$.

2.2   Received Signal

The array at the receiver has M elements located at $\boldsymbol{p}_m \in \mathbb{R}^2$ $m \in \{1, \ldots, M\} \triangleq \mathcal{M}$, see Fig. 1. Its center of gravity is $\boldsymbol{p} = M^{-1} \sum_{m=1}^{M} \boldsymbol{p}_m$ and its orientation determined by angle ψ as depicted in the figure. We also define $d_m = \|\boldsymbol{p}_m - \boldsymbol{p}\|$ and $\varphi_m = \angle(\boldsymbol{p}_m - \boldsymbol{p}) - \psi$, the distance of the m-th element to the reference location $\boldsymbol{p}$ and its angle relative to the array orientation, respectively.

Signals are represented by their complex envelope with respect to a center frequency f_c. Under the assumptions made in Sec. 2.1 and with the definitions introduced above, the signal at the output of the mth antenna element reads

$$
\begin{aligned}
r_m(t) &= \sum_{k \in \mathcal{K}} \tilde{\alpha}_k s\big(t; \tilde{\tau}_k, \tilde{\varphi}_k, \boldsymbol{p}_m\big) \\
&\quad + \iint s\big(t; \tau, \varphi, \boldsymbol{p}_m\big) \nu(\tau, \varphi) \mathrm{d}\tau \mathrm{d}\varphi + n_{\mathrm{w},m}(t)
\end{aligned}
\tag{3}
$$

152

where

$$s(t; \tau, \varphi, \boldsymbol{p}_m) = e^{j2\pi f_c g(\varphi, \boldsymbol{p}_m)} \underline{s}(t - \tau + g(\varphi, \boldsymbol{p}_m)), \qquad (4)$$

with $\underline{s}(t)$ as transmitted pulse. The function

$$g(\varphi, \boldsymbol{p}_m) = \frac{d_m \cos(\varphi - \psi - \varphi_m)}{c} \qquad (5)$$

gives the delay shift of a plane wave incident with AoA φ, and measured relative to the array orientation ψ, at the mth antenna position with respect to the array center of gravity. The measurement noise processes $n_{w,m}(t)$, $m \in \mathcal{M}$ are independent additive white Gaussian noise (AWGN) with double-sided power spectral density $N_0/2$.

2.3   Discrete-Time Signal Model

The signals $r_m(t)$, $m \in \mathcal{M}$ are synchronously sampled with frequency $f_s = 1/T_s$ and $N = T/T_s$ consecutive samples collected and arranged in vectors $\boldsymbol{r}_m$.[6] The M so-obtained length-N-vectors of samples are stacked to the length-NM vector $\boldsymbol{r} = [\boldsymbol{r}_1^T \cdots \boldsymbol{r}_M^T]^T$ which can be expressed as

$$\boldsymbol{r} = \boldsymbol{S}(\tilde{\boldsymbol{\psi}})\tilde{\boldsymbol{\alpha}} + \boldsymbol{n} \quad \in \mathbb{C}^{NM \times 1}. \qquad (6)$$

In the first summand $\tilde{\boldsymbol{\alpha}} = [\tilde{\alpha}_1 \cdots \tilde{\alpha}_K]^T \in \mathbb{C}^{K \times 1}$, $\tilde{\boldsymbol{\psi}} = [\tilde{\boldsymbol{\psi}}_1 \cdots \tilde{\boldsymbol{\psi}}_K]$ with entries $\tilde{\boldsymbol{\psi}}_k = [\tilde{\tau}_k \quad \tilde{\varphi}_k]$, $k \in \mathcal{K}$ and $\boldsymbol{S}(\tilde{\boldsymbol{\psi}}) = [\boldsymbol{s}(\tilde{\boldsymbol{\psi}}_1) \cdots \boldsymbol{s}(\tilde{\boldsymbol{\psi}}_K)] \in \mathbb{C}^{NM \times K}$ with columns given by

$$\boldsymbol{s}(\tilde{\boldsymbol{\psi}}_k) = [\boldsymbol{s}_1(\tilde{\boldsymbol{\psi}}_k)^T \cdots \boldsymbol{s}_M(\tilde{\boldsymbol{\psi}}_k)^T]^T \in \mathbb{C}^{NM \times 1}, \qquad (7)$$

$k \in \mathcal{K}$. The mth entry in the column vector in (7) reads

$$\boldsymbol{s}_m^T(\tilde{\boldsymbol{\psi}}_k) \triangleq [s(0; \tilde{\tau}_k, \tilde{\varphi}_k, \boldsymbol{p}_m) \cdots s((N-1)T_s; \tilde{\tau}_k, \tilde{\varphi}_k, \boldsymbol{p}_m)] \in \mathbb{C}^{1 \times N}. \qquad (8)$$

It contains the entries associated with the mth antenna element, $m \in \mathcal{M}$.

We can write the NM-vector $\boldsymbol{n}$ in (6) as $\boldsymbol{n} = \boldsymbol{n}_c + \boldsymbol{n}_w$, where the entries in $\boldsymbol{n}_c$ and $\boldsymbol{n}_w$ are the (arranged) samples of the integral summand and the measurement noise, respectively, in (3) when m ranges in $\mathcal{M}$.

From the made assumption on the DMC $\boldsymbol{n}_c$ is a complex circular symmetric Gaussian random vector, i.e. with zero mean, and $MN \times MN$ covariance matrix following from (2) to be

$$[\boldsymbol{C}_c(\boldsymbol{\vartheta})]_{m,m'} = \iint P(\tau, \varphi; \boldsymbol{\vartheta}) \boldsymbol{s}_m(\tau, \varphi) \boldsymbol{s}_{m'}(\tau, \varphi)^H d\tau d\varphi, \qquad (9)$$

$(m, m') \in \mathcal{M}^2$. From the assumptions made on the noise measurement process $\boldsymbol{n}_w$ is a complex circular symmetric Gaussian random vector with covariance matrix $\boldsymbol{C}_w = \sigma^2 \boldsymbol{I}$ with $\sigma^2 = N_0/T_s$ and $\boldsymbol{I}$ being an identity matrix of appropriate dimension. We assume that $\boldsymbol{n}_c$ and $\boldsymbol{n}_w$ are uncorrelated, so that the covariance matrix of $\boldsymbol{n}$ reads

$$\boldsymbol{C}(\boldsymbol{\eta}) = \boldsymbol{C}_c(\boldsymbol{\vartheta}) + \boldsymbol{C}_w = \boldsymbol{C}_c(\boldsymbol{\vartheta}) + \sigma^2 \boldsymbol{I} \qquad (10)$$

with $\boldsymbol{\eta} = [\sigma^2, \boldsymbol{\vartheta}]$.

---

[6]Note that the received signal $r_m(t)$ before sampling is Nyquist low-pass filtered with an equivalent bandwidth of $1/T_s$.
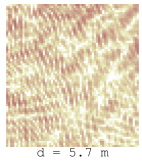
2.4 Selected Model for the DMC

To simplify the design of the estimator we shall make a series of assumptions on the modelling of the DMC.

a) We consider a separable delay-AoA power spectrum, i.e., $P(\tau, \varphi) = P\, p(\tau)p(\varphi)$. Here, $P = \iint P(\tau, \varphi)\mathrm{d}\tau\mathrm{d}\varphi$ is the power of the DMC, and $p(\tau)$ and $p(\varphi)$ are respectively the normalized delay power spectrum (DPS) and the normalized azimuth power spectrum (APS), [48].

b) In the computation of (9) we discard the second occurrence of the term $g(\varphi, \boldsymbol{p}_m)$ in (4). In doing so we neglect the relative delays of the complex envelopes induced by impinging waves across the array elements, which amounts to adopting a narrowband representation [17, 53].

As a result of the two above assumptions, the DMC covariance matrix factorizes as

$$\boldsymbol{C}_{\mathrm{c}} = P\,\boldsymbol{C}_M \otimes \boldsymbol{C}_N, \tag{11}$$

with $\otimes$ denoting the Kronecker product [17, 53]. The first factor is the spatial correlation matrix given by

$$\boldsymbol{C}_M = \int p(\varphi)\bar{\boldsymbol{s}}_M(\varphi)\bar{\boldsymbol{s}}_M^{\mathrm{H}}(\varphi)\mathrm{d}\varphi \tag{12}$$

with $\bar{\boldsymbol{s}}_M(\varphi) = [\mathrm{e}^{-j2\pi f_c g(\varphi, \boldsymbol{p}_1)} \cdots \mathrm{e}^{-j2\pi f_c g(\varphi, \boldsymbol{p}_m)}]^{\mathrm{T}} \in \mathbb{C}^{M \times 1}$ being the narrowband array response. The second factor is the delay correlation matrix:

$$\boldsymbol{C}_N = \int p(\tau)\bar{\boldsymbol{s}}_N(\tau)\bar{\boldsymbol{s}}_N^{\mathrm{H}}(\tau)\mathrm{d}\tau \tag{13}$$

with $\bar{\boldsymbol{s}}_N(\tau) = [\underline{s}(-[(N-1)/2]T_{\mathrm{s}} - \tau) \cdots \underline{s}([(N-1)/2]T_{\mathrm{s}} - \tau)]^{\mathrm{T}}$.

c) We neglect the spatial correlations across antenna elements, i.e., we set $\boldsymbol{C}_M = \boldsymbol{I}$ [17, 54]. This assumption is approximately fullfilled in case of uniform azimuth dispersion, i.e., constant APS $p(\varphi) = 1/2\pi$, for the antenna-element spacings used in practice.[7]

d) The DPS is given by the gamma function

$$p(\tau; \bar{\boldsymbol{\vartheta}}) = \frac{1}{\gamma_f^\beta \Gamma(\beta)}\big(\tau - \tau_{\mathrm{on}}\big)^{\beta-1}\mathrm{e}^{\left(-\frac{\tau - \tau_{\mathrm{on}}}{\gamma_f}\right)}u(\tau - \tau_{\mathrm{on}}), \tag{14}$$

where $\bar{\boldsymbol{\vartheta}} = [\tau_{\mathrm{on}}, \gamma_f, \beta]$ and $u(\tau)$ is the unit step function. We refer to $\tau_{\mathrm{on}}, \gamma_f$, and β as respectively the onset, the scale, and the shape parameters of the DMC process. Experimental evidence motivates the selection of a gamma-function to describe time-dispersion. The DPS typically exhibits an exponentially decaying tail [17, 51, 55] and a smooth onset [51, 56, 57]. This behaviour is well represented by a gamma function.

Combing all above assumptions, we arrive at the following model of the covariance matrix $\boldsymbol{C}(\boldsymbol{\eta})$:

$$\boldsymbol{C}(\boldsymbol{\eta}) = \boldsymbol{I} \otimes P\boldsymbol{C}_N(\bar{\boldsymbol{\vartheta}}) + \sigma^2 \boldsymbol{I}_{NM}, \tag{15}$$

with $\boldsymbol{\vartheta} = [P, \bar{\boldsymbol{\vartheta}}]$.

---

[7]This assumption is exact for a uniform linear array with half-a-wavelengh element spacing in the case of 3 dimensional propagation. For horizontal-only propagation, a suitable antenna spacing is approximately 40% of the wavelength, leading to zero correlations for adjacent antennas.

154

2.5   Discrete-Time Signal Model for Inference

Since K is unknown, we adopt the framework of SBL and modify the original signal model (6) by assuming a large, but fixed, number L of hypothetical SMCs. Parameter L is a design parameter set so that $NM \leq L$ is fulfilled. Moreover we shall assume that K is not larger than the number NM of observations. In summary, we have that $K \leq NM \leq L$. Similarly as in the previous subsection we define the vector $\boldsymbol{\psi} = [\boldsymbol{\psi}_1 \ \cdots \ \boldsymbol{\psi}_L]$ with entries $\boldsymbol{\psi}_l = [\tau_l \ \varphi_l]$, where $\tau_l \in [0, T)$, and $\varphi_l \in [-\pi + \pi)$, $l \in \{1, \ldots, L\} \triangleq \mathcal{L}$. With the above modifications we arrive at the discrete-time signal model used for inference:

$$\boldsymbol{r} = \boldsymbol{S}(\boldsymbol{\psi})\boldsymbol{\alpha} + \boldsymbol{n} \quad \in \mathbb{C}^{NM \times 1}, \tag{16}$$

where $\boldsymbol{\alpha} = [\alpha_1 \ \cdots \ \alpha_L]^{\mathrm{T}} \in \mathbb{C}^{L \times 1}$, and $\boldsymbol{S}(\boldsymbol{\psi}) = [\boldsymbol{s}(\boldsymbol{\psi}_1) \ \cdots \ \boldsymbol{s}(\boldsymbol{\psi}_L)] \in \mathbb{C}^{NM \times L}$ with $\boldsymbol{s}(\boldsymbol{\psi}_l)$ defined similarly to (7).

Under the assumptions made, the likelihood function of this model is given by

$$f(\boldsymbol{r}|\boldsymbol{\psi}, \boldsymbol{\eta}, \boldsymbol{\alpha}) = \frac{\mathrm{e}^{-(\boldsymbol{r} - \boldsymbol{S}(\boldsymbol{\psi})\boldsymbol{\alpha})^{\mathrm{H}} \boldsymbol{C}(\boldsymbol{\eta})^{-1}(\boldsymbol{r} - \boldsymbol{S}(\boldsymbol{\psi})\boldsymbol{\alpha})}}{\pi^{NM} \det(\boldsymbol{C}(\boldsymbol{\eta}))}, \tag{17}$$

where $\det(\cdot)$ is the determinant of a matrix.

In the following section, model (16) and its likelihood function (17) are the baseline for deriving the sparse variational Bayesian inference algorithm that estimates the unknown model parameters, including the model order K.

3   Problem Formulation

If the number of components K was known, the dispersion parameters $\tilde{\boldsymbol{\psi}}$ and complex amplitudes $\tilde{\boldsymbol{\alpha}}$ of the SMCs and the parameters $\boldsymbol{\eta}$ of the DMC and noise process could be inferred using a maximum a posteriori or maximum likelihood estimation technique applied to generative model (6). In the case where K is unknown, sparse Bayesian learning (SBL) [58,59] allows for including the estimation of this parameter by reformulating the initial inference problem as that of inferring the parameter vectors $\boldsymbol{\psi}, \boldsymbol{\eta}, \boldsymbol{\alpha}$ of model (16). Adopting the Bayesian framework, we assign a prior to each of these vectors and compute their posterior distributions given the observation $\boldsymbol{r}$. The SBL approach considers a hierarchical prior for each entry α_l in form of a Gaussian scale mixture,[8] i.e.

$$f(\boldsymbol{\alpha}, \boldsymbol{\gamma}) = f(\boldsymbol{\alpha}|\boldsymbol{\gamma})f(\boldsymbol{\gamma}) = \Pi_{l \in \mathcal{L}} f(\alpha_l|\gamma_l)f(\gamma_l) \tag{18}$$

where $f(\alpha_l|\gamma_l) = \mathcal{CN}(\alpha_l|0, \gamma_l^{-1})$, $l \in \mathcal{L}$ and $\boldsymbol{\gamma} = [\gamma_1 \ \cdots \ \gamma_L]^{\mathrm{T}} \in \mathbb{R}_+^{L \times 1}$. The entries in $\boldsymbol{\gamma}$ are referred to as hyperparameters and their priors with pdfs $f(\gamma_l)$, $l \in \mathcal{L}$ hyperpriors. With these specifications we obtain the probabilistic model

$$f(\boldsymbol{\psi}, \boldsymbol{\eta}, \boldsymbol{\alpha}, \boldsymbol{r}) = f(\boldsymbol{r}|\boldsymbol{\psi}, \boldsymbol{\eta}, \boldsymbol{\alpha})f(\boldsymbol{\alpha}|\boldsymbol{\gamma})f(\boldsymbol{\gamma})f(\boldsymbol{\psi})f(\boldsymbol{\eta}) \tag{19}$$

used for inference. In this study, we select flat priors for $\boldsymbol{\psi}, \boldsymbol{\gamma}, \boldsymbol{\eta}$, i.e. $f(\boldsymbol{\psi}) \propto 1$, $f(\boldsymbol{\gamma}) \propto 1$, $f(\boldsymbol{\eta}) \propto 1$.

---

[8]A recent work [33] generalizes the initial hierarchical priors of SBL to power exponential scale mixtures.

Following [29,41], we solve the inference problem using a Type-II estimation method [27,29]. The method estimates first $\boldsymbol{\psi}$, $\boldsymbol{\eta}$, $\boldsymbol{\gamma}$ by marginalizing the complex amplitude vector $\boldsymbol{\alpha}$ out in (19) and then infers a posterior distribution for $\boldsymbol{\alpha}$ from these estimates. The posterior pdf $f(\boldsymbol{\psi},\boldsymbol{\eta},\boldsymbol{\gamma}|\boldsymbol{r})$ is obtained from (19) to be

$$f(\boldsymbol{\psi},\boldsymbol{\eta},\boldsymbol{\gamma}|\boldsymbol{r}) \propto \int f(\boldsymbol{r}|\boldsymbol{\psi},\boldsymbol{\eta},\boldsymbol{\alpha})f(\boldsymbol{\alpha}|\boldsymbol{\gamma})\mathrm{d}\boldsymbol{\alpha}$$
$$\propto \det(\boldsymbol{C}(\boldsymbol{\psi},\boldsymbol{\eta},\boldsymbol{\gamma}))^{-1}\mathrm{e}^{-\boldsymbol{r}^{\mathrm{H}}\boldsymbol{C}(\boldsymbol{\psi},\boldsymbol{\eta},\boldsymbol{\gamma})^{-1}\boldsymbol{r}}, \tag{20}$$

where $\boldsymbol{C}(\boldsymbol{\psi},\boldsymbol{\eta},\boldsymbol{\gamma}) = \boldsymbol{C}(\boldsymbol{\eta}) + \boldsymbol{S}(\boldsymbol{\psi})\boldsymbol{\Gamma}^{-1}\boldsymbol{S}(\boldsymbol{\psi})^{\mathrm{H}}$ with $\boldsymbol{\Gamma} = \mathrm{diag}[\gamma_1,\ldots,\gamma_L]$. MAP estimates of $\boldsymbol{\psi}$, $\boldsymbol{\eta}$, $\boldsymbol{\gamma}$ are then computed. Due to the selected priors they coincide with the ML estimates:

$$\hat{\boldsymbol{\psi}}_{\mathrm{ML}},\hat{\boldsymbol{\eta}}_{\mathrm{ML}},\hat{\boldsymbol{\gamma}}_{\mathrm{ML}} = \underset{\boldsymbol{\psi},\boldsymbol{\eta},\boldsymbol{\gamma}}{\mathrm{argmax}}\, f(\boldsymbol{\psi},\boldsymbol{\eta},\boldsymbol{\gamma}|\boldsymbol{r}). \tag{21}$$

From (19) we obtain the conditional pdf

$$f(\boldsymbol{\alpha}|\boldsymbol{r},\boldsymbol{\psi},\boldsymbol{\eta},\boldsymbol{\gamma}) \propto f(\boldsymbol{r}|\boldsymbol{\psi},\boldsymbol{\eta},\boldsymbol{\alpha})f(\boldsymbol{\alpha}|\boldsymbol{\gamma}) \tag{22}$$

which is readily shown to be Gaussian, see discussion around (25) and (26). Vector $\boldsymbol{\alpha}$ is inferred using $f(\boldsymbol{\alpha}|\boldsymbol{r},\hat{\boldsymbol{\psi}}_{\mathrm{ML}},\hat{\boldsymbol{\eta}}_{\mathrm{ML}},\hat{\boldsymbol{\gamma}}_{\mathrm{ML}})$.

4 Sparse Variational Bayesian Channel Estimation

4.1 Variational Bayesian Inference

Since the maximizer of the posterior pdf $f(\boldsymbol{\psi},\boldsymbol{\eta},\boldsymbol{\gamma}|\boldsymbol{r})$ in (20) cannot be calculated analytically, even though this pdf is given in an analytical form, and a numerical solution is computationally prohibitive, we resort to variational Bayesian inference to compute an approximation thereof. Variational Bayesian inference relies on a family of proxy pdfs $q(\boldsymbol{\psi},\boldsymbol{\eta},\boldsymbol{\gamma}|\boldsymbol{r})$ together with a lower bound on the log evidence $\log f(\boldsymbol{r})$, i.e.,

$$\log f(\boldsymbol{r}) \geq \mathbb{E}_{q(\boldsymbol{\psi},\boldsymbol{\eta},\boldsymbol{\gamma}|\boldsymbol{r})}\left[\log\left(\frac{f(\boldsymbol{\psi},\boldsymbol{\eta},\boldsymbol{\gamma},\boldsymbol{r})}{q(\boldsymbol{\psi},\boldsymbol{\eta},\boldsymbol{\gamma}|\boldsymbol{r})}\right)\right]. \tag{23}$$

One recognizes in the expectation the negative Kullback-Leibler divergence from the posterior pdf $f(\boldsymbol{\psi},\boldsymbol{\eta},\boldsymbol{\gamma}|\boldsymbol{r})$ to $q(\boldsymbol{\psi},\boldsymbol{\eta},\boldsymbol{\gamma}|\boldsymbol{r})$ [58, Ch. 10], [59].

The approximate posterior pdf is that proxy pdf that maximizes the lower bound in (23) or equivalently minimizes the aforementioned Kullback-Leibler divergence. However, maximizing (23) jointly over $q(\boldsymbol{\psi},\boldsymbol{\eta},\boldsymbol{\gamma}|\boldsymbol{r})$ is not viable. We simplify the problem by postulating that the proxy pdf $q(\boldsymbol{\psi},\boldsymbol{\eta},\boldsymbol{\gamma}|\boldsymbol{r})$ factorizes as (structured mean-field assumption)

$$q(\boldsymbol{\psi},\boldsymbol{\eta},\boldsymbol{\gamma}|\boldsymbol{r}) = q(\boldsymbol{\eta}|\boldsymbol{r})q(\boldsymbol{\psi}|\boldsymbol{r})q(\boldsymbol{\gamma}|\boldsymbol{r}). \tag{24}$$

We then maximize (23) alternately with respect to each factor $q(\boldsymbol{\eta}|\boldsymbol{r})$, $q(\boldsymbol{\psi}|\boldsymbol{r})$, and $q(\boldsymbol{\gamma}|\boldsymbol{r})$ individually while keeping the others fixed. Furthermore, we restrict

156

these factors to be Dirac delta distributions, i.e. $q(\boldsymbol{\psi}|\boldsymbol{r}) = \delta(\boldsymbol{\psi} - \bar{\boldsymbol{\psi}})$, $q(\boldsymbol{\eta}|\boldsymbol{r}) = \delta(\boldsymbol{\eta} - \bar{\boldsymbol{\eta}})$, and $q(\boldsymbol{\gamma}|\boldsymbol{r}) = \delta(\boldsymbol{\gamma} - \bar{\boldsymbol{\gamma}})$, where $\bar{\boldsymbol{\psi}}$, $\bar{\boldsymbol{\eta}}$, and $\bar{\boldsymbol{\gamma}}$ are arbitrary. By doing so we enforce point estimates for $\boldsymbol{\psi}$, $\boldsymbol{\eta}$ and $\boldsymbol{\gamma}$.[9] With this restriction, the proxy pdf $q(\boldsymbol{\alpha}|\boldsymbol{r}) \propto \mathbb{E}_{q(\boldsymbol{\eta}|\boldsymbol{r})q(\boldsymbol{\psi}|\boldsymbol{r})q(\boldsymbol{\gamma}|\boldsymbol{r})}[f(\boldsymbol{r}|\boldsymbol{\psi}, \boldsymbol{\eta}, \boldsymbol{\alpha})f(\boldsymbol{\alpha}|\boldsymbol{\gamma})]$ is Gaussian with mean

$$\hat{\boldsymbol{\mu}}_\alpha = \hat{\boldsymbol{C}}_\alpha\big(\boldsymbol{S}(\hat{\boldsymbol{\psi}})^{\mathrm{H}}\boldsymbol{C}(\hat{\boldsymbol{\eta}})^{-1}\boldsymbol{r}\big) \tag{25}$$

and covariance matrix

$$\hat{\boldsymbol{C}}_\alpha = \big(\boldsymbol{S}(\hat{\boldsymbol{\psi}})^{\mathrm{H}}\boldsymbol{C}(\hat{\boldsymbol{\eta}})^{-1}\boldsymbol{S}(\hat{\boldsymbol{\psi}}) + \hat{\boldsymbol{\Gamma}}\big)^{-1}, \tag{26}$$

where $\boldsymbol{S}(\hat{\boldsymbol{\psi}}) = \boldsymbol{S}(\boldsymbol{\psi})|_{\boldsymbol{\psi}=\hat{\boldsymbol{\psi}}}$ (see Section 4.2), $\boldsymbol{C}(\hat{\boldsymbol{\eta}}) = \boldsymbol{C}(\boldsymbol{\eta})|_{\boldsymbol{\eta}=\hat{\boldsymbol{\eta}}}$ (see Section 4.3), and $\hat{\boldsymbol{\Gamma}} = \mathrm{diag}[\hat{\gamma}_1, \dots \hat{\gamma}_L]$ (see Section 4.4).

4.2 Inferring the Dispersion Parameters

Keeping its arguments $q(\boldsymbol{\gamma}|\boldsymbol{r})$ and $q(\boldsymbol{\eta}|\boldsymbol{r})$ fixed, the bound on the log evidence $\log f(\boldsymbol{r})$ in (23) can be written as [58, Ch. 10]

$$\log f(\boldsymbol{r}) \geq \mathbb{E}_{q(\boldsymbol{\psi}|\boldsymbol{r})}\left[\log\left(\frac{\tilde{f}(\boldsymbol{r}, \boldsymbol{\psi})}{q(\boldsymbol{\psi}|\boldsymbol{r})}\right)\right] + \mathrm{const} \tag{27}$$

with

$$\begin{aligned}\log(\tilde{f}(\boldsymbol{r}, \boldsymbol{\psi})) &\propto \mathbb{E}_{q(\boldsymbol{\gamma}, \boldsymbol{\eta}|\boldsymbol{r})}[\log(f(\boldsymbol{r}, \boldsymbol{\psi}, \boldsymbol{\eta}, \boldsymbol{\gamma}))] \\ &\propto -\mathbb{E}_{q(\boldsymbol{\gamma}, \boldsymbol{\eta}|\boldsymbol{r})}[\log(\det(\boldsymbol{C}(\boldsymbol{\psi}, \boldsymbol{\eta}, \boldsymbol{\gamma})))] \\ &\quad - \boldsymbol{r}^{\mathrm{H}}\mathbb{E}_{q(\boldsymbol{\gamma}, \boldsymbol{\eta}|\boldsymbol{r})}[\boldsymbol{C}(\boldsymbol{\psi}, \boldsymbol{\eta}, \boldsymbol{\gamma})^{-1}]\boldsymbol{r}.\end{aligned} \tag{28}$$

With the point estimate restriction $q(\boldsymbol{\psi}|\boldsymbol{r}) = \delta(\boldsymbol{\psi} - \bar{\boldsymbol{\psi}})$, the expectation in (27) is maximized for $\bar{\boldsymbol{\psi}} = \hat{\boldsymbol{\psi}}$ with[10]

$$\hat{\boldsymbol{\psi}} = \arg\min_{\boldsymbol{\psi}}\ \log(\det(\boldsymbol{C}(\boldsymbol{\psi}, \hat{\boldsymbol{\eta}}, \hat{\boldsymbol{\gamma}}))) + \boldsymbol{r}^{\mathrm{H}}\boldsymbol{C}(\boldsymbol{\psi}, \hat{\boldsymbol{\eta}}, \hat{\boldsymbol{\gamma}})^{-1}\boldsymbol{r}. \tag{29}$$

4.3 Inferring the DMC and Noise Parameters

Similarly, keeping its arguments $q(\boldsymbol{\psi}|\boldsymbol{r})$ and $q(\boldsymbol{\gamma}|\boldsymbol{r})$ fixed, the bound on the log evidence $\log f(\boldsymbol{r})$ in (23) takes the form

$$\log(f(\boldsymbol{r})) \geq \mathbb{E}_{q(\boldsymbol{\eta}|\boldsymbol{r})}\left[\log\left(\frac{\tilde{f}(\boldsymbol{r}, \boldsymbol{\eta})}{q(\boldsymbol{\eta}|\boldsymbol{r})}\right)\right] + \mathrm{const} \tag{30}$$

with

$$\begin{aligned}\log(\tilde{f}(\boldsymbol{r}, \boldsymbol{\eta})) &\propto \mathbb{E}_{q(\boldsymbol{\psi}, \boldsymbol{\gamma}|\boldsymbol{r})}[\log(f(\boldsymbol{r}, \boldsymbol{\psi}, \boldsymbol{\eta}, \boldsymbol{\gamma}))] \\ &\propto -\mathbb{E}_{q(\boldsymbol{\psi}, \boldsymbol{\gamma}|\boldsymbol{r})}[\log(\det(\boldsymbol{C}(\boldsymbol{\psi}, \boldsymbol{\eta}, \boldsymbol{\gamma})))]\end{aligned}$$

---

[9]Using (28), (31), and (34) one could derive a full Bayesian estimator that finds more generic proxy pdfs [12, 44] However, this would be computationally demanding.

[10]The negative Kullback-Leibler divergence in (27) is maximized if the mode of $q(\boldsymbol{\psi}|\boldsymbol{r})$ is aligned with the maximum of $\log(\tilde{f}(\boldsymbol{r}, \boldsymbol{\psi}))$.
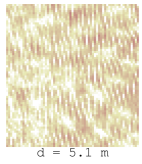
$$- \boldsymbol{r}^{\mathrm{H}} \mathbb{E}_{q(\boldsymbol{\psi}, \boldsymbol{\gamma} | \boldsymbol{r})} [\boldsymbol{C}(\boldsymbol{\psi}, \boldsymbol{\eta}, \boldsymbol{\gamma})^{-1}] \boldsymbol{r}. \tag{31}$$

Given the restriction $q(\boldsymbol{\eta} | \boldsymbol{r}) = \delta(\boldsymbol{\eta} - \bar{\boldsymbol{\eta}})$, the expectation in (30) is maximized for $\bar{\boldsymbol{\eta}} = \hat{\boldsymbol{\eta}}$ with

$$\hat{\boldsymbol{\eta}} = \underset{\boldsymbol{\eta}}{\arg\min} \ \log(\det(\boldsymbol{C}(\hat{\boldsymbol{\psi}}, \boldsymbol{\eta}, \hat{\boldsymbol{\gamma}}))) + \boldsymbol{r}^{\mathrm{H}} \boldsymbol{C}(\hat{\boldsymbol{\psi}}, \boldsymbol{\eta}, \hat{\boldsymbol{\gamma}})^{-1} \boldsymbol{r}. \tag{32}$$

4.4 Inferring the Hyperparameters

Finally, keeping the arguments $q(\boldsymbol{\psi} | \boldsymbol{r})$ and $q(\boldsymbol{\eta} | \boldsymbol{r})$ of the bound on the log evidence $\log f(\boldsymbol{r})$ in (23) fixed yields

$$\log(f(\boldsymbol{r})) \geq \mathbb{E}_{q(\boldsymbol{\gamma} | \boldsymbol{r})} \left[\log\left(\frac{\tilde{f}(\boldsymbol{r}, \boldsymbol{\gamma})}{q(\boldsymbol{\gamma} | \boldsymbol{r})} \right) \right] + \text{const} \tag{33}$$

with

$$\begin{aligned} \log(\tilde{f}(\boldsymbol{r}, \boldsymbol{\gamma})) &\propto \mathbb{E}_{q(\boldsymbol{\psi}, \boldsymbol{\eta} | \boldsymbol{r})} [\log(f(\boldsymbol{r}, \boldsymbol{\psi}, \boldsymbol{\eta}, \boldsymbol{\gamma}))] \\ &\propto -\mathbb{E}_{q(\boldsymbol{\psi}, \boldsymbol{\eta} | \boldsymbol{r})} [\det(\log(\boldsymbol{C}(\boldsymbol{\psi}, \boldsymbol{\eta}, \boldsymbol{\gamma})))] \\ &\quad - \boldsymbol{r}^{\mathrm{H}} \mathbb{E}_{q(\boldsymbol{\psi}, \boldsymbol{\eta} | \boldsymbol{r})} [\boldsymbol{C}(\boldsymbol{\psi}, \boldsymbol{\eta}, \boldsymbol{\gamma})^{-1}] \boldsymbol{r}. \end{aligned} \tag{34}$$

Given the restriction $q(\boldsymbol{\gamma} | \boldsymbol{r}) = \delta(\boldsymbol{\gamma} - \bar{\boldsymbol{\gamma}})$, the expectation in (33) is maximized for $\bar{\boldsymbol{\gamma}} = \hat{\boldsymbol{\gamma}}$ with

$$\hat{\boldsymbol{\gamma}} = \underset{\boldsymbol{\gamma}}{\arg\min} \ \log(\det(\boldsymbol{C}(\hat{\boldsymbol{\psi}}, \hat{\boldsymbol{\eta}}, \boldsymbol{\gamma}))) + \boldsymbol{r}^{\mathrm{H}} \boldsymbol{C}(\hat{\boldsymbol{\psi}}, \hat{\boldsymbol{\eta}}, \boldsymbol{\gamma})^{-1} \boldsymbol{r}. \tag{35}$$

Following [60], (35) can be replaced by a sequential optimization over the individual entries in $\boldsymbol{\gamma}$. Doing so yields

$$\hat{\gamma}_l = \begin{cases} (|\rho_l|^2 - \zeta_l)^{-1} & , \ \frac{|\rho_l|^2}{\zeta_l} > \kappa^* \\ \infty & , \ \frac{|\rho_l|^2}{\zeta_l} \leq \kappa^* \end{cases} \qquad l \in \mathcal{L}, \tag{36}$$

with $\kappa^* = 1$. The parameters $\rho_l = \rho(\hat{\psi}_l)$ and $\zeta_l = \zeta(\hat{\psi}_l)$ are the posterior estimates of the mean and the variance, respectively, of the complex amplitude when $\hat{\gamma}_l = 0$. They are given as

$$\zeta_l = \Big(\boldsymbol{s}(\hat{\psi}_l)^{\mathrm{H}} \boldsymbol{C}(\hat{\boldsymbol{\eta}})^{-1} \boldsymbol{s}(\hat{\psi}_l) \tag{37}$$

$$- \boldsymbol{s}(\hat{\psi}_l)^{\mathrm{H}} \boldsymbol{C}(\hat{\boldsymbol{\eta}})^{-1} \boldsymbol{S}(\hat{\psi}_{\bar{l}}) \hat{\boldsymbol{C}}_{\bar{l}, \alpha} \boldsymbol{S}(\hat{\psi}_{\bar{l}})^{\mathrm{H}} \boldsymbol{C}(\hat{\boldsymbol{\eta}})^{-1} \boldsymbol{s}(\hat{\psi}_l) \Big)^{-1}$$

$$\begin{aligned} \rho_l &= \zeta_l \boldsymbol{s}(\hat{\psi}_l)^{\mathrm{H}} \boldsymbol{C}(\hat{\boldsymbol{\eta}})^{-1} \boldsymbol{r} \\ &\quad - \zeta_l \boldsymbol{s}(\hat{\psi}_l)^{\mathrm{H}} \boldsymbol{C}(\hat{\boldsymbol{\eta}})^{-1} \boldsymbol{S}(\hat{\psi}_{\bar{l}}) \hat{\boldsymbol{C}}_{\bar{l}, \alpha} \boldsymbol{S}(\hat{\psi}_{\bar{l}})^{\mathrm{H}} \boldsymbol{C}(\hat{\boldsymbol{\eta}})^{-1} \boldsymbol{r} \\ &= \zeta_l \boldsymbol{s}(\hat{\psi}_l)^{\mathrm{H}} \boldsymbol{C}(\hat{\boldsymbol{\eta}})^{-1} \bar{\boldsymbol{r}}_l \end{aligned} \tag{38}$$

with

$$\bar{\boldsymbol{r}}_l = \boldsymbol{r} - \boldsymbol{S}(\hat{\psi}_{\bar{l}}) \boldsymbol{\mu}_{\bar{l}, \alpha}, \tag{39}$$

$$\hat{\boldsymbol{\mu}}_{\bar{l}, \alpha} = \hat{\boldsymbol{C}}_{\bar{l}, \alpha} (\boldsymbol{S}(\hat{\psi}_{\bar{l}})^{H} \boldsymbol{C}(\hat{\boldsymbol{\eta}})^{-1} \boldsymbol{r}), \tag{40}$$

158
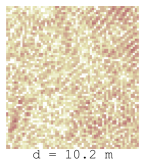
$$\hat{C}_{\bar{l},\alpha} = (S(\hat{\psi}_{\bar{l}})^H C(\hat{\eta})^{-1} S(\hat{\psi}_{\bar{l}}) + \hat{\Gamma}_{\bar{l}}))^{-1}, \tag{41}$$

$$\hat{\Gamma}_{\bar{l}} = \mathrm{diag}([\hat{\gamma}_1, \dots, \hat{\gamma}_{l-1}, \hat{\gamma}_{l+1}, \dots, \hat{\gamma}_L]), \tag{42}$$

and $\hat{\psi}_{\bar{l}} = [\hat{\psi}_1, \dots, \hat{\psi}_{l-1}, \hat{\psi}_{l+1}, \dots, \hat{\psi}_L]$.

It is worth noting that the computation step of $\hat{\gamma}_l$ (36) contains a condition that determines whether or not the lth atom shall be retained (is relevant). Indeed, $\hat{\gamma}_l = \infty$ implies $q(\alpha_l|r) = \delta(\alpha)$, i.e. the lth atom is effectively pruned if $|\rho_l|^2/\zeta_l \leq \kappa^*$.

The proposed algorithm incorporates an incremental implementation [40, 42] that solves (36). Details can be found in these references.

5 Analysis of Pruning Condition

Numerical experiments have shown that the SBL algorithm with its built-in pruning condition $\frac{|\rho_l|^2}{\zeta_l} > \kappa^*$ with $\kappa^* = 1$ computes artifacts. The number of these artifacts increases when either the SNR or the number of samples increases. Similarly to [41], we modify the threshold κ^* in (36) to $\kappa^* > 1$ to reduce the occurrence of artifacts.

In the following, we compute the probability of artifacts when the threshold κ^* in this condition varies. This relationship is exploited to control the probability of detecting artifacts at a prespecified level.

5.1 Derivation of Probability of Artifact for Array Processing

We define the set of estimated components $\hat{\mathcal{K}} = \{l \in \mathcal{L} : \hat{\gamma}_l < \infty\}$, with $\hat{K} = |\hat{\mathcal{K}}|$ components. Adopting the definitions in [41], we have the signal support $\tilde{\Psi} \triangleq \{\tilde{\psi}_k : k \in \mathcal{K}\}$ with the neighborhood $\tilde{\Psi}^{(r)} \triangleq \cup_{k \in \mathcal{K}} B_r(\tilde{\psi}_k)$, where $B_r(\psi)$ is the open ball of radius $r > 0$ centered at $\psi \in \Psi$.

Assumption 1. *We assume that the noise covariance matrix $C \triangleq C(\eta)$ is known and that the Kronecker factorization in (15) holds.*

Assumption 2. *We assume that signal atoms of artifacts are mutually orthogonal [41], i.e., for any $\hat{\psi}_{l'}, \hat{\psi}_{l''} \in \Psi \setminus \tilde{\Psi}^{(r)}$ with $l', l'' \in \hat{\mathcal{K}}$ and $l' \neq l''$ $s(\hat{\psi}_{l'})^{\mathrm{H}} C^{-1} s(\hat{\psi}_{l''}) = 0$. We assume that these atoms are orthogonal to the estimated signal atoms, i.e., $s(\hat{\psi}_l)^{\mathrm{H}} C^{-1} s(\hat{\psi}_{l'}) = 0$ with $\hat{\psi}_l \in \tilde{\Psi}^{(r)}$ and $\hat{\psi}_{l'} \in \Psi \setminus \tilde{\Psi}^{(r)}$ with $l, l' \in \hat{\mathcal{K}}$.*

The probability of artifact is defined as [41]

$$P_A^{(r)}(\kappa) \triangleq \mathbb{P}\big[\exists l \in \mathcal{L} : \hat{\psi}_l \in \Psi \setminus \tilde{\Psi}^{(r)} \wedge \hat{\gamma}_l < \infty\big]$$
$$= \mathbb{P}\Big[\bigcup_{l \in \mathcal{L}} \big\{\hat{\psi}_l \in \Psi \setminus \tilde{\Psi}^{(r)} \wedge \tilde{u}(\hat{\psi}_l) \geq \kappa\big\}\Big], \tag{43}$$

where $\tilde{u}(\psi_l) = \zeta_l^{-1}|\varrho_l|^2$.

Theorem 1. *When Assumption 1 and 2 hold, the probability of artifacts in (43) can be upper-bounded according to [41, 48]*

$$P_A^{(r)}(\kappa) \leq \mathbb{P}\Big[\sup_{\psi \in \Psi} \tilde{u}(\psi) \geq \kappa\Big]. \tag{44}$$

159
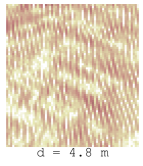
The numerical value of the bound is given as

$$\mathbb{P}\Big[\sup_{\boldsymbol{\psi} \in \Psi} \tilde{u}(\boldsymbol{\psi}) > \kappa \Big] \sim 4\pi \int_0^T \int_0^{2\pi} \sqrt{\frac{1}{M} \sum_{m \in \mathcal{M}} D_m^2(\varphi)}$$

$$\times \beta_w(\boldsymbol{\psi})\xi_\tau(\boldsymbol{\psi})\sqrt{f_c^2 - f_c\xi_\varphi(\boldsymbol{\psi}) + \beta_w^2(\boldsymbol{\psi})} \, \mathrm{d}\tau\mathrm{d}\varphi \, \kappa \, e^{-\kappa} \tag{45}$$

where $D_m(\varphi) = \frac{d^{(m)}}{c} \sin\big(\varphi - \varphi^{(m)}\big)$, $m \in \mathcal{M}$, *and we introduced the effective square bandwidth* $\beta_w^2(\boldsymbol{\psi})$, *and the two loss factors* $\xi_\tau(\boldsymbol{\psi})$ *and* $\xi_\varphi(\boldsymbol{\psi})$ *whose definitions[11] can be found in the supplementary material in Appendix B.*

Note that the term $\sqrt{\frac{1}{M}\sum_m D_m(\varphi)^2}$ captures the impact of the array geometry. The terms $\beta_w(\boldsymbol{\psi})$, $\xi_\tau(\boldsymbol{\psi})$, and $\xi_\varphi(\boldsymbol{\psi})$ capture the impact of the baseband signal parameters and DMC plus noise parameters.

Proof. We can rewrite (39) as

$$\bar{\boldsymbol{r}}_l = \boldsymbol{n} + \sum_{k \in \mathcal{K}, \tilde{\boldsymbol{\psi}}_k \in \tilde{\Psi}} \mu_{\alpha,k} \boldsymbol{s}(\tilde{\boldsymbol{\psi}}_k) - \sum_{l' \in \hat{\mathcal{K}} \setminus l, \hat{\boldsymbol{\psi}}_{l'} \in \tilde{\Psi}^{(r)}} \hat{\mu}_{\alpha,l'} \boldsymbol{s}(\hat{\boldsymbol{\psi}}_{l'})$$

$$- \sum_{l' \in \hat{\mathcal{K}} \setminus l, \hat{\boldsymbol{\psi}}_{l'} \in \Psi \setminus \tilde{\Psi}^{(r)}} \hat{\mu}_{\alpha,l'} \boldsymbol{s}(\hat{\boldsymbol{\psi}}_{l'}), \tag{46}$$

where $\mu_{\alpha,k} \triangleq \tilde{\alpha}_k$. Inserting (46) into (38) and (37) and using Assumption 1 and Assumption 2, we get for artifacts $\hat{\boldsymbol{\psi}}_l \in \Psi \setminus \tilde{\Psi}^{(r)}$ with $l \in \hat{\mathcal{K}}$

$$\zeta(\hat{\boldsymbol{\psi}}_l) = \boldsymbol{s}(\hat{\boldsymbol{\psi}}_l)^{\mathrm{H}} \boldsymbol{C}^{-1} \boldsymbol{s}(\hat{\boldsymbol{\psi}}_l), \tag{47}$$

$$\rho(\hat{\boldsymbol{\psi}}_l) = \zeta(\hat{\boldsymbol{\psi}}_l) \boldsymbol{s}(\hat{\boldsymbol{\psi}}_l)^{\mathrm{H}} \boldsymbol{C}^{-1} \boldsymbol{n}. \tag{48}$$

Inserting (47) and (48) into (43) leads to the upper bound, stated in Theorem 1, i.e.

$$P_{\mathrm{A}}^{(r)}(\kappa) \leq \mathbb{P}\Big[\sup_{\boldsymbol{\psi} \in \Psi} \tilde{u}(\boldsymbol{\psi}) \geq \kappa \Big]. \tag{49}$$

The upper boundedness comes from the fact that the support of the dispersion parameters is not restricted to $\Psi \setminus \tilde{\Psi}^{(r)}$, but rather Ψ. Therefore, we have also dropped the index l. The upper bound on the probability of artifacts is the excursion probability that the maximum of the random process $\tilde{u}(\boldsymbol{\psi})$ with $\boldsymbol{\psi} \in \Psi$ exceeds the threshold κ [48,62]. Therefore, the probability of artifacts is derived by finding the excursion probability of the two dimensional χ^2-random field (random process with two dimensions)

$$u(\boldsymbol{\psi}) = 2\tilde{u}(\boldsymbol{\psi}) = \frac{2\Big| \sum_{m \in \mathcal{M}} \big\langle \boldsymbol{n}^{(m)}, \boldsymbol{s}^{(m)}(\boldsymbol{\psi}) \big\rangle_{\mathcal{H}} \Big|^2}{\sum_{m \in \mathcal{M}} \big\| \boldsymbol{s}^{(m)}(\boldsymbol{\psi}) \big\|_{\mathcal{H}}^2} \tag{50}$$

for large κ, where $\boldsymbol{n}^{(m)}$ is the DMC plus noise vector for antenna m. For easier readability we introduced the Hilbert space $\mathcal{H}$ with the weighted inner-product

---

[11] These terms are related to the Fisher information on the position error exploiting SMCs and their in-depth explanation can be found in [6,61].

$\langle \boldsymbol{x}, \boldsymbol{y} \rangle_{\mathcal{H}} \triangleq \sigma_{\mathrm{w}}^2 \boldsymbol{y}^{\mathrm{H}} \tilde{\boldsymbol{C}}^{-1} \boldsymbol{x}$, with the (m,m)th $N \times N$ block of the covariance matrix $\tilde{\boldsymbol{C}} = [\boldsymbol{C}(\boldsymbol{\eta})]_{m,m}$. This weighted inner-product induces the norm $\|\boldsymbol{x}\|_{\mathcal{H}}^2 \triangleq \langle \boldsymbol{x}, \boldsymbol{x} \rangle_{\mathcal{H}}$ [61]. Note that since the variance of $\tilde{u}(\boldsymbol{\psi})$ is one, we need to multiply it by 2 to be in line with the definition of a χ^2-distribution with two degrees of freedom [41]. We reformulate $u(\boldsymbol{\psi}) \triangleq |x(\boldsymbol{\psi})|^2 = \Re\{x(\boldsymbol{\psi})\}^2 + \Im\{x(\boldsymbol{\psi})\}^2$, where $\Re\{x(\boldsymbol{\psi})\}$ and $\Im\{x(\boldsymbol{\psi})\}$ are the imaginary and real part of $x(\boldsymbol{\psi})$, respectively. Using [45] in [41] it is shown that the results of [62] can be extended to circular complex processes. The circularly-symmetric complex Gaussian random process $x(\boldsymbol{\psi})$ is given as

$$x(\boldsymbol{\psi}) = \frac{\sqrt{2} \sum_{m \in \mathcal{M}} \langle \boldsymbol{n}^{(m)}, \boldsymbol{s}^{(m)}(\boldsymbol{\psi}) \rangle_{\mathcal{H}}}{\sqrt{\sum_{m \in \mathcal{M}} \left\| \boldsymbol{s}^{(m)}(\boldsymbol{\psi}) \right\|_{\mathcal{H}}^2}}, \tag{51}$$

where $x(\boldsymbol{\psi}) \triangleq x(\tau, \varphi)$. This process has autocorrelation function $\mathbb{E}[x(\boldsymbol{\psi})x(\boldsymbol{\psi}')^*]$ and has the following properties (the proofs can be found in the supplementary material in Appendix A):

1. The variances of the real and imaginary parts of $x(\boldsymbol{\psi})$ are $\mathbb{E}\big[|\Re\{x(\boldsymbol{\psi})|^2\big] = 1$ and $\mathbb{E}\big[|\Im\{x(\boldsymbol{\psi})|^2\big] = 1$.

2. The real part $\Re\{x(\boldsymbol{\psi})\}$ and the imaginary part $\Im\{x(\boldsymbol{\psi})\}$ are independent processes, i.e., $\mathbb{E}[\Re\{x(\boldsymbol{\psi})\}\Im\{x(\boldsymbol{\psi}')\}] = 0 \ \forall \ \boldsymbol{\psi}, \boldsymbol{\psi}' \in \boldsymbol{\Psi}$.

Since $\Re\{x(\boldsymbol{\psi})\}$ and $\Im\{x(\boldsymbol{\psi})\}$ are independent and $\boldsymbol{\psi}$ is 2-dimensional, $u(\boldsymbol{\psi})$ is described by a 2-dimensional χ^2-random field [48, 62] with two degrees of freedom (real and imaginary part). In our case, $\boldsymbol{\psi} = [\tau, \varphi]^{\mathrm{T}} \in \Psi = [0, T) \times [0, 2\pi)$, the domain Ψ represents a cylinder. Note that in general $x(\boldsymbol{\psi})$ is non-stationary w.r.t. τ and φ. Applying Weyl's tube formula [49, Theorem 3.3.1] on the non-stationary 2-dimensional χ^2-random field and using [49, Theorem 4.4.1] combined with the results of k-dimensional χ^2-random fields [49, Section 4.5.2], yields the following excursion probability asymptotically in κ, i.e. for $\kappa \to \infty$

$$\mathbb{P}\Big[\sup_{\boldsymbol{\psi}} 2\tilde{u}(\boldsymbol{\psi}) \geq \kappa \Big] \sim \int_{\Psi} \sqrt{\frac{|\det(\boldsymbol{\Lambda}(\boldsymbol{\psi})|}{4\pi^2}} \, \mathrm{d}\boldsymbol{\psi} \kappa \mathrm{e}^{-\frac{\kappa}{2}}, \tag{52}$$

where $\boldsymbol{\Lambda}(\boldsymbol{\psi}) \in \mathbb{R}^{2 \times 2}$ is the covariance matrix of the 2-dimensional χ^2 random field:

$$\boldsymbol{\Lambda}(\boldsymbol{\psi}) = \frac{1}{2} \mathbb{E}\left[\frac{\partial x(\boldsymbol{\psi})}{\partial \boldsymbol{\psi}} \left[\frac{\partial x(\boldsymbol{\psi})}{\partial \boldsymbol{\psi}} \right]^{\mathrm{H}} \right]$$

$$= \frac{1}{2} \begin{bmatrix} \mathbb{E}\left[\frac{\partial x(\boldsymbol{\psi}) \partial x(\boldsymbol{\psi})^*}{\partial \tau^2} \right] & \mathbb{E}\left[\frac{\partial x(\boldsymbol{\psi}) \partial x(\boldsymbol{\psi})^*}{\partial \tau \partial \varphi} \right] \\ \mathbb{E}\left[\frac{\partial x(\boldsymbol{\psi}) \partial x(\boldsymbol{\psi})^*}{\partial \varphi \partial \tau} \right] & \mathbb{E}\left[\frac{\partial x(\boldsymbol{\psi}) \partial x(\boldsymbol{\psi})^*}{\partial \varphi^2} \right] \end{bmatrix}. \tag{53}$$

The entries in (53) are computed to be

$$\mathbb{E}\left[\frac{\partial x(\boldsymbol{\psi}) \partial x(\boldsymbol{\psi})^*}{\partial \tau^2} \right] = 8\pi^2 \beta_{\mathrm{w}}^2(\boldsymbol{\psi}) \xi_\tau^2(\boldsymbol{\psi}) \tag{54}$$

$$\mathbb{E}\left[\frac{\partial x(\boldsymbol{\psi}) \partial x(\boldsymbol{\psi})^*}{\partial \varphi^2} \right] = \frac{8\pi^2}{M} \sum_{m \in \mathcal{M}} D_m^2(\varphi) \Big(f_{\mathrm{c}}^2 + f_{\mathrm{c}} \xi_\varphi(\boldsymbol{\psi}) + \beta_{\mathrm{w}}^2(\boldsymbol{\psi}) \Big) \tag{55}$$

161
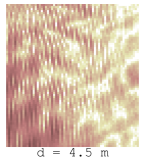
$$\mathbb{E}\left[\frac{\partial x(\boldsymbol{\psi})\partial x(\boldsymbol{\psi})^*}{\partial\tau\partial\varphi}\right] = \mathbb{E}\left[\frac{\partial x(\boldsymbol{\psi})\partial x(\boldsymbol{\psi})^*}{\partial\varphi\partial\tau}\right] = 0. \tag{56}$$

The detailed derivations can be found in the supplementary material in Appendix B. Using (54)-(56), $\det(\boldsymbol{\Lambda}(\boldsymbol{\psi}))$ is calculated and plugged into (52)[12]. By multiplying κ by 2 in (52), we obtain (45), which completes the proof of Theorem 1. $\qquad\square$

To obtain a numerical value for the threshold κ we can state the following:

Corollary 1. *Under Assumption 1 and 2, given $\epsilon > 0$,*

$$P_A(\kappa^*) \leq \mathbb{P}\left[\sup_{\boldsymbol{\psi}} \tilde{u}(\boldsymbol{\psi}) \geq \kappa^*\right] \lesssim \epsilon, \tag{57}$$

where the symbol $\lesssim$ means "less than but close to", provided κ^* satisfies

$$\kappa^* \geq -\mathrm{W}_{-1}\Bigg(-\frac{\epsilon}{4\pi}\bigg(\int_0^{2\pi}\int_0^T \sqrt{\frac{1}{M}\sum_{m\in\mathcal{M}} D_m^2(\varphi)}$$
$$\times \beta_w(\boldsymbol{\psi})\xi_\tau(\boldsymbol{\psi})\sqrt{f_c^2 + f_c\xi_\varphi(\boldsymbol{\psi}) + \beta_w^2(\boldsymbol{\psi})}\,\mathrm{d}\varphi\mathrm{d}\tau\bigg)^{-1}\Bigg). \tag{58}$$

Proof. We need to determine the minimum level of $\kappa^* > 1$ such that the right-hand side of (52) satisfies $\int_\Psi \sqrt{|\det(\boldsymbol{\Lambda}(\boldsymbol{\psi}))|/\pi^2}\,\mathrm{d}\boldsymbol{\psi}\kappa\mathrm{e}^{-\kappa} \leq \epsilon$ (κ is multiplied by 2). To that end we take the logarithm on both sides of the latter expression and consider equality. After rearranging, we obtain

$$\kappa - \log\kappa = \int_\Psi \sqrt{\frac{|\det(\boldsymbol{\Lambda}(\boldsymbol{\psi})|}{\pi^2}}\,\mathrm{d}\boldsymbol{\psi} - \log\epsilon. \tag{59}$$

Solving for κ yields

$$\kappa^* = -\mathrm{W}_{-1}\left(-\frac{\pi\epsilon}{\int_\Psi \sqrt{|\det(\boldsymbol{\Lambda}(\boldsymbol{\psi})|}\,\mathrm{d}\boldsymbol{\psi}}\right), \tag{60}$$

where $\mathrm{W}_{-1}(\cdot)$ is the second real branch of the Lambert W function. Using (54) and (56), $\det(\boldsymbol{\Lambda}(\boldsymbol{\psi}))$ is calculated and plugged into (60), which completes the proof of Corollary 1. $\qquad\square$

Remark 1. *Inequalities (57) and (58) of Corollary 1 can be used to control the probability of artifacts of SBL algorithms.*

6   Implementation

A summary of the proposed algorithm is shown in Algorithm 1. The algorithm is split in two basic blocks, the acquisition and the refinement phase. Furthermore, there is an overarching loop due to the iterative nature of the algorithm. More details about the chosen scheduling can be found in the supplementary material in Appendix C.

---

[12]Since $\boldsymbol{\Lambda}(\boldsymbol{\psi})$ is a non-negative hermitian its determinate is non-negative.

Algorithm 1: Summary of the proposed algorithm.

   Input   : signal measurement r

   Output: Estimates of model order $\hat{K}$, dispersion parameters $\hat{\boldsymbol{\Psi}}$, noise
           and DMC parameters $\hat{\boldsymbol{\eta}}$, and mean and covariance of the
           complex amplitudes $\hat{\boldsymbol{\mu}}_\alpha$ and $\hat{\boldsymbol{C}}_\alpha$, respectively.

1 $\hat{\boldsymbol{\Psi}}, \hat{\boldsymbol{\gamma}}, \hat{\boldsymbol{\mu}}_\alpha, \hat{\boldsymbol{C}}_\alpha \leftarrow [\,]$

2 $\hat{\boldsymbol{\eta}} \leftarrow [\hat{\sigma}_{\mathrm{w}}^2, \hat{\boldsymbol{\vartheta}}^{\mathrm{T}}]^{\mathrm{T}}$
     with $\hat{\sigma}_{\mathrm{w}}^2 \leftarrow \frac{\|\boldsymbol{r}\|^2}{NM}$ and $\hat{\boldsymbol{\vartheta}} \leftarrow [\,]$ (AWGN only)

3 **do**

4 | `acquisition()`

5 | `refinement()`

6 | **if** *DMC not yet initialized* **then**

7 | | $\hat{\boldsymbol{\vartheta}} \leftarrow [1\mathrm{m}/c, \hat{\sigma}_{\mathrm{w}}^2/2NT_{\mathrm{s}}, T/2, T_{\mathrm{s}}]^{\mathrm{T}}$

8 | | $\hat{\boldsymbol{\eta}} \leftarrow [\hat{\sigma}_{\mathrm{w}}^2/2, \hat{\boldsymbol{\vartheta}}^{\mathrm{T}}]^{\mathrm{T}}$

9 | | initialize $\hat{\boldsymbol{\eta}}$ with least square curve fit

10 | | `refinement()`

11 | **end**

12 | $\hat{\boldsymbol{\mu}}_\alpha, \hat{\boldsymbol{C}}_\alpha \leftarrow$ (25), (26), respectively

13 **while** $\|\hat{\boldsymbol{\mu}}_\alpha\|_0$ *changes*

14 $\hat{K} \leftarrow \|\hat{\boldsymbol{\mu}}_\alpha\|_0$

For the acquisition, we follow [63] and employ a bottom-up strategy, meaning that we start with an empty model and add signal atoms iteratively into the model. During the first acquisition and refinement phase, we choose to utilize an AWGN-only model, i.e., (15) reduces to $\boldsymbol{C}(\boldsymbol{\eta}) = \sigma_{\mathrm{w}}^2 \boldsymbol{I}_{NM}$. After that, the parameters of the DMC process $\boldsymbol{\vartheta}$ are initialized using a least square curve fit (line 6).

The acquisition procedure to fill the model is described in detail in Procedure 1. In the acquisition phase, SMCs are added until the number of SMCs $\|\hat{\boldsymbol{\mu}}_\alpha\|_0$ is not changing anymore or a maximum number of SMCs $\|\hat{\boldsymbol{\mu}}_\alpha\|_0 \leq L$ is reached. The operator $\|\hat{\boldsymbol{\mu}}_\alpha\|_0$ gives the number of non-zero elements of the vector $\hat{\boldsymbol{\mu}}_\alpha$ [23]. A candidate SMC is found by an "incoherent" estimation from the residual signal followed by an update of the vectors $\boldsymbol{\eta}$, $\boldsymbol{\Psi}$, κ^*, and $\boldsymbol{\gamma}$ using (32), (29), (58), and (36), respectively.

The refinement procedure is described in more detail in Procedure 2. In the refinement phase, the parameters $\boldsymbol{\eta}$, $\boldsymbol{\Psi}$, κ^*, and $\boldsymbol{\gamma}$ (provided by the acquisition phase) are updated using (32), (29), (58), and (36), respectively.

7   Experimental Results

To validate the algorithm, we first test it with synthetically generated measurements according to the model given in (6) with the noise covariance given in (15). We then apply the algorithm to measurements acquired in an indoor environment. For all experiments, the transmitted pulse $s(t)$ is a root-raised cosine pulse with a roll-off factor of 0.6, and duration of $T_{\mathrm{p}} = 1\,\mathrm{ns}$. The center frequency is $6\,\mathrm{GHz}$ and the received signal is critically sampled.
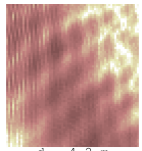
Procedure 1: Acquisition phase to add new components.

1 Procedure `acquisition()`

2   **do**

3 $\boldsymbol{r}_{\mathrm{res}} = \boldsymbol{r} - \boldsymbol{S}(\hat{\boldsymbol{\Psi}})\hat{\boldsymbol{\mu}}_\alpha$

4 $\hat{\boldsymbol{\psi}}_{\mathrm{candidate}} = \arg\min\limits_{\boldsymbol{\psi}} \frac{|\boldsymbol{r}_{\mathrm{res}}^{\mathrm{H}} \boldsymbol{C}(\hat{\boldsymbol{\eta}})^{-1} \boldsymbol{s}(\boldsymbol{\psi})|^2}{\boldsymbol{s}(\boldsymbol{\psi})^{\mathrm{H}} \boldsymbol{C}(\hat{\boldsymbol{\eta}})^{-1} \boldsymbol{s}(\boldsymbol{\psi})}$

5 $\hat{\gamma}_{\mathrm{candidate}} = (|\rho_{\mathrm{candidate}}|^2 - \zeta_{\mathrm{candidate}})^{-1}$ (37), (38)

6   append $(\hat{\boldsymbol{\psi}}_{\mathrm{candidate}}, \hat{\gamma}_{\mathrm{candidate}})$ to $(\hat{\boldsymbol{\Psi}}, \hat{\boldsymbol{\gamma}})$

7 $\hat{\boldsymbol{\eta}} \leftarrow$ update according to (32)

8 $\hat{\boldsymbol{\Psi}} \leftarrow$ update according to (29)

9 $\kappa^* \leftarrow$ (58)

10 $\hat{\boldsymbol{\gamma}} \leftarrow$ update according to (36)

11   **if** any($\hat{\boldsymbol{\gamma}} == \infty$) **then**

12   remove component with minimal $\frac{|\rho_l|^2}{\zeta_l}$ from $(\hat{\boldsymbol{\Psi}}, \hat{\boldsymbol{\gamma}})$

13   **end**

14 $\hat{\boldsymbol{\mu}}_\alpha, \hat{\boldsymbol{C}}_\alpha \leftarrow$ (25), (26), respectively

15   **while** $\|\hat{\boldsymbol{\mu}}_\alpha\|_0$ *grows or* $\|\hat{\boldsymbol{\mu}}_\alpha\|_0 \leq L$

Procedure 2: Refinement phase of the proposed algorithm.

1 Procedure `refinement()`

2   **do**

3 $\hat{\boldsymbol{\eta}} \leftarrow$ update according to (32)

4 $\hat{\boldsymbol{\Psi}} \leftarrow$ update according to (29)

5 $\kappa^* \leftarrow$ (58)

6 $\hat{\boldsymbol{\gamma}} \leftarrow$ update according to (36)

7   **if** any($\hat{\boldsymbol{\gamma}} == \infty$) **then**

8   remove component with minimal $\frac{|\rho_l|^2}{\zeta_l}$ from $(\hat{\boldsymbol{\Psi}}, \hat{\boldsymbol{\gamma}})$

9   **end**

10   **while** *not converged*

7.1 Synthetic Radio Channels

The DMC process is generated using (14) with $\tau_{\mathrm{on}} = 1\mathrm{m}/c$, $\gamma_f = 5\,\mathrm{ns}$ and $\beta = 1.8$. The power of the DMC process is specified via the specular-to-dense-ratio SDR $= 10\log_{10}\left(\frac{\frac{1}{M}\|\sum_{k\in\mathcal{K}}\tilde{\alpha}_k \boldsymbol{s}(\tilde{\boldsymbol{\psi}}_k)\|^2}{P/T_{\mathrm{s}}}\right)$. In addition, AWGN is generated with noise variance σ_{w}^2, specified by the signal-to-noise ratio
SNR $= 10\log_{10}\left(\frac{\frac{1}{M}\|\sum_{k\in\mathcal{K}}\tilde{\alpha}_k \boldsymbol{s}(\tilde{\boldsymbol{\psi}}_k)\|^2 + P/T_{\mathrm{s}}}{\sigma_{\mathrm{w}}^2}\right)$. Both ratios are defined for a single-antenna channel.

7.1.1 Estimation of a Single Component

We first empirically validate the probability of artifacts given in (45) and the probability of missed detection. For a single SMC, the probability of missed detection can be approximated in line with [41]. For $NM \to \infty$ and a given $\boldsymbol{\psi} \in \tilde{\Psi}^{(r)}$, the distribution of $u(\boldsymbol{\psi}) = 2\zeta(\boldsymbol{\psi})^{-1}|\rho(\boldsymbol{\psi})|^2$ can be approximated

by a non-central chi-square distribution with 2 degrees of freedom and non-centrality parameter $2\eta = 2\frac{|\tilde{\alpha}|^2}{\sigma_{\mathrm{w}}^2}\sum_{m\in\mathcal{M}}\langle \boldsymbol{s}^{(m)}(\tilde{\boldsymbol{\psi}}), \boldsymbol{s}^{(m)}(\boldsymbol{\psi})\rangle_{\mathcal{H}}$, with $\tilde{\boldsymbol{\psi}}$ and $\tilde{\alpha}$ as the true dispersion parameters and complex amplitude of the SMC, respectively. The proof that $u(\boldsymbol{\psi})$ is asymptotically approximated by a non-central chi-square distribution can be found in [41]. Therefore, the probability of missed detection $P_{\mathrm{M}}^{(r)}(\kappa) \leq \mathbb{P}[1/2u(\boldsymbol{\psi}) < \kappa]$ of a model component is approximated by [41]

$$P_{\mathrm{M}}^{(r)}(\kappa) = \int_0^{\kappa} \mathrm{e}^{-(x+\eta)} I_0(2\sqrt{\eta x})\mathrm{d}x. \tag{61}$$

To analyze the probability of missed detection and get an operating characteristic, we synthesize a signal with a single SMC according to (6) for a 5×2 array with an inter-element spacing of $2\,\mathrm{cm}$. We adapt the algorithm presented in Algorithm 1 to utilize a fixed threshold κ^* and set $L = 10$.[13] The parameters of the SMC are set as follows: we fix the delay of the SMC to $\tilde{\tau}_1 = 3\mathrm{m}/c$, and draw the AoA of the SMC uniformly over its range $\tilde{\varphi}_1 \sim \mathcal{U}(0, 2\pi)$. The SDR $= -5\,\mathrm{dB}$, the SNR $= \{5, 10, 20\}\,\mathrm{dB}$ and the number of samples $N = 54$. By fixing the delay of the SMC, we are able to evaluate the probability of missed detection, as the non-centrality parameter stays constant at $\eta = \{8.2, 12.2, 16.7\}\,\mathrm{dB}$ for the different values of the SNR. For the detection of the SMC, the non-centrality parameter η plays a more important role than the SNR. In fact, the DMC process has a saturating effect on the non-centrality parameter which can be seen as a signal-to-interference-plus-noise-ratio [61].[14]

Fig. 2 shows a comparison of the analytical probability of artifacts $P_{\mathrm{A}}^{(r)}(\kappa)$ (dashed lines) with the relative frequency of artifacts (solid lines) computed empirically from 1000 trials according to the setup described above. If one of the estimated components falls within 5 times the square root of the Cramér Rao lower bound [64] around the true value of $\tilde{\boldsymbol{\psi}}_1$ it is recognized as a successful detection and used to compute the empirical relative frequency of missed detection (dotted lines) which is compared to the analytical probability of missed detection $P_{\mathrm{M}}^{(r)}(\kappa)$ (dash dotted lines).

The derivations in the previous section have been made with the assumption that the covariance matrix is known. Thus, we compare the results for known (Fig. 2a) and estimated (Fig. 2b) covariance matrix. The influence of the estimation of the covariance matrix is only small with respect to the probability of artifact and missed detection. For the latter, the following observation can be made: If the parameters of the covariance matrix are estimated, the probability of missed detection is slightly lower. This is because during the first acquisition procedure, SMCs are favored with respect to the DMC. For small SNR, the relative frequency of missed detection shows a floor at small values of the threshold κ. For these SNRs when κ is small, the estimated components are outside the previously defined radius around the true component.

7.1.2 Estimation of overlapping SMCs

In Fig. 3, we highlight the super-resolution capabilities of the algorithm (note that in Fig. 3 we depict the delays as distances (remember that $d = \tau c$ with c

---

[13]We restrict the value of L to reduce the computational load.

[14]In an AWGN-only setup (neglecting the DMC), the non-centrality parameter reduces to the SNR.
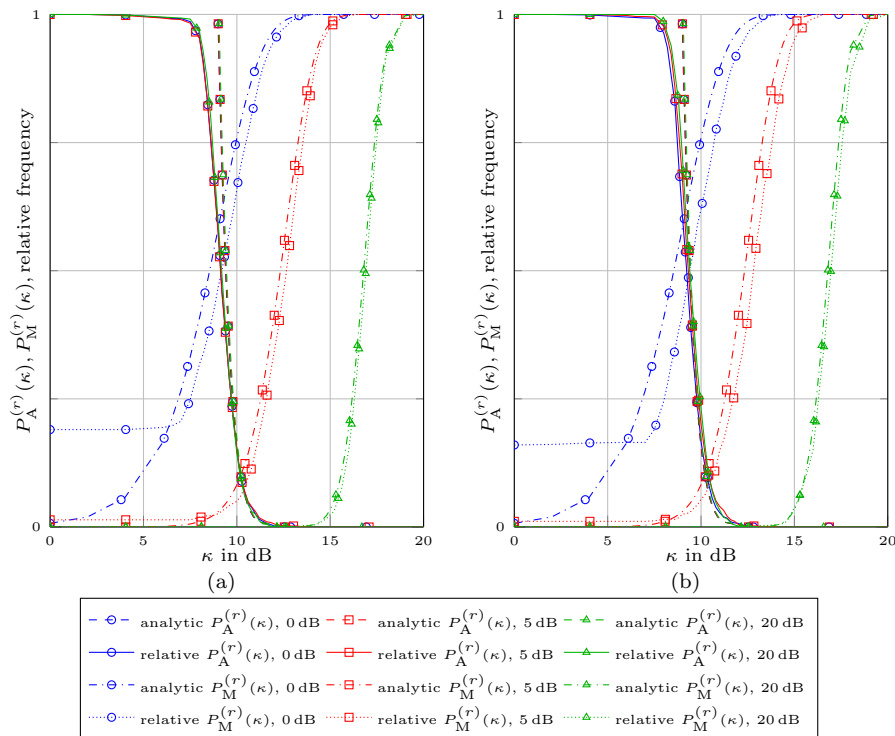
Figure 2: Operating characteristics of the algorithm for the estimation of a single SMC for known (a) and unknown (b) covariance matrix for three different values of SNR $= [5, 10, 20]$ dB. The analytical probability of artifact $P_{\mathrm{A}}^{(r)}(\kappa)$ and the analytical probability of missed detection $P_{\mathrm{m}}^{(r)}(\kappa)$ are compared to the relative frequency of artifacts and the relative frequency of missed detection for 1000 realizations, respectively.

as speed-of-light) for easier readability of the plots). To this end, signals with $K = 2$ SMCs are synthesized with different spacings in the delay and angular domains. The location $\boldsymbol{\psi}_1$ of the first SMC in the 2D delay-angular space is drawn uniformly within the support of the delay[15] and angular domains. The location of the second dispersion parameter is then given by $\tilde{\boldsymbol{\psi}}_2 = \tilde{\boldsymbol{\psi}}_1 + [\Delta d/c, 0]^{\mathrm{T}}$ or $\tilde{\boldsymbol{\psi}}_2 = \tilde{\boldsymbol{\psi}}_1 + [0, \Delta\varphi]^{\mathrm{T}}$.

The spacing Δd, depicted by the bottom x-axis (blue solid curves), and $\Delta\varphi$, depicted by the top x-axis (red dashed curves), are fractions of the reciprocal Nyquist bandwidth $(0.3\,\mathrm{m})$ and Rayleigh resolution $(56°)$, respectively [65]. Both complex amplitudes have a magnitude of 1 and a uniformly drawn phase. In Fig. 3 we depict the delays as distances (remember that $d = \tau c$ with c as speed-of-light) for easier readability of the plots. The used array is a two-dimensional 3×3 rectangular array with an inter-element spacing of $2\,\mathrm{cm}$. The SDR $= 6\,\mathrm{dB}$, the SNR $= \{10, 30, 50\}$ dB and the number of samples $N = 54$. As before, we set the number of estimated SMCs to $L = 10$ and the probability of artifact to $0.1\,\%$ and compute the according threshold κ^* online.

---

[15] For this experiment the support of the delay of the first SMC is restricted to be in $[2T_p, T - (2T_p + \Delta d/c)]$. The reason for this is that the SMCs shall be within the observation duration.

166
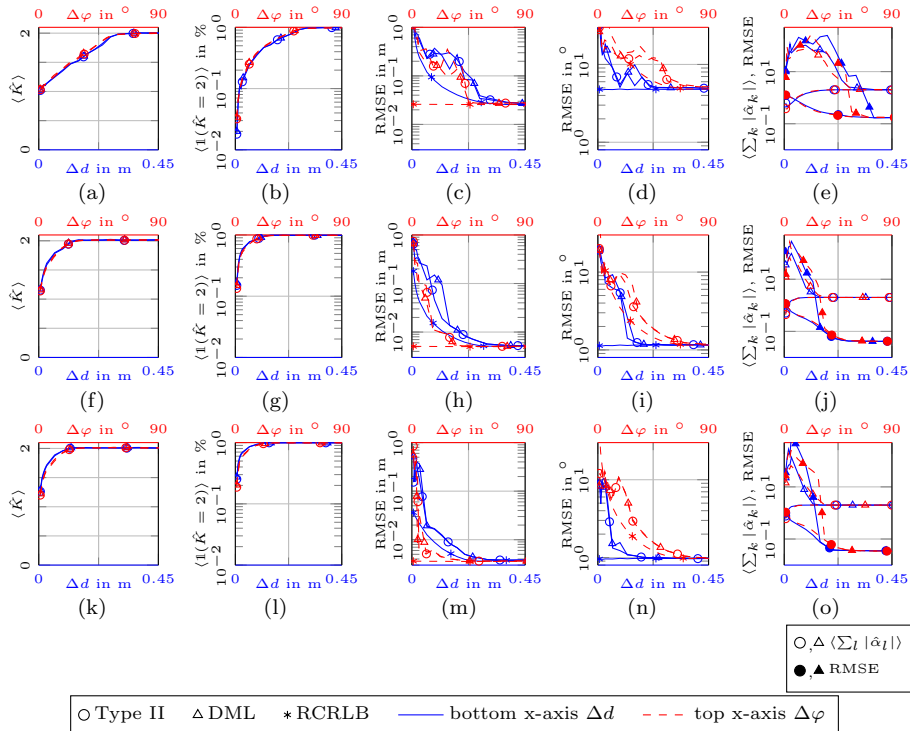
Figure 3: Estimation of two closely spaced SMCs with a 3×3 array with inter-element spacing of $2\,\mathrm{cm}$ in AWGN plus DMC with unknown covariance matrix. Blue solid lines and red dashed lines refer to the bottom and top x-axis, respectively. The rows depict different SNR: (a)-(e) SNR = $10\,\mathrm{dB}$, (f)-(j) SNR = $30\,\mathrm{dB}$, and (k)-(o) SNR = $50\,\mathrm{dB}$. The columns depict the mean number of estimated SMCs ((a), (f), and (k)), the relative frequency that exactly 2 SMCs are found ((b), (g), and (l)), the RMSE of the delay ((c), (h), and (m)), the RMSE of the AoA ((d), (i), and (n)), and the mean value (unfilled) and RMSE (filled) of the absolute value of the complex amplitudes ((e), (j), and (o)).

In Fig. 3 we compare the proposed Type-II algorithm (circles) to a deterministic maximum likelihood (DML) algorithm (triangles) with the same scheduling. The derivation of the DML algorithm and the detailed update equations can be found in the supplementary material in Appendix D. As classical DML does not include model-order selection, we utilize similar reasoning as in [46], adapt it to the signal model in the supplementary material in Appendix D and apply the threshold derived in Sec. 5.

The first two columns of Fig. 3 show the mean number of estimated SMCs $\langle \hat{K} \rangle$ and the relative frequency that exactly 2 SMCs are estimated $\langle \mathbb{1}(\hat{K} = 2) \rangle$ over the spacing in the delay (blue solid curves) and angular (red dashed curves) domain. Both the proposed Type-II and the DML algorithm are able to find the correct number of SMCs if the spacing between the two SMCs is *wide* enough. For a high SNR (see Fig. 3 (k) to (o)) this spacing is as low as $0.15\,\mathrm{m}$ or $20\,°$ for the simulated system parameters. At lower SNR (see Fig. 3 (a) to (e)) the spacing to robustly detect both SMCs rises to the reciprocal Nyquist bandwidth

Figure 4: Picture of the investigated room. The anchor position $\boldsymbol{p}_\mathrm{A}$, the agent position $\boldsymbol{p}_1$ as well as some items are labeled (cf. Fig. 5).

(0.3 m) and Rayleigh resolution (56°). However, the spacing to robustly detect two SMCs is not only influenced by the AWGN but also by the DMC, meaning that for high SNR the detection capability is capped by the SDR. Furthermore, both algorithms tend to underestimate the model order for very small spacings and do not produce artifacts.

Columns three and four depict the root-mean-square error (RMSE) of the delay (distance) and the AoA, respectively, if exactly 2 SMCs are found. We associate the two estimated SMCs to the true SMCs via the optimal sub-pattern assignment (OSPA) metric [66]. To be able to use the OSPA metric we normalize the estimated delays and AoAs with the reciprocal Nyquist bandwidth and Rayleigh resolution, respectively. Additionally, the root of the sum CRLB for the delays and AoAs are depicted (solid lines with stars). The estimated values approach the root CRLB if the spacing is large enough for both estimators.

The last column presents the mean of the absolute value of the complex amplitudes $\langle \sum_l |\hat{\alpha}_l| \rangle$ (empty markers) and the RMSE of the absolute value of the complex amplitudes (filled markers) if exactly 2 SMCs are found.

While the two estimators show nearly no difference in the estimation of the dispersion parameters delay and AoA, the estimation of the complex amplitudes is clearly different for narrow spacings. This can be explained by the fact that the DML utilizes a least-squares estimator for the complex amplitudes. If the two estimated SMCs are closely spaced, the inverse needed for the least squares estimator is close to singular, leading to estimates for the complex amplitudes that are huge but have opposite sign.

7.2 Measured Radio Channels

The measurements were performed in the room depicted in Fig. 4 using an m-sequence correlative channel sounder [67]. More details about the measurement setup can be found in [68]. The channel sounder measures within a bandwidth of 7 GHz centered at 7 GHz. We reduced the overall bandwidth by filtering with a root-raised-cosine pulse at a center frequency of 6 GHz. This filtered signal does not include any noticeable AWGN, hence, to arrive at the model described in (3), we artificially add AWGN with an SNR = 40 dB. By using a positioning table during the measurement campaign, a virtual 3×3 antenna array with inter-element spacing of 2 cm is employed. Furthermore, we set the observation duration to range from -4 to 40 m, leading to $N = 235$ samples. For the algorithm, we set the probability of artifact to 1 % and compute the

168
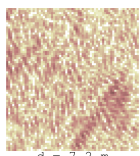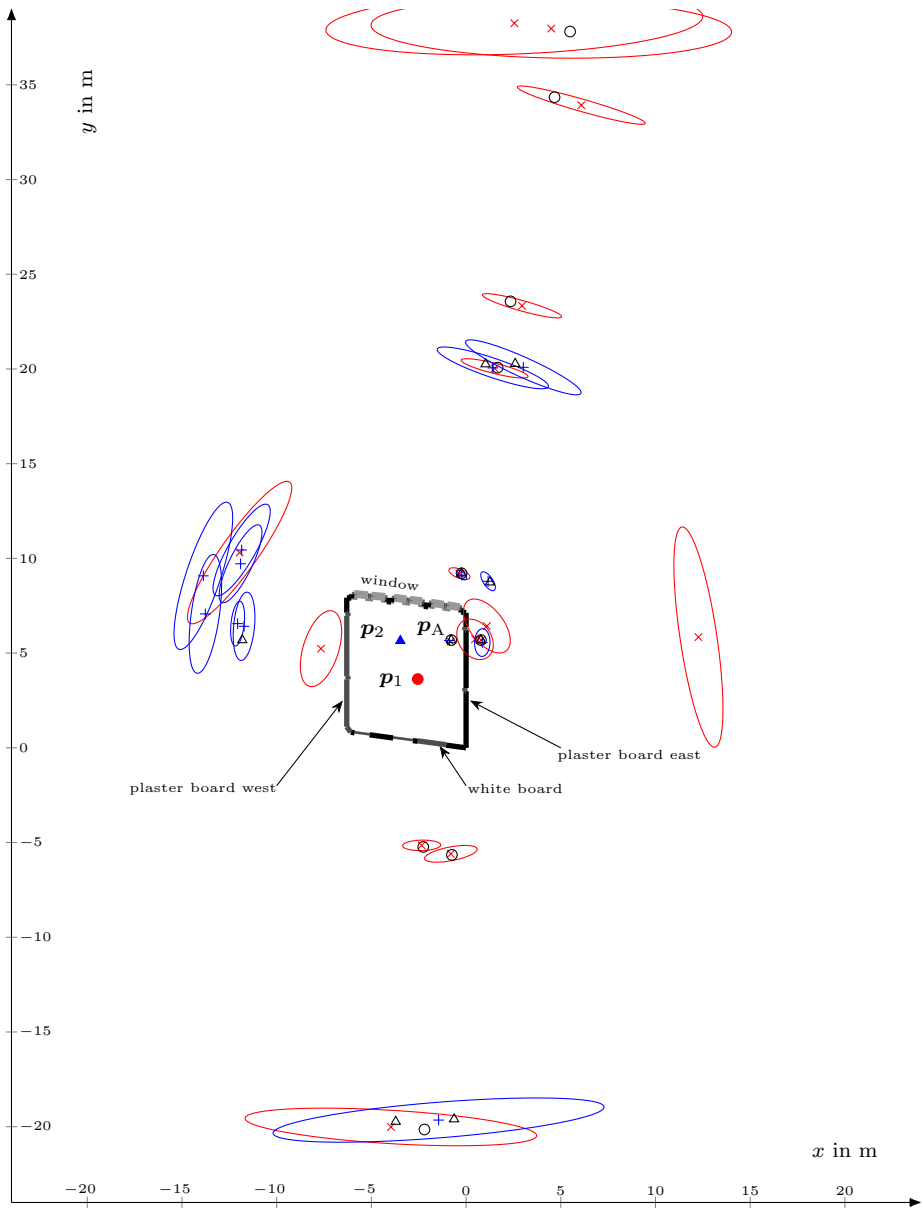
Figure 5: Floorplan of the investigated environment including the anchor position $\boldsymbol{p}_A$, the two agent positions $\boldsymbol{p}_1$ (red filled circle) and $\boldsymbol{p}_2$ (blue filled triangle), the estimated VAs for agent 1 (red crosses) and agent 2 (blue pluses) and the associated VAs (black circles and triangles, respectively). The ellipses around the estimated VAs depict root CRLBs (magnified by a factor of 50 in the delay domain and 5 in the AoA domain).

according threshold κ^* online. Furthermore, we set $L = MN$ to the number of samples.

The layout of the room is depicted in Fig. 5. This is an exact model of the room, including the position of the anchor $\boldsymbol{p}_A$. We placed the agent at two
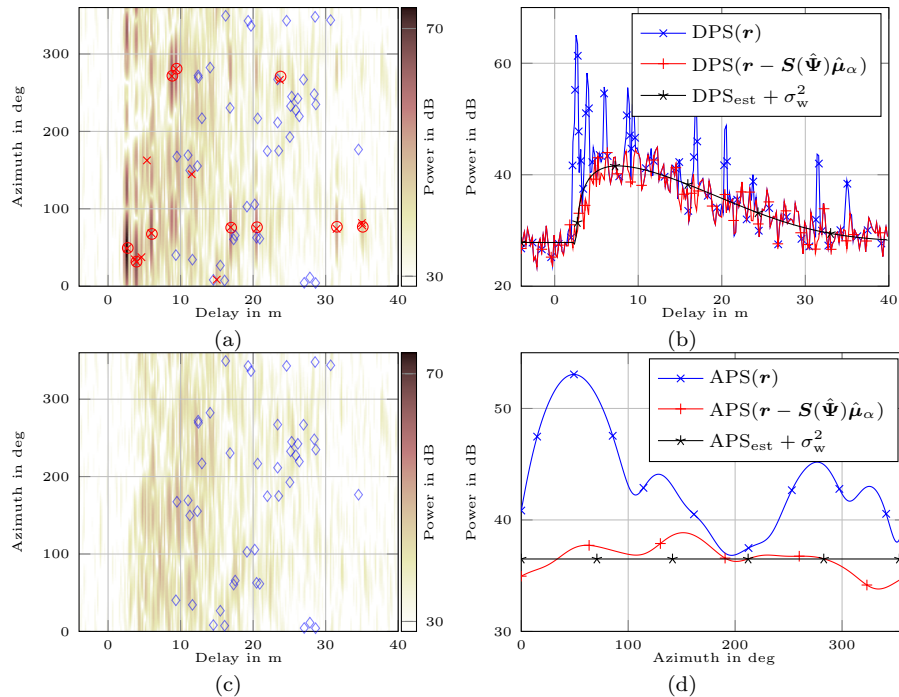
Figure 6: Detailed analysis for one array: (a): Estimated delay-azimuth power spectrum of the received signal r including the estimated SMCs (red crosses), associated predicted SMCs (red circles) and non-associated predicted SMCs (blue diamonds). (b): Estimated DPS of the received signal r (solid blue with crosses), the residual signal $r - S(\hat{\Psi})\hat{\mu}_\alpha$ (solid red with pluses), and the estimated parametrized DPS plus AWGN (solid black with stars). (c): Estimated delay-azimuth power spectrum of the residual signal $r - S(\hat{\Psi})\hat{\mu}_\alpha$ and non-associated predicted SMCs (blue diamonds) (d): Estimated APS for the same signals as in (b).

different positions p_1 and p_2 equipped with the virtual array. SMCs are predicted arising from virtual anchors (VAs). These VAs are obtained as mirror images of the anchor with respect to the walls [6]. Up to 5th-order reflections are considered. SMCs can be seen as if they originate from these VAs, meaning inversely that an estimated VA position can be inferred from the estimates of the SMCs $\hat{\psi}_l$ as $\hat{p}_{A,l} = p + c\hat{\tau}_l[\cos(\hat{\varphi}_l)\ \sin(\hat{\varphi}_l)]^T$. These estimated VA positions are depicted by red crosses and blue pluses for agent positions $p \in \{p_1, p_2\}$, respectively. To associate estimated SMCs with predicted SMCs, we use a frequentist approach: we compute the CRLB of the estimated delay and AoA and associate a predicted SMC if both its delay and AoA fall within 5 times the estimated root-CRLB. Due to calibration artifacts in the measured data[16], we added 10 cm to the estimated root-CRLB in the delay domain. These associated predicted VAs are depicted in Fig. 5 by black circles and triangles for agent 1 and 2, respectively. Clearly, most of the estimated SMCs are associated to

---

[16]The measurement setup was calibrated up to the antenna connectors, meaning that the antennas are not calibrated for.
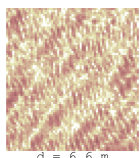
predicted VAs. Additionally, in Fig. 5 we added the estimated root-CRLBs for the estimated VA positions as error ellipses with a 50-fold increase in the delay domain and a 5-fold increase in the angular domain.

For both agent positions the algorithm is able to identify the LOS, most of the first-order reflections and some higher-order reflections. Especially the second-order reflections via the white board and the window are found as these surfaces are made of highly reflective materials. In comparison, the "plaster board west" and "plaster board east" reflections correspond to much less reflective plasterboard walls. Furthermore, a metallic frame has been present (see Fig. 4) This could also explain the detected component at approximately $[-8, 6]^{\mathrm{T}}$ m close to the plaster board west which probably stems from scattering from this metallic frame. For agent position 2 many SMCs are found in the region at $[-15, 8]^{\mathrm{T}}$ m which can probably also be attributed to the metallic frame which is not modeled in the floorplan, hence no predicted VAs are generated.

In Fig. 6 the results are shown in more detail for agent position 1. In Fig. 6(a), the estimated delay-azimuth power spectrum is depicted [69] for the received signal. The red crosses mark the delay and angle of the estimated SMCs, the red circles mark the associated predicted SMCs, and the blue diamonds mark the non-associated predicted SMCs. Again, most of the estimated SMCs are associated with geometrically expected SMCs. Furthermore, it could be argued that the estimated SMCs at $15\,\mathrm{m}$ and $10\,^\circ$, and at $12\,\mathrm{m}$ and $150\,^\circ$ should be associated to the close predicted VAs. Again, it has to be mentioned, that the red circles and blue diamonds are purely due to 'geometric' ray tracing and do not consider reflection coefficients, blocking by some furniture, etc. In Fig. 6(c) the estimated delay-azimuth power spectrum is shown for the residual signal $\boldsymbol{r} - \boldsymbol{S}(\hat{\boldsymbol{\Psi}})\hat{\boldsymbol{\mu}}_\alpha$ and compared to the non-associated VAs (blue triangles). Clearly, the strong peaks have vanished. Fig. 6(b) shows the estimated DPS for the original signal (solid blue with crosses), the residual signal (solid red with pluses), and the estimated parametrized DPS plus AWGN (solid black with stars). The estimated DPS is computed by averaging the corresponding delay-azimuth power spectrum. The residual estimated DPS and the estimated parametrized DPS match well. This empirically justifies the choice of a gamma-function for the DPS. Finally, Fig. 6(d) depicts the estimated angle-power-spectrum (APS) for the same signals as in Fig. 6(b). The APS is computed by averaging the corresponding delay-azimuth power spectrum over the delay domain. It can be seen that the APS of the residual signal is already quite flat over the whole azimuth range.

8   Conclusions

In this paper, we investigate a super-resolution SBL algorithm for single-input-multiple-output (SIMO) multipath channel parameter estimation using a hierarchical Gaussian prior. Particularly, a Type-II point-estimate-based SBL algorithm is developed with a hierarchical Gaussian prior, which is applicable to colored non-stationary noise models, capable of representing measurement noise plus DMC. The algorithm jointly estimates the delays and AoAs of the SMCs, the DMC and noise parameters, and the number of SMCs (model order). Whether an SMC is considered as part of the model or discarded as an estimation artifact is based on a sparsity parameter, which is only finite, if a built-in
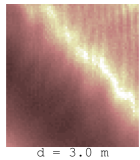
pruning condition exceeds a (detection) threshold. This threshold is derived by a probability of artifacts using two-dimensional non-stationary χ^2-random fields. It is suitable for common signal pulses, i.e., even or odd waveforms, general symmetric array-geometries, and a general noise covariance matrix.

The numerical results show that the expected probability of artifacts based on the derived threshold predicts very accurately the actual relative frequency of the proposed algorithm. We also show that the proposed algorithm is capable of determining the correct model order and estimating the parameters of the SMCs, the DMC and noise with high accuracy (close to the CRLB performance) even for SMC spacings far below the Nyquist and Rayleigh separation (in delay and angle domain). The comparison to an equivalent Type-I point-estimate-based ML algorithm shows that both algorithms perform similarly in terms of accurate model-order estimation and accuracy of model parameters. However, the complex amplitudes estimated by the Type-I point-estimate-based ML algorithm show a very high estimation bias and variance for closely-spaced SMCs, while this is not the case for the proposed Type-II point-estimate-based SBL algorithm.

References

[1] F. Boccardi, R. W. Heath, A. Lozano, T. L. Marzetta, and P. Popovski, "Five disruptive technology directions for 5G," *IEEE Commun. Mag.*, vol. 52, no. 2, pp. 74–80, Feb. 2014.

[2] M. Simsek, A. Aijaz, M. Dohler, J. Sachs, and G. Fettweis, "5G-enabled tactile internet," *IEEE J. Sel. Areas Commun.*, vol. 34, no. 3, pp. 460–473, Mar. 2016.

[3] R. Di Taranto, S. Muppirisetty, R. Raulefs, D. Slock, T. Svensson, and H. Wymeersch, "Location-aware communications for 5G networks: How location information can improve scalability, latency, and robustness of 5G," *IEEE Signal Process. Mag.*, vol. 31, no. 6, pp. 102–112, Nov. 2014.

[4] L. Muppirisetty, T. Svensson, and H. Wymeersch, "Spatial wireless channel prediction under location uncertainty," *IEEE Trans. Wireless Commun.*, vol. 15, no. 2, pp. 1031–1044, Feb. 2016.

[5] K. Witrisal, P. Meissner, E. Leitinger, Y. Shen, C. Gustafson, F. Tufvesson, K. Haneda, D. Dardari, A. F. Molisch, A. Conti, and M. Z. Win, "High-accuracy localization for assisted living: 5G systems will turn multipath channels from foe to friend," *IEEE Signal Process. Mag.*, vol. 33, no. 2, pp. 59–70, Mar. 2016.

[6] E. Leitinger, P. Meissner, C. Rudisser, G. Dumphart, and K. Witrisal, "Evaluation of position-related information in multipath components for indoor positioning," *IEEE J. Sel. Areas Commun.*, vol. 33, no. 11, pp. 2313–2328, Nov. 2015.

[7] R. Mendrzik, H. Wymeersch, G. Bauch, and Z. Abu-Shaban, "Harnessing NLOS components for position and orientation estimation in 5G millimeter wave MIMO," *IEEE Trans. Wireless Commun.*, vol. 18, no. 1, pp. 93–107, Jan. 2019.
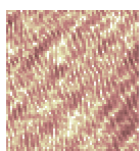
[8] R. Mendrzik, F. Meyer, G. Bauch, and M. Z. Win, "Enabling situational awareness in millimeter wave massive MIMO systems," *IEEE J. Sel. Topics Signal Process.*, vol. 13, no. 5, pp. 1196–1211, Sep. 2019.

[9] E. Leitinger, F. Meyer, F. Hlawatsch, K. Witrisal, F. Tufvesson, and M. Z. Win, "A belief propagation algorithm for multipath-based SLAM," *IEEE Trans. Wireless Commun.*, vol. 18, no. 11, pp. 1–17, Dec. 2019.

[10] C. Gentner, T. Jost, W. Wang, S. Zhang, A. Dammann, and U. C. Fiebig, "Multipath assisted positioning with simultaneous localization and mapping," *IEEE Trans. Wireless Commun.*, vol. 15, no. 9, pp. 6104–6117, Sep. 2016.

[11] P. Stoica and R. Moses, *Spectral Analysis of Signals*. Pearson Prentice Hall, 2005. [Online]. Available: https://books.google.se/books?id=h78ZAQAAIAAJ

[12] M. A. Badiu, T. L. Hansen, and B. H. Fleury, "Variational Bayesian inference of line spectra," *IEEE Trans. Signal Process.*, vol. 65, no. 9, pp. 2247–2261, May 2017.

[13] T. L. Hansen, B. H. Fleury, and B. D. Rao, "Superfast line spectral estimation," *IEEE Trans. Signal Process.*, vol. PP, no. 99, pp. 1–1, 2018.

[14] A. P. Dempster, N. M. Laird, and D. B. Rubin, "Maximum likelihood from incomplete data via the EM algorithm," *J R Stat Soc Series B Stat Methodol*, vol. 39, no. 1, pp. 1–38, 1977.

[15] J. A. Fessler and A. O. Hero, "Space-alternating generalized expectation-maximization algorithm," *IEEE Trans. Signal Process.*, vol. 42, no. 10, pp. 2664–2677, Oct. 1994.

[16] B. H. Fleury, M. Tschudin, R. Heddergott, D. Dahlhaus, and K. I. Pedersen, "Channel parameter estimation in mobile radio environments using the SAGE algorithm," *IEEE J. Sel. Areas Commun.*, vol. 17, no. 3, pp. 434–450, Mar. 1999.

[17] A. Richter, "Estimation of Radio Channel Parameters: Models and Algorithms," Ph.D. dissertation, Ilmenau University of Technology, 2005.

[18] P. Stoica and Y. Selen, "Model-order selection: A review of information criterion rules," *IEEE Signal Process. Mag.*, vol. 21, no. 4, pp. 36–47, Jul. 2004.

[19] P. M. Djuric, "A model selection rule for sinusoids in white Gaussian noise," *IEEE Trans. Signal Process.*, vol. 44, no. 7, pp. 1744–1751, July 1996.

[20] J. Rissanen, "Modeling by shortest data description," *Automatica*, vol. 14, no. 5, pp. 465–471, Sep. 1978. [Online]. Available: http://dx.doi.org/10.1016/0005-1098(78)90005-5

[21] A. Mariani, A. Giorgetti, and M. Chiani, "Model order selection based on information theoretic criteria: Design of the penalty," *IEEE Trans. Signal Process.*, vol. 63, no. 11, pp. 2779–2789, Jun. 2015.
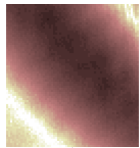
[22] E. J. Candes and T. Tao, "Near-optimal signal recovery from random projections: Universal encoding strategies?" *IEEE Trans. Inf. Theory*, vol. 52, no. 12, pp. 5406–5425, Dec. 2006.

[23] D. L. Donoho, "Compressed sensing," *IEEE Trans. Inf. Theory*, vol. 52, no. 4, pp. 1289–1306, Apr. 2006.

[24] R. Tibshirani, "Regression shrinkage and selection via the LASSO," *J. Roy. Statist. Soc.*, vol. 58, no. 1, pp. 267–288, 1996. [Online]. Available: http://www.jstor.org/stable/2346178

[25] J. A. Tropp and S. J. Wright, "Computational methods for sparse solution of linear inverse problems," *Proc. IEEE*, vol. 98, no. 6, pp. 948–958, Jun. 2010.

[26] S. S. Chen, D. L. Donoho, and M. A. Saunders, "Atomic decomposition by basis pursuit," *SIAM Rev.*, vol. 43, no. 1, pp. 129–159, 2001. [Online]. Available: http://dx.doi.org/10.1137/S003614450037906X

[27] D. P. Wipf, B. D. Rao, and S. Nagarajan, "Latent variable Bayesian models for promoting sparsity," *IEEE Trans. Inf. Theory*, vol. 57, no. 9, pp. 6236–6255, Sept 2011.

[28] M. E. Tipping, "Sparse Bayesian learning and the relevance vector machine," *J. Mach. Learn. Res.*, vol. 1, pp. 211–244, Sep. 2001. [Online]. Available: https://doi.org/10.1162/15324430152748236

[29] D. P. Wipf and B. D. Rao, "Sparse Bayesian learning for basis selection," *IEEE Trans. Signal Process.*, vol. 52, no. 8, pp. 2153–2164, Aug. 2004.

[30] D. G. Tzikas, A. C. Likas, and N. P. Galatsanos, "The variational approximation for Bayesian inference," *IEEE Signal Process. Mag.*, vol. 25, no. 6, pp. 131–146, Nov. 2008.

[31] C. M. Bishop and M. E. Tipping, "Variational relevance vector machines," in *Proc. UAI-2000*. Morgan Kaufmann Publishers Inc., 2000, pp. 46–53.

[32] T. Buchgraber, "Variational sparse Bayesian learning: Centralized and distributed processing," Ph.D. dissertation, 2013.

[33] R. Giri and B. Rao, "Type I and type II Bayesian methods for sparse signal recovery using scale mixtures," *IEEE Trans. Signal Process.*, vol. 64, no. 13, pp. 3418–3428, July 2016.

[34] Y. Chi and Y. Chen, "Compressive two-dimensional harmonic retrieval via atomic norm minimization," *IEEE Trans. Signal Process.*, vol. 63, no. 4, pp. 1030–1042, Feb. 2015.

[35] Y. Hua, "Estimating two-dimensional frequencies by matrix enhancement and matrix pencil," *IEEE Trans. Signal Process.*, vol. 40, no. 9, pp. 2267–2280, Sep. 1992.

[36] B. N. Bhaskar, G. Tang, and B. Recht, "Atomic norm denoising with applications to line spectral estimation," *IEEE Trans. Signal Process.*, vol. 61, no. 23, pp. 5987–5999, Dec. 2013.
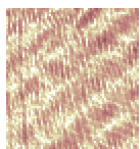
[37] K. Konstantinides and K. Yao, "Statistical analysis of effective singular values in matrix rank determination," *IEEE Trans. Acoust., Speech, Signal Process.*, vol. 36, no. 5, pp. 757–763, May 1988.

[38] E. J. Candes and C. Fernandez-Granda, "Towards a mathematical theory of super-resolution," *Commun. Pure Appl. Math.*, vol. 67, no. 6, pp. 906–956, 2012.

[39] D. Malioutov, M. Cetin, and A. S. Willsky, "A sparse signal reconstruction perspective for source localization with sensor arrays," *IEEE Trans. Signal Process.*, vol. 53, no. 8, pp. 3010–3022, Aug. 2005.

[40] D. Shutin and B. H. Fleury, "Sparse variational Bayesian SAGE algorithm with application to the estimation of multipath wireless channels," *IEEE Trans. Signal Proces.*, vol. 59, no. 8, pp. 3609–3623, Aug. 2011.

[41] D. Shutin, B. H. Fleury, and N. Schneckenburger, "Artifact suppresion for super-resolution sparse Bayesian learning," *Corr*, 2018.

[42] D. Shutin, T. Buchgraber, S. R. Kulkarni, and H. V. Poor, "Fast variational sparse Bayesian learning with automatic relevance determination for superimposed signals," *IEEE Trans. Signal Process.*, vol. 59, no. 12, pp. 6257–6261, Dec. 2011.

[43] D. Shutin, S. R. Kulkarni, and H. V. Poor, "Incremental reformulated automatic relevance determination," *IEEE Trans. Signal Process.*, vol. 60, no. 9, pp. 4977–4981, Sept. 2012.

[44] C. Andrieu and A. Doucet, "Joint Bayesian model selection and estimation of noisy sinusoids via reversible jump MCMC," *IEEE Trans. Signal Process.*, vol. 47, no. 10, pp. 2667–2676, Oct. 1999.

[45] K. F. Turkman and A. M. Walker, "On the asymptotic distributions of maxima of trigonometric polynomials with random coefficients," *Adv. Appl. Probab.*, vol. 16, no. 4, pp. 819–842, 1984. [Online]. Available: http://www.jstor.org/stable/1427342

[46] B. Nadler and A. Kontorovich, "Model selection for sinusoids in noise: Statistical analysis and a new penalty term," *IEEE Trans. Signal Process.*, vol. 59, no. 4, pp. 1333–1345, Apr. 2011.

[47] S. Kay, *Fundamentals of Statistical Signal Processing: Detection Theory.* Upper Saddle River, NJ, USA: Prentice Hall, 1998.

[48] R. J. Adler and J. E. Taylor, *Random Fields and Geometry.* New York, NY, USA: Springer, 2007.

[49] R. J. Adler, J. E. Taylor, and K. J. Worsley, "Applications of random fields and geometry: Foundations and case studies," 2015.

[50] P. Bello, "Characterization of randomly time-variant linear channels," *Communications Systems, IEEE Transactions on*, vol. 11, no. 4, pp. 360 –393, december 1963.

[51] J. Karedal, S. Wyne, P. Almers, F. Tufvesson, and A. Molisch, "A measurement-based statistical model for industrial ultra-wideband channels," *IEEE Trans. Wireless Commun.*, vol. 6, no. 8, pp. 3028–3037, Aug. 2007.

[52] B. H. Fleury, "First- and second-order characterization of direction dispersion and space selectivity in the radio channel," *IEEE Trans. Inf. Theory*, vol. 46, no. 6, pp. 2027–2044, Sept. 2000.

[53] W. Weichselberger, "Spatial Structure of Multiple Antenna Radio Channels: A Signal Processing Viewpoint," Ph.D. dissertation, Technische Universität Wien, 2003.

[54] J. Salmi, A. Richter, and V. Koivunen, "Detection and tracking of MIMO propagation path parameters using state-space approach," *IEEE Trans. Signal Process.*, vol. 57, no. 4, pp. 1538–1550, Apr. 2009.

[55] J. Andersen, J. Nielsen, G. Pedersen, G. Bauch, and M. Herdin, "Room electromagnetics," *Antennas and Propagation Magazine, IEEE*, vol. 49, no. 2, pp. 27–33, 2007.

[56] A. F. Molisch, D. Cassioli, C.-C. Chong, S. Emami, A. Fort, B. Kannan, J. Karedal, J. Kunisch, H. G. Schantz, K. Siwiak *et al.*, "A comprehensive standardized model for ultrawideband propagation channels," *IEEE Trans. Antennas Propag.*, vol. 54, no. 11, pp. 3151–3166, Nov. 2006.

[57] T. Pedersen, "Stochastic multipath model for the in-room radio channel based on room electromagnetics," *IEEE Trans. Antennas Propag*, vol. 67, no. 4, pp. 2591–2603, April 2019.

[58] C. M. Bishop, *Pattern Recognition and Machine Learning (Information Science and Statistics)*. Secaucus, NJ, USA: Springer-Verlag New York, Inc., 2006.

[59] M. Beal, "Variational algorithms for approximate Bayesian inference," Ph.D. dissertation, University College London, 2003.

[60] M. E. Tipping and A. C. Faul, "Fast marginal likelihood maximisation for sparse Bayesian models," in *Proc. AISTATS-2003*, C. M. Bishop and B. J. Frey, Eds., 2003, pp. 3–6.

[61] K. Witrisal, E. Leitinger, S. Hinteregger, and P. Meissner, "Bandwidth scaling and diversity gain for ranging and positioning in dense multipath channels," *IEEE Wireless Commun. Lett.*, 2016.

[62] K. J. Worsley, "Local maxima and the expected euler characteristic of excursion sets of χ^2, f and t fields," *Adv. Appl. Probab.*, vol. 26, no. 1, pp. 13–42, 1994. [Online]. Available: http://www.jstor.org/stable/1427576

[63] A. C. Faul and M. E. Tipping, "Analysis of sparse bayesian learning," in *Advances in neural information processing systems*, 2002, pp. 383–389.

[64] T. Wilding, S. Grebien, E. Leitinger, U. Mühlmann, and K. Witrisal, "Single-anchor, multipath-assisted indoor positioning with aliased antenna arrays," in *Proc. Asilomar-18*, Pacifc Grove, CA, USA, Oct. 2018, pp. 525–531.

176
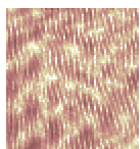
[65] H. L. Van Trees, *Optimum Array Processing, PartIV of Detection, Estimation and Modulation Theory.* Wiley Press, 2002.

[66] D. Schuhmacher, B.-T. Vo, and B.-N. Vo, "A consistent metric for performance evaluation of multi-object filters," *IEEE Trans. Signal Process.*, vol. 56, no. 8, pp. 3447–3457, Aug. 2008.

[67] Ilmsens Channel Sounder, accessed 22. Sept. 2016. [Online]. Available: http://www.ilmsens.com

[68] S. Hinteregger, E. Leitinger, P. Meissner, J. Kulmer, and K. Witrisal, "Bandwidth dependence of the ranging error variance in dense multipath," in *Proc. EUSIPCO-16*, Budapest, Hungary, Aug. 2016, pp. 733–737.

[69] A. Molisch, *Wireless Communications.* Wiley-IEEE Press, 2005.

d = 2.1 m

d = 4.2 m

178
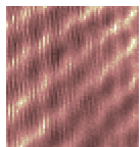
Supplementary Material:

Super-Resolution Channel Estimation Including the Dense Multipath Component — A Sparse Variational Bayesian Approach

Stefan Grebien[*], Erik Leitinger[*], Klaus Witrisal, Bernard H. Fleury

[*] Have equally contributed as first authors.

A Properties of Gaussian Process

Assuming that $\boldsymbol{n}^{(m)}$ is zero-mean complex Gaussian noise with known covariance matrix $\tilde{\boldsymbol{C}} = [\boldsymbol{C}(\boldsymbol{\eta})]_{m,m}$ (the (m,m)th $N \times N$ block of the covariance matrix), we get:

$$\mathbb{E}\big[x(\boldsymbol{\psi})\big] = C_1 \sum_{m \in \mathcal{M}} \mathbb{E}\big[\langle \boldsymbol{n}^{(m)}, \boldsymbol{s}^{(m)}(\boldsymbol{\psi}) \rangle_{\mathcal{H}}\big] = 0 \tag{1}$$

where $C_1 = \sqrt{2}/\big(\sum\limits_{m \in \mathcal{M}} \big\|\boldsymbol{s}^{(m)}(\boldsymbol{\psi})\big\|_{\mathcal{H}}^2 \big)^{1/2}$.

Furthermore,

$$
\begin{aligned}
\mathbb{E}\big[|\Re\{x(\boldsymbol{\psi})\}|^2\big] &= \mathbb{E}\big[\Re\{x(\boldsymbol{\psi})\}^{\mathrm{T}} \Re\{x(\boldsymbol{\psi})\}\big] \\
&= C_1^2 \mathbb{E}\big[\big| \sum_{m \in \mathcal{M}} \langle \Re\{\boldsymbol{n}^{(m)}\}, \Re\{\boldsymbol{s}^{(m)}(\boldsymbol{\psi})\} \rangle_{\mathcal{H}} \\
&\quad + \langle \Im\{\boldsymbol{n}^{(m)}\}, \Im\{\boldsymbol{s}^{(m)}(\boldsymbol{\psi})\}\rangle_{\mathcal{H}} \big|^2\big] \\
&= C_1^2 \frac{1}{2} \sum_{m \in \mathcal{M}} \|\Re\{\boldsymbol{s}^{(m)}\}\|_{\mathcal{H}}^2 + \|\Im\{\boldsymbol{s}^{(m)}\}\|_{\mathcal{H}}^2 = 1.
\end{aligned}
$$

A similar derivation leads to $\mathbb{E}\big[|\Im\{x(\boldsymbol{\psi})\}|^2\big] = 1$.

To show that $\mathbb{E}[\Re\{x(\boldsymbol{\psi})\}\Im\{x(\boldsymbol{\psi}')\}^{\mathrm{T}}] = 0$, we assume that the real and imaginary part of the transmitted complex baseband signal are equal, i.e., $\Re\{\underline{s}(t)\} = \Im\{\underline{s}(t)\} = \tilde{s}(t)$, and define $\tilde{\underline{\boldsymbol{s}}}^{(m)}(\boldsymbol{\psi}) = [\tilde{\underline{s}}\big(- (N - 1)/2T_{\mathrm{s}} - \tau +$

$$g\big(\varphi,\boldsymbol{p}^{(m)}\big)\big)\ \cdots\ \underline{\tilde{\boldsymbol{s}}}\big((N-1)/2T_{\mathrm{s}}-\tau+g\big(\varphi,\boldsymbol{p}^{(m)}\big)\big)\big]^{\mathrm{T}}\in\mathbb{R}^{N\times 1}$$

$$\mathbb{E}\big[\Re\{x(\boldsymbol{\psi})\}\Im\{x(\boldsymbol{\psi}')\}^{\mathrm{T}}\big]=$$
$$=C_1C_2\mathbb{E}\big[\Re\{\sum_{m\in\mathcal{M}}\langle\boldsymbol{n}^{(m)},\boldsymbol{s}^{(m)}(\boldsymbol{\psi})\rangle_{\mathcal{H}}\}\Im\{\sum_{m\in\mathcal{M}}\langle\boldsymbol{n}^{(m)},\boldsymbol{s}^{(m)}(\boldsymbol{\psi}')\rangle_{\mathcal{H}}\}\big]$$
$$=C_1C_2\sum_{m\in\mathcal{M}}\langle\underline{\tilde{\boldsymbol{s}}}^{(m)}(\boldsymbol{\psi}),\underline{\tilde{\boldsymbol{s}}}^{(m)}(\boldsymbol{\psi}')\rangle_{\mathcal{H}}\sin\big(2\pi f_{\mathrm{c}}\big(g\big(\varphi,\boldsymbol{p}^{(m)}\big)-g\big(\varphi',\boldsymbol{p}^{(m)}\big)\big)\big)$$
$$\approx C_1C_2\langle\underline{\tilde{\boldsymbol{s}}}^{(\mathrm{cg})}(\boldsymbol{\psi}),\underline{\tilde{\boldsymbol{s}}}^{(\mathrm{cg})}(\boldsymbol{\psi}')\rangle_{\mathcal{H}}$$
$$\times\sum_{m\in\mathcal{M}}\sin\big(2\pi f_{\mathrm{c}}\big(\cos(\varphi^{(m)})C_3+\sin(\varphi^{(m)})C_4\big)\big)\tag{2}$$
$$=0\,,\tag{3}$$

where $C_2=\sqrt{2}/\big(\sum\limits_{m\in\mathcal{M}}\big\|\boldsymbol{s}^{(m)}(\boldsymbol{\psi}')\big\|_{\mathcal{H}}^2\big)^{1/2}$. For (2) we assumed $\langle\underline{\tilde{\boldsymbol{s}}}^{(m)}(\boldsymbol{\psi}),\underline{\tilde{\boldsymbol{s}}}^{(m)}(\boldsymbol{\psi}')\rangle_{\mathcal{H}}\approx\langle\underline{\tilde{\boldsymbol{s}}}^{(m')}(\boldsymbol{\psi}),\underline{\tilde{\boldsymbol{s}}}^{(m')}(\boldsymbol{\psi}')\rangle_{\mathcal{H}}\approx\langle\underline{\tilde{\boldsymbol{s}}}^{(\mathrm{cg})}(\boldsymbol{\psi}),\underline{\tilde{\boldsymbol{s}}}^{(\mathrm{cg})}(\boldsymbol{\psi}')\rangle_{\mathcal{H}}$ with $\underline{\tilde{\boldsymbol{s}}}^{(\mathrm{cg})}(\boldsymbol{\psi})$ at the center of gravity of the array[1], and defined $C_3=\cos(\varphi-\psi)-\cos(\varphi'-\psi)$, and $C_4=\sin(\varphi-\psi)-\sin(\varphi'-\psi)$. Finally, to get from (2) to (3) we need the antenna array to be symmetric w.r.t. the x-axis and y-axis, i.e., $\boldsymbol{p}^{(m)}=-\boldsymbol{p}^{(M-m+1)}$.

B Covariance of 2-dimensional χ^2 Random Field

One entry of (52) is given in general as (4).

$$\mathbb{E}\Big[\frac{\partial x(\boldsymbol{\psi})\partial x(\boldsymbol{\psi})^*}{\partial\psi_i\partial\psi_j}\Big]=2\bigg(\frac{\sum\limits_{m\in\mathcal{M}}\langle\frac{\partial\boldsymbol{s}^{(m)}(\boldsymbol{\psi})}{\partial\psi_i},\frac{\partial\boldsymbol{s}^{(m)}(\boldsymbol{\psi})}{\partial\psi_j}\rangle_{\mathcal{H}}}{\sum\limits_{m\in\mathcal{M}}\|\boldsymbol{s}^{(m)}(\boldsymbol{\psi})\|_{\mathcal{H}}^2}\tag{4}$$
$$-\frac{\sum\limits_{m\in\mathcal{M}}\langle\boldsymbol{s}^{(m)}(\boldsymbol{\psi}),\frac{\partial\boldsymbol{s}^{(m)}(\boldsymbol{\psi})}{\partial\psi_i}\rangle_{\mathcal{H}}\Re\big\{\sum\limits_{m'\in\mathcal{M}}\langle\boldsymbol{s}^{(m')}(\boldsymbol{\psi}),\frac{\partial\boldsymbol{s}^{(m')}(\boldsymbol{\psi})}{\partial\psi_j}\rangle_{\mathcal{H}}\big\}}{\big|\sum\limits_{m\in\mathcal{M}}\|\boldsymbol{s}^{(m)}(\boldsymbol{\psi})\|_{\mathcal{H}}^2\big|^2}$$
$$-\frac{\sum\limits_{m\in\mathcal{M}}\langle\frac{\partial\boldsymbol{s}^{(m)}(\boldsymbol{\psi})}{\partial\psi_j},\boldsymbol{s}^{(m)}(\boldsymbol{\psi})\rangle_{\mathcal{H}}\Re\big\{\sum\limits_{m'\in\mathcal{M}}\langle\boldsymbol{s}^{(m')}(\boldsymbol{\psi}),\frac{\partial\boldsymbol{s}^{(m')}(\boldsymbol{\psi})}{\partial\psi_i}\rangle_{\mathcal{H}}\big\}}{\big|\sum\limits_{m\in\mathcal{M}}\|\boldsymbol{s}^{(m)}(\boldsymbol{\psi})\|_{\mathcal{H}}^2\big|^2}$$
$$+\frac{\Re\big\{\sum\limits_{m\in\mathcal{M}}\langle\boldsymbol{s}^{(m)}(\boldsymbol{\psi}),\frac{\partial\boldsymbol{s}^{(m)}(\boldsymbol{\psi})}{\partial\psi_i}\rangle_{\mathcal{H}}\big\}\Re\big\{\sum\limits_{m'\in\mathcal{M}}\langle\boldsymbol{s}^{(m')}(\boldsymbol{\psi}),\frac{\partial\boldsymbol{s}^{(m')}(\boldsymbol{\psi})}{\partial\psi_j}\rangle_{\mathcal{H}}\big\}}{\big|\sum\limits_{m\in\mathcal{M}}\|\boldsymbol{s}^{(m)}(\boldsymbol{\psi})\|_{\mathcal{H}}^2\big|^2}\bigg)$$

We define the partial derivative w.r.t. the delay, i.e., $\partial\boldsymbol{s}^{(m)}(\boldsymbol{\psi})/\partial\tau=-\mathrm{e}^{j2\pi f_{\mathrm{c}}g(\varphi,\boldsymbol{p}^{(m)})}\underline{\dot{\boldsymbol{s}}}^{(m)}(\boldsymbol{\psi})$ and w.r.t. the AoA, i.e., $\partial\boldsymbol{s}^{(m)}(\boldsymbol{\psi})/\partial\varphi=-D_m(\varphi)\exp(j2\pi f_{\mathrm{c}}g(\varphi,\boldsymbol{p}^{(m)}))(\underline{\dot{\boldsymbol{s}}}^{(m)}(\boldsymbol{\psi})+j2\pi f_{\mathrm{c}}\underline{\boldsymbol{s}}^{(m)}(\boldsymbol{\psi}))$ with

---

[1]This approximation is exact for a wideband signal model for the array, i.e., $s(t;\tau,\varphi,\boldsymbol{p}^{(m)})=\mathrm{e}^{j2\pi f_{\mathrm{c}}g(\varphi,\boldsymbol{p}^{(m)})}\underline{s}(t-\tau)$.

$D_m(\varphi) = \frac{d^{(m)}}{c} \sin\left(\varphi - \psi - \varphi^{(m)}\right)$, $\underline{\boldsymbol{s}}^{(m)}(\boldsymbol{\psi}) = [\underline{s}\left(0 - \tau + g(\varphi, \boldsymbol{p}^{(m)})\right) \cdots \underline{s}\left((N-1)T_{\mathrm{s}} - \tau + g(\varphi, \boldsymbol{p}^{(m)})\right)]^{\mathrm{T}} \in \mathbb{C}^{N \times 1}$, and $\underline{\dot{\boldsymbol{s}}}^{(m)}(\boldsymbol{\psi}) = \partial \underline{\boldsymbol{s}}^{(m)}(\boldsymbol{\psi})/\partial t$. To present the more intuitive results from the main text, we introduce the following approximations

$$\|\underline{\dot{\boldsymbol{s}}}^{(m)}(\boldsymbol{\psi})\|_{\mathcal{H}} \approx \|\underline{\dot{\boldsymbol{s}}}^{(\mathrm{cg})}(\boldsymbol{\psi})\|_{\mathcal{H}} \tag{5}$$

$$\langle \underline{\boldsymbol{s}}^{(m)}(\boldsymbol{\psi}), \underline{\dot{\boldsymbol{s}}}^{(m)}(\boldsymbol{\psi})\rangle_{\mathcal{H}} \approx \langle \underline{\boldsymbol{s}}^{(\mathrm{cg})}(\boldsymbol{\psi}), \underline{\dot{\boldsymbol{s}}}^{(\mathrm{cg})}(\boldsymbol{\psi})\rangle_{\mathcal{H}} \tag{6}$$

$$\|\underline{\boldsymbol{s}}^{(m)}(\boldsymbol{\psi})\|_{\mathcal{H}} \approx \|\underline{\boldsymbol{s}}^{(\mathrm{cg})}(\boldsymbol{\psi})\|_{\mathcal{H}} \tag{7}$$

where (5)-(7) hold $\forall m \in \mathcal{M}$ and the superscript $^{(\mathrm{cg})}$ indicates the signals at the center of gravity of the array[2].

The specific entries are then given as:

$$\mathbb{E}\left[\frac{\partial x(\boldsymbol{\psi})\partial x(\boldsymbol{\psi})^*}{\partial \tau^2}\right] = 2\Bigg(\frac{\sum\limits_{m \in \mathcal{M}} \|\underline{\dot{\boldsymbol{s}}}^{(m)}(\boldsymbol{\psi})\|_{\mathcal{H}}}{\sum\limits_{m \in \mathcal{M}} \|\underline{\boldsymbol{s}}^{(m)}(\boldsymbol{\psi})\|_{\mathcal{H}}^2}$$

$$-\frac{\Re\Big\{\sum\limits_{m \in \mathcal{M}} \langle \underline{\boldsymbol{s}}^{(m)}(\boldsymbol{\psi}), \underline{\dot{\boldsymbol{s}}}^{(m)}(\boldsymbol{\psi})\rangle_{\mathcal{H}}\Big\}^2}{\Big|\sum\limits_{m \in \mathcal{M}} \|\underline{\boldsymbol{s}}^{(m)}(\boldsymbol{\psi})\|_{\mathcal{H}}^2\Big|^2}\Bigg) \tag{8}$$

$$\approx 2\frac{\|\underline{\dot{\boldsymbol{s}}}^{(\mathrm{cg})}(\boldsymbol{\psi})\|_{\mathcal{H}}^2}{\|\underline{\boldsymbol{s}}^{(\mathrm{cg})}(\boldsymbol{\psi})\|_{\mathcal{H}}^2}\left(1 - \frac{\Re\big\{\langle \underline{\boldsymbol{s}}^{(\mathrm{cg})}(\boldsymbol{\psi}), \underline{\dot{\boldsymbol{s}}}^{(\mathrm{cg})}(\boldsymbol{\psi})\rangle_{\mathcal{H}}\big\}^2}{\|\underline{\boldsymbol{s}}^{(\mathrm{cg})}(\boldsymbol{\psi})\|_{\mathcal{H}}^2 \|\underline{\dot{\boldsymbol{s}}}^{(\mathrm{cg})}(\boldsymbol{\psi})\|_{\mathcal{H}}^2}\right), \tag{9}$$

$$= 8\pi^2 \beta_{\mathrm{w}}^2(\boldsymbol{\psi})\xi_\tau^2(\boldsymbol{\psi}), \tag{10}$$

where $\beta_{\mathrm{w}}^2(\boldsymbol{\psi}) = \|\underline{\dot{\boldsymbol{s}}}^{(\mathrm{cg})}(\boldsymbol{\psi})\|_{\mathcal{H}}^2/(4\pi^2\|\underline{\boldsymbol{s}}^{(\mathrm{cg})}(\boldsymbol{\psi})\|_{\mathcal{H}}^2)$ as the whitened effective square bandwidth and $\xi_\tau^2(\boldsymbol{\psi}) = 1 - \frac{\Re\big\{\langle \underline{\boldsymbol{s}}^{(\mathrm{cg})}(\boldsymbol{\psi}), \underline{\dot{\boldsymbol{s}}}^{(\mathrm{cg})}(\boldsymbol{\psi})\rangle_{\mathcal{H}}\big\}^2}{\|\underline{\boldsymbol{s}}^{(\mathrm{cg})}(\boldsymbol{\psi})\|_{\mathcal{H}}^2 \|\underline{\dot{\boldsymbol{s}}}^{(\mathrm{cg})}(\boldsymbol{\psi})\|_{\mathcal{H}}^2}$ as a loss factor w.r.t. the delay τ [1].

$$\mathbb{E}\left[\frac{\partial x(\boldsymbol{\psi})\partial x(\boldsymbol{\psi})^*}{\partial \varphi^2}\right] \approx \frac{2}{M}\sum_{m \in \mathcal{M}} D_m^2(\varphi)\Bigg(4\pi^2\beta_{\mathrm{w}}^2(\boldsymbol{\psi})$$

$$+ 4\pi^2 f_{\mathrm{c}}^2 - 4\pi f_{\mathrm{c}}\frac{\Im\big\{\langle \underline{\boldsymbol{s}}^{(\mathrm{cg})}(\boldsymbol{\psi}), \underline{\dot{\boldsymbol{s}}}^{(\mathrm{cg})}(\boldsymbol{\psi})\rangle_{\mathcal{H}}\big\}}{\|\underline{\boldsymbol{s}}^{(\mathrm{cg})}(\boldsymbol{\psi})\|_{\mathcal{H}}^2}\Bigg)$$

$$= \frac{8\pi^2}{M}\big(\beta_{\mathrm{w}}^2(\boldsymbol{\psi}) + f_{\mathrm{c}}^2 - f_{\mathrm{c}}\xi_\varphi(\boldsymbol{\psi})\big)\sum_{m \in \mathcal{M}} D_m^2(\varphi) \tag{11}$$

where $\xi_\varphi(\boldsymbol{\psi}) = \Im\big\{\langle \underline{\boldsymbol{s}}^{(\mathrm{cg})}(\boldsymbol{\psi}), \underline{\dot{\boldsymbol{s}}}^{(\mathrm{cg})}(\boldsymbol{\psi})\rangle_{\mathcal{H}}\big\}/(\pi\|\underline{\boldsymbol{s}}^{(\mathrm{cg})}(\boldsymbol{\psi})\|_{\mathcal{H}}^2)$ as a loss factor w.r.t. the AoA and the last three terms in (4) become zero as all include only one derivative w.r.t. the AoA leading to a single $\sum_{m \in \mathcal{M}} D_m(\varphi)$ which is zero.

Finally,

$$\mathbb{E}\left[\frac{\partial x(\boldsymbol{\psi})\partial x(\boldsymbol{\psi})^*}{\partial \tau \partial \varphi}\right] \approx 0, \tag{12}$$

as all terms in (4) become zero because all include only one derivative w.r.t. the AoA leading to a single $\sum_{m \in \mathcal{M}} D_m(\varphi)$ being zero.

---

[2]The approximations (5)-(7) hold exactly for either a stationary covariance matrix or the wideband signal model.

C Scheduling

To highlight the scheduling of the estimator, we chose to present results for the following (rather easy) setup: The main parameters are set to the same values as in the main text of the paper [2]. Furthermore, the number of samples $N = 107$, the number of SMCs $K = 3$ with parameters according to Table 1, the SNR = 23 dB, and the SDR = 0.7 dB.

	Parameters of SMCs	
	$\tilde{\tau}_k c$	$\tilde{\varphi}_k$
1	3	0
2	4	70
3	13	130

Table 1: Parameters of the SMCs including the delay expressed as a distance im m, and the AoA in °.

Fig. 1 depicts the results after certain parts of the algorithm have been computed. All subfigures include the squared absolute value of the residual signals (at the individual antennas, ——), the mean squared received signal (——), the mean squared residual signal (——), and the diagonal of the estimated covariance matrix (——) over relative delay expressed as a distance. Additionally, the parameters of the SMCs with a finite hyperparameter value are included in each subfigure in the table.

Fig. 1a shows the results after the first acquisition phase. As mentioned in the main part of the paper, the first acquisition phase is executed with an AWGN only model, meaning that the covariance matrix does only depend on σ_w^2. Due to the AWGN only model, the algorithm is not able (in the first acquisition phase) to find the correct SMCs, but rather underestimates the number of SMCs in the latter part of the signal and overestimates the number of SMCs in the first part of the signal. Fig. 1b shows the results after the parameters of the DMC have been initialized, including the refinement phase thereafter. One can see that the SMC at 3.75 m is pruned and only the first two SMCs are included in the model. After the second acquisition phase, presented in Fig. 1c, the third SMC is added to the model. Finally, Fig. 1d depicts the results after final convergence of the algorithm.

D Deterministic ML - Type I ML

As a comparison method, we utilize a Type I maximum likelihood estimator (also known as deterministic ML (DML)). This method is comparable to SAGE [3] or Rimax [4]. In comparison to the Type II maximum likelihood estimator (stochastic ML (SML)), the Type I ML looks at the complex amplitudes as deterministic unknowns. The log-likelihood function is given as

$$\log(f(\boldsymbol{r}|\boldsymbol{\Psi}, \boldsymbol{\eta}, \boldsymbol{\alpha})$$
$$\propto -\log(\det(\boldsymbol{C}(\boldsymbol{\eta}))) - \boldsymbol{r}^\mathrm{H} \boldsymbol{C}(\boldsymbol{\eta})^{-1} \boldsymbol{r}$$
$$+ \boldsymbol{\alpha}^\mathrm{H} \boldsymbol{S}(\boldsymbol{\Psi})^\mathrm{H} \boldsymbol{C}(\boldsymbol{\eta})^{-1} \boldsymbol{r} + \boldsymbol{r}^\mathrm{H} \boldsymbol{C}(\boldsymbol{\eta})^{-1} \boldsymbol{S}(\boldsymbol{\Psi}) \boldsymbol{\alpha}$$

182
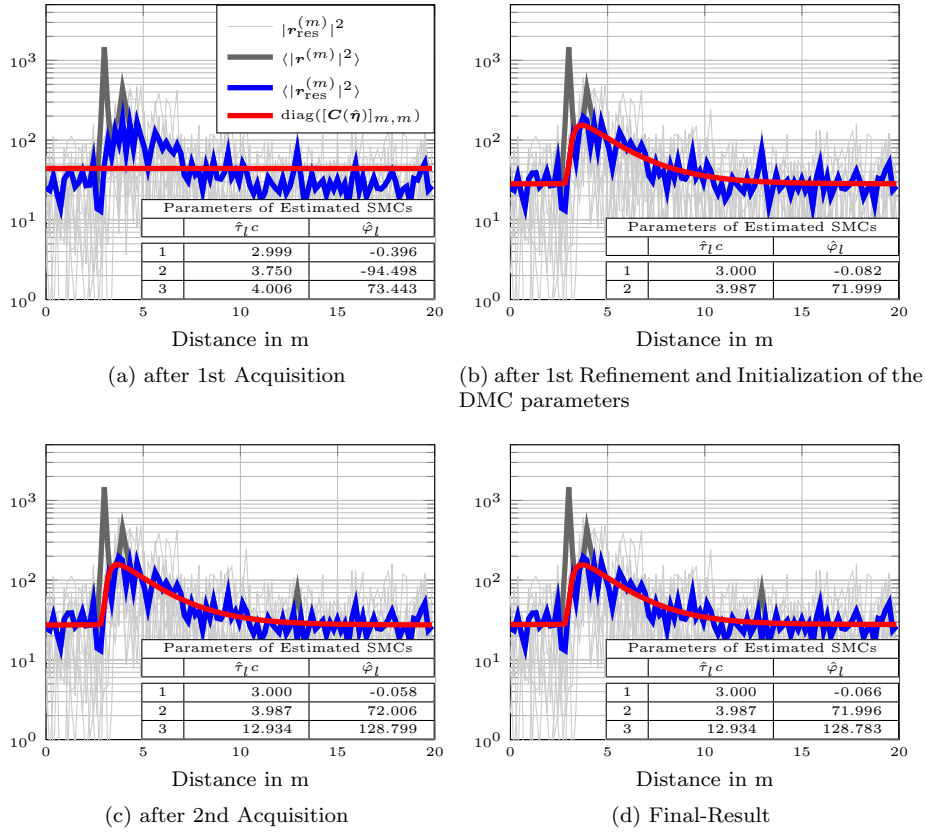
Figure 1: Exemplary view of the acquisition and refinement phases of the algorithm. Each subfigure shows a plot of the squared absolute value of the residual signal (———), the mean squared received signal (——), the mean squared residual signal (——), and the diagonal of the estimated covariance matrix (——) over the relative delay expressed as a distance. The estimated parameters of the SMCs with finite hyperparameter are included within the small table in each subfigure.).

$$- \boldsymbol{\alpha}^{\mathrm{H}} \boldsymbol{S}(\boldsymbol{\Psi})^{\mathrm{H}} \boldsymbol{C}(\boldsymbol{\eta})^{-1} \boldsymbol{S}(\boldsymbol{\Psi}) \boldsymbol{\alpha}. \tag{13}$$

Solving for the complex amplitude $\boldsymbol{\alpha}$ with $\boldsymbol{\eta}$ and $\boldsymbol{\Psi}$ kept fixed

$$\hat{\boldsymbol{\alpha}} = (\boldsymbol{S}(\boldsymbol{\Psi})^{\mathrm{H}} \boldsymbol{C}(\boldsymbol{\eta})^{-1} \boldsymbol{S}(\boldsymbol{\Psi}))^{-1} \boldsymbol{S}(\boldsymbol{\Psi})^{\mathrm{H}} \boldsymbol{C}(\boldsymbol{\eta})^{-1} \boldsymbol{r}. \tag{14}$$

Reinserting (14) into (13) leads to the concentrated log-likelihood function

$$
\begin{aligned}
\log(f(\boldsymbol{r}|\boldsymbol{\Psi}, \boldsymbol{\eta}, \boldsymbol{\alpha}) \\
\propto\; & -\log(\det(\boldsymbol{C}(\boldsymbol{\eta}))) - \boldsymbol{r}^{\mathrm{H}} \boldsymbol{C}(\boldsymbol{\eta})^{-1} \boldsymbol{r} \\
& + \boldsymbol{r}^{\mathrm{H}} \boldsymbol{C}(\boldsymbol{\eta})^{-1} \boldsymbol{S}(\hat{\boldsymbol{\Psi}}) (\boldsymbol{S}(\hat{\boldsymbol{\Psi}})^{\mathrm{H}} \boldsymbol{C}(\boldsymbol{\eta})^{-1} \boldsymbol{S}(\hat{\boldsymbol{\Psi}}))^{-1} \\
& \times \boldsymbol{S}(\hat{\boldsymbol{\Psi}})^{\mathrm{H}} \boldsymbol{C}(\boldsymbol{\eta})^{-1} \boldsymbol{r}.
\end{aligned}
\tag{15}
$$

183

Algorithm 1: Summary of the Type-I ML algorithm.

   Input   : signal measurement $\boldsymbol{r}$

   Output: Estimates of model order $\hat{K}$, atom parameters $\hat{\boldsymbol{\Psi}}$, noise and
               DMC parameters $\hat{\boldsymbol{\eta}}$, and complex amplitudes $\hat{\boldsymbol{\alpha}}$.

1 $\hat{\boldsymbol{\Psi}}, \hat{\boldsymbol{\alpha}} \leftarrow [\,]$

2 $\hat{\boldsymbol{\eta}} \leftarrow [\hat{\sigma}_{\mathrm{w}}^2, \hat{\boldsymbol{\vartheta}}^{\mathrm{T}}]^{\mathrm{T}}$ with $\hat{\sigma}_{\mathrm{w}}^2 \leftarrow \frac{\|\boldsymbol{r}\|^2}{NM}$ and $\hat{\boldsymbol{\vartheta}} \leftarrow [\,]$ (AWGN only)

3 **do**

4   `acquisition()`

5   `refinement()`

6   **if** *DMC not yet initialized* **then**

7 $\hat{\boldsymbol{\vartheta}} \leftarrow [1/c, \hat{\sigma}_{\mathrm{w}}^2/2NT_{\mathrm{s}}, T/2, T_{\mathrm{s}}]^{\mathrm{T}}$

8 $\hat{\boldsymbol{\eta}} \leftarrow [\hat{\sigma}_{\mathrm{w}}^2/2, \hat{\boldsymbol{\vartheta}}^{\mathrm{T}}]^{\mathrm{T}}$

9   initialize $\hat{\boldsymbol{\eta}}$ with least square curve fit

10   `refinement()`

11   **end**

12 $\hat{\boldsymbol{\alpha}} \leftarrow$ (14)

13 **while** $\|\hat{\boldsymbol{\mu}}_\alpha\|_0$ *changes*

14 $\hat{K} \leftarrow \|\hat{\boldsymbol{\alpha}}\|_0$

Based on the concentrated log-likelihood function in (15) we came up with the following Type I ML update rules for $\boldsymbol{\Psi}$ and $\boldsymbol{\eta}$

$$\hat{\boldsymbol{\Psi}} = \arg\min_{\boldsymbol{\Psi}} \; -\boldsymbol{r}^{\mathrm{H}}\boldsymbol{C}(\hat{\boldsymbol{\eta}})^{-1}\boldsymbol{S}(\boldsymbol{\Psi})(\boldsymbol{S}(\boldsymbol{\Psi})^{\mathrm{H}}\boldsymbol{C}(\hat{\boldsymbol{\eta}})^{-1}\boldsymbol{S}(\boldsymbol{\Psi}))^{-1}$$
$$\times \, \boldsymbol{S}(\boldsymbol{\Psi})^{\mathrm{H}}\boldsymbol{C}(\hat{\boldsymbol{\eta}})^{-1}\boldsymbol{r} \tag{16}$$

$$\hat{\boldsymbol{\eta}} = \arg\min_{\boldsymbol{\eta}} \; \log(\det(\boldsymbol{C}(\boldsymbol{\eta}))) + \boldsymbol{r}^{\mathrm{H}}\boldsymbol{C}(\boldsymbol{\eta})^{-1}\boldsymbol{r}$$
$$- \boldsymbol{r}^{\mathrm{H}}\boldsymbol{C}(\boldsymbol{\eta})^{-1}\boldsymbol{S}(\hat{\boldsymbol{\Psi}})(\boldsymbol{S}(\hat{\boldsymbol{\Psi}})^{\mathrm{H}}\boldsymbol{C}(\boldsymbol{\eta})^{-1}\boldsymbol{S}(\hat{\boldsymbol{\Psi}}))^{-1}$$
$$\times \, \boldsymbol{S}(\hat{\boldsymbol{\Psi}})^{\mathrm{H}}\boldsymbol{C}(\boldsymbol{\eta})^{-1}\boldsymbol{r}. \tag{17}$$

These update equations could also be derived by utilizing the same framework as in the main text of the paper. By postulating that the proxy pdfs factorize as $q(\boldsymbol{\Psi}, \boldsymbol{\eta}|\boldsymbol{r}) = q(\boldsymbol{\Psi}|\boldsymbol{r})q(\boldsymbol{\eta}|\boldsymbol{r})$ and assuming point estimates (to derive an ML) for $q(\boldsymbol{\Psi}|\boldsymbol{r}) = \delta(\boldsymbol{\Psi} - \bar{\boldsymbol{\Psi}})$ and $q(\boldsymbol{\eta}|\boldsymbol{r}) = \delta(\boldsymbol{\eta} - \bar{\boldsymbol{\eta}})$. Applying variational Bayesian inference on (15) we came up with the update rules in (16) and (17).

A summary of the proposed Type I ML algorithm is shown in Algorithm 1. We used the same scheduling as for the Type II ML to compare the two algorithms in a fair way.

To be able to infer the number of SMCs with the Type I framework, we utilized an adapted version of [5]. More specifically, we compute the following test statistic (compared to [5] we need to incorporate the non-stationary colored covariance matrix $\boldsymbol{C}$)

$$T(\hat{\boldsymbol{\psi}}_l) = \frac{|\langle \boldsymbol{C}^{-1/2}\boldsymbol{n}, P_{\bar{l}}^{\perp}\boldsymbol{C}^{-1/2}\boldsymbol{s}(\hat{\boldsymbol{\psi}}_l)\rangle|^2}{\|(P_{\bar{l}}^{\perp})^{1/2}\boldsymbol{C}^{-1/2}\boldsymbol{s}(\hat{\boldsymbol{\psi}}_l)\|^2}, \tag{18}$$

Procedure 1: Acquisition phase to add new components.

---

1 **Procedure** `acquisition()`
2   **do**
3 $\boldsymbol{r}_{\text{res}} = \boldsymbol{r} - \boldsymbol{S}(\hat{\boldsymbol{\Psi}})\hat{\boldsymbol{\alpha}}$
4 $\hat{\boldsymbol{\psi}}_{\text{candidate}} = \arg\min\limits_{\boldsymbol{\psi}} \frac{|\boldsymbol{r}_{\text{res}}^{\text{H}}\boldsymbol{C}(\hat{\boldsymbol{\eta}})^{-1}\boldsymbol{s}(\boldsymbol{\psi})|^2}{\boldsymbol{s}(\boldsymbol{\psi})^{\text{H}}\boldsymbol{C}(\hat{\boldsymbol{\eta}})^{-1}\boldsymbol{s}(\boldsymbol{\psi})}$
5   append $\hat{\boldsymbol{\psi}}_{\text{candidate}}$ to $\hat{\boldsymbol{\Psi}}$
6 $\hat{\boldsymbol{\eta}} \leftarrow$ update according to (17)
7 $\hat{\boldsymbol{\Psi}} \leftarrow$ update according to (16)
8 $\kappa^* \leftarrow$ (57) in main text [2]
9 $\boldsymbol{T} \leftarrow$ update according to (18)
10   **if** any($\boldsymbol{T} < \kappa^*$) **then**
11   remove component with minimal $\boldsymbol{T}$ from $\hat{\boldsymbol{\Psi}}$
12   **end**
13 $\hat{\boldsymbol{\alpha}} \leftarrow$ (14)
14   **while** $\|\hat{\boldsymbol{\alpha}}\|_0$ *grows or* $\|\hat{\boldsymbol{\alpha}}\|_0 \geq L$

Procedure 2: Refinement phase of the proposed algorithm.

---

1 **Procedure** `refinement()`
2   **do**
3 $\hat{\boldsymbol{\eta}} \leftarrow$ update according to (17)
4 $\hat{\boldsymbol{\Psi}} \leftarrow$ update according to (16)
5 $\kappa^* \leftarrow$ (57) in main text [2]
6 $\boldsymbol{T} \leftarrow$ update according to (18)
7   **if** any($\boldsymbol{T} < \kappa^*$) **then**
8   remove component with minimal $\boldsymbol{T}$ from $\hat{\boldsymbol{\Psi}}$
9   **end**
10   **while** *not converged*

---

where

$$P_{\bar{l}}^{\perp} = \boldsymbol{I} - \boldsymbol{C}^{-1/2}\boldsymbol{S}(\hat{\boldsymbol{\Psi}}_{\bar{l}})(\boldsymbol{S}(\hat{\boldsymbol{\Psi}}_{\bar{l}})^{\text{H}}\boldsymbol{C}^{-1}\boldsymbol{S}(\hat{\boldsymbol{\Psi}}_{\bar{l}}))^{-1}$$
$$\times \boldsymbol{S}(\hat{\boldsymbol{\Psi}}_{\bar{l}})^{\text{H}}\boldsymbol{C}^{-1/2} \tag{19}$$

is defined as the orthogonal projection operator onto the space spanned by $\boldsymbol{C}^{-1/2}\boldsymbol{S}(\hat{\boldsymbol{\Psi}}_{\bar{l}})$ and $\hat{\boldsymbol{\Psi}}_{\bar{l}}$ is the vector $\hat{\boldsymbol{\Psi}}$ without the l-th entry. Furthermore, we define $\boldsymbol{T} = [T(\hat{\boldsymbol{\psi}}_1)\dots T(\hat{\boldsymbol{\psi}}_L)]^{\text{T}}$. Using the same reasoning as in [5], we can utilize the threshold derived in the main text [2].

References

[1] K. Witrisal, E. Leitinger, S. Hinteregger, and P. Meissner, "Bandwidth scaling and diversity gain for ranging and positioning in dense multipath channels," *IEEE Wireless Commun. Lett.*, 2016.

[2] S. Grebien, E. Leitinger, K. Witrisal, and B. H. Fleury, "Super-resolution channel estimation including the dense multipath component — A sparse variational Bayesian approach," in preperation for submission to IEEE Trans. Signal Process.

[3] B. H. Fleury, M. Tschudin, R. Heddergott, D. Dahlhaus, and K. I. Pedersen, "Channel parameter estimation in mobile radio environments using the SAGE algorithm," *IEEE J. Sel. Areas Commun.*, vol. 17, no. 3, pp. 434–450, Mar. 1999.

[4] A. Richter, "Estimation of Radio Channel Parameters: Models and Algorithms," Ph.D. dissertation, Ilmenau University of Technology, 2005.

[5] B. Nadler and A. Kontorovich, "Model selection for sinusoids in noise: Statistical analysis and a new penalty term," *IEEE Trans. Signal Process.*, vol. 59, no. 4, pp. 1333–1345, Apr. 2011.

186

Additional Material for Reviewers:

Super-Resolution Channel Estimation Including the Dense Multipath Component — A Sparse Variational Bayesian Approach

Stefan Grebien[*], Erik Leitinger[*], Klaus Witrisal, Bernard H. Fleury

[*] Have equally contributed as first authors.

1   Special Cases of the Pruning Condition

In the following, we present some cases of special interest of the bound derived in [1, (44)]:

Corollary 1. *For blockspectrum (sinc-pulse in the time domain) and AWGN only, the bound in [1, (44)] reduces to*

$$\mathbb{P}\Big[\sup_{\boldsymbol{\psi}\in\Psi}\tilde{u}(\boldsymbol{\psi}) > \kappa\Big] \sim 4\pi\sqrt{\frac{N^2-1}{12}\left(f_{\mathrm{c}}^2 + \frac{N^2-1}{12N^2T_{\mathrm{s}}^2}\right)} \tag{1}$$

$$\times \int_{\varphi}\sqrt{\frac{1}{M}\sum_{m\in\mathcal{M}}D_m^2(\varphi)}\,\mathrm{d}\varphi\,\kappa\mathrm{e}^{-\kappa}.$$

Proof. By assuming AWGN only, $\beta_{\mathrm{w}}^2(\boldsymbol{\psi})$ reduces to the effective square bandwidth β^2. For block spectrum the effective square bandwidth is given as $\beta^2 = \|\underline{\dot{s}}^{(\mathrm{cg})}(\boldsymbol{\psi})\|^2/(4\pi^2\|\underline{s}^{(\mathrm{cg})}(\boldsymbol{\psi})\|^2) = (N^2-1)/(12N^2T_{\mathrm{s}}^2)$. The loss factors reduce to $\xi_\tau(\boldsymbol{\psi}) = 1 - \frac{\Re\left\{\langle\underline{s}^{(\mathrm{cg})}(\boldsymbol{\psi}),\underline{\dot{s}}^{(\mathrm{cg})}(\boldsymbol{\psi})\rangle\right\}^2}{\|\underline{s}^{(\mathrm{cg})}(\boldsymbol{\psi})\|^2\|\underline{\dot{s}}^{(\mathrm{cg})}(\boldsymbol{\psi})\|^2} = 1$ and $\xi_\varphi(\boldsymbol{\psi}) = \Im\left\{\langle\underline{s}^{(\mathrm{cg})}(\boldsymbol{\psi}),\underline{\dot{s}}^{(\mathrm{cg})}(\boldsymbol{\psi})\rangle\right\}/(\pi\|\underline{s}^{(\mathrm{cg})}(\boldsymbol{\psi})\|^2) = 0$ for an even or odd pulse waveform $\underline{s}(t)$ which completes the proof. □

Corollary 2. *In the case of a rectangular array with equally spaced antennas, (1) can be rewritten as*

$$\mathbb{P}\Big[\sup_{\boldsymbol{\psi}\in\Psi}\tilde{u}(\boldsymbol{\psi}) > \kappa\Big] \sim 4\pi\sqrt{\frac{N^2-1}{12}\left(f_{\mathrm{c}}^2 + \frac{N^2-1}{12N^2T_s^2}\right)} \tag{2}$$

$$\times \int_{\varphi}\sqrt{\left(\frac{d_x^2}{c^2}\sin^2(\varphi-\psi)\frac{M_x^2-1}{12} + \frac{d_y^2}{c^2}\cos^2(\varphi-\psi)\frac{M_y^2-1}{12}\right)}\mathrm{d}\varphi\kappa\mathrm{e}^{-\kappa},$$

where M_x and M_y are the numbers of antennas in x and y direction, respectively, and d_x and d_y are the spacings between the antennas in x and y direction,

187

respectively. For quadratic uniform arrays, the bound given in (2) *reduces to*

$$\mathbb{P}\Big[\sup_{\boldsymbol{\psi}\in\Psi}\tilde{u}(\boldsymbol{\psi})>\kappa\Big] \sim 8\pi^2\sqrt{\frac{N^2-1}{12}\left(f_{\mathrm{c}}^2+\frac{N^2-1}{12N^2T_{\mathrm{s}}^2}\right)\frac{d^2}{c^2}\frac{M-1}{12}}\kappa\mathrm{e}^{-\kappa}, \qquad (3)$$

where $d = d_x = d_y$ *is the spacing between antennas and* $M = M_xM_y$ *is the number of antennas.*

Proof. For a rectangular array, the square aperture function is given as

$$\sum_{m\in\mathcal{M}} D_m^2(\varphi) = M_y\frac{d_x^2}{c^2}\sin^2(\varphi-\psi)\frac{M_x(M_x^2-1)}{12}$$
$$+ M_x\frac{d_y^2}{c^2}\cos^2(\varphi-\psi)\frac{M_y(M_y^2-1)}{12}.$$

Plugging this into (1) yields (3). □

2 Comparison to Atomic Norm Soft Thresholding

In the last few years, several publications utilizing atomic norm denoising for spectral line estimation have been proposed [2,3]. While [2] focus on a single domain (either delay or AoA), [3] highlights the application of atomic norm denoising for two or more domains. For a single domain, an exact semidefinite program to solve atomic norm minimization can be developed [2]. However, for higher dimensional domain problems only an approximate semidefinite program can be formulated [3]. Furthermore, it is important to highlight that atomic norm methods denoise the received signal and do not directly estimate the number of components or the spectral frequencies of these components. Thus, another algorithm is needed, applied subsequently on the denoised signal. Thus, matrix enhancement and matrix pencil [4] is proposed to be applied to the denoised signal [3]. Furthermore, for atomic norm denoising to work, the following prerequisites need to be given: (i) additive white Gaussian noise, (ii) block spectrum, (iii) uniform linear array(ULA).

In the following two plots we compare the proposed algorithm with the algorithm proposed in [3], called Atomic Norm Soft Thresholding (ANST), and with the plain (without previously applying ANST) matrix enhancement and matrix pencil (MEMP) algorithm [4]. We chose to utilize the same simulation framework as in [1, Fig. 3] (estimation of two closely spaced SMCs).

In Fig. 1 the signal model as presented in [1, (3)] is used to generate the signal. The SDR $= \infty$ dB (or no DMC is simulated), SNR $= \{10, 30, 50\}$ dB, the number of samples is set to $N = 11$, and the number of antennas is 5. The location of the first SMC is drawn uniformly within the support of the delay and angular domain[1]. The location of the second dispersion parameter is then

---

[1]For this experiment the support of the delay of the first SMC $\tilde{\psi}_1$ is restricted to be in $[2T_p/c, T-(2T_p+\Delta\tau)/c$. The reason for this is that the SMCs shall be within the observation duration. For the angular domain the support of the AoA is restricted to be in $[-\pi/2 + \delta\varphi, \pi/2 - \delta\varphi + \Delta\varphi)$, where $\delta\varphi$ is the Rayleigh resolution of the ULA.
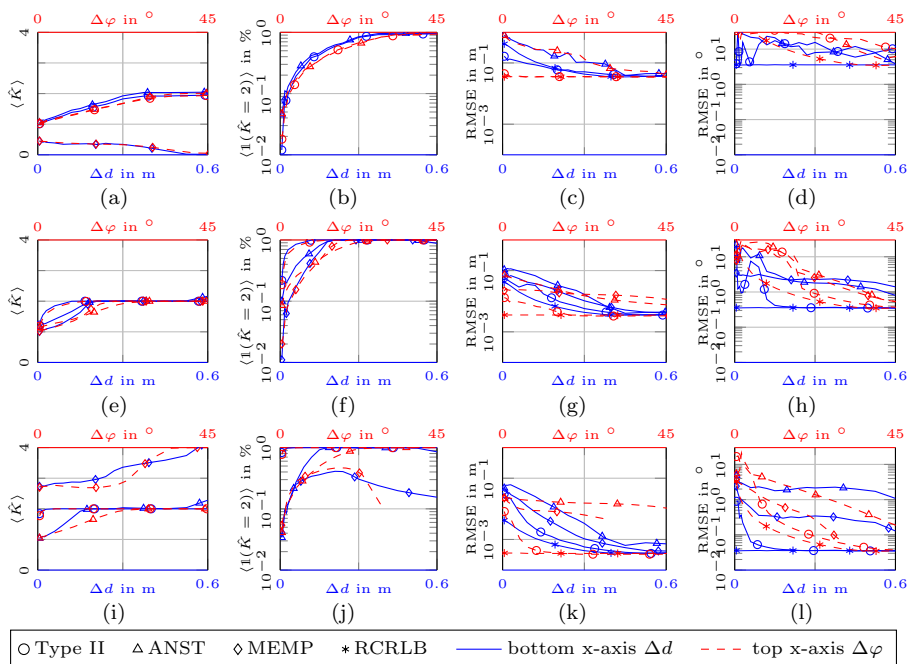
Figure 1: Estimation of two closely spaced SMCs with a 1×5 uniform linear array in AWGN with known covariance matrix. Blue solid lines and red dashed lines refer to the bottom and top x-axis, respectively. The rows depict different SNR: (a)-(d) SNR = 10 dB, (e)-(h) SNR = 30 dB, and (i)-(l) SNR = 50 dB. The columns depict the mean number of estimated SMCs ((a), (e), and (i)), the relative frequency that exactly 2 SMCs are found ((b), (f), and (j)), the RMSE of the delay ((c), (g), and (k)), the RMSE of the AoA ((d), (h), and (l)).

given by $\tilde{\boldsymbol{\psi}}_2 = \tilde{\boldsymbol{\psi}}_1 + [\Delta\tau, 0]^{\mathrm{T}}$ or $\tilde{\boldsymbol{\psi}}_2 = \tilde{\boldsymbol{\psi}}_1 + [0, \Delta\varphi]^{\mathrm{T}}$ for the bottom x-axis (blue solid curves) and top axis (red dashed curves) in Fig. 1, respectively. In Fig. 1 we actually depict the delays as distances (remember that $d = \tau c$ with c as speed-of-light) for better readability of the plots.

The first column in Fig. 1 shows the mean number of estimated components. The Type II (circles) and ANST (triangles) estimators show a comparable performance for low SNR. The MEMP only (diamonds) estimator does not work anymore and only estimates an single SMC if the components start overlapping and may add up constructively. Remember that the complex amplitudes are drawn randomly, thus the two overlapping SMCs can add up constructively or destructively. For a higher SNR (second row) the Type II estimator outperforms both, the ANST and MEMP estimator which perform similarly. For very high SNR (third row), the MEMP estimates too many SMCs. This is due to a model mismatch of the generative and inference signal model. The generative signal model is based on [1, (3)] which we refer to as ultra-wideband (UWB) signal model. The inference model for MEMP (and also ANST) is based on a wideband signal model which neglects the time delay between different antenna elements,

189

thus [1, (3)] becomes

$$r^{(m)}(t) = \sum_{k \in \mathcal{K}} \tilde{\alpha}_k \mathrm{e}^{j2\pi f_c g(\tilde{\varphi}_k, \boldsymbol{p}^{(m)})} \underline{s}(t - \tilde{\tau}_k). \tag{4}$$

This model mismatch leads to additional estimated SMCs for the MEMP estimator. The ANST method reduces this problem, as the denoising process takes part of this mismatch and contributes it to noise. The subsequently applied MEMP algorithm, used on the denoised signal, is then able to find the correct number of SMCs. However, for a spacing of exactly twice the inverse of the Nyquist bandwidth, the ANST algorithm shows more outliers. This is due to the fact, that the sidelobes of the two SMCs overlap exactly, leading to potentially constructive interference between the two mismodeled SMCs. We verified that at spacings of multiples of the inverse of the Nyquist bandwidth this behavior occurs again.

The second column in Fig. 1 presents the probability that exactly two SMCs are detected. The third and fourth column depict the RMSE if exactly 2 SMCs are found of the distance and the AoA, respectively. The same association process as in [1] is utilized. The proposed Type II estimator outperforms the ANST and MEMP estimators nearly for all SNRs. Only the RMSE for the AoA at the lowest SNR (Fig. 1d) shows larger outliers than the ANST and MEMP estimators. This can be explained by the large sidelobes of a ULA (especially at AoAs approaching endfire) and the iterative nature of the proposed algorithm. As the ANST and MEMP algorithm perform a global optimization they do not show this behavior. However, in our opinion, this behavior is not a big problem. By reducing the aperture of the array slightly, meaning that we reduce the antenna spacing to values below $\lambda/2$, these outliers vanish. For the MEMP estimator it is not possible to reduce the array aperture, as it operates in the spatial frequency domain, meaning that the estimated frequency is in the range from $[-0.5, 0.5]$. However, for array spacings below $\lambda/2$ the frequency is generally in a smaller range $[-f_r, f_r]$, where $f_r < 0.5$.

In Fig. 2, the same analysis as in Fig. 1 is presented if the generative model is changed to the wideband model given in (4). For the proposed Type II estimator we also changed the inference model to the wideband model. Now the ANST and MEMP estimator do not show the outliers at high SNR. Nevertheless, the proposed estimator outperforms both the ANST and the MEMP estimator. At low SNR (first row) the ANST estimator performs better than the MEMP estimator as the denoising of the received signal leads to an increased detection of the SMCs. At high SNR (second row) both the ANST and MEMP estimator perform nearly similar and at very high SNR (third row) the MEMP estimator outperforms the ANST estimator. This can be explained, as for the ANST algorithm a subsequent MEMP algorithm is applied after denoising. However, for MEMP to estimate the number of components a noise estimate is necessary. While for the MEMP only method the noise is assumed to be known (as for the denoising process in ANST), the noise of the denoised signal is unknown and needs to be estimated [4, 5].

190
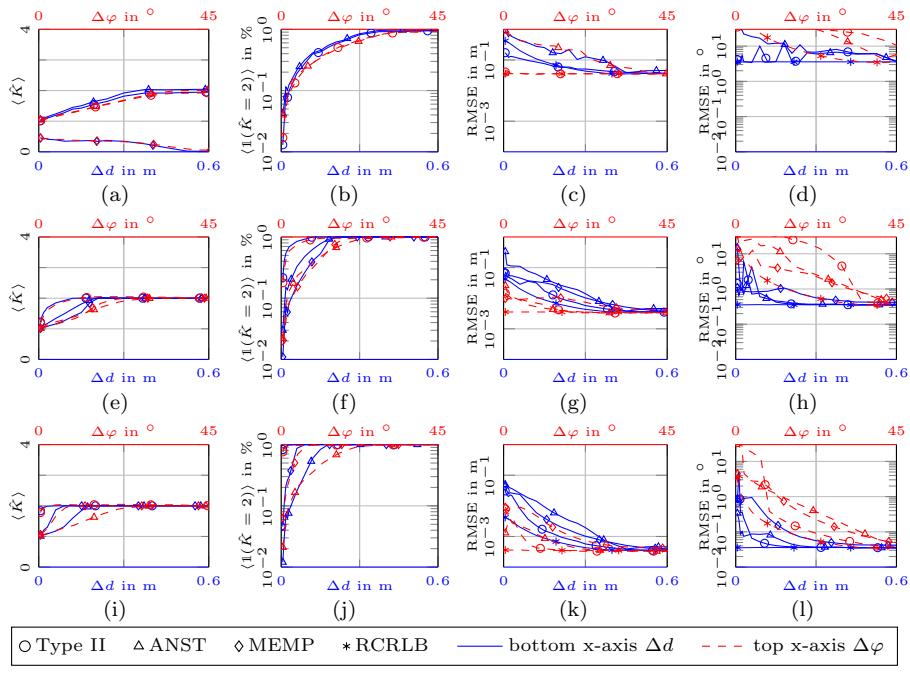
Figure 2: Estimation of two closely spaced SMCs with a 1×5 uniform linear array in AWGN with known covariance matrix. Blue solid lines and red dashed lines refer to the bottom and top x-axis, respectively. The rows depict different SNR: (a)-(d) SNR = 10 dB, (e)-(h) SNR = 30 dB, and (i)-(l) SNR = 50 dB. The columns depict the mean number of estimated SMCs ((a), (e), and (i)), the relative frequency that exactly 2 SMCs are found ((b), (f), and (j)), the RMSE of the delay ((c), (g), and (k)), the RMSE of the AoA ((d), (h), and (l)).

References

[1] S. Grebien, E. Leitinger, K. Witrisal, and B. H. Fleury, "Super-resolution channel estimation including the dense multipath component — A sparse variational Bayesian approach," in preperation for submission to IEEE Trans. Signal Process.

[2] B. N. Bhaskar, G. Tang, and B. Recht, "Atomic norm denoising with applications to line spectral estimation," *IEEE Trans. Signal Process.*, vol. 61, no. 23, pp. 5987–5999, Dec. 2013.

[3] Y. Chi and Y. Chen, "Compressive two-dimensional harmonic retrieval via atomic norm minimization," *IEEE Trans. Signal Process.*, vol. 63, no. 4, pp. 1030–1042, Feb. 2015.

[4] Y. Hua, "Estimating two-dimensional frequencies by matrix enhancement and matrix pencil," *IEEE Trans. Signal Process.*, vol. 40, no. 9, pp. 2267–2280, Sep. 1992.

[5] K. Konstantinides and K. Yao, "Statistical analysis of effective singular values in matrix rank determination," *IEEE Trans. Acoust., Speech, Signal Process.*, vol. 36, no. 5, pp. 757–763, May 1988.

192

193

194